REVIEW

The history and future of semiconductor heterostructures

Zh. I. Alferov

A. F. Ioffe Physicotechnical Institute, Russian Academy of Sciences, 194021 St. Petersburg, Russia
(Submitted July 22, 1997; accepted for publication July 27, 1997)
Fiz. Tekh. Poluprovodn. **32**, 1–18 (January 1998)

The history of the development of semiconductor heterostructures and their applications in various electron devices is presented, along with a brief historical survey of the physics, production technology, and applications of quantum wells and superlattices. Advances in recent years in the fabrication of structures utilizing quantum wires and especially quantum dots are discussed. An outline of future trends and prospects for the development and application of these latest types of heterostructures is presented. © *1998 American Institute of Physics.*
[S1063-7826(98)00101-X]

1. INTRODUCTION

It would be very difficult today to imagine solid state physics without semiconductor heterostructures. Semiconductor heterostructures and especially double heterostructures, including quantum wells, quantum wires, and quantum dots, currently comprise the object of investigation of two thirds of all research groups in the physics of semiconductors.

While the feasibility of controlling the type of conductivity of a semiconductor by doping it with various impurities and the concept of nonequilibrium carrier injection are the seeds from which semiconductor electronics has sprung, heterostructures provide the potential means for solving the far more general problem of controlling fundamental parameters in semiconductor crystals and devices, such as the width of the bandgap, the effective masses and mobilities of charge carriers, the refractive index, and the electron energy spectrum.

The development of the physics and technology of semiconductor heterostructures has brought about tremendous changes in our everyday lives. Heterostructure-based electron devices are widely used in many areas of human activity. Life without telecommunication systems utilizing double-heterostructure (DH) lasers, without heterostructure light-emitting diodes (LEDs) and bipolar transistors, or without the low-noise, high-electron-mobility transistors (HEMTs) used in high-frequency devices, including satellite television systems, is scarcely conceivable. The DH laser is now found in virtually every home as part of the compact-disk (CD) player. Solar cells incorporating heterostructures are used extensively in both space and terrestrial programs; for almost a decade now the Mir space station has been utilizing solar cells based on AlGaAs heterostructures.

Our interest in semiconductor heterostructures did not come about by accident. A systematic investigation of semiconductor heterostructures was launched in the very early thirties at the Physicotechnical Institute (FTI) under the direct supervision of its founder, Abram Fedorovich Ioffe. In 1932, V. P. Zhuze and B. V. Kurchatov studied the intrinsic and impurity conductivities of semiconductor heterostructures.[1] In the same year A. F. Ioffe and Ya. I. Frenkel' formulated the theory of current rectification at a metal-semiconductor interface, based on the tunneling effect.[2] In 1931 and in 1936 Frenkel' published his celebrated papers,[3] in which he predicted excitonic phenomena and, naming them as such, developed the theory of excitons in semiconductor heterostructures. Excitons were eventually detected experimentally by Gross in 1951.[4] The first diffusion theory of a rectifying $p-n$ heterojunction, laying the foundation for W. Shockley's theory of the $p-n$ junction, was published by B. I. Davydov in 1939.[5] Research on intermetallic compounds commenced at the Physicotechnical Institute at the end of the forties on the initiative of Ioffe. The theoretical prediction and experimental discovery of the properties of III–V semiconductor compounds were achieved independently by N. H. Welker[6] and by N. A. Goryunova and A. R. Regel' at the Physicotechnical Institute.[7] We have drawn very heavily from the high theoretical, technological, and experimental level of the research conducted at the Physicotechnical Institute in that era.

2. CLASSICAL HETEROSTRUCTURES

The idea of using heterostructures in semiconductor electronics emerged at the very dawn of electronics. Already in the first patent associated with $p-n$ junction transistors W. Shockley[8] proposed the application of a wide-gap emitter to achieve one-way injection. At our Institute A. I. Gubanov first analyzed theoretically the current-voltage ($I-V$) curves of isotypic and anisotypic heterojunctions[9]; however, some of the most important theoretical explorations in this early stage of heterostructure research were carried out by H. Kroemer, who introduced the concept of quasielectric and quasimagnetic fields in a smooth heterojunction and hypothesized that heterojunctions could possess extremely high injection efficiencies in comparison with homojunctions.[10] Various notions concerning the application of semiconductor heterostructures in solar cells evolved in that same time period.

The next important step was taken several years later, when we and Kroemer[11] independently formulated the concept of DH–based lasers. In our patent we noted the feasi-

bility of attaining a high density of injected-carriers and population inversion by ''double'' injection. We specifically mentioned that homojunction lasers ''do not provide continuous lasing at elevated temperatures,'' and to demonstrate an added benefit of DH lasers, we explored the possibility of ''increasing the emitting surface and utilizing new materials to achieve emission in different regions of the spectrum.''

In his article Kroemer proposed that DHs be used to confine carriers to the active zone. He postulated that a pair of heterojunction injectors could be used to achieve lasing in many indirect-gap semiconductors and to improve it in the direct-gap kind.

In the beginning theoretical research significantly outpaced its experimental implementation. In 1966, we predicted[12] that the injected-carrier density could well be several orders of magnitude greater than the carrier density in a wide-gap emitter (the ''superinjection'' phenomenon). That same year, in a paper[13] submitted to the new Soviet journal *Fizika i Tekhnika Poluprovodnikov* [in translation: *Soviet Physics Semiconductors*], I generalized our conception of the principal advantages of DHs for various devices, particularly for lasers and high-power rectifiers:

''The regions of recombination, light emission, and population inversion coincide and are concentrated entirely in the middle layer. Owing to potential barriers at the boundary of semiconductors with different bandgap widths, even for large displacements in the direction of transmission, there is absolutely no indirect passage of electron and hole currents, and the emitters have zero recombination (in contrast with $p-i-n$, $p-n-n^{+}$, $n-p-p^{+}$, where recombination plays a decisive role).

''Population inversion to generate stimulated emission can be achieved by pure injection means (double injection) and does not require a high doping level of the middle region and especially does not require degeneracy. Because of the appreciable difference in the dielectric constants, light is concentrated entirely in the middle layer, which functions as a high-Q waveguide, and optical losses in the passive regions (emitters) are therefore nonexistent.''

Following are the most important advantages discerned by us on the part of semiconductor heterostructures at that time:

- superinjection of carriers;
- optical confinement;
- electron confinement.

All that now remained was to find a heterostructure in which these effects could be implemented.

At the time there was widespread skepticism regarding the feasibility of fabricating an ''ideal'' heterojunction with a defect-free boundary and especially one that exhibited the theoretically predicted injection properties. Even the pioneering work of R. L. Anderson[14] on the first epitaxial single-crystal heterojunction with exactly identical Ge–GeAs lattice constants failed to give any proof of nonequilibrium carrier injection in heterostructures. The actual construction of efficient, wide-gap emitters was regarded as a sheer impossibility, and many viewed the patent for a DH laser as a ''paper patent.''

It was mainly on account of this general skepticism that only a few research groups were attempting to find the ''ideal'' pair, and indeed the task was a formidable one. Many conditions had to be met to find the right compatibility between the thermal, electrical, and crystal-chemical properties of the interfaced materials, not to mention their crystal and band structures.

At that time an auspicious combination of several properties—specifically low effective masses and a wide bandgap, effective radiative recombination and a sharp optical absorption edge due to the ''direct'' band structure, high electron mobility at the absolute minimum of the conduction band and a drastic reduction in mobility at the nearest minimum at the (100) point—had already garnered gallium arsenide a reputable place in semiconductor physics and electronics. Since the maximum effect is attainable by interposing a heterojunction between a semiconductor functioning as the active zone of a device and a material having a wider bandgap, the most promising systems studied at the time were GaP–GaAs and AlAs–GaAs. For ''compatibility'' the materials of the pair had to satisfy the first and most important condition: closest proximity of the lattice constants. Heterojunctions in the system AlAs–GaAs were the preferred choice for this reason. However, a certain psychological barrier had to be overcome before work could begin on the preparation and investigation of the properties of these heterojunctions. By that time AlAs had already long been in production,[15] but many properties of this compound had yet to be studied, because AlAs was known to be chemically unstable and to decompose in a humid atmosphere. The possibility of obtaining a stable heterojunction suitable for practical applications held little promise in this system.

Our attempts to construct a double heterostructure initially focused on the incompatible-lattice system GaAsP. We successfully fabricated the first lasers using DHs in this system by vapor-phase epitaxy (VPE). However, owing to the incompatibility of the lattice parameters, lasing could be achieved, as in homojunction lasers, only at liquid-nitrogen temperatures.[16] It is interesting to note, however, that this was the first practical result for an incompatible-lattice and even partially relaxing structure.

Our experience acquired in studying the system GaAsP was of utmost importance toward understanding many specific physical properties of heterojunctions and the fundamentals of heteroepitaxy. The development of multichamber VPE for the system GaAsP enabled us in 1970 to build superlattice structures with a period of 200 Å and to demonstrate the splitting of the conduction band into minibands.[17]

By the end of 1966, however, we had concluded that even a small discrepancy between the lattice parameters in $GaP_{0.15}As_{0.85}$–GaAs heterostructures stood in the way of achieving the potential advantages of DHs. At that time a colleague in my group, D. N. Tret'yakov, gave me a status report on small crystals that had been prepared from $Al_xGa_{1-x}As$ solid solutions two years earlier and placed in a desk drawer by A. S. Borshchevskiĭ: Nothing happened with them during that period. At that moment it immediately became clear that $Al_xGa_{1-x}As$ solutions were chemically stable and were suitable candidates for the preparation of

long-lived heterostructures and devices. An investigation of the phase diagrams and growth kinetics in this system, along with the development of a modification of the liquid-phase epitaxy (LPE) method in adaptation to the growth of heterostructures, promptly resulted in the fabrication of the first compatible-lattice AlGaAs heterostructure. When we published the first paper on this topic, we were elated to know that we had been the first to observe the unique and, in fact, ideal heterostructure—a compatible-lattice system for GaAs, but as so often happens, the same results were achieved simultaneously and independently by H. Rupprecht, J. Woodall, and G. Pettit at the IBM Thomas J. Watson Research Center.[18]

Subsequent progress in the area of semiconductor heterostructures was swift. First and foremost, we confirmed experimentally the unique injection properties of wide-gap emitters and the superinjection phenomenon,[19] demonstrated stimulated emission in AlGaAs double-heterostructures,[20] established the band diagram of an $Al_xGa_{1-x}As$–GaAs heterojunction, and conducted a meticulous investigation of the luminescence properties and carrier diffusion in a smooth heterojunction, along with the extremely interesting characteristics of the current flowing through a heterojunction, for example, diagonal tunnel-recombination transitions directly between holes from the narrow-gap component and electrons from the wide-gap component of a heterojunction.[21]

In that same time period we fabricated the majority of the most important devices exploiting the principal advantages of heterostructures:

- low-threshold, room-temperature DH lasers[22] (Fig. 1);
- high-efficiency LEDs operating on single and double heterostructures[23];
- heterostructure solar cells[24];
- bipolar transistors utilizing heterostructures[25];
- thyristor *p–n–p–n* switches utilizing heterostructures.[26]

Most of these results were reproduced in other laboratories in the next year or two, in some cases even later. In 1970, however, international competition became very heated. One of our major competitors in the years to follow, I. Hayashi, who worked with M. Panish at Bell Telephone Laboratories in Murray Hill, New Jersey, wrote[27]: ''In September of 1969, Zhores Alferov of the Ioffe Institute in Leningrad visited our laboratory. We learned that he had obtained $J_{th}^{(300)}=4.3\ \mathrm{kA/cm^2}$ using a double heterostructure. Until that time, we had not been aware that the competition was so intense, and we redoubled our efforts...'' In a paper submitted in May of 1970[28] we reported the achievement of a continuous lasing regime in lasers with a stripe geometry, formed by photolithography and mounted on silver-coated copper heat conduits (Fig. 2). The lowest threshold current density J_{th} at 300 K was $940\ \mathrm{A/cm^2}$ for wide lasers and $2.7\ \mathrm{kA/cm^2}$ for stripe lasers. A continuous lasing regime in DH lasers was reported independently by Izuyo Hayashi and Morton Panish[29] (for wide lasers with a diamond heat conduit) in a paper submitted one month later than our own. The achievement of continuous lasing at room temperature triggered an explosion of interest in the physics and technology of semiconductor heterostructures. In 1969, AlGaAs heterostructures had been studied in a scant few laboratories, mainly in the USSR (at the A. F. Ioffe Physicotechnical Institute and in the Polyus and Kvant Industrial Laboratories, where we introduced our technologies for applications programs) and in the United States (at Bell Telephone Laboratories, the RCA David Sarnoff Research Center, and the IBM Thomas J. Watson Research Center), whereas in the beginning of 1971 many universities, industrial laboratories in the USA, the USSR, Great Britain, Japan, and also in Brazil and Poland were launching investigations of heterostructures and devices utilizing them on the basis of III-V compounds.

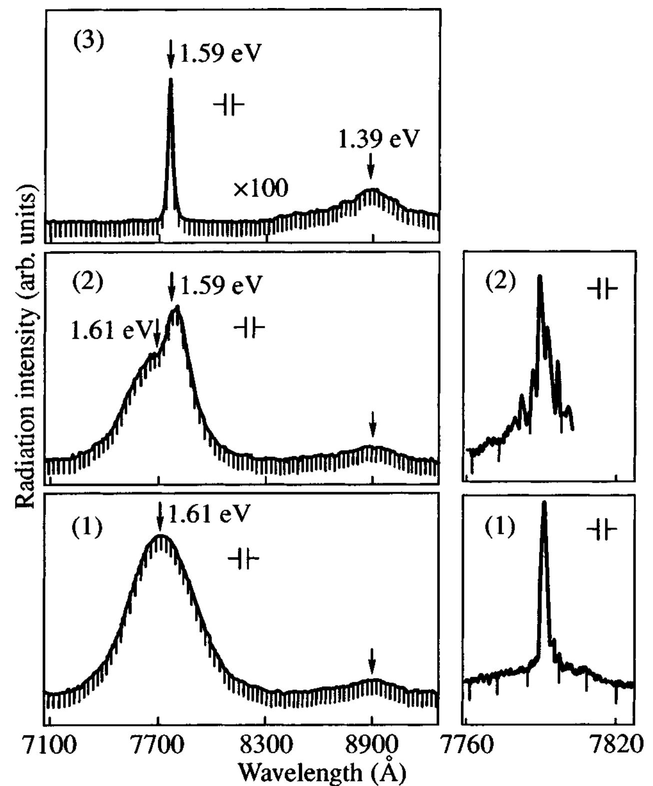

FIG. 1. Emission spectrum of the first low-threshold $Al_xGa_{1-x}As$ DH laser operating at room temperature (300 K), $J_{th}=4300\ \mathrm{A/cm^2}$. The current rises from 1) 0.7 A to 2) 8.3 A and then to 3) 13.6 A (Ref. 22).

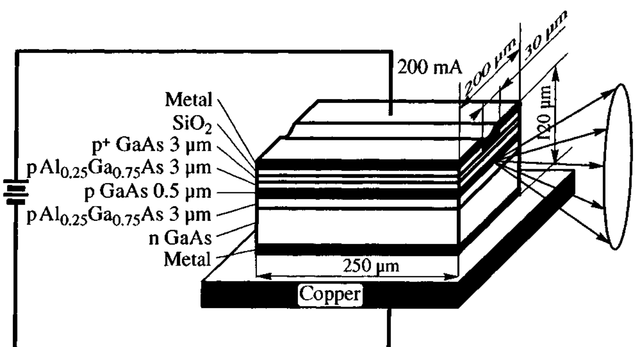

FIG. 2. Schematic view of the structure of the first injection DH laser operating in the CW regime at room temperature.

It was soon clear in this early stage of development of the physics and technology of heterostructures that we needed to look for new compatible-lattice heterostructures if we were to extend the spectral range. The first important step was taken in our laboratory in 1970. At that time, we reported[30] the feasibility of obtaining different compatible-lattice heterojunctions by using four III-V solid solutions, which permit the lattice constant and the width of the bandgap to be varied independently. Antipas *et al.*[31] later arrived at the same conclusion. As a practical example utilizing this idea, we investigated various InGaAsP compositions, which soon emerged as one of the most important materials for a number of applied problems: photocathodes[32] and especially lasers operating in the infrared range for fiber-optic communications[33] and also in the visible range.[34]

We formulated the basic concepts of the distributed-feedback (DFB) laser in a 1971 Soviet inventor's certificate.[35] That same year H. Kogelnik and C. Shank explored the possibility of replacing Fabry-Perot or similar cavities in dye lasers by periodic bulk inhomogeneities.[36] It should be noted that their approach is not applicable to semiconductor lasers, and all investigators of semiconductor lasers with DFB or distributed Bragg reflectors (DBRs) use the ideas formulated by Alferov *et al.*:[35]

1) The diffraction grating is formed not in the bulk, but on the surface of the waveguide layer.

2) The interaction of waveguide modes with the surface diffraction grating produces not only distributed feedback, but also well-collimated radiation at the output.

A detailed theoretical analysis of the operation of a semiconductor laser with a surface grating was published in 1972.[37] In that study the authors confirmed the feasibility of single-mode lasing. The first semiconductor lasers with a surface grating and DFB were obtained nearly simultaneously at the Physicotechnical Institute,[38] Caltech in Pasadena,[39] and Xerox Laboratory in Palo Alto.[40]

In the early eighties, H. Kroemer and G. Griffiths published a paper[41] that heightened interest in heterostructures having a stepped band structure (type-II heterojunctions). The spatial separation of electrons and holes at such heterointerfaces means that their optical properties can be regulated between wide limits.[21c,42] The stepped band structure affords the possibility of obtaining optical radiation with photon energies much smaller than the width of the bandgap of each semiconductor forming the heterojunction. The creation of an injection laser on the basis of type-II heterojunctions in the system GaInAsSb–GaSb (Ref. 42) has opened up excellent opportunities for the construction of efficient coherent light sources in the infrared optical range. Emission takes place in structures of this type as a result of the recombination of electrons and holes localized in self-consistent potential wells situated on opposite sides of a heterojunction. Type-II heterostructures have thus generated new possibilities, both in fundamental research and for device applications otherwise impossible to fulfill using type-I heterostructures in the system of III–V compounds. So far, however, the practical application of type-II heterostructures has been restricted by inadequate comprehension of their fundamental

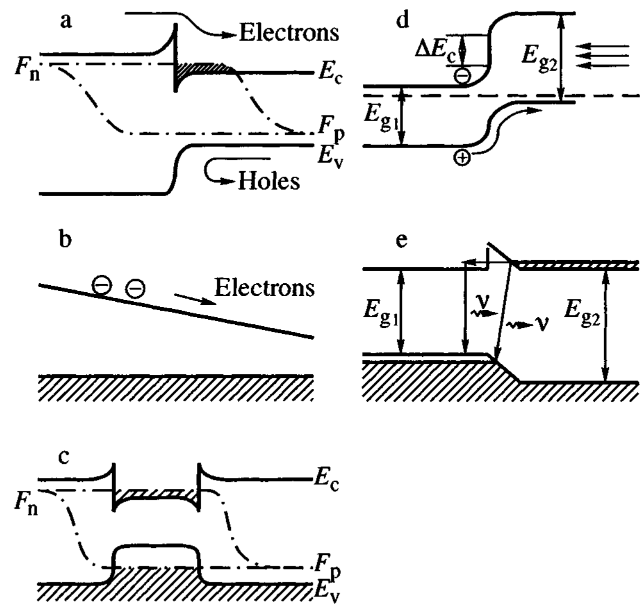

FIG. 3. Main physical phenomena in classical heterostructures. a) One-way injection and superinjection; b) diffusion in an imbedded quasielectric field; c) electron and optical confinement; d) wide-gap window effect; e) diagonal tunneling through a heterojunction.

physical properties and the limited number of experimentally investigated systems.

We now present a brief summary of the most important results in the development of classical heterostructures, classifying them by what we think should be a sensible scheme.

Classical heterostructures

I. *Fundamental physical phenomena* (Fig. 3):

- one-way injection;
- superinjection;
- diffusion in the imbedded quasielectric field;
- electron confinement;
- optical confinement;
- the wide-gap window effect;
- diagonal tunneling through the heterojunction.

II. *Major implications for applications in semiconductor devices:*

- low-threshold semiconductor lasers operating in the continuous-wave (CW) regime at room temperature, distributed-feedback lasers, lasers with distributed Bragg reflectors, surface-emitting lasers, and infrared lasers utilizing type-II heterostructures;
- high-efficiency light-emitting diodes;
- solar cells and photodetectors based on the wide-gap window effect;
- semiconductor integrated optics based on DFB and DBR semiconductor lasers;
- heterobipolar transistors with a wide-gap emitter;
- transistors, thyristors, and dynistors with light-signal transmission;
- high-power diodes and thyristors;
- infrared and visible-range light converters;
- efficient cold cathodes.

III. *Important technological considerations*

• fundamental need for structures with well-matched lattice parameters;

• the use of multicomponent solid solutions to match the lattice parameters;

• fundamental need for epitaxial growth technologies.

This brief survey of the early development of ''bulk'' heterostructures is aptly concluded with the statement that the fabrication of an ''ideal'' heterojunction and the introduction of the heterostructure concept in semiconductor physics and technology has resulted in the discovery of new physical phenomena, dramatic improvement in the characteristics of essentially all known semiconductor devices, and the construction of new types of the latter.

3. HETEROSTRUCTURES WITH QUANTUM WELLS AND SUPERLATTICES

Because of electron confinement in double heterostructures, DH lasers have essentially become the direct precursors to quantum-well structures, which have a narrow-gap middle layer with a thickness of a few hundred angstroms, an element that has the effect of splitting the electron levels as a result of quantum-well effects. However, high-quality DHs with ultrathin layers could not be attained until new methods were developed for the growth of heterostructures. Two principal modern-day epitaxial growth techniques with precision monitoring of thickness, planarity, composition, etc., were developed in the seventies. Today molecular-beam epitaxy (MBE) has grown into one of the most important technologies for the growth of heterostructures using III–V compounds, primarily through the pioneering work of A. Cho.[43] The basic concepts of metal-organic vapor-phase epitaxy (MOVPE) were set forth in the early work of H. Manasevit[44] and have enjoyed widespread application for the growth of heterostructures from III–V compounds, particularly in the wake of a paper by R. Dupuis and P. Dapkus reporting the successful use of this technique to create a room-temperature injection DH laser in the system AlGaAs.[45]

The distinct manifestation of quantum-well effects in the optical spectra of GaAs–AlGaAs semiconductor heterostructures with an ultrathin GaAs layer (quantum well) was demonstrated by R. Dingle *et al.* in 1974.[46] The authors observed a characteristic step structure in the absorption spectra and a systematic shift of the characteristic energies as the thickness of the quantum well was decreased.

The experimental investigation of superlattices commenced in 1970 with L. Esaki and R. Tsu's work[47] on electron transport in a superlattice, i.e., in a structure with an auxiliary periodic potential generated by doping or by varying the composition of semiconductor materials with a period greater than, but still comparable with the lattice constant. In this crystal, what Leo Esaki called a ''man-made crystal,'' the parabolic bands split into minibands, which were separated by small bandgaps and had a Brillouin zone dictated by the period of the superlattice. Similar ideas had been formulated by L. V. Keldysh back in 1962 in a study[48] of a periodic potential generated on the surface of a semiconductor by a high-intensity ultrasonic wave. At the Physicotechnical Institute in the seventies, R. Kazarinov and R. Suris conducted a theoretical investigation of current transmission in superlattice structures.[49] They showed that the passage of current is governed by tunneling through potential barriers separating the wells. The authors also predicted important physical effects: carrier tunneling under the influence of an electric field when the ground state of one well coincides with an excited state of the next well, and stimulated emission produced when optically excited carriers tunnel from the ground state of one well to an excited state of a neighbor at a lower energy level due to an applied electric field. Independently and at essentially the same time L. Esaki and R. Tsu investigated resonance tunneling effects in superlattice structures.[50]

The first experimental studies of structures with superlattices were carried out by L. Esaki and R. Tsu on superlattices formed by VPE in the system GaP_xAs_{1-x}–GaAs. In our laboratory at that time we developed the first multichamber device and, as mentioned before, prepared structures with $GaP_{0.3}As_{0.7}$–GaAs superstructures incorporating a total of 200 layers, each with a thickness of 100 Å (Ref. 17). The observed prominent features of the $I-V$ curves, their temperature dependences, and the photoconduction effect were attributed to splitting of the conduction band under the influence of the one-dimensional periodic potential of the superlattice. These first superlattices appeared concurrently with the first strained-layer superlattices. In the mid-seventies A. E. Blakeslee and J. Matthews, working in collaboration with Easki and Tsu at IBM, achieved remarkable advances in the growth of strained superlattices exhibiting a very low defect density. However, not until a much later date, following the theoretical work of G. Osbourn[51] of Sandia National Laboratories and the growth of the first high-quality GaAs–$In_{0.2}Ga_{0.8}As$ strained-layer superlattice by M. Ludowise at Varian Associates, was N. Holonyak of the University of Illinois successful in using these structures to build a CW laser capable of operating at room temperature.[52] It came to light that the stress of the lattice in strained-layer superlattices constitutes an additional degree of freedom, and such fundamental parameters as the width of the bandgap, the lattice constant, etc., can be varied continuously and independently of each other by varying the thickness and composition of the layers.

In the early seventies, L. Esaki *et al.* applied MBE technology to the system AlGaAs (Ref. 53), and in March of 1974 they published a paper on resonance tunneling.[54] This was the first experimental demonstration of the new physical properties of quantum-well heterostructures. They measured the variations of the tunneling current and conductivity as functions of the applied stress in a double-barrier GaAs–GaAlAs heterostructure (Fig. 4) and observed current maxima associated with resonance tunneling. Later in that same year Esaki and Chang observed the resonance tunneling phenomenon in a superlattice.[55] The heightened preoccupation with resonance tunneling was obviously also attributable to the potential applications of this phenomenon in high-speed electronics. Toward the end of the eighties, picosecond switching times were attained for a double resonance-tunneling diode, and oscillations at a frequency of 420 GHz

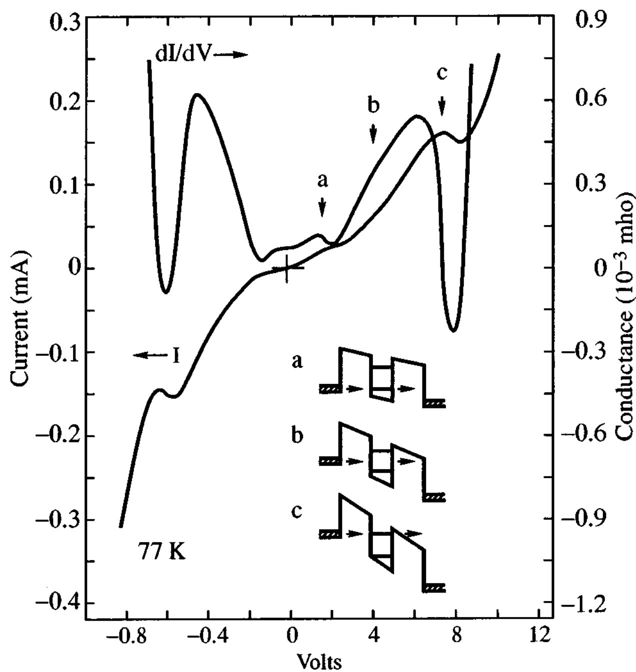

FIG. 4. $I-V$ curve and conductance-voltage curve of a two-barrier GaAs–GaAlAs structure. Resonance (a, c) and nonresonance (b) conditions are indicated by arrows in the inset (according to Chang, Esaki, and Tsu[54]).

were obtained at room temperature in GaAs resonance-tunneling diodes.

The transition to two-dimensional electron motion in field-effect transducers had been confirmed quite some time ago and in 1966 was first verified for electrons trapped in an inversion layer by A. B. Fowler *et al.*[57] in magnetoconductivity experiments. Spectral effects associated with spatial quantization were also observed in bismuth thin films by V. N. Lutskii and L. A. Kulik in 1968.[58]

The first study of modulation-doped superlattices,[59] in which the enhancement of mobility in comparison with bulk crystals was demonstrated, stimulated the development of research on the use of a two-dimensional electron gas with high mobility for microwave amplification. Almost simultaneously in France and Japan new types of transistors were designed using a single modulation-doped n-AlGaAs–n-GaAs heterostructure, acquiring the names TEGFET (two-dimensional electron-gas field-effect transistor) in France[60] and HEMT (high-electron mobility transistor) in Japan.[61]

Lasing by means of quantum wells was first accomplished by J. P. van der Ziel *et al.*,[62] but the lasing parameters fell short of average DH lasers. It was 1978 before R. Dupuis and P. Dapkus in collaboration with N. Holonyak reported the first construction of a quantum-well (QW) laser with parameters to match those of standard DH lasers.[63] The term ''quantum well'' first surfaced in this paper. The real advantage of QW lasers was demonstrated much later by W. T. Tsang of Bell Telephone Laboratories. Through a major improvement in MBE growth technology and the synthesis of an optimized structure in the form of a separate-confinement (double) heterostructure with a smooth variation of the refractive index in the waveguide region (graded-index separate-confinement heterostructure—GRINSCH) it was possible to lower the threshold current density to 160 A/cm^2 (Ref. 64).

Not until the end of the seventies did MBE and MOVPE techniques for the growth of III–V heterostructures begin to be developed at the Physicotechnical Institute. Our primary efforts were directed toward the development and construction of the first Soviet MBE device in our electronics industry. Several years were spent in the development of three generations of MBE devices; the last of the three, called *Tsna* (after a picturesque river flowing near the city of Ryazan, home of the Scientific-Research and Technological Institute of the Electronics Industry—NITI—where the MBE devices were developed), was good enough for the implementation of scientific programs. Very soon thereafter we launched the parallel development of MBE systems at the Scientific-Technical Branch of the Academy of Sciences in Leningrad. Several systems of this class were produced by the Physicotechnical Institute in the mid-eighties. Both types of MBE systems are still in operation at the Physicotechnical Institute and in other Russian laboratories.

We developed MOVPE systems at our Institute and later in the eighties, with our active participation, the Epiquip Company in Sweden specially designed a pair of systems for our Institute, which have continued to be used in scientific research up to the present time.

Considerable interest in the study of low-dimensional structures and the lack of equipment for MBE and MOVPE growth technologies motivated us to work on the development of a liquid-phase epitaxy technique suitable for the growth of QW heterostructures.

Until the end of the seventies, however, it appeared to be impossible to grow III–V heterostructures with an active zone of thickness less than 500 Å by LPE, owing to the existence of extended transition regions of variable chemical composition near the heterojunctions.

The situation changed thanks to the work of N. Holonyak *et al.*,[65] who proposed that a LPE system with rotating ''boats'' be used to grow superlattices based on InGaAsP compounds. In our laboratory we developed a modified LPE method with conventional sequential displacement of the substrate in a standard horizontal ''boat'' geometry for InGaAsP heterostructures[66] and a low-temperature LPE method for AlGaAs heterostructures.[67] These methods enabled us to grow QW heterostructures of exceptional quality in essentially any form with active zones having thicknesses as small as 20 Å and with transition zones comparable in size with the lattice constant (Fig. 5). An important practical asset was the attainment, using LPE, of unprecedented threshold current densities in lasers utilizing separate confinement and a single quantum well based on InGaAsP/InP heterostructures ($\lambda = 1.3\,\mu$m and $1.55\,\mu$m) and InGaAsP/GaAs ($\lambda = 0.65 - 0.9\,\mu m$). In the case of high-power InGaAsP/GaAs lasers ($\lambda = 0.8\,\mu$m) (Fig. 6) constructed in a stripe geometry, 66% efficiency and a radiated power of 5 W for a stripe of width 100 μm were attained in CW operation.[69] These lasers were the first to implement the effective cooling of a high-power semiconductor device through recombination radiation, as predicted earlier in Ref. 13. Another impor-

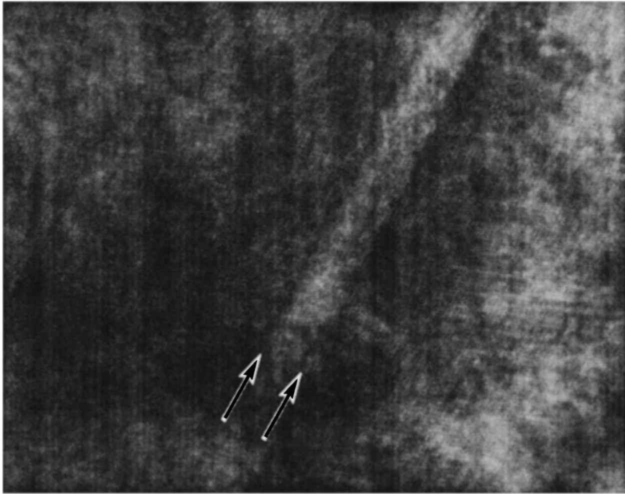

FIG. 5. Thin InGaAsP layer in an InGaP/InGaAsP/InGaP/GaAs structure with a quantum well grown by MBE. The image was produced by end-on TEM.

tant feature of InGaAsP heterostructures was their fairly high resistance to the onset and growth of dislocations and defects (Fig. 7).[70] The cited investigations marked the beginning of the widespread application of aluminum-free heterostructures.

The most complex QW laser structure, consolidating a single quantum well and short-period superlattices (SPSs) to form a GRINSCH (by far the preferred configuration for minimizing threshold currents), was grown in our laboratory in 1988 (Ref. 71, Fig. 8). Using SPSs, we succeeded not only in obtaining the desired index profile in the waveguide region and creating a barrier against the motion of dislocations

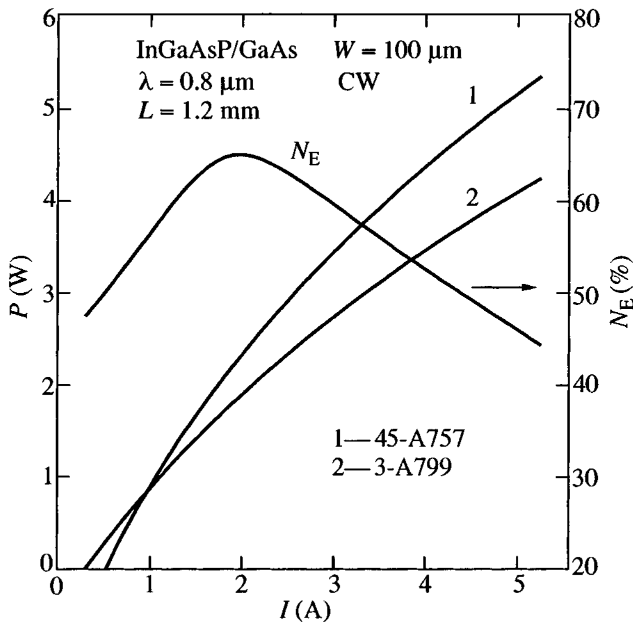

FIG. 6. Power-current ($P-I$) curves of InGaAsP-GaAs laser diodes with a single quantum well in the CW regime. *1*) Diode with strongly and weakly reflecting surfaces; *2*) diode with strongly reflecting surfaces only. The $N_E(I)$ curve represents the dependence of the energy conversion efficiency on the current.

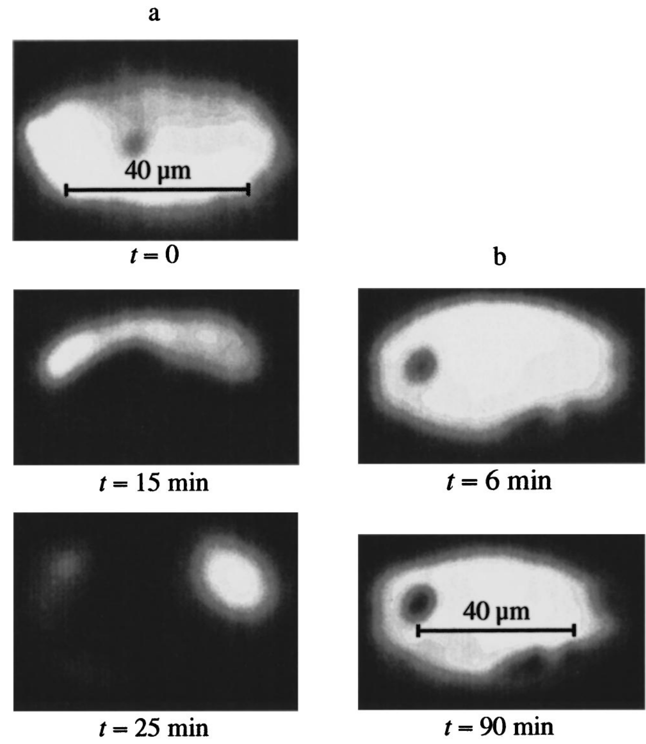

FIG. 7. Time evolution of the luminescence pattern from the active zone in AlGaAs–GaAs (a) and InGaAsP–GaAs (b) separate-confinement DHs with a single quantum well at a high photoexcitation level. Diameter of the excitation spot of the Kr^+ laser ~40 μm. Excitation levels: a) 10^4 W/cm^2; b) 10^5 W/cm^2.

into the active zone, but also in acquiring the capability of growing different parts of the structure at significantly different temperatures. We therefore achieved excellent surface morphology simultaneously with a high internal quantum efficiency on a planar GaAs(100) surface. We obtained threshold current densities J_{th}=52 A/cm^2 and, after a certain optimization, J_{th}=40 A/cm^2, which still stands as the world

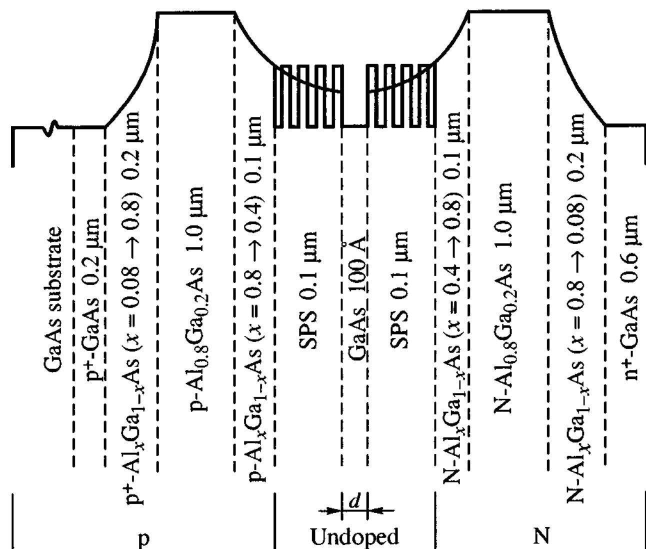

FIG. 8. Structure of a separate-confinement double-heterostructure laser with a quantum well bounded by an MBE-grown short-period superlattice.

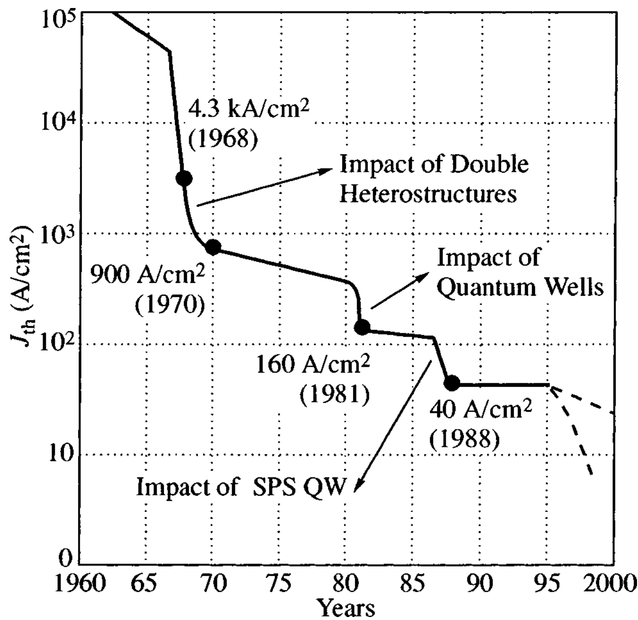

FIG. 9. Evolution of the threshold current of semiconductor lasers.

record for semiconductor injection lasers and affords a good demonstration of the effective use of quantum wells and superlattices in electron devices.

The concept of stimulated emission in superlattices, set forth by R. Kazarinov and R. Suris,[49] was made a reality by F. Capasso *et al.*[72] almost a quarter-century later. The previously proposed structure was substantially optimized, and the cascade laser developed by Capasso gave birth to a new generation of unipolar lasers operating in the mid-IR range.

From a certain standpoint, the history of semiconductor lasers is the history of the campaign to lower the threshold current, as graphically illustrated in Fig. 9. The most significant changes in this endeavor did not take place until the concept of DH lasers had been introduced. The application of SPS quantum wells actually brought us to the theoretical limit of this most important parameter. Subsequent possibilities associated with the use of new structures utilizing quantum wires and quantum dots will be discussed in the next section of the article.

Quite possibly the most significant discovery associated with the study of quantum wells was the quantum Hall effect.[73] This discovery and its comprehensive investigation in AlGaAs–GaAs heterostructures, quickly culminating in the discovery of the fractional quantum Hall effect,[74] had a fundamental influence on all of solid state physics. The disclosure of this effect, which involves only fundamental quantities and does not depend on the specific characteristics of the band structure or the carrier mobility and density in the semiconductor, showed that heterostructures can also be used to model certain fundamental physical phenomena. A large portion of the research in this area has recently been focused on gaining insight into the electron condensation mechanism and looking for Wigner crystallization.

We now briefly generalize the basic tenets of this section by a scheme similar to that used in the preceding section on classical heterostructures.

Quantum-well and superlattice heterostructures

I. *Fundamental physical phenomena in quantum-well and superlattice heterostructures:*

- two-dimensional electron gas;
- step function describing the density of states;
- quantum Hall effect;
- fractional quantum Hall effect;
- existence of excitons at room temperature;
- resonance tunneling in double-barrier and superlattice structures;
- carrier energy spectrum in superlattices determined by the choice of potential and elastic stresses;
- stimulated emission by resonance tunneling in superlattices;
- pseudomorph growth of strained structures.

II. *Major implications for applications in semiconductor devices:*

- shorter emission wavelengths, lower threshold current, higher differential gain, and weaker temperature dependence of the threshold current in semiconductor lasers;
- infrared quantum cascade lasers;
- lasers with quantum wells bounded by short-period superlattices;
- optimization of electron and optical confinement and of the waveguide characteristics in semiconductor lasers;
- two-dimensional, electron-gas, field-effect transistors (TEGFETs);
- resonance-tunneling diodes;
- high-current resistance standards;
- devices based on the electroabsorption effect and electrooptical modulators;
- infrared photodetectors based on absorption between quantum-well levels.

III. *Important technological considerations*

- no need to match lattice parameters;
- fundamental need to use slow-growth technologies (MBE and MOVPE);
- submonolayer growth method;
- suppression of the propagation of mismatch dislocations during epitaxial growth;
- radical diversification of materials available for heterostructure components.

4. QUANTUM-WIRE AND QUANTUM-DOT HETEROSTRUCTURES

During the eighties progress in the physics of two-dimensional quantum-well heterostructures and their practical applications lured many scientists to the study of systems of even lower dimensionality: quantum wires and quantum dots. In contrast with quantum wells, where carriers are restrained in the direction perpendicular to the layers and can move freely in the plane of the layer, the carriers in quantum wires are restrained in two directions and are free to move only along the axis of the wire. In quantum ''dots'' we have in effect ''artificial atoms,'' where the charge carriers are now restrained in all three directions and have a completely

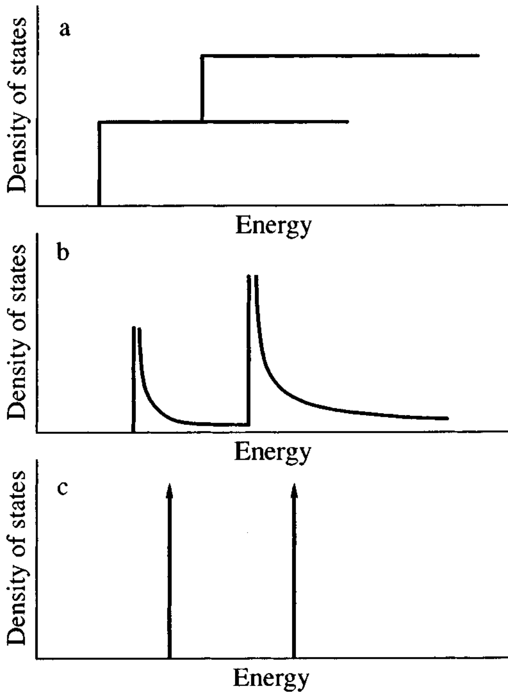

FIG. 10. Schematic diagrams of the density of states function for structures with quantum wells (a), quantum wires (b), and quantum dots (c).

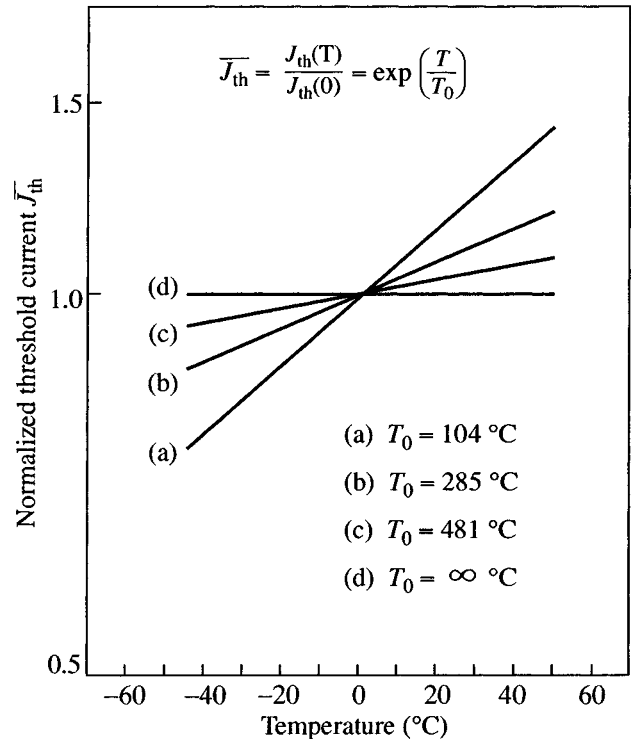

FIG. 11. Normalized temperature dependence of the threshold current for various DH lasers. a) Bulk; b) with QWs; c) with QWs; d) with QDs.

discrete energy spectrum. Figure 10 shows a schematic diagram of the density of states function for QWs, quantum wires (QWs), and quantum dots (QDs).

Experimental work on the construction and investigation of QW structures began more than a decade ago.[75] At the same time, theoretical investigations were addressing problems associated with one of the most interesting applications: QW lasers.[76] Y. Arakawa and H. Sakaki[76] suggested the possibility of abating the temperature dependence of the threshold current density for a QW laser and postulated the total temperature stability of QD lasers (Fig. 11). A vast number of papers, both theoretical and experimental, have been published to date in this area. The transport and capacitance properties of QWs have been investigated, along with vertical and transverse tunneling in QW and QD structures. In QW laser structures photoluminescence measurements have been carried out in the far-IR region of the spectrum, the Raman spectra have been studied, optical gains have been measured, and the anomalies of the optical properties have been investigated with special attention to polarization effects. The greatest success in the construction of QW lasers has probably been achieved by S. Simhony *et al.*[77] So far, however progress in this field has been very slow, and the most interesting applications of structures utilizing quantum wires have yet to be implemented sometime in the future.

The first superconducting dots—microcrystals of II–VI compounds formed in a glass matrix—were proposed and created by A. I. Ekimov and A. A. Onushchenko.[78] Their work was an outgrowth of important theoretical QD research begun by Al. I. Éfros and A. L. Éfros at the Physicotechnical Institute.[79] However, the imbedding of the semiconductor QDs in an insulating glass matrix and the poor quality of the heterojunction between the glass and the superconducting dot imposed definite limitations both on fundamental investigations and on device applications. The most intriguing possibilities emerged with the formation of three-dimensional QDs coherent with the superconductive matrix surrounding them.[80]

Several methods have been proposed for the preparation of these structures. Indirect methods, which include the preparation of QDs by transverse etching out from SW structures, often suffer from inadequate resolution and damage to the heterojunction during the etching process. The outlook is better for the application of direct methods of preparation such as growth in V-grooves and on corrugated surfaces, resulting in the formation of QWs and QDs. The laboratories of the Physicotechnical Institute and the Technical University of Berlin—lately engaged in close collaboration researching the subject–have made considerable strides in precisely this direction.

We have now concluded that the most promising method for the formation of ordered arrays of QWs and QDs is one that utilizes the phenomenon of self-organization, or self-assembly, on crystal surfaces. Stress relaxation at the edges of steps or facets can lead to the formation of ordered arrays of QWs and QDs in the growth of materials, regardless of whether the lattice parameters match or mismatch. The spontaneous formation of various ordered structures on crystal surfaces with a periodicity much greater than the lattice parameter has been the subject of vigorous theoretical investigations.[81,82] Our ultimate aim is to produce an ideal semiconductor quantum dot, whose energy spectrum, like that of an atom, would be described by a δ-function. To exploit the advantages of this approach to the fullest, it is

necessary to create a dense, homogeneous array of wires and dots, otherwise nonuniform broadening can totally negate the advantages of reduced dimensionality. Such nanostructures must have dimensions confined to a few nanometers to ensure energy gaps equal to a few times kT between the electron and hole sublevels at room temperature. They must also be free of dislocations and defects.

One mechanism for the formation of ordered nanostructures is faceting, where the flat crystal surface is reorganized into a periodic ''hills-and-valleys'' structure to diminish the free energy on the surface.[81,82]

Another class of self-organized structures suitable for the preparation of QWs and QDs comprises ordered arrays of highly strained ''islands'' of monolayer height, which form spontaneously during the submonolayer deposition of one material on another with a stark mismatch between the two lattice parameters.[85,86]

Very uniform arrays of three-dimensional QDs, also with transverse ordering, have been produced recently in the system InAs–GaAs by the deposition of InAs coatings with a thickness greater than one monolayer using both MBE and MOVPE growth techniques.[87,88]

The mechanism driving the formation of an array of homogeneous strained islands on the crystal surface is stress relaxation at the facet edges and interaction of the islands through the stresses generated by them in the substrate.[89] In most cases experiments show that the islands have a fairly narrow size distribution[87] and, in addition, that the coherent InAs islands under certain conditions form a quasiperiodic square grid. The shape of the QDs can be significantly altered during the formative growth period, during postgrowth annealing, or by means of complex growth manipulations. The alternate short-period deposition of different stressed materials results in splitting of the QDs and the formation of superlattices from planes of vertically coupled QDs (Figs. 12 and 13).[90–94] It has been observed that the emission energy from the ground state of a QD coincides with the absorption edge and the lasing energy.[87] The observation of ultranarrow (<0.15 meV) luminescence lines from solitary QDs[87] (Fig. 14), which do not exhibit any tendency to broaden as the temperature rises (Fig. 15),[91] is proof of the formation of QDs with an energy spectrum described by a δ-function.

It is anticipated that QD lasers will have higher characteristics than standard quantum-well lasers. They are expected to simultaneously exhibit such unique attributes as high differential gain, ultralow current density thresholds, and high temperature stability of the threshold current density.[76] In addition, ordered arrays of QDs formed in the optical waveguide region can induce distributed feedback and (or) stabilize single-mode laser emission. Quantum-dot structures buried *in situ* in a semiconductor spatially localize carriers and prevent their nonradiative recombination at the mirrors of a cavity. This technique avoids overheating of the cavity mirrors, which is one of the most serious problems of high-power and high-efficiency AlGaAs–GaAs and AlGaAs–InGaAs lasers.

In our first publication on InGaAs QD lasers[92] we have shown that: 1) the threshold current density is extremely stable, with a characteristic temperature (T_0) of approximately 350–400 K in the temperature range 30–150 K, and a low threshold current density (120 A/cm^2) is obtained in the temperature range 70–150 K; 2) single-mode lasing in a longitudinal mode is observed at both low and high tempera-

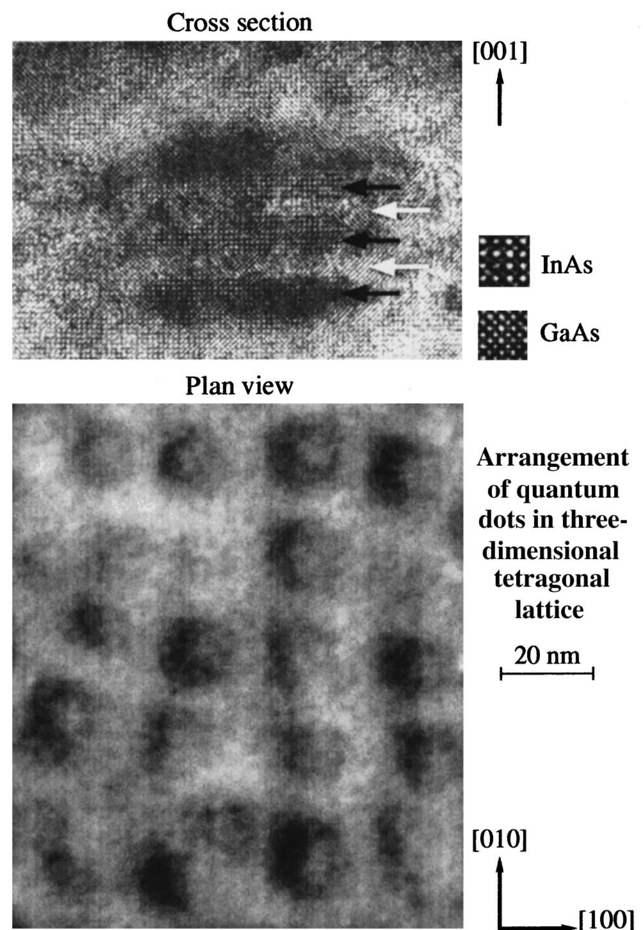

FIG. 12. Vertical and transverse ordering of coupled QDs in the system InAs–GaAs.

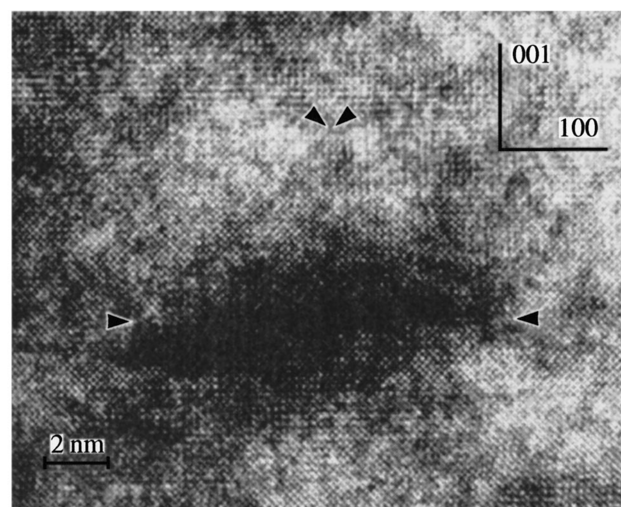

FIG. 13. High-resolution end-on TEM image of a single quantum dot in the deposition of three InAs monolayers. The facets are indicated by arrows.

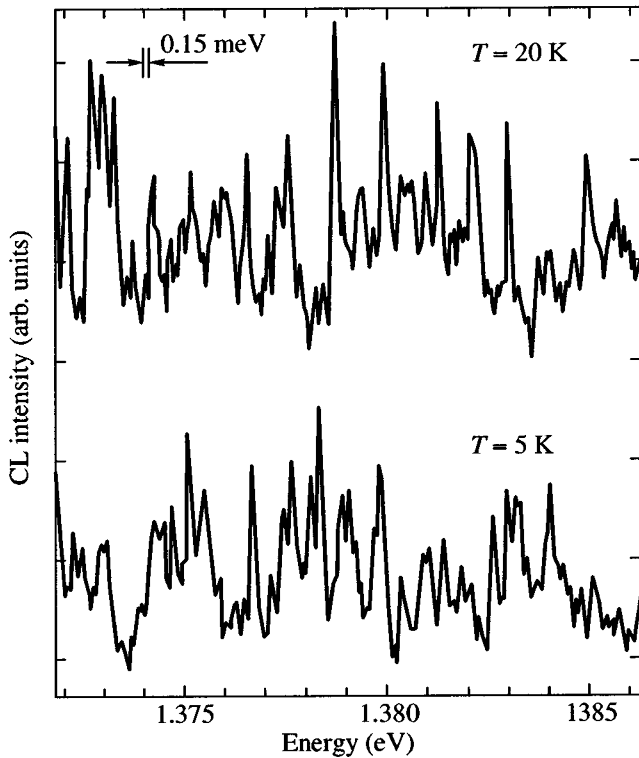

FIG. 14. High-resolution cathodoluminescence (CL) spectrum of InAs–GaAs QD structures.

tures (300 K). The characteristic temperature (T_0 = 350 K) far exceeds the theoretical limit for a QW laser.

The relatively small energy difference between the exciton ground states in a QD and the wetting layer (~100 meV) and between the exciton state in the QD and the exciton state in the GaAs barrier (~200 meV) leads to the highly effective delocalization of excitons and carriers from QDs at high temperatures (>170 K). As a result, T_0 is lowered (T_0~60 K), the lasing energy shifts closer to the exciton energy in the wetting layer, and the threshold current density increases to 950 A/cm^2 at 300 K to compensate the resulting drop in gain.

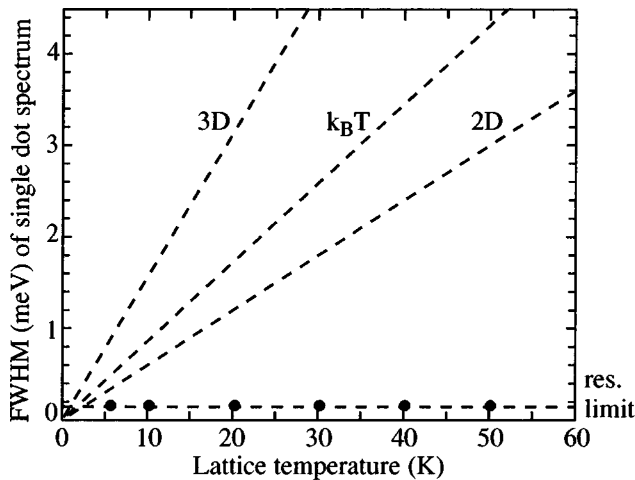

FIG. 15. Temperature dependence of the full width at half-maximum (FWHM) of the cathodoluminescence peak.

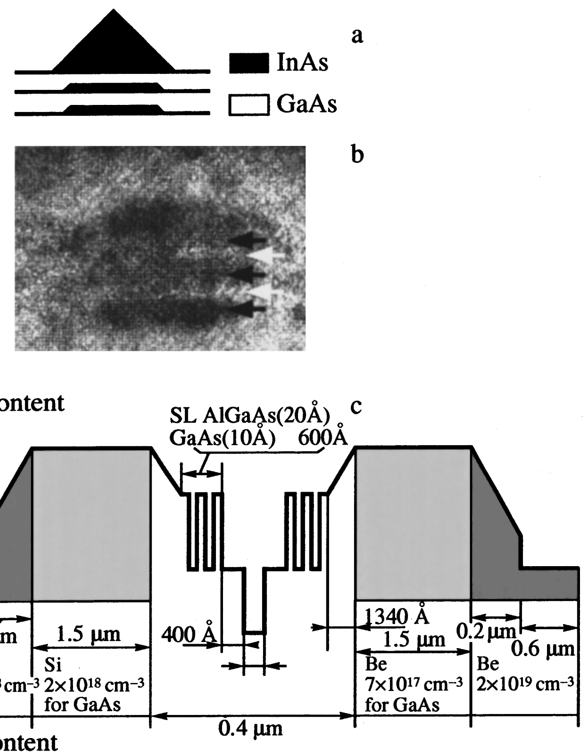

FIG. 16. Lasers utilizing vertically coupled quantum-dot arrays. a) Schematic diagram of three vertically coupled sheets of InAs–GaAs dots; b) end-on TEM image of vertically coupled QDs; c) schematic diagram of a laser structure.

Emission via the ground state has been observed at 300 K in lasers whose active zone is obtained by the growth of vertically coupled QD arrays (VCQDAs) (Ref. 90, Fig. 16) through the alternate short-period deposition of GaAs–(InGa)As layers. Despite a subsequent increase in T_0 (T_0 = 430 K in the temperature range 70–150 K) and lowering of the threshold current density (J_{th}=40 A/cm^2 at 80 K), the room-temperature value of J_{th} was still high (660 A/cm^2), and T_0 remained equal to 60 K. The InGaAs QDs in these lasers were grown within a single GaAs QW as part of the composition of the above-mentioned SPS laser structure.[71]

Extremely high temperature stability (T_0 = 530 K in the temperature range 70–220 K) has been demonstrated for lasers utilizing MOVPE-grown QDs. Up to 220 K the threshold current density was approximately 50 A/cm^2 and was essentially independent of the temperature. Further optimization of the growth parameters and geometry of the structure made it possible to extend the range of extremely high temperature stability of the threshold current (T_0 = 385 K) to 50 °C (Ref. 92).

We have recently investigated[94,95] the influence of the number of InGaAs QD sheets (N) on the structural and optical properties and on the lasing parameters in structures with InGaAs–GaAs VCQDAs grown by MBE on GaAs(100) substrates and introduced into the active zone of AlGaAs–GaAs SPS QW lasers. We found that the coupled dots are formed by virtue of self-organized reconfiguration, where InGaAs material is transferred from a lower to a

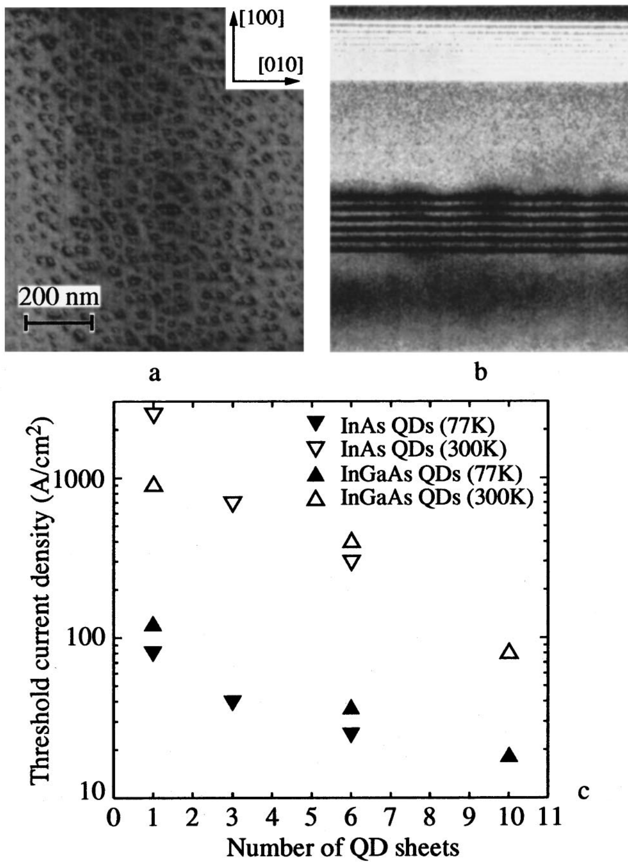

FIG. 17. Plan-view (a) and end-on (b) TEM images of a structure with six sheets of vertically coupled QDs; c) dependence of the threshold current density on the number of QD sheets in the active zone of a QD laser.

higher QD and is replaced by GaAs. The transverse width and volume of the upper QDs constantly increase as N is increased. A QD superlattice is formed in the vertical direction for large N (Fig. 17).

An increase in N produces a substantial drop in J_{th} at 300 K, owing to the increase in the optical confinement factor (from 900 A/cm^2 at $N=1$ to 260 A/cm^2 at $N=6$ and to 90 A/cm^2 at $N=10$). At room temperature, on the other hand, the emission wavlength increases with N, attaining the photoluminescence wavelength at low excitation densities (1.05 μm, 300 K, $N=10$), and T_0 in the vicinity of room temperature increases from 60 K at $N=1$ to 150 K at $N=10$. However, the high-T_0 region at low temperatures becomes narrower, indicating the formation of minibands due to the formation of a vertical SPS in the case of large N.

Another reason for my including this somewhat more detailed portrayal of the evolution of QD laser structures is to demonstrate the circuitous and sophisticated route leading to fulfillment of the hypothetical advantages of quantum dots. Again we wish to summarize this section, following the same outline as before.

Quantum-wire and quantum-dot heterostructures

I. *Fundamental physical phenomena in QW and QD heterostructures:*

- one-dimensional electron gas (QWs);
- density of states as a function with sharp maxima (QWs);
- zero-dimensional electron gas (QDs);
- δ-function density of states (QDs);
- increased exciton binding energy.

II. *Major implications for applications in semiconductor devices:*

- reduced lasing threshold current together with increased differential gain, diminished temperature dependence of the threshold current (QWs), temperature stability of the threshold current (QDs), discrete amplification spectrum, and the possibility of obtaining performance characteristics similar to those of solid-state or gas lasers (QDs);
- higher modulation factor in electrooptical modulators;
- the capability of fabricating ''single-electron'' devices;
- a new opportunity for the development of field-effect transistors.

III. *Important technological considerations:*

- the application of self-organization effects for growth;
- epitaxial growth in V-grooves;
- high-resolution lithography and etching of quantum-well structures.

FUTURE TRENDS

Impressive results have been obtained recently for short-wavelength emission sources using II–VI selenides and III–N nitrides. The application of heterostructure concepts and growth methods developed for quantum wells and superlattices based on III–V compounds is responsible in large part for the success of these investigations. The natural and most predictable trend will be the application of heterostructure concepts and technological methods to new materials. The variety of recently developed III–V, II–VI, and IV–VI heterostructures provides good examples of this assertion.

From a more general and incisive point of view, heterostructures (with regard to all: classical, QW and superlattice, QW, and QD) represent a technique for the synthesis of new types of materials: heterosemiconductors. To echo once again the words of Leo Easki, instead of ''crystals made by God'' we ourselves are creating ''man-made crystals.''

Classical heterostructures, quantum wells, and superlattices are already highly sophisticated, and we are putting many of their unique properties to use. Quantum-wire and quantum-dot structures, on the other hand, are still in their infancy; awaiting us down this road are intriguing discoveries as well as new and unexpected applications. At his very moment, we can state that ordered equilibrium arrays of quantum dots are ready to be used in many devices: lasers, optical modulators, detectors and emitters in the IR range, etc. Resonance tunneling through semiconductor atoms injected into wider-gap layers can significantly improve device characteristics. In a broader sense, QD structures will be developed in breadth and in depth. ''In breadth'' refers to new material systems capable of spanning new ranges of the energy spectrum. The most highly developed system, InGaAs–GaAs, has already found use for substantially refining the

characteristics of semiconductor lasers. Type-II GaSb–GaAs quantum dots have recently been formed on a GaAs(100) surface.[96] A similar concept of forming QDs also works in the system InSb–GaSb, making quantum dots potentially alluring for applications in mid-IR lasers. It is highly probable that problems associated with the service life of semiconductor green and blue lasers and even the more general problems of building defect-free structures on the basis of wide-gap II–VI semiconductors and III–N nitrides can be solved by using QD structures in these systems.

The ''in-depth'' approach means that the degree of order depends to a large extent on the very complex growth conditions, the constants of the and the specific values of the surface free energy. The way to resonance-tunneling and single-electron devices and equipment is by the deep-rooted, careful study and assessment of these parameters with a view toward maximizing the possible degree of order. On the whole, it will be necessary to find more powerful self-organizing mechanisms for the formation of ordered quantum-dot arrays. Coupled arrays of self-organized QWs and QDs are very promising for Esaki-Tsu transverse superlattices. Vertically coupled dots can be conceived as a one-dimensional superlattice—an entirely new object of investigation.

It is scarcely possible in one article to reflect the sumtotal of even the main directions of the present-day physics and technology of semiconductor heterostructures. They are far greater in number than indicated. Many scientists have contributed to this remarkable progress, which not only determines in large measure the future prospects of solid state physics, but in a certain sense affects the future of human society as well. I would also like to emphasize most especially the role of previous generations of scientists, who have paved the way for us. I am fortunate to have had the opportunity to work in this field from its first inception. I am fortunate to be able to continue the work today.

I am deeply indebted to P. S. Kop'ev and N. N. Ledentsov for rewarding discussions, and also to A. V. Gordeeva and N. E. Sergeeva for technical assistance in the preparation of the article.

[1] V. P. Zhuze and B. V. Kurchatov, Zh. Éksp. Teor. Fiz. **2**, 309 (1932); V. P. Zhuze and B. V. Kurchatov, Phys. Z. Sowjetunion **2**, 463 (1932).

[2] Ya. I. Frenkel and A. F. Ioffe, Phys. Z. Sowjetunion **1**, 60 (1932).

[3] Ya. I. Frenkel', Phys. Rev. **37**, 17 (1931); Phys. Rev. **37**, 1276 (1931); Zh. Éksp. Teor. Fiz. **6**, 647 (1936).

[4] E. F. Gross and N. A. Kariev, Dokl. Akad. Nauk SSSR **84**, 261 (1952); E. F. Gross and N. A. Kariev, Dokl. Akad. Nauk SSSR **84**, 471 (1952).

[5] B. I. Davydov, Zh. Éksp. Teor. Fiz. **9**, 451 (1939).

[6] N. H. Welker, Z. Naturforsch. **7**[a], 744 (1952); Z. Naturforsch. **8**[a], 248 (1953).

[7] N. A. Goryunova, *Author's Abstract of Dissertation* [in Russian] (LGU, FTI, 1951); A. I. Blyum, N. P. Mokrovskiĭ, and A. R. Regel', in *Proceedings of the Seventh Conference on the Properties of Semiconductors* [in Russian], Izv. Akad. Nauk Ser. Fiz. **16**, 139 (1952).

[8] W. Shockley, U.S. Patent 2,569,347 (September 25, 1951).

[9] A. I. Gubanov, Zh. Tekh. Fiz. **20**, 1287 (1950); Zh. Tekh. Fiz. **21**, 304 (1951).

[10] H. Kroemer, Proc. IRE **45**, 1535 (1957); RCA Rev. **28**, 332 (1957).

[11] Zh. I. Alferov and R. F. Kazarinov, Inventor's Certificate No. 181737 [in Russian], Application No. 950840, priority as of March 30, 1963; H. Kroemer, Proc. IEEE **51**, 1782 (1963).

[12] Zh. I. Alferov, V. B. Khalfin, and R. F. Kazarinov, Fiz. Tverd. Tela (Leningrad) **8**, 3102 (1966) [Sov. Phys. Solid State **8**, 2480 (1966)].

[13] Zh. I. Alferov, Fiz. Tekh. Poluprovodn. **1**, 436 (1967) [Sov. Phys. Semicond. **1**, 358 (1967)].

[14] L. Anderson, IBM J. Res. Dev. **4**, 283 (1960); Solid-State Electron. **5**, 341 (1962).

[15] G. Natta and L. Passerini, Gazz. Chim. Ital. **58**, 458 (1928); V. M. Goldschmidt, Trans. Faraday Soc. **25**, 253 (1929).

[16] Zh. I. Alferov, D. Z. Garbuzov, V. S. Grigor'eva, Yu. V. Zhilyaev, L. V. Kradinova, V. I. Korol'kov, E. P. Morozov, O. A. Ninua, E. L. Portnoĭ, V. D. Prochukhan, and M. K. Trukan, Fiz. Tverd. Tela (Leningrad) **9**, 279 (1967) [Sov. Phys. Solid State **9**, 208 (1967)].

[17] Zh. I. Alferov, Yu. V. Zhilyaev, and Yu. V. Shmartsev, Fiz. Tekh. Poluprovodn. **5**, 196 (1971) [Sov. Phys. Semicond. **5**, 174 (1971)].

[18] Zh. I. Alferov, V. M. Andreev, V. I. Korol'kov, D. N. Tret'yakov, and V. M. Tuchkevich, Fiz. Tekh. Poluprovodn. **1**, 1579 (1967) [Sov. Phys. Semicond. **1**, 1313 (1967)]; H. S. Rupprecht, J. M. Woodall, and G. D. Pettit, Appl. Phys. Lett. **11**, 81 (1967).

[19] Zh. I. Alferov, V. M. Andreev, V. I. Korol'kov, E. L. Portnoĭ, and D. N. Tret'yakov, Fiz. Tekh. Poluprovodn. **2**, 1016 (1968) [Sov. Phys. Semicond. **2**, 843 (1968)].

[20] Zh. I. Alferov, V. M. Andreev, V. I. Korol'kov, E. L. Portnoĭ, and D. N. Tret'yakov, Fiz. Tekh. Poluprovodn. **2**, 1545 (1968) [Sov. Phys. Semicond. **2**, 1289 (1968)].

[21] a) Zh. I. Alferov, V. M. Andreev, V. I. Korol'kov, E. L. Portnoĭ, and D. N. Tret'yakov, in *Proceedings of the Ninth International Conference on Semiconductor Structures*, *Moscow*, *July 23–29, 1968*, Vol. **1** [in Russian] (Nauka, Leningrad, 1969), p. 534; b) Zh. I. Alferov, in *Proceedings of the International Conference on Luminescence*, *Newark, Delaware*, *August 25–29, 1969*, J. Lumin. **1**, 869 (1970); c) Zh. I. Alferov, D. Z. Garbuzov, E. P. Morozov, and E. L. Portnoĭ, Fiz. Tekh. Poluprovodn. **3**, 1054 (1969) [Sov. Phys. Semicond. **3**, 885 (1969)]; d) Zh. I. Alferov, V. M. Andreev, V. I. Korol'kov, E. L. Portnoĭ, and A. A. Yakovenko, Fiz. Tekh. Poluprovodn. **3**, 541 (1969) [Sov. Phys. Semicond. **3**, 460 (1969)].

[22] Zh. I. Alferov, V. M. Andreev, E. L. Portnoĭ, and M. K. Trukan, Fiz. Tekh. Poluprovodn. **3**, 1328 (1969) [Sov. Phys. Semicond. **3**, 1107 (1969)].

[23] Zh. I. Alferov, V. M. Andreev, V. I. Korol'kov, E. L. Portnoĭ, and A. A. Yakovenko, Fiz. Tekh. Poluprovodn. 930 (1966) [Sov. Phys. Semicond. **3**, 785 (1966)].

[24] Zh. I. Alferov, V. M. Andreev, M. V. Kagan, I. I. Protasov, and V. G. Trofim, Fiz. Tekh. Poluprovodn. **4**, 2378 (1970) [Sov. Phys. Semicond. **4**, 2047 (1970)].

[25] Zh. I. Alferov, F. A. Akhmedov, V. I. Korol'kov, and V. G. Nikitin, Fiz. Tekh. Poluprovodn. **7**, 1159 (1973) [Sov. Phys. Semicond. **7**, 780 (1973)].

[26] Zh. I. Alferov, V. M. Andreev, V. I. Korol'kov, V. G. Nikitin, and A. A. Yakovenko, Fiz. Tekh. Poluprovodn. **4**, 578 (1970) [Sov. Phys. Semicond. **4**, 481 (1970)].

[27] I. Hayashi, IEEE Trans. Electron Devices **ED-31**, 1630 (1984).

[28] Zh. I. Alferov, V. M. Andreev, D. Z. Garbuzov, Yu. V. Zhilyaev, E. P. Morozov, E. L. Portnoĭ, and V. G. Trofim, Fiz. Tekh. Poluprovodn. **4**, 1826 (1970) [Sov. Phys. Semicond. **4**, 1573 (1970)].

[29] I. Hayashi, M. B. Panish, P. W. Foy, and S. Sumski, Appl. Phys. Lett. **17**, 109 (1970).

[30] Zh. I. Alferov, V. M. Andreev, S. G. Konnikov, V. G. Nikitin, and D. N. Tret'yakov, in *Proceedings of the International Conference on the Physics and Chemistry of Semiconductor Heterojunctions and Layer Structures*, *Budapest*, *October, 1970*, Vol. 1, edited by G. Szigeti (Académiai Kiadó, Budapest, 1971), p. 93.

[31] G. A. Antipas, R. L. Moon, L. W. James, J. Edgecumbe, and R. L. Bell, *Institute of Physics Conference Series*, No. 17 (IOP Publ., Bristol, 1973), p. 48.

[32] L. James, G. Antipas, R. Moon, J. Edgecumbe, and R. L. Bell, Appl. Phys. Lett. **22**, 270 (1973).

[33] A. P. Bogatov, L. M. Dolginov, L. V. Druzhinina, P. G. Eliseev, LB. N. Sverdlova, and E. G. Shevchenko, Kvantovaya Élektron. **1**, 2294 (1974) [Sov. J. Quantum Electron. **4**, 1281 (1974)]; J. J. Hsieh, Appl. Phys. Lett. **28**, 283 (1976).

[34] Zh. I. Alferov, I. N. Arsent'ev, D. Z. Garbuzov, S. G. Konnikov, and V. D. Rumyantsev, Pis'ma Zh. Tekh. Fiz. **1**, 305 (1975) [Sov. Tech. Phys. Lett. **1**, 147 (1975)]; Pis'ma Zh. Tekh. Fiz. **1**, 406 (1975) [Sov. Tech. Phys. Lett. **1**, 191 (1975)]; W. R. Hitchens, N. Holonyak, Jr., P. D. Wright, and J. J. Coleman, Appl. Phys. Lett. **27**, 245 (1975).

[35] Zh. I. Alferov, V. M. Andreev, R. F. Kazarinov, E. L. Portnoĭ, and R. A.

Suris, Inventor's Certificate No. 392875 [in Russian], Application No. 1677436, priority as of July 19, 1971.
[36] H. Kogelnik and C. V. Shank, Appl. Phys. Lett. **18**, 152 (1971).
[37] R. F. Kazarinov and R. A. Suris, Fiz. Tekh. Poluprovodn. **6**, 1359 (1972) [Sov. Phys. Semicond. **6**, 1184 (1972)].
[38] Zh. I. Alferov, S. A. Gurevich, R. F. Kazarinov, M. N. Mizerov, E. L. Portnoĭ, R. P. Seĭsyan, and R. A. Suris, Fiz. Tekh. Poluprovodn. **8**, 832 (1974) [Sov. Phys. Semicond. **8**, 541 (1974)]; Zh. I. Alferov, S. A. Gurevich, N. V. Klepikova, V. I. Kuchinskiĭ, M. N. Mizerov, and E. L. Portnoĭ, Pis'ma Zh. Tekh. Fiz. **1**, 645 (1975) [Sov. Tech. Phys. Lett. **1**, 286 (1975)].
[39] N. Nakamura, A. Yariv, H. W. Yen, S. Somekh, and H. L. Garvin, Appl. Phys. Lett. **22**, 315 (1973).
[40] D. R. Scifres, R. D. Burnham, and W. Streifer, Appl. Phys. Lett. **25**, 203 (1974).
[41] H. Kroemer and G. Griffiths, IEEE Trans. Electron Devices **EDL-4**, 20 (1983).
[42] A. N. Baranov, B. E. Dzhurtanov, A. N. Imenkov, A. A. Rogachev, Yu. M. Shernyakov, and Yu. P. Yakovlev, Fiz. Tekh. Poluprovodn. **20**, 2217 (1986) [Sov. Phys. Semicond. **20**, 1385 (1986)].
[43] A. Y. Cho, J. Vac. Sci. Technol. **8**, 31 (1971); A. Y. Cho, Appl. Phys. Lett. **19**, 467 (1971).
[44] H. M. Manasevit, Appl. Phys. Lett. **12**, 156 (1968).
[45] R. D. Dupuis and P. D. Dapkus, Appl. Phys. Lett. **31**, 466 (1977).
[46] R. Dingle, W. Wiegmann, and C. H. Henry, Phys. Rev. Lett. **33**, 827 (1974).
[47] L. Esaki and R. Tsu, IBM J. Res. Dev. **14**, 61 (1970).
[48] L. V. Keldysh, Fiz. Tverd. Tela (Leningrad) **4**, 2265 (1962) [Sov. Phys. Solid State **4**, 1658 (1962)].
[49] R. F. Kazarinov and R. A. Suris, Fiz. Tekh. Poluprovodn. **5**, 707 (1971) [Sov. Phys. Semicond. **5**, 619 (1971)]; Fiz. Tekh. Poluprovodn. **6**, 120 (1972) [Sov. Phys. Semicond. **6**, 96 (1972)]; Fiz. Tekh. Poluprovodn. **7**, 346 (1973) [Sov. Phys. Semicond. **7**, 246 (1973)].
[50] R. Tsu and L. Esaki, Appl. Phys. Lett. **22**, 562 (1973).
[51] G. Osbourn, J. Appl. Phys. **53**, 1586 (1982).
[52] M. Ludowise, W. T. Dietze, C. R. Lewis, M. D. Camras, N. Holonyak, B. K. Fuller, and M. A. Nixon, Appl. Phys. Lett. **42**, 487 (1983).
[53] L. L. Chang, L. Easki, W. E. Howard, and R. Ludke, J. Vac. Sci. Technol. **10**, 11 (1973).
[54] L. L. Chang, L. Easki, and R. Tsu, Appl. Phys. Lett. **24**, 593 (1974).
[55] L. Esaki and L. L. Chang, Phys. Rev. Lett. **33**, 686 (1974).
[56] J. R. Schrieffer, in *Semiconductor Surface Physics*, edited by R. H. Kingston (Univ. Penn. Press, Philadelphia, 1956), p. 68.
[57] A. B. Fowler, F. F. Fang, W. E. Howard, and P. J. Stilee, Phys. Rev. Lett. **16**, 901 (1966).
[58] V. N. Lutskii, Phys. Status Solidi A **1**, 199 (1970).
[59] R. Dingle, H. L. Stormer, H. L. Gossard, and W. Wiegmann, Appl. Phys. Lett. **33**, 665 (1978).
[60] D. Delagebeaudeuf *et al.*, Electron. Lett. **16**, 667 (1980).
[61] T. Mimura, S. Hiyamizu, T. Fuji, and K. A. Nanbu, Jpn. J. Appl. Phys. **19**, L225 (1980).
[62] J. P. van der Ziel, R. Dingle, R. C. Miller, W. Wiegmann, and W. A. Nordland, Jr., Appl. Phys. Lett. **26**, 463 (1975).
[63] R. D. Dupuis, P. D. Dapkus, N. Holonyak, Jr., E. A. Rezek, and R. Chin, Appl. Phys. Lett. **32**, 295 (1978).
[64] W. T. Tsang, Appl. Phys. Lett. **40**, 217 (1982).
[65] E. Rezek, H. Shichijo, B. A. Vojak, and N. Holonyak, Jr., Appl. Phys. Lett. **31**, 534 (1977).
[66] Zh. I. Alferov, D. Z. Garbuzov, I. N. Arsent'ev, B. Ya. Ber, L. S. Vavilova, V. V. Krasovskiĭ, and A. V. Chudinov, Fiz. Tekh. Poluprovodn. **19**, 1108 (1985) [Sov. Phys. Semicond. **19**, 679 (1985)].
[67] Zh. I. Alferov, V. M. Andreev, A. A. Vodnev, S. G. Konnikov, V. R. Larionov, K. Yu. Pogrebitskiĭ, V. D. Rumyantsev, and V. P. Khvostikov, Pis'ma Zh. Tekh. Fiz. **12**, 1089 (1986) [Sov. Tech. Phys. Lett. **12**, 450 (1986)].
[68] Zh. I. Alferov, D. Z. Garbuzov, K. Yu. Kizhaev, A. B. Nivin, S. A. Nikishin, A. V. Ovchinnikov, Z. P. Sokolova, I. S. Tarasov, and A. V. Chudinov, Pis'ma Zh. Tekh. Fiz. **12**, 210 (1986) [Sov. Tech. Phys. Lett. **12**, 87 (1986)]; Zh. I. Alferov, D. Z. Garbuzov, S. V. Zaĭtsev, A. B. Nivin, A. V. Ovchinnikov, and I. S. Tarasov, Fiz. Tekh. Poluprovodn. **21**, 824 (1987) [Sov. Phys. Semicond. **21**, 503 (1987)].
[69] Zh. I. Alferov, N. Yu. Antonishkis, I. N. Arsent'ev, D. Z. Garbuzov, V. I. Kolyshkin, T. N. Nalet, N. A. Strugov, and A. S. Tikunov, Fiz. Tekh. Poluprovodn. **22**, 1031 (1988) [Sov. Phys. Semicond. **22**, 650 (1988)]; D. Z. Garbuzov *et al.*, in *Technical Digest CLEO*, Paper THU44 (1988), p. 396.
[70] D. Z. Garbuzov *et al.*, in *Conference Digest of the 12th International Semiconductor Laser Conference* (Davos, Switzerland, 1990), p. 238.
[71] Zh. I. Alferov, A. I. Vasil'ev, S. V. Ivanov, P. S. Kop'ev, N. N. Ledentsov, M. É. Lutsenko, B. Ya. Mel'tser, and V. M. Ustinov, Pis'ma Zh. Tekh. Fiz. **14**, 1803 (1988) [Sov. Tech. Phys. Lett. **14**, 782 (1988)].
[72] J. Faist *et al.*, Science **264**, 553 (1994); Electron. Lett. **30**, 865 (1994).
[73] K. V. Klitzing, G. Dorda, and M. Pepper, Phys. Rev. Lett. **45**, 494 (1980).
[74] D. C. Tsui, H. L. Stormer, and A. C. Gossard, Phys. Rev. Lett. **48**, 1559 (1982).
[75] P. M. Petroff, A. C. Gossard, R. A. Logan, and W. Wiegmann, Appl. Phys. Lett. **41**, 635 (1982).
[76] Y. Arakawa and H. Sakaki, Appl. Phys. Lett. **40**, 939 (1982).
[77] S. Simhony, E. Kapon, T. Colas, D. M. Hwang, N. G. Stoffel, and P. Worland, Appl. Phys. Lett. **59**, 2225 (1991).
[78] A. I. Ekimov and A. A. Anushchenko, JETP Lett. **34**, 347 (1981).
[79] Al. L. Éfros and A. L. Éfros, Fiz. Tekh. Poluprovodn. **16**, 1209 (1982) [Sov. Phys. Semicond. **16**, 772 (1982)].
[80] L. Goldstein, F. Glas, J. Y. Marzin, M. N. Charasse, G. Le Roux, Appl. Phys. Lett. **47**, 1099 (1985).
[81] A. F. Andreev, Zh. Éksp. Teor. Fiz. **80**, 2042 (1981) [Sov. Phys. JETP **53**, 1063 (1981)].
[82] V. I. Marchenko, Zh. Éksp. Teor. Fiz. **81**, 1141 (1981) [Sov. Phys. JETP **54**, 605 (1981)].
[83] R. Nötzel, N. N. Ledentsov, L. Däweritz, M. Hohenstein, and K. Ploog, Phys. Rev. Lett. **67**, 3812 (1991).
[84] V. A. Shchukin, A. I. Borovkov, N. N. Ledentsov, and P. S. Kop'ev, Phys. Rev. B **51**, 17767 (1995).
[85] P. D. Wang, N. N. Ledentsov, C. M. Sotomayor Torres, P. S. Kop'ev, and V. M. Ustinov, Appl. Phys. Lett. **64**, 1526 (1994).
[86] V. Bressler Hill, A. Lorke, S. Varma, P. M. Petroff, K. Pond, and W. H. Weinberg, Phys. Rev. B **50**, 8479 (1994).
[87] N. N. Ledenstov *et al.*, in *Proceedings of the 22nd International Conference on the Physics of Semiconductors*, *Vancouver, Canada*, *1994*, World Scientific, Singapore, 1995.
[88] Zh. I. Alferov, N. Yu. Gordeev, S. V. Zaĭtsev, P. S. Kop'ev, I. V. Kochnev, V. V. Khomin, I. L. Krestnikov, N. N. Ledentsov, A. V. Lunev, M. V. Maksimov, S. S. Ruvimov, A. V. Sakharov, A. F. Tsatsul'nikov, Yu. M. Shernyakov, and D. Bimberg, Fiz. Tekh. Poluprovodn. **30**, 357 (1996) [Semiconductors **30**, 197 (1996)].
[89] V. A. Shchukin, N. N. Ledentsov, P. S. Kop'ev, and D. Bimberg, Phys. Rev. Lett. **75**, 2968 (1995); V. A. Shchukin, N. N. Ledentsov, M. Grundmann, P. S. Kop'ev, and D. Bimberg, Surf. Sci. **352–354**, 117 (1996).
[90] Zh. I. Alferov, N. A. Bert, A. Yu. Egorov, A. E. Zhukov, P. S. Kop'ev, A. O. Kosogov, I. L. Krestnikov, N. N. Ledentsov, A. V. Lunev, M. V. Maksimov, A. V. Sakharov, V. M. Ustinov, A. F. Tsatsul'nikov, Yu. M. Shernyakov, and D. Bimberg, Fiz. Tekh. Poluprovodn. **30**, 351 (1996) [Semiconductors **30**, 194 (1996)].
[91] M. Grundmann *et al.*, Phys. Rev. Lett. **74**, 4043 (1995).
[92] N. Kirstaedter *et al.*, Electron. Lett. **30**, 1416 (1994).
[93] M. V. Maksimov *et al.*, Fiz. Tekh. Poluprovodn. **31**, 670 (1997) [Semiconductors **31**, 571 (1997)].
[94] M. Grundmann *et al.*, in *Proceedings of the Eighth International Conference on Indium Phosphide and Related Materials* (Schwäbisch Gmünd, Germany, 1996).
[95] V. M. Ustinov *et al.*, in *Ninth International Conference on MBE* (Malibu, USA, August, 1996) (*Proceedings* to be published in J. Crystal Growth).
[96] F. Hatami, N. N. Ledentsov, M. Grundmann, J. Böhrer, F. Heinrichsdorff, M. Beer, and D. Bimberg *et al.*, Appl. Phys. Lett. **67**, 656 (1995).

Translated by James S. Wood

Relaxation of light-induced metastable state of boron-doped *p*-type *a*-Si:H

A. G. Kazanskiĭ* and E. V. Larina

M. V. Lomonosov Moscow State University, 119899 Moscow, Russia
(Submitted February 20, 1997; accepted for publication June 3, 1997)
Fiz. Tekh. Poluprovodn. **32**, 117–120 (January 1998)

Relaxation of the dark conductivity of boron-doped a-Si : H films after illumination in the temperature range 360–470 K has been studied. It is shown that the measuring conductivity relaxation after illumination under different conditions (illumination time and temperature) makes it possible to separately investigate relaxation of the concentration of light-induced metastable defects of the ''dangling-bonds'' type and relaxation of the concentration of metastable states associated with impurity atoms. In both cases the relaxation obeys a stretched-exponential law. The main parameters of both relaxations and their temperature dependence have been measured. The experimental results can be explained within the framework of a model of the annealing activation energy distribution for light-induced metastable states. © *1998 American Institute of Physics.* [S1063-7826(97)01012-0]

It is known that illumination of a-Si : H films leads to the appearance of a metastable state.[1] Annealing at temperatures of $100-200$ K (depending on the level and type of doping) restores the original parameters of the films. Most studies of the metastable state have examined undoped a-Si : H films. It is taken for granted that the appearance and relaxation of the metastable state in undoped films are connected with monotonic variation of the concentration of defects of dangling-bond type, where the kinetics of this variation are characterized by a stretched-exponential law.[2,3]

The metastable state caused by illumination of doped a-Si : H films has been studied to a significantly lesser extent. The presence of dopant impurities substantially complicates the processes of formation of the metastable state. In particular, variations of the conductivity that are nonmonotonic in the illumination have been associated with the contribution of possible processes associated with the impurity atoms (variation of the concentration of electrically active impurities,[4,5] and variation of the concentration of defects correlated with the impurities[6]). The relaxation of the conductivity after termination of illumination associated with relaxation of the metastable state of phosphorus-doped,[7] boron-doped,[4] and compensated a-Si : H[6] also has a nonmonotonic character. This indicates that relaxation of the metastable state of doped a-Si : H is, in general, governed by at least two processes.

To secure a proper account of the indicated processes, it would be advantageous to perform measurements under conditions in which one of them is suppressed. As was noted in Ref. 8, this can be done by measuring relaxation of the conductivity of doped a-Si : H after illuminating it at different temperatures for different lengths of time. In the present study, measurements were made on boron-doped, p-type a-Si : H films.

The investigated a-Si : H films were roughly 1 μm thick and were obtained by decomposition of a mixture of monosilane (SiH_4) and diborane (B_2H_6) in an rf glow discharge at a substrate temperature of 250 °C. (The substrate was quartz.) The volume ratio of B_2H_6 to SiH_4 was 10^{-5} (sample 10 ppm) and 3×10^{-5} (sample 30 ppm). The films were illuminated by light from an incandescent lamp through a thermal filter with an intensity of 60 mW/cm^2. The films were illuminated at temperatures in the interval $360-470$ K. Relaxation was measured at the illumination temperatures and was recorded with the help of an S 9-8 digital storage oscilloscope. Before the measurements the films were annealed in vacuum at 190 °C for 30 min.

Figure 1 plots the dependence on illumination time (t_{ill}) of the relative variation at different temperatures of the dark conductivity (σ^B/σ^A) of the 10-ppm film, where σ^A and σ^B are the dark conductivity before and after illumination, respectively. The measurements were made 3 s after turning off the illumination. As can be seen from the figure, for $T<400$ K the dependence $\sigma^B/\sigma^A(t_{\mathrm{ill}})$ has a nonmonotonic character, falling at short illumination times and growing at longer ones. Similar behavior of σ^B/σ^A was observed for the 30-ppm film. Increasing the doping level led only to a shift of the minimum of σ^B/σ^A to shorter illumination times. The observed dependence of $\sigma^B/\sigma^A(t_{\mathrm{ill}})$ indicates that the variation of σ^B/σ^A is controlled by a competition of two processes caused by illumination. The one leading to a decrease of σ^B/σ^A at short illumination times can be linked with the appearance of donor-like states (DS) lying above the Fermi level (E_f). It is believed[4,9] that these states may be dangling-bond states. The second process, the one responsible for the growth of σ^B/σ^A at longer illumination times, can be linked with the appearance of acceptor-like states (AS) below the Fermi level. In the opinion of the authors of Ref. 4, this is a consequence of an increase in the concentration of electrically active boron atoms caused by illumination. As the temperature is increased, the position of the minimum (t_{min}) of $\sigma^B/\sigma^A(t_{\mathrm{ill}})$ shifts toward shorter illumination times. This indicates a growth of the role of the second process in the

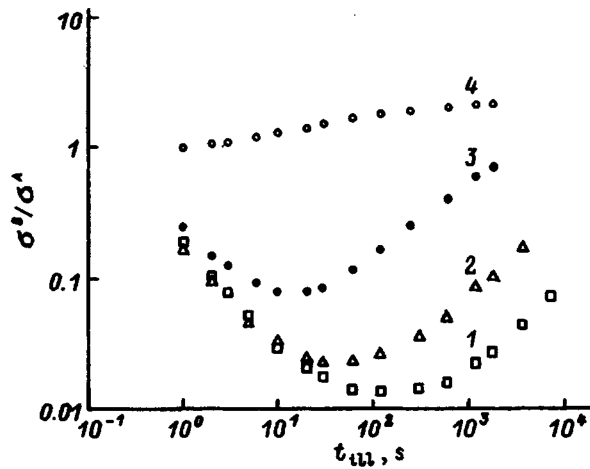

FIG. 1. Relative dark conductivity σ^B/σ^A of a 10 ppm film plotted versus illumination time t_{ill} for different temperatures: *1* — 360, *2* — 380, *3* — 400, *4* — 440 K.

variation of the conductivity with increase of the temperature.

Let us consider the high-temperature region. As can be seen from Fig. 1, monotonic growth of σ^B/σ^A is observed at $T=440$ K. Such variation of σ^B/σ^A testifies to the prevalent role of the second process in the high-temperature region. According to Ref. 8, this is connected with a difference in the characteristic annealing temperatures of the changes caused by the first process (360–380 K) and the second process (460–480 K).

The above results point to the possibility of separate investigation of relaxation of the light-induced changes associated with the first process (a change in the defect concentration) and with the second process (a possible change in the concentration of electrically active impurities). In particular, relaxation of the conductivity after brief illumination ($t<t_{\min}$) at $T<400$ K should be associated with the first process, while relaxation of conductivity after illumination at high temperatures should be associated with the second process.

The change in the concentration of states (ΔN) brought about by the first or second process leads to a shift of the Fermi level $\Delta E_f=E_f^B-E_f^A\cong N(E_f)\Delta N$, where $N(E_f)$ is the density of states in the region of the shift of E_f, and $\Delta E_f=kT\cdot\ln(\sigma^A/\sigma^B)$. Assuming that $N(E_f)=\text{const}$, we have $\Delta E_f\sim\Delta N$. Thus, measurement of relaxation of $\Delta E_f(t)$ allows one to judge relaxation of $\Delta N(t)$.

Figure 2a shows relaxation of ΔE_f after illumination of the 10-ppm film for 1 s at $T\leqslant 400$ K. Relaxation of ΔE_f under these conditions is governed by relaxation of the changes in σ^B/σ^A caused by the first process (the process leading to a decrease of the conductivity upon illumination). As can be seen from the figure, with the exception of the initial segment, the relaxation of ΔE_f linked with relaxation of the metastable states is satisfactorily described by a stretched exponential $\Delta E_f\sim[\exp-(t/\tau_r)^\beta]$ (solid curves). An analysis of the initial segment of relaxation was performed in Ref. 9. Figure 2b shows relaxation of ΔE_f after illumination of the 10-ppm film for 5 min at $T\leqslant 440$ K. Under these conditions, relaxation of ΔE_f should be determined mainly by relaxation of the changes in σ^B/σ^A caused by the second process (the process leading to an increase in the conductivity upon illumination). For $T=440$ K in the initial stage of relaxation, some increase in $-\Delta E_f$, which is associated with the contribution to the relaxation of states created by the first process, is observed. It can be seen from the figure that the

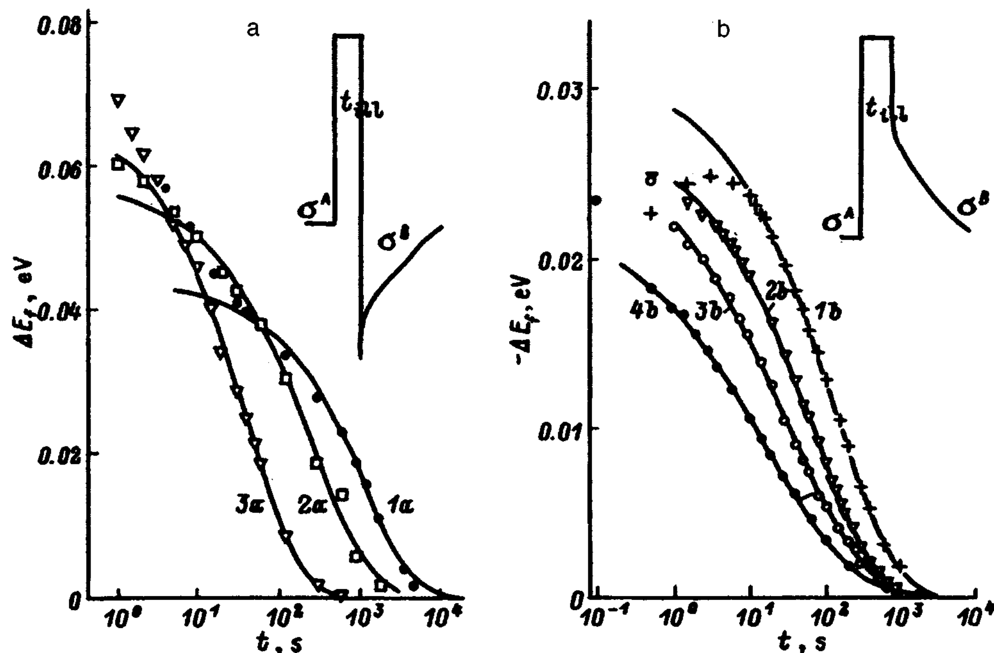

FIG. 2. Relaxation of the position of the Fermi level ΔE_f ($-\Delta E_f$) after illumination of a 10-ppm film for 1 s at $T<400$ K (a) and 5 min for $T>440$ K (b). The solid curves were obtained by nonlinear regression to stretched exponentials. T, K: *1a* — 360, *2a* — 380, *3a* — 400; *1b* — 440, *2b* — 450, *3b* — 460, *4b* — 470.

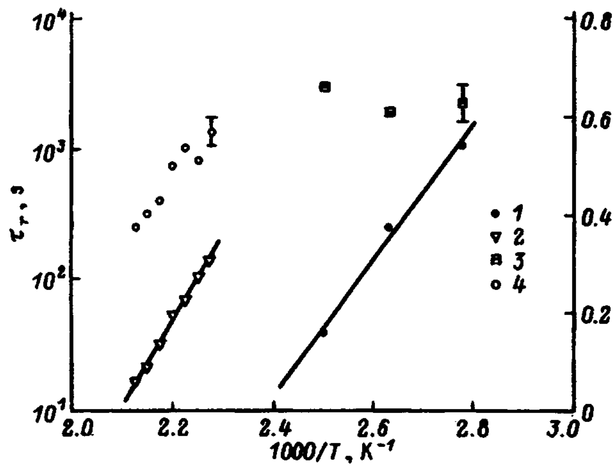

FIG. 3. Effect of temperature on the relaxation parameters τ_r (*1, 2*) and β (*3, 4*), determined from an analysis of the data plotted in Fig. 2a (*1, 3*) and Fig. 2b (*2, 4*).

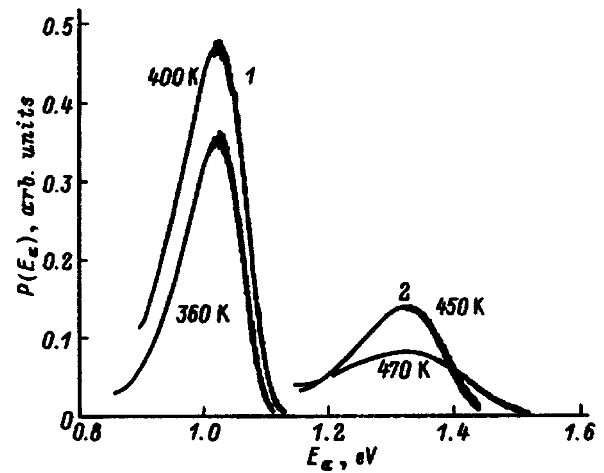

FIG. 4. Effect of illumination temperature on the distribution of the activation energy of annealing $P(E_a)$ of metastable states corresponding to the first process (*1*) and the second process (*2*).

relaxation obtained at higher temperatures, as in the case of lower temperatures, is satisfactorily described by a stretched exponential (solid curves).

If we assume that the first and second processes are associated with the appearance of donor states and acceptor states, respectively, then the curves in Figs. 2a and 2b reflect relaxation of their concentrations. Figure 3 plots the temperature dependence of the stretched-exponential parameters for relaxation of the donor-state and acceptor-state concentrations shown in Fig. 2. The effective relaxation time τ_r for the donor states has an activation-type temperature dependence $\tau_r = \tau_0 \exp(E/kT)$ with activation energy $E = 1.02$ eV and $\tau_0 = 5 \times 10^{-12}$ s. This value of E is close to the activation energy of annealing of light-induced dangling bonds in a-Si : H. In the case of the acceptor states in the high-temperature region, τ_r also decreases in an activation-like way as the temperature is raised, with activation energy $E = 1.33$ eV and $\tau_0 = 5 \times 10^{-14}$ s. At the same time, as can be seen from Fig. 3, varying the temperature has a substantially different effect on the parameter β, which characterizes relaxation of the donor-state and acceptor-state concentrations. In the case of the donor states, the parameter β is essentially independent of temperature (it tends to increase with temperature). In the case of relaxation of the concentration of acceptor states, on the other hand, β decreases substantially with increasing temperature. Similar behavior of β was observed for the 30-ppm sample. Note that a similar temperature dependence of β and the value $E = 1.39$ eV for τ_r were obtained in Ref. 10 for relaxation of conductivity of boron-doped a-Si : H films after quenching and subsequent annealing at various temperatures. It is believed that under these conditions relaxation (decrease) of the concentration of electrically active impurities takes place.[11]

Let us consider the results. According to Ref. 12, the relaxation observed upon annealing of the concentration of metastable states according to a stretched-exponential law may be an indication of the activation energy distribution $P(E_a)$ of annealing of the light-induced metastable states. A smaller value of β corresponds to a wider distribution. At the same time, for a given distribution, β should increase with growth of the annealing temperature. Relaxation was examined at various illumination temperatures under the conditions of our experiment. Thus, if a change in the illumination temperature leads to a change in the $P(E_a)$ for the light-induced metastable states, this should show up in the observed temperature dependence $\beta(T)$. As was shown in Ref. 13, the distribution $P(E_a)$ can be obtained by differentiating the relaxation curves of the concentration of photo-induced metastable states ΔN (which in our case corresponds to relaxation of ΔE_f), specifically $P(E_a) \sim d[\Delta N(t)]/d[kT \cdot \ln(t/\tau_0)]$. Values of $P(E_a)$ inferred from our measurements at different temperatures for the donor states and for the acceptor states are shown in Fig. 4. To calculate them, we used the above-indicated values of τ_0. As can be seen from the figure, the maxima of $P(E_a)$ correspond to the measured activation energies τ_r. In the case of the donor states the width of $P(E_a)$ is essentially independent of the illumination temperature, while for the acceptor states a substantial broadening of $P(E_a)$ is observed with growth of the illumination temperature. This may explain the observed dependence of $\beta(T)$ and indicates the substantial difference between the mechanisms driving the first and second process.

In summary, our studies have allowed us to determine the main parameters characterizing relaxation of the changes in conductivity associated with the process of defect formation leading to a decrease in the conductivity as a result of illumination of p-type a-Si : H and the process leading to an increase in the conductivity and apparently associated with impurities.

We are grateful to Prof. W. Fuhs and Dr. H. Mell for preparation of the boron-doped a-Si : H films, and to I. A. Kurova for helpful discussions.

This work was carried out with the partial financial support of INTAS (Grant No. 93-1916) and the State Committee on Higher Education of the Russian Federation (Grant No. 95-0-7.1-153) in the area of fundamental natural science.

*E-mail: Kazanskiscon279.phys.msu.su (Kazanskii); Fax: (095) 939 37 31 (Kazanskii)

[1] D. L. Staebler and C. R. Wronski, Appl. Phys. Lett. **31**, 292 (1977).
[2] W. B. Jackson and J. Kakalios, Phys. Rev. B **37**, 1020 (1988).
[3] W. B. Jackson and M. D. Moyer, Phys. Rev. B **36**, 6217 (1987).
[4] J. Jang, S. C. Park, S. C. Kim, and C. Lee, Appl. Phys. Lett. **51**, 1804 (1987).
[5] A. G. Kazanskiĭ and D. G. Yarkin, Fiz. Tekh. Poluprovodn. **27**, 1693 (1993) [Semiconductors **27**, 935 (1993)].
[6] A. G. Kazanskiĭ, I. A. Kurova, I. P. Zvyagin, and D. G. Yarkin, J. Non-Cryst. Solids **198–200**, 470 (1996).
[7] X.-M. Deng and H. Fritzsche, Phys. Rev. B **36**, 9378 (1987).
[8] A. G. Kazanskiĭ, Vest. MGU [Bulletin of Moscow State Univ.], Ser. 3, Fiz., Astron. **33**, 70 (1992).
[9] A. G. Kazanskiĭ, Fiz. Tekh. Poluprovodn. **31**, 347 (1997) [Semiconductors **31**, 287 (1997)].
[10] R. Meaudre, M. Meaudre, and P. Roca i Gabarrocas, Appl. Phys. Lett. **62**, 594 (1993).
[11] C. E. Nebel, R. A. Street, W. B. Jackson, and N. M. Jonson, Philos. Mag. B **69**, 291 (1994).
[12] D. Redfield, Mater. Res. Soc. Symp. Proc. **258**, 341 (1992).
[13] M. Stutzmann, W. B. Jackson, and C. C. Tsai, Phys. Rev. B **32**, 23 (1985).

Translated by Paul F. Schippnick

Relation between the optoelectronic parameters of amorphous hydrogenated silicon films deposited at high temperatures and their microstructure

G. J. Adriaenssens and W. Grevendonk

Katholieke Universiteit Leuven, B-3001, Heverlee, Belgium

O. A. Golikova

A. F. Ioffe Physicotechnical Institute, Russian Academy of Sciences, 194021 St. Petersburg, Russia
(Submitted May 12, 1997; accepted for publication May 15, 1997)
Fiz. Tekh. Poluprovodn. **32**, 121–123 (January 1998)

The optical modulation spectra and photoconductivity of a number of a-Si:H films containing 5–6 at.% hydrogen with different microstructure parameters ($R=0.2-0.8$) have been investigated. Information about the defect density in the films, spreading of band edges (tailing), the gap width, and the product of the mobility and the lifetime of the electrons has been obtained. The microstructure is shown to have a substantial effect on the optoelectronic parameters of films with low hydrogen content. © *1998 American Institute of Physics.*
[S1063-7826(97)01112-5]

In the present paper we report the results of an experimental study of the opto-electronic properties of amorphous hydrated-silicon films (a-Si : H) deposited by decomposition of SiH_4 at constant current in a magnetic field (magnetically assisted silicon deposition, MASD). As was shown earlier,[1–3] this method allows one to vary the microstructure parameter of films deposited at high substrate temperatures $T_s=300-400$ °C (the microstructure parameter R, as is well known, characterizes the content of SiH_2 complexes relative to the total content of SiH_2-SiH complexes). As a result of the high substrate temperatures, wide variations of R are achieved simultaneously with low hydrogen content of the films ($C_H<10$ at.%) (Fig. 1), which is not possible with other methods. Therefore, films deposited by MASD are new objects of study for elucidating the effect of the microstructure on the optoelectronic parameters of amorphous hydrated silicon. Such studies are especially interesting since MASD has a number of features that are attractive from the technological point of view.

It should be noted that MASD allows one to obtain undoped a-Si : H films of device quality having C_H as high as 3 at.% by using a strongly diluted mixture of SiH_4 and Ar. Doped films can be prepared by sputtering a strongly doped silicon target which is used as a cathode in the magnetron chamber,[1–3] or by co-sputtering (e.g., by using a Si + Er target[4]). MASD has been employed successfully to obtain alloys of a-Si : H with germanium.[5]

The main method used by us was optical modulation spectroscopy (OMS).[6–10] For the experiments we chose films that have been described earlier.[1–3] They have similar values of C_H for $R=$var and are also characterized by similar values of $\varepsilon_c-\varepsilon_F$, i.e., roughly identical values of the Fermi level relative to the edge of the conduction band. This latter fact is important since, as is well known, the density of defects (dangling Si–Si-bonds) N_D and the product of the mobility and lifetime of the electrons, $\mu\tau$ are functions of the equilibrium Fermi level, although with a large spread of the experimental data with $\varepsilon_c-\varepsilon_F=$const (Ref. 11).

Optical modulation spectroscopy, as a method making it possible to obtain information about localized states of the mobility gap, E_g, can be described as follows.[6–10] The sample is acted upon by two light beams—the monochromatic probe beam and the pump beam. The excess charge carriers created as a result of pumping alter the population of localized gap states, which affects the transitions between them and the band states. The experimentally determined quantity is $-\Delta T/T$, where T is the transmittance of the probe light beam through the sample in the absence of pumping, and $-\Delta T$ is the change in the transmittance due to pumping. The latter quantity is proportional to the change in the absorption coefficient. As the pump we used an argon laser (30 mW/cm^{-2}). The probe beam was produced by an incandescent lamp and a monochromator, and the optical modulation spectra were taken in the energy interval $E=0.5-2.2$ eV at room temperature.

Figure 2 plots the OMS curves for the investigated series of samples. Three regions can be distinguished in each curve. The central region is found in the vicinity of the maximum at $E=1$ eV. The value of $-\Delta T/T$ at the maximum is proportional to the defect density N_D. Variations of $-\Delta T/T$ in the low-energy region yield information about smearing of the band edges (tailing). However, as a result of technical details, the measurements in this regions are not distinguished by high accuracy; therefore, the obtained information is only of a qualitative character.[12] Finally, for values of E near the fundamental absorption edge an abrupt growth of $-\Delta T/T$ is observed (this effect is called thermal modulation). However, it is possible to estimate the value of the gap E_g.

Thus, the OMS method is very informative, and the information it reveals about the defect density in the films is especially valuable. As is well known, the constant photocurrent method (CPM), which due to its comparative simplicity is widely used to determine N_D, has been the subject recently of serious criticism.[13,14] It should be noted that to determine N_D the total absorption associated with the defects is normalized to the density of unpaired spins, determined by electron paramagnetic resonance.[15] This is unquestionably correct if the defects are found in the neutral state ($D°$), but

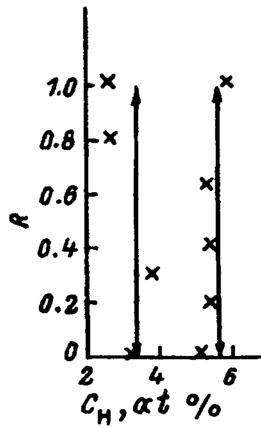

FIG. 1. Variations of the microstructure parameter of a-Si : H films deposited by the MASD method for C_H=const.

it ceases to be completely correct if the charge state of the defect varies, i.e., when the a-Si : H film is not "intrinsic."[11]

Let us consider how the defect density varies as R varies (Fig. 2). The a-Si : H films with the smallest values of R, deposited by MASD, are comparable in their value of N_D with a-Si : H films of device quality, deposited by the glow-discharge method, for which the OMS method was used in Ref. 12 to obtain similar data. At the same time, it follows from Fig. 2 that growth of R leads to a significant increase in N_D. For the maximum values of R, in fact, all of the hydrogen is found in the form of SiH_2 complexes and, although the total hydrogen content C_H is not large and, consequently, the number of these complexes is also not large, the microstructure of the films has a great influence both on N_D and on the spreading of the band tails (Fig. 2). The latter is assumed to be an indicator of inhomogeneity of the a-Si : H structure. The increase in E_g observed for almost all the films deposited by MASD should apparently be linked with peculiarities of the microstructure. From the estimates $E_g = 1.8-2.0$ eV (Fig. 2), which is not characteristic of a-Si : H deposited by

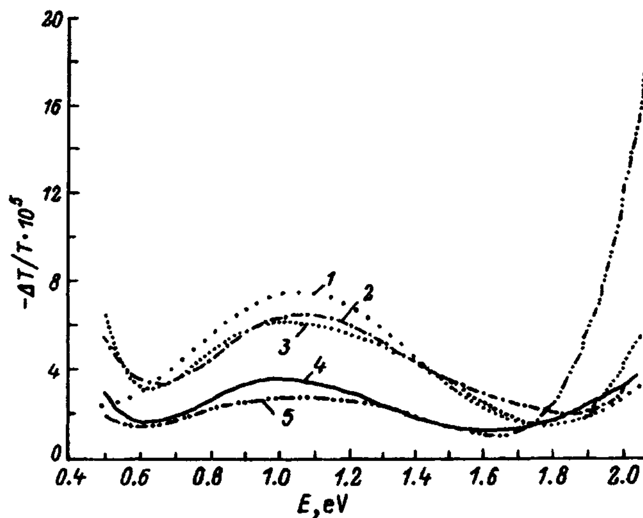

FIG. 2. OMS curves for films *1*, *2*, *3*, *4*, and *5* having R=0.8, 0.8, 0.6, 0.2, 0.3, respectively, and $C_H = 5-6$ at.%.

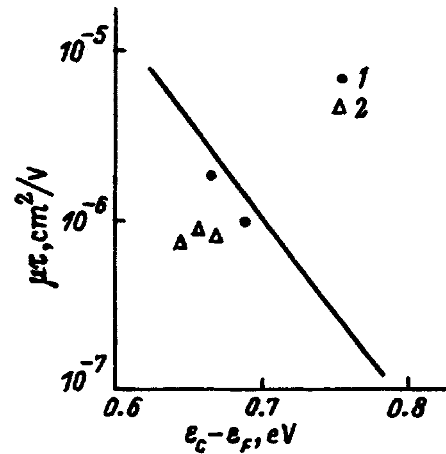

FIG. 3. Product of the mobility by the lifetime of the electrons, plotted as a function of the position of the Fermi level of an a-Si : H film of device quality (straight line). The points represent data for films 4 and 5 (*1*) and 1–3 (*2*); see Fig. 2.

the glow-discharge method at $T_s = 300-400$ °C. Figure 3 plots the product of the mobility by the lifetime of the electrons, $\mu\tau$, as a function of the position of the Fermi level. The straight line is for device quality a-Si : H (Ref. 3) and the points correspond to the films examined in the present study. The values of $\mu\tau$ were determined from the photoconductivity measured at room temperature for rate of generation $\sim 10^{19}$ cm^{-3}s^{-1} and $h\nu = 2$ eV. It can be seen that the films with high R and correspondingly enhanced N_D are distinguished by depressed values of $\mu\tau$ for $\varepsilon_c - \varepsilon_F$=const.

Thus, by using the MASD method of film deposition we have succeeded in establishing that variations in the microstructure of a-Si : H films (variations in the content of SiH_2 complexes relative to the total content of SiH_2 and SiH complexes) have a substantial effect on the optoelectronic parameters of a-Si : H films with low hydrogen content.

This work was supported by an INTAS Grant (No. 931916) and was carried out within the scope of a program of joint study.

[1]O. A. Golikova, A. N. Kuznetsov, V. Kh. Kudoyarova, and M. M. Kazanin, Fiz. Tekh. Poluprovodn. **30,** 1879 (1996) [Semiconductors **30**, 983 (1996)].

[2]O. A. Golikova, A. N. Kuznetsov, V. Kh. Kudoyarova, M. M. Kazanin, and A. I. Kosarev, Mater. Res. Soc. Symp. Proc. **420**, 353 (1996).

[3]O. A. Golikova, A. N. Kuznetsov, V. Kh. Kudoyarova, and M. M. Kazanin, Fiz. Tekh. Poluprovodn. **31**, 816 (1997) [Semiconductors **31**, 691 (1997).

[4]M. S. Bresler, O. B. Gusev, V. Kh. Kudoyarova, A. N. Kuznetsov, P. E. Pak, E. I. Terukov, I. N. Yassievich, B. A. Zakharchenya, W. Fuhs, and A. Sturm, Appl. Phys. Lett. **67**, 3599 (1995).

[5]V. Kh. Kudoyarova, N. A. Rogachev, J. T. Ishakov, E. I. Terukov, and E. P. Milichevich, *Proceedings of the Thirteenth European Photovoltaic Solar Energy Conference* (Nice, France, 1995), p. 165.

[6]Z. Vardeny, T. X. Zhou, and J. Tauc, *Amorphous Silicon and Related Materials*, edited by H. Fritzsche (World Scientific, Singapore, 1989), p. 513.

[7]P. O'Connor and J. Tauc, Phys. Rev. B **25**, 2748 (1982).

[8]J. Tauc and Z. Vardeny, Philos. Mag. B **52**, 313 (1985).

[9]H. A. Stoddart, Z. Vardeny, and J. Tauc, Phys. Rev. B **38**, 1362 (1988).

[10] W. Grevendonk, M. Verluyten, J. Dauven, G. J. Adriaenssens, and J. Bezemer, Philos. Mag. B **61**, 393 (1990).
[11] O. A. Golikova, Fiz. Tekh. Poluprovodn. **25**, 1517 (1991) [Sov. Phys. Semicond. **25**, 915 (1991)].
[12] J. Dauven and W. Grevendonk, J. Non-Cryst. Solids **114**, 295 (1989).
[13] H. Stiebig and F. Siebke, Mater. Res. Soc. Symp. Proc. **377**, 287 (1995).
[14] P. Stradis, H. Fritzsche, and M. Tram Mater. Res. Soc. Symp. Proc. **377**, 467 (1995).
[15] J. Kočka, M. Vaneček, J. Kožišek, O. Stika, and J. Beichler, J. Non-Cryst. Solids **59-60**, 293 (1983).

Translated by Paul F. Schippnick

Generation in a microstrip-resonator-stabilized double-barrier resonant tunneling structure

A. A. Beloushkin, Yu. A. Efimov, A. S. Ignat'ev, A. L. Karuzskiĭ,* V. N. Murzin,
A. V. Perestoronin, G. K. Rasulova, A. M. Tskhovrebov, and E. G. Chizhevskiĭ

P. M. Lebedev Physical Institute, Russian Academy of Sciences, 117924 Moscow, Russia
(Submitted August 21, 1995; accepted for publication August 11, 1997)
Fiz. Tekh. Poluprovodn. **32**, 124–127 (January 1998)

Generation in a microstrip-resonator-stabilized double-barrier resonant tunneling structure based on GaAs/AlAs heterostructures has been investigated for the first time. The structures fabricated contain near-contact layers (spacers) that prevent impurities from penetrating into the active part of the structure and improve the temporal characteristics of the system. AuNiGe alloy microstrip contacts, which connect the structure with an external rf circuit, were prepared in a planar implementation, making it possible to minimize the RC delay time in the negative differential conductance region by decreasing the series resistance and capacitance of the structure. In structures with spacer layers, the negative differential conductance exhibits a complex behavior due to the influence of the space charge. © *1998 American Institute of Physics.*
[S1063-7826(98)03001-4]

1. INTRODUCTION

Recent theoretical and experimental studies of negative differential conductance (NDC) in double-barrier resonant tunneling structures (DBRTSs) have shown that the characteristic charge-transport times in such structures are very short (less than 100 fs).[1,2] Asymmetric structures consisting of two or more quantum wells[3–6] are even more promising in this respect because of the sharp decrease in the barrier transmittance when the resonance conditions for the energy levels in the quantum wells break down. Combining microstrip technology with nonlinear millimeter- and submillimeter-range devices based on such structures promises progress in advancement of the generation frequency into the terahertz frequency range.

The peak-to-valley current ratio on the NDC section of the current-voltage characteristic (IVC) is an indicator of DBRTS quality and strongly depends on the degree of current-carrier scattering by ionized impurities. To increase this ratio, nondoped separating layers (spacers) are inserted into the structure between heavily doped electrodes and the tunneling barriers, thereby preventing impurities from penetrating into the active part of the structure during the epitaxial-growth process.[7–11] The introduction of spacers decreases impurity scattering and improves the frequency characteristics of DBRTSs. As shown in the present work, the presence of such layers produces in both the IVCs and the high-frequency behavior of DBRTSs characteristic features which are determined by band bending and by the appearance of quasibound levels in the region of the spacer near the heavily doped electrode,[9,11] as well as by the accumulation of space charge in the quantum well and in the region of the spacer. These effects are accompanied by the appearance of bistability and hysteresis in the static and dynamic characteristics of the system,[9,10,12] as well as the appearance of characteristic features in the nonlinear properties of the DBRTSs.

2. TECHNOLOGY OF FABRICATION OF DOUBLE-BARRIER RESONANT TUNNELING STRUCTURES AND EXPERIMENTAL PROCEDURE

The experimental structures were fabricated by molecular-beam epitaxy using the results of a computer simulation. A structure was prepared on a semi-insulating GaAs substrate. This structure contained: 1000 nm n^+-AlGaAs doped with Si to 10^{18} cm^{-3}, 14 nm nondoped GaAs, 4.5 nm AlAs, 4 nm GaAs, 4.5 nm AlAs, 7 nm nondoped GaAs, 10 nm n^--GaAs doped with Si to 5×10^{17} cm^{-3}, and 500 nm n^+-GaAs doped with Si to 3×10^{18} cm^{-3}. Mesa structures with a diameter of 0.014 or 0.028 mm and planar collector contact pads were formed by the photolithographic method on the bottom n^+ layer followed by etching. SiO_2 insulation and the metal alloy AuGeNi were used to form ohmic contacts. Planar square (0.05×0.05 mm^2) emitter and collector ohmic contacts consisting of this alloy formed segments of microstrip lines with SiO_2 insulator that connected the DBRTSs with an external microwave circuit.

For use in microwave experiments, the plate on which the DBRTSs were prepared was cleaved into $0.25\times0.25\times0.1$ mm^3 crystals. A crystal together with the mesa structure contained on it were mounted into the microstrip plate of the holder and the plate was in turn connected with the microstrip resonator. Aluminum oxide was used as the insulator substrate in the microstrip plate of the holder. The microstrip line on the GaAs crystal was connected with a gold-plated microstrip line on the holder plate by soldering with gold wires. To study generation processes, the microstrip holder with the structure was mounted in a microstrip resonator for the purpose of performing with a spectrum analyzer microwave measurements in the range 0.01–40 GHz or

 1063-7826/98/010112-04$15.00 © 1998 American Institute of Physics

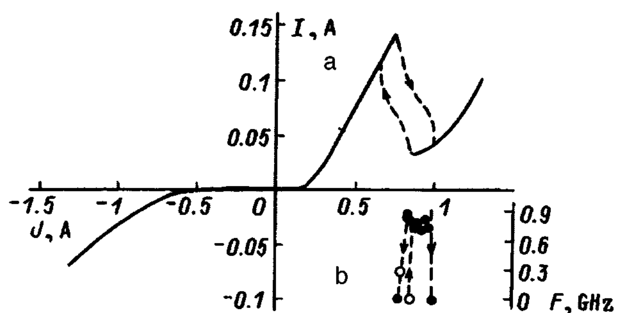

FIG. 1. Current-voltage characteristic of a 0.028 mm in diameter double-barrier resonant tunneling structure at 77 K (a). The dashed line shows the region of hysteresis where current instability is observed. The generation frequency F versus the bias voltage U applied to the structure at $T=77$ K (b). The arrows mark the values of U at which excitation (↑) and breakoff (↓) of generation occur; the open circles correspond to unstable states.

for measuring frequency with a frequency meter. The resonator consisted of a quarter-wave segment (with one end open and the other end shorted) of a 2-mm-wide and 200-mm-long microstrip line that was connected with an external coaxial line through a resistance divider. The resonator was fabricated by the method of etching out of Cu on one side of a flat 1.5-mm-thick insulating substrate with bilateral metallization. The metallized layer on the other side of the substrate played the role of a second, grounded, flat conductor of the microstrip line. The substrate consisted of a 200-mm-long and 30-mm-wide rectangle of glass textolite with a permittivity of 2. The frequency of the fundamental harmonic of the resonator was equal to 0.29 GHz. The bias voltage on the DBRTS was applied to the collector contact through a resistance divider. The emitter contact of the structure was connected to a strip conductor of the resonator at a point 70 nm from the short-circuited end of the resonator. The microwave characteristics of this microstrip circuit, employed for stabilizing the oscillations of the DBRTS in a frequency range of the order of 1 GHz, were first investigated with a serial 3I101V $p-n$ junction tunnel diode, which was mounted in the microstrip resonator instead of the DBRTS. Generation with output power of the order of tens of microwatts at 0.58 GHz, corresponding to a half-wave resonance mode of the resonator, was obtained with the tunnel diode. Quarter-wave and one-wave harmonics with frequencies of 0.29 and 1.1 GHz, respectively, whose output power was two orders of magnitude lower, were also observed.

3. STATIC CHARACTERISTICS

The static current-voltage characteristic (IVC) of the DBRTS is shown in Fig. 1 (line a). The peak-to-valley ratio was equal to 4.3 at 77 K (the ratio is somewhat lower at room temperature[9,10]) and the peak current density was equal to 2.2×10^4 A/cm^2. The measurements were performed on a 0.028-mm-diam mesa structure with a 2.5-Ω series resistance of the external circuit. A negative bias voltage was applied to the collector contact. Instability and hysteresis of the IVC were observed experimentally at voltages 0.6–1.0 V corresponding to the NDC region. These effects could be caused by the internal bistability of the structure. On account of the planar configuration of the contacts, this bistability is intensified by the instability of the system.[9,10]

4. MICROWAVE GENERATION

Microwave generation based on resonance tunneling in a DBMTS with spacer layers was observed when a negative bias voltage between 0.78 and 1.0 V was applied in the NDC region. The measurements were performed at 77 K. The output power in this case was several times lower than the output power observed in the case of the $p-n$ junction based tunnel diode. Dynamic hysteresis was observed in the frequency behavior of the structure. Generation appeared near the critical value 0.85 V both with increasing and decreasing voltage. After generation appeared, stable generation was then observed with the bias voltage varying in the interval 0.78 $V<V<1.0$ V. The generation frequency varied, as shown in Fig. 1 (curve b), and generation stopped at the end points of this interval. The clear correlation between the characteristic points of the curve of the dynamic hysteresis of self-excitation of generation and the static IVC suggests that internal bistability due to spatial redistribution of the charge is present in the structure. We note that dynamic hysteresis was not observed in the case of the $p-n$ junction tunnel diode.

The dynamic resistance in the NDC region for the DBRTS was much larger than for the $p-n$ junction tunnel diode; this is indicated by the difference of the generation frequencies between the DBRTS (0.8 GHz) and the tunnel diode (0.58 GHz), which were stabilized by the same microstrip resonator. The generation frequency of the DBRTS corresponds to the (3/4)λ-mode of the resonator, for which the point where the DBRTS and the resonance strip are connected corresponds to an antinode of the transverse electric field of this resonance mode. Since the DBRTS is connected in the direction of the transverse electric field, the presence of an antinode of this field at the point where the structure is connected in the resonator circuit indicates that the dynamic resistance of the structure is large. Another important difference of behavior between the DBRTS and the tunnel diode was the observation of a high degree of amplitude modulation (of the order 50%) of the oscillations generated by the DBRTS. Two characteristic modulation frequencies were observed. For bias voltages in the range from 0.8 to 0.96 V, the modulation frequency was equal to 20 MHz, the degree of modulation was of the order of 50%, and amplitude modulation with frequency 1 MHz and degree $\leqslant 10\%$ was observed at the edges of the region of existence of the undamped oscillations near 0.78 and 1.0 V. Since the characteristic nonresonance tunneling times in structures consisting of several quantum wells with parameters close to those of the DBRTS studied at 77 K are of the order of several nanoseconds or of the order of 200 ns (long-lived component),[13] the observed amplitude modulation could be due to oscillations of the space charge accumulated in the DBRTS with spacer layers as a result of nonresonance tunneling processes.

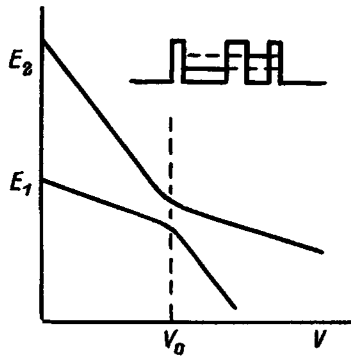

FIG. 2. Position of the size-well energy levels E_1 and E_2 in an asymmetric structure consisting of two quantum wells (see inset) plotted as a function of applied voltage V. V_0—Voltage at which the smallest splitting, as determined by barrier transmittance, of the resonance levels in the wells occurs and the electron density distribution in the levels is equalized between the wells.

5. MULTIWELL RESONANT TUNNELING STRUCTURES

The results presented above are for DBRTS-type structures. As shown in Refs. 3–6, quantum-well resonant tunneling structures with several quantum wells, specifically, three-barrier (double-well) structures, are more promising. The resonance condition in an electric field corresponds to the situation where the Fermi level and the lower quantum-well levels in both wells are close to one another; i.e., the structure must be asymmetric (the well widths are different). The smallest splitting between the levels corresponds to the anti-crossing region (see the inset in Fig. 2). Changes in the parameters of an asymmetric quantum-well structure make it possible to change in an independent manner both the peak-to-valley ratio and the peak current, in contrast to the DBRTS where such a change is precluded in principle. This makes it possible to achieve with a high electronic transmittance in a wide voltage range (Fig. 3) and with the same peak-to-valley ratio much higher peak currents than with a DBRTS (Fig. 4). Scattering of charge carriers by impurities was ignored in the calculations presented.[8] However, the possibility of varying separately the parameters of the system, which arises in this case, opens up, in principle, new prospects for producing resonant tunneling structures with optimal characteristics. Estimates show that inserting these structures in systems with microstrip resonators should greatly improve the high-frequency parameters of generators based on them.

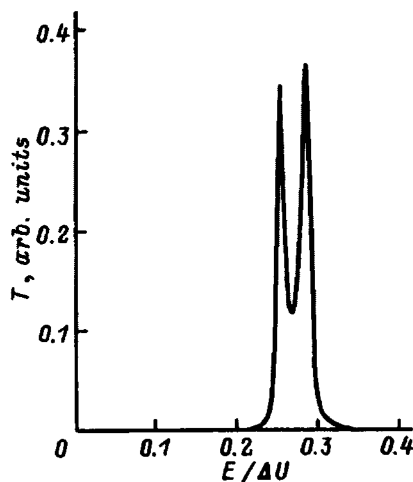

FIG. 3. Transmittance T versus current carrier energy E in the case of the transmittance of an asymmetric double-barrier structure with the following thicknesses: 1st barrier—3 nm; 1st well—6 nm; 2nd barrier—5 nm; 2nd well—6.5 nm; 3rd barrier–3 nm; ΔU—barrier height.

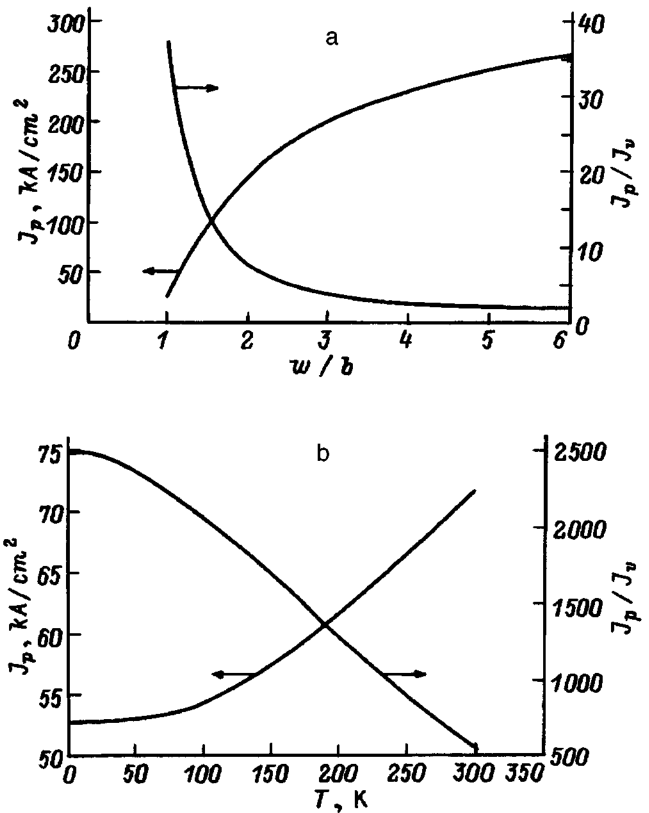

FIG. 4. Computed curves of the peak current density J_p and peak-to-valley ratio J_p/J_v for the current-voltage characteristic: a—versus the relative barrier thickness b/w for a symmetric single-well structure with well thickness $w=45$ nm; b—versus temperature T for a double-well structure with the following thicknesses: 1st barrier—2.83 nm; 1st well—7.358 nm, 2nd barrier—5.66 nm, 2nd well—3.962 nm, 3rd barrier—5.943 nm.

6. CONCLUSIONS

It has been demonstrated for the first time that microstrip-resonator-stabilized microwave generation based on DBRTS with spacer layers can be obtained. Dynamic hysteresis and modulation of microwave oscillations were observed in the system. The results obtained indicate that resonant tunneling structures with several quantum wells are promising from the standpoint of advancing generation in the direction of terahertz frequencies.

This work was supported by the State Science and Technology Programs ''Promising technologies and devices of micro- and nanoelectronics'' (Grant 133/57/2), ''Physics of solid-state nanostructures'' (Grant 1-012), ''Current directions in the physics of condensed media period. Superconductivity'' (Grant 93190), and by the international association INTAS (Grant 93-1704).

*e-mail: karuz@sci.fian.msk.su; fax: (007-095)-9382251

[1] E. R. Brown, T. C. L. G. Sollner, C. D. Parker, W. D. Goodhue, and C. L. Chen, Appl. Phys. Lett. **55**, 1777 (1989).
[2] E. R. Brown, J. R. Soderstrom, C. D. Parker, L. J. Mahoney, K. M. Molvar, and T. C. McGill, Appl. Phys. Lett. **58**, 2291 (1991).
[3] A. A. Gorbatchev and V. M. Koltyzhenkov in *Proceedings of International Workshop on Physics and Modeling of Low-Dimensional Structures Based Devices*, Aizu, Japan, 1995, p. 68.
[4] W. S. Truscott, Solid-State Electron. **37**, 1235 (1994).
[5] H. G. Roskos, M. C. Nuss, J. Shah, K. Leo, D. A. B. Miller, A. M. Fox, S. Schmitt-Rink, and K. Kohler, Phys. Rev. Lett. **68**, 2216 (1992).
[6] E. R. Brown, C. D. Parker, A. R. Calawa, and M. J. Manfra, Appl. Phys. Lett. **62**, 3016 (1993).
[7] A. A. Belouskkin, E. G. Chizhevskii, Yu. A. Efimov, A. S. Ignatyev, A. L. Karuzskii, V. N. Murzin, A. V. Perestoronin, G. K. Rasulova, and A. M. Tskhovrebov in *Abstracts of International Symposium ''Nanostructures: physics and technology,''* St. Petersburg, Russia, May–June 1995, p. 431.
[8] S. Muto, T. Inata, H. Ohnishi, N. Yokoyama, and S. Hiamizu, J. Appl. Phys. **25**, 577 (1986).
[9] A. S. Ignat'ev, V. E. Kaminskiĭ, V. B. Kopylev, V. G. Mokerov, G. Z. Nemtsev, S. S. Shmelev, and V. S. Shubin, Fiz. Tekh. Poluprovodn. **26**, 1795 (1992) [Sov. Phys. Semicond. **26**, 1005 (1992)].
[10] A. S. Ignat'ev, A. V. Kamenev, V. B. Kopylov, and D. V. Posvinskiĭ, Fiz. Tekh. Poluprovodn. **27**, 775 (1993) [Semiconductors **27**, 423 (1993)].
[11] F. Laruelle and G. Faini, Solid-State Electron. **37**, 987 (1994).
[12] S. A. Stoklitskiĭ, V. N. Murzin, Yu. A. Mityagin, V. I. Kadushkin, Yu. A. Efimov, and G. K. Rasulov, Kr. Soobshch. Po Fizike FIAN, No. 9–10, 10 (1994).
[13] A. V. Kvit, A. L. Karuzskiĭ, V. N. Murzin, and A. V. Perestoronin, Kr. Soobshch. Po Fizike FINA, No. 9–10, 3 (1994).

Translated by M. E. Alferieff

Nonequilibrium segregation of phosphorus in the system silicon dioxide-silicon

O. V. Aleksandrov

Svetlana-Poluprovodniki, a Closed Joint-Stock Company, 191156 St. Petersburg, Russia

N. N. Afonin

Voronezh State Pedagogical University, 394043 Voronezh, Russia

(Submitted May 5, 1997; accepted for publication June 10, 1997)
Fiz. Tekh. Poluprovodn. **32**, 19–23 (January 1998)

A model of diffusion-segregation impurity redistribution in the system SiO_2–Si during the thermal oxidation of silicon is developed, taking into account the nonequilibrium character of the segregation process at the moving phase boundary. The temperature dependence of the mass transfer of phosphorus and its mass-transfer coefficient at the SiO_2–Si interface are determined by the numerical analysis of experimental data. *© 1998 American Institute of Physics.* [S1063-7826(98)00301-9]

Impurity redistribution by diffusion and segregation in the system silicon dioxide-silicon plays an important role in the formation of impurity distributions in the skin layer of silicon during thermal oxidation. Existing theory and models of this phenomenon are based on the assumption that the segregation of impurities at the SiO_2–Si interface essentially takes place in thermal equilibrium.[1–3] However, this assumption is not justified in a number cases characterized by rapid advancement of the interface. The nonequilibrium character of the segregation process is indicated, for example, by experimental results published in Ref. 4, where the quantity of phosphorus in silicon after oxidation in wet oxygen in the temperature range 750–900 °C has been observed to decrease significantly, by as much as 20% of the original value. When segregation is an equilibrium process, essentially all the phosphorus impurity should be left in the silicon, having been steadily pushed back by the moving interface.

Our objective in this study is to develop a model of nonequilibrium diffusion-segregation impurity redistribution in the system SiO_2–Si with a moving interface and, on the basis of the model, to describe the prominent characteristics of phosphorus redistribution at high silicon oxidation rates.

According to the thermodynamics of heterogeneous systems,[5] the establishment of equilibrium at the interface is accompanied by equalization of the chemical potentials of the impurity at the interface on the dioxide side μ_{ox} and on the silicon side μ_{Si} with the annealing time:

$$\mu_{ox}=\mu_{Si}, \qquad (1)$$

where $\mu=kT\ \ln(C)+\varphi$, C is the impurity concentration, k is the Boltzmann constant, φ is the concentration-independent part of the chemical potential, and T is the temperature. It follows from the equilibrium condition (1) that the ratio of the thermodynamic-equilibrium impurity concentrations at the interface on the silicon side C_{Si}^{eq} and on the dioxide side C_{ox}^{eq} is a constant, defined as the equilibrium segregation factor:

$$m_{eq}=C_{Si}^{eq}/C_{ox}^{eq}=\exp[(\varphi_{ox}-\varphi_{Si})/kT], \qquad (2)$$

which is a function of the temperature and does not depend on the oxidation rate.

Since the diffusion coefficients of the principal dopants in silicon dioxide (B, P, As, and Sb) are very small, the main factor governing the tendency of the segregation process at the SiO_2–Si interface to establish equilibrium is impurity diffusion in the silicon. When the diffusion rate of impurity atoms exceeds the rate of advancement of the interface into the depth of the silicon, the relation (2) continues to hold at the interface during the entire process. In the nonequilibrium case the impurity atoms, which have a low mobility in comparison with the velocity of the interface, are trapped by the growing dioxide layer. This process is manifested by a departure of the ratio of the instantaneous impurity concentrations on the silicon and dioxide sides $m=C_{Si}/C_{ox}$ from the equilibrium segregation factor and, accordingly, in a deviation of the chemical potentials of the impurity on opposite sides of the interface from their equilibrium values. In this case the equality $m=m_{eq}$ is a criterion of the equilibrium of the impurity redistribution at the interface.

So far, mechanisms of impurity transport across a SiO_2–Si interface have not been developed in detail. Consequently, the segregation flux, which reflects the transition of impurity atoms across the interface without thermodynamic equilibrium, is described phenomenologically by means of a first-order kinetic model:[2]

$$F_s=h_s(C_{ox}-C_{Si}/m_{eq}), \qquad (3)$$

where h_s is the mass-transfer coefficient, which has units of velocity.

The boundary condition for the impurity at the moving interface is deduced from the following considerations. Let a layer of silicon of thickness Δx be oxidized in the time interval Δt, forming a dioxide layer of thickness ΔW_{ox}, $\Delta x=\alpha\cdot\Delta W_{ox}$ ($\alpha=0.44$ is the ratio of the thickness of the oxidized silicon to the thickness of the newly formed diox-

 1063-7826/98/010015-04$15.00 © 1998 American Institute of Physics

ide). The silicon layer Δx initially contains a quantity of impurity Q_1, and the quantity of impurity left in the SiO_2 layer grown from it is Q_2. During the time Δt the impurity excess $(Q_1 - Q_2)$ must be redistributed beyond the limits of the given element by diffusion and segregation. Diffusion transport of impurity in the dioxide is small, and we disregard it. Now the mass balance at the interface has the form

$$Q_1 - Q_2 = (F_d + F_s)\Delta t, \tag{4}$$

where $F_d = -D\nabla C_{\mathrm{Si}}$ is the diffusion flux in silicon at the interface with SiO_2, D is the impurity diffusion coefficient in the silicon, and $\nabla = \delta/\delta x$ is the gradient operator.

Letting $\Delta t \to 0$ and noting that $Q_1 \to \alpha dW_{\mathrm{ox}} C_{\mathrm{Si}}$ and $Q_2 \to dW_{\mathrm{ox}} C_{\mathrm{ox}}$ in this case, from Eq. (4) we obtain the equation of continuity of the flux at the SiO_2–Si interface during oxidation

$$-D\nabla C_{\mathrm{Si}} + h_s(C_{\mathrm{ox}} - C_{\mathrm{Si}}/m_{eq}) + V_{\mathrm{ox}}(C_{\mathrm{ox}} - \alpha C_{\mathrm{Si}}) = 0, \tag{5}$$

where $V_{\mathrm{ox}} = dW_{\mathrm{ox}}/dt$ is the SiO_2 growth rate.

When segregation takes place under equilibrium conditions $(F_s = 0)$, Eq.(5), with allowance for (2), reduces to the well-known relation[6]

$$-D\nabla C_{\mathrm{Si}} + V_{\mathrm{ox}}(1/m_{eq} - \alpha)C_{\mathrm{Si}} = 0. \tag{6}$$

In a coordinate system rigidly attached to the position of the silicon surface at the initial time $t=0$ the impurity flux in the bulk of the dioxide is proportional to the oxidation rate:

$$F_{\mathrm{ox}} = -(1-\alpha)V_{\mathrm{ox}} C_{\mathrm{ox}}. \tag{7}$$

Diffusion-segregation dopant redistribution in the system SiO_2-Si with moving gas-SiO_2 and SiO_2–Si interfaces at $x_1(t)$ and $x_2(t)$, respectively, is described by the Stefan boundary-value problem for the equations

$$\dot{C}_{\mathrm{ox}} = -\mathrm{div}(F_{\mathrm{ox}}) = \nabla((1-\alpha)V_{\mathrm{ox}} C_{\mathrm{ox}}), \quad x_1 < x < x_2, \tag{8}$$

$$\dot{C}_{\mathrm{Si}} = -\mathrm{div}(F_d) = \nabla(D(C_{\mathrm{Si}})\nabla C_{\mathrm{Si}}), \quad x_2 < x < l, \tag{9}$$

where x is the coordinate measured from the position $x_2(0)$ of the SiO_2–Si interface at the initial time in the depth of the silicon, l is the depth of the region of solution in silicon, which is chosen so as to maintain a constant impurity concentration at this depth during the entire anneal, and the overdot signifies the derivative with respect to the time t.

Problem (5), (8), (9) is solved numerically by reducing it, with a change of variables, to a problem with fixed boundaries, which is solved on a computer by factorization using homogeneous, implicit, conservative differencing schemes.[7]

The experimental data of Ref. 4, in which (111)- and (100)-oriented silicon with phosphorus ion-doped layers (ion energy 38 keV, dose 1×10^{16} cm^{-2}) was subjected to isochronous (1 h) wet-oxygen annealing in the temperature range 700–1000 °C, are analyzed on the basis of our model of nonequilibrium diffusion-segregation redistribution. The temperature dependence of the quantity of phosphorus Q_{Si} remaining in the silicon after annealing is shown in Fig. 1 (points).

For the initial impurity concentration distribution we use the distribution of the impurity formed directly after ion implantation. We model the ion implantation process by a type-4 Pearson function, using the values of its moments given in Ref. 8.

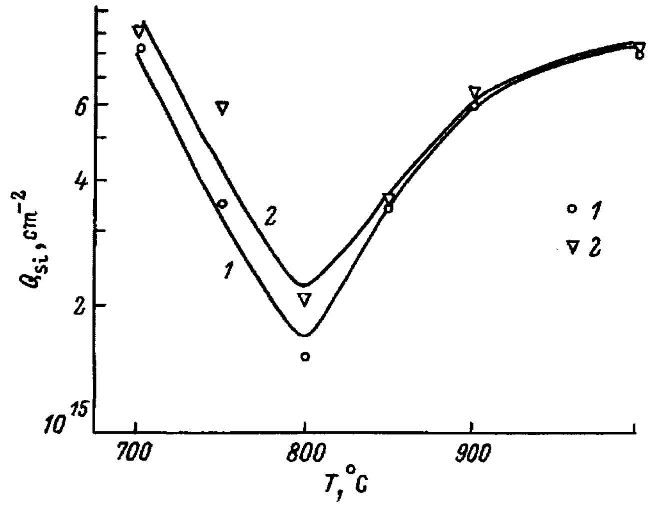

FIG. 1. Quantity of residual phosphorus in Si versus wet-O_2 oxidation, experimental (points) and calculated (solid curves). *1)* Si(111); *2)* Si(100).

We calculate the diffusion coefficients from a concentration dependence of the form[1,9]

$$D = h_e[D_i^0 + D_i^-(n/n_i) + D_i^{=}(n/n_i)^2], \tag{10}$$

where h_e is a coefficient characterizing the acceleration of diffusion by the internal electric field, D^0, D^-, and $D_i^{=}$ are the intrinsic partial diffusion coefficients via native point defects existing in the neutral, negative, and double negative charge state, and n and n_i are the densities of majority and intrinsic charge carriers at the diffusion temperature, respectively.

The concentration of electrically active impurity n is determined from the known total phosphorus concentration C_{Si} using the previously derived[10] functional relation

$$C_{\mathrm{Si}} = n\left[1 + \sum_{j\geq 2}\left(\frac{n}{C_m}\right)^{j-1}\right], \tag{11}$$

where C_m denotes approximation factors having the units of concentration.

The oxidation kinetics is described by the linear-parabolic relation

$$t = W_{\mathrm{ox}}^2/K_p + W_{\mathrm{ox}}/K_l, \tag{12}$$

where K_l and K_p are the linear and parabolic dioxide growth rate constants, respectively.

The values of K_l and K_p are determined from the experimentally measured[4] dioxide thicknesses; here the concentration dependence of K_l is given in the form

$$K_l = K_{l_i}(1 + 0.01(V_t - 1)), \tag{13}$$

where K_{l_i} is the value of K_l in the oxidation of native Si (Ref. 11), and V_t is the normalized total concentration of vacancies in the doped Si (Ref. 12).

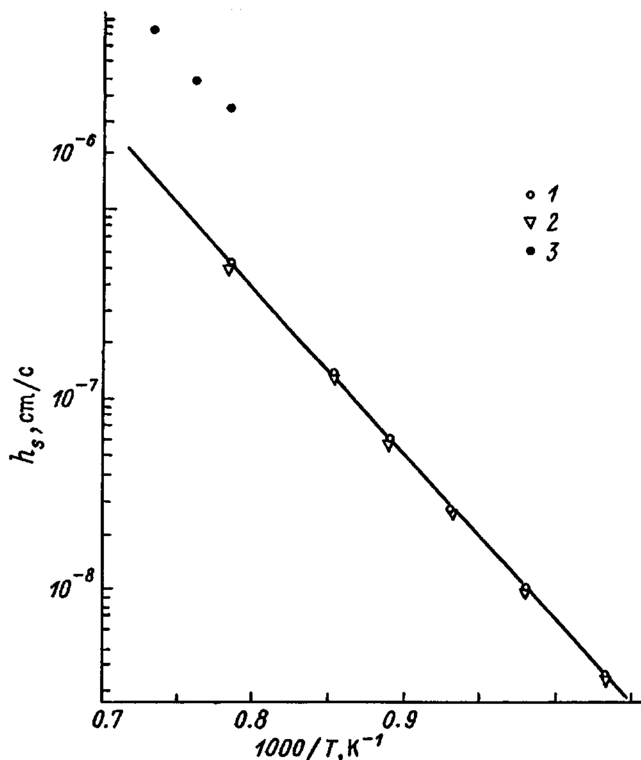

FIG. 2. Mass-transfer coefficient versus temperature. *1*) (111)-oriented Si wafer, wet-O_2 oxidation medium, present study; *2*) (100), wet O_2, our study; *3*) (100), dry O_2, Ref. 13.

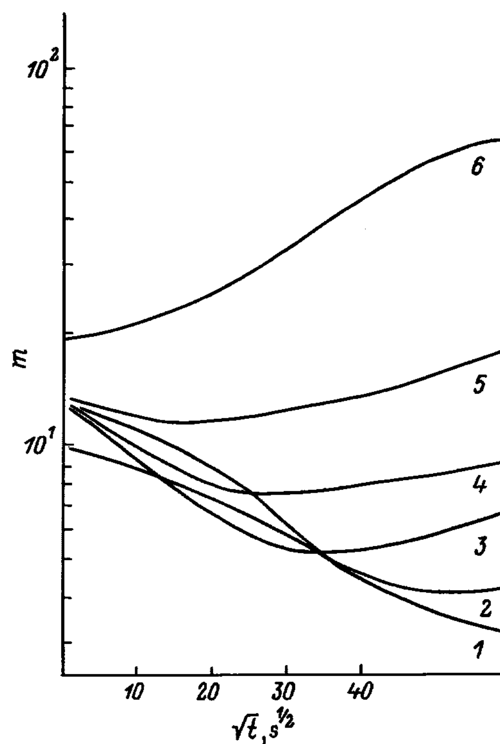

FIG. 3. Concentration ratio m versus oxidation time for various temperatures. *1*) 700 °C; *2*) 750 °C; *3*) 800 °C; *4*) 850 °C; *5*) 900 °C; *6*) 1000 °C.

The equilibrium phosphorus segregation factor in the system SiO_2–Si is assumed to have the value $m_{eq}=1000$ (Ref. 13).

In numerical analysis based on the model of the data from Ref. 4, for each experimental point of the temperature range 700–1000 °C we determine the values of the mass-transfer coefficient h_s, for which the results of calculating the quantity of impurity Q_{Si} left in the silicon after isochronous annealing match the experimental data (see Fig. 1). It is evident from Fig. 2, which shows the results of the analysis (points *1* and *2*), that the coefficient h_s is essentially independent of the silicon orientation and is a function only of the temperature. The temperature dependence of the mass-transfer coefficient can be approximated by a function of the form

$$h_s=5.7\exp(-1.78\ \text{eV}/kT)\ \text{cm/s}. \tag{14}$$

The results of calculations of the quantity Q_{Si} of phosphorus left in the silicon after oxidation during isochronous oxidative annealing for the temperature dependence (14) are represented by the solid curve in Fig. 1 in comparison with the experimental data.[4] If segregation were an equilibrium process here, for $m \gg 1$ essentially all the phosphorus would be pushed back by the moving interface, irrespective of the time and temperature, and the residual quantity in the silicon would be constant. However, as the oxidation temperature is lowered, the process deviates more and more from equilibrium; the leading edge of the interface advances into the depth of the Si far more rapidly than the impurity atoms migrating away from it. The latter are therefore trapped in the dioxide, and Q_{Si} decreases. Beginning with a certain temperature, the thickness of the growing dioxide layer becomes increasingly smaller and, even though the level of nonequilibrium is high, ever-increasing amounts of impurity are left after oxidation. Consequently, the $Q_{Si}(T)$ should have a minimum at a certain temperature, as is indeed observed in Fig. 1.

The modeling results suggest a practical criterion of equilibrium of the segregation process: $r=h_s/V_{ox}>10$, by which, even though m does not attain its equilibrium value, most of the phosphorus is left in the silicon after oxidation.

Figure 3 shows the calculated dependence of the impurity concentration ratio at the silicon dioxide-silicon interface on the anneal time $m(t)$ for (111)-oriented samples at various oxidation temperatures. The shape of the $m(t)$ curve at high temperatures ($T \geq 900$ °C) is explained by m tending to its equilibrium value. At low anneal temperatures ($T \leq 800$ °C) the behavior of the curves is influenced by the concentration dependence of the oxidation rate; this dependence causes r and, hence, m to decrease as the oxidation front approaches the maximum of the ion-implanted phosphorus distribution.

Under the experimental conditions of Ref. 4 the oxidation of (111)-oriented silicon is characterized by a higher oxidation rate than (100)-oriented silicon. The difference is attributable to the orientation dependence of the linear oxidation rate constant K_{l_i} (Ref. 11) and is most conspicuous in the temperature interval 700–850 °C, where the oxidation kinetics is dominated by the linear component. As a result, (111)-oriented samples have a greater thickness of the growing dioxide in isochronous annealing, so that in the presence

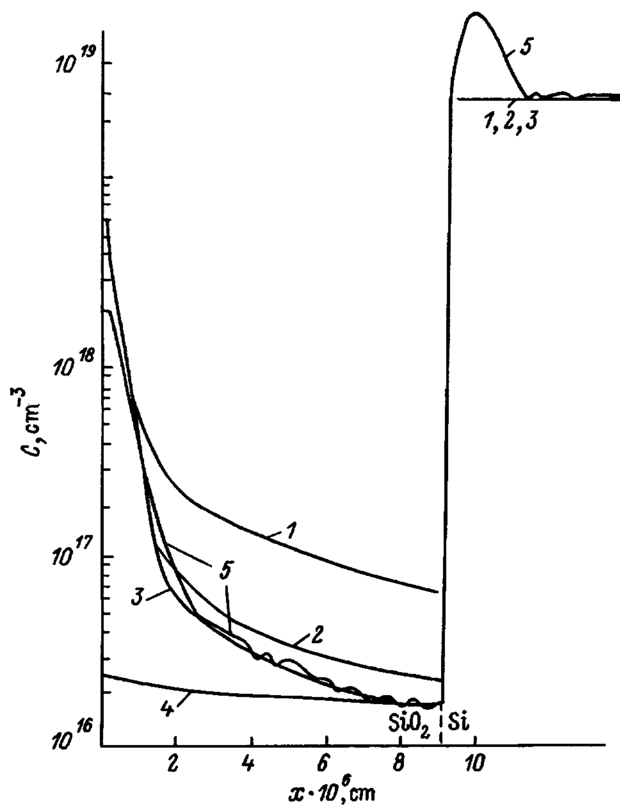

FIG. 4. Concentration distributions of P in the system SiO_2–Si ($T = 1100$ °C, $t = 30$ min). *1–3*) Calculated on the basis of the model in the present study: *1*) $h_s = 1.7\times10^{-6}$ cm/s; *2*) $h_s = 8.7\times10^{-6}$ cm/s; *3*) $h_s = 1.4\times10^{-5}$ cm/s; *4*) calculated on the basis of the model in Ref. 13 with $h_s = 1.4\times10^{-5}$ cm/s; *5*) experimental.

of nonequilibrium segregation they have greater impurity losses in the silicon than (100)-oriented samples, as illustrated in Fig. 1. Oxidation in the temperature range above 850 °C is characterized by an ever-increasing trend of the segregation process toward equilibrium, manifested by gradual leveling-off of the orientation dependence of Q_{Si} as the anneal temperature is raised.

The quantity h_s has been determined previously[13] by numerical analysis of the concentration distributions of phosphorus in silicon dioxide, which were obtained by secondary-ion mass spectrometry, within the framework of a model based on the assumption that the impurity concentration at the interface on the silicon side is constant, and that diffusion can be disregarded both in the dioxide and in the silicon:

$$C_{ox} = C_{Si}(m_{eq}\cdot\alpha\cdot V_{ox} + h_s)[1-\exp(-h_s/V_{ox})]/(m_{eq}\cdot h_s). \quad (15)$$

The values of h_s obtained in Ref. 13 for the dry-O_2 oxidation of phosphorus-implanted (dose 1×10^{15} cm^{-2}), (100)-oriented silicon at a temperature of 1000–1100 °C (Fig. 2, points *3*) are approximately an order of magnitude higher than the corresponding values calculated from our temperature dependence (14) derived for wet-O_2 oxidation.

A numerical analysis of the results of Ref. 13 for a temperature of 1100 °C with an oxidative anneal time of 30 min (Fig. 4) shows that the model developed by us (curves *1–3*) more adequately describes the experimental concentration distributions of phosphorus in the dioxide (curve *5*) than relation (15) (curve *4*), particularly near the surface of the silicon dioxide. The main cause of such a pronounced discrepancy is that the model in Ref. 13 fails to take into account impurity diffusion in the silicon as one of the driving forces leading to thermodynamic equilibrium of the segregation process, so that the surface impurity concentration C_{Si} in the silicon during annealing is decreased 2.7-fold. The value of the coefficient determine on the basis of our model, $h_s = 1.4\times10^{-5}$ cm/s (curve *3*), like the value given in Ref. 13 for dry oxygen, $h_s = 8.7\times10^{-6}$ cm/s (curve *2*), exceeds the value calculated from the temperature dependence (14) (curve *1*) for wet oxygen, justifying the assumption that the annealing medium influences the mass transfer of impurity across the SiO_2–Si interface.

We note that the accumulation of phosphorus in a narrow layer near the interface on the silicon side (curve *5*) has nothing to do with the segregation process and is described by a separate model.[14]

We have thus developed a model of the diffusion-segregation redistribution of an impurity in the system SiO_2–Si, taking into account the nonequilibrium character of the segregation process at the interface. Under the conditions of low-temperature oxidative annealing at high dioxide growth rates the model can be used to describe such attributes of phosphorus redistribution as trapping by the growing impurity oxide with high m_{eq}, the minimum of the temperature curve $Q_{Si}(T)$, and the influence of silicon orientation on $Q_{Si}(T)$.

[1] R. B. Fair, in *Impurity Doping Process in Silicon*, edited by F. F. Y. Wang (North-Holland, Amsterdam-New York, 1981), p. 315.
[2] D. A. Antoniadis, M. Rodoni, and R. W. Dutton, J. Electrochem. Soc. **126**, 1939 (1979).
[3] O. V. Aleksandrov, and N. N. Afonin, Izv. Vyssh. Uchebn. Zaved. Fiz. No. 12, 97 (1990).
[4] K. Yagi K. Oyu, M. Tamura, and T. Tokuyama, Appl. Phys. Lett. **35**, 275 (1979).
[5] I. P. Bazarov, *Thermodynamics* [in Russian] (Vyssh. Shkola, Moscow, 1983), p. 179.
[6] A. V. Kolosovskiĭ, in *Reviews of Electrical Engineering, Series on Semiconductor Devices* [in Russian], No. 6(288) (Moscow, 1971).
[7] A. A. Samarskiĭ, *Theory of Differencing Schemes* [in Russian] (Nauka, Moscow, 1977).
[8] A. F. Burenkov, F. F. Komarov, M. A. Kumakhov, and M. M. Temkin, *Spatial Distributions of Energy Released in a Cascade of Atomic Collisions in Solids* [in Russian] (Énergoizdat, Moscow, 1985).
[9] C. P. Ho, J. D. Plummer, S. E. Hansen, and R. W. Dutton, IEEE Trans. Electron Devices **ED-30**, 1438 (1983).
[10] O. V. Aleksandrov, N. V. Ashkinadze, and R. Z. Tumarov, Fiz. Tverd. Tela (Leningrad) **26**, 632 (1984) [Sov. Phys. Solid State **26**, 384 (1984)].
[11] E. A. Taft, J. Electrochem. Soc. **136**, 3476 (1989).
[12] C. P. Ho, J. D. Plummer, J. D. Meindl, and B. E. Deal, J. Electrochem. Soc. **125**, 813 (1978).
[13] K. Sakamoto, K. Nishi, F. Ichikawa, and S. Ushio, J. Appl. Phys. **61**, 1553 (1987).
[14] O. V. Aleksandrov and N. N. Afonin, Fiz. Tekh. Poluprovodn. **30**, 1570 (1996) [Semiconductors **30**, 823 (1996)].

Translated by James S. Wood

High-resolution x-ray diffraction study of InAs-GaAs superlattices grown by molecular-beam epitaxy at low temperature

N. N. Faleev, V. V. Chaldyshev, A. E. Kunitsyn, and V. V. Tret'yakov

A. F. Ioffe Physicotechnical Institute, Russian Academy of Sciences, 194021 St. Petersburg, Russia

V. V. Preobrazhenskiĭ, M. A. Putyato, and B. R. Semyagin

Institute of Semiconductor Physics, Siberian Branch of the Russian Academy of Sciences, 630090 Novosibirsk, Russia

(Submitted July 28, 1997; accepted for publication July 31, 1997)
Fiz. Tekh. Poluprovodn. **32**, 24–31 (January 1998)

InAs-GaAs superlattices grown by molecular-beam epitaxy at low temperature are investigated by high-resolution x-ray diffractometry. It is shown that despite a very high density of point defects due to the presence of excess arsenic, the as-grown superlattice has high crystal perfection. An analysis of the changes in the x-ray diffraction curves shows that high-temperature annealing, which is accompanied by the formation of As clusters and diffusion of indium, produces significant structural transformations in the GaAs matrix and at the interfaces. © *1998 American Institute of Physics.* [S1063-7826(98)00401-3]

INTRODUCTION

In recent years InAs-GaAs superlattices have been steadily attracting attention as objects of investigation by virtue of interesting physical phenomena associated with two-dimensional electron-gas confinement in deep, narrow quantum wells.[1] Normally in the growth of superlattices of this type by molecular beam epitaxy (MBE) the temperature of the substrate is chosen in the range 400–500 °C. This choice represents a compromise between regimes where the density of point defects increases at low growth temperatures and where the interfaces are diffused at high temperatures as a result of the segregation and diffusion of indium (a temperature of approximately 600 °C is known to be the absolute optimum for growing highly perfect GaAs layers).[1] However, InAs-GaAs superlattices grown at very low temperatures (e.g., at 200 °C) are also of major interest. This material is distinguished by a substantial quantity of excess arsenic, which is trapped in the crystal lattice of the grown epitaxial film.[2,3] Thin InAs layers in a GaAs matrix function not only as electron (hole) quantum wells, but can also trap arsenic clusters formed during annealing. As a result of this process, a secondary periodic As-GaAs structure can form in the annealed epitaxial film, coinciding spatially with the InAs-GaAs superlattice.[4,5]

Here we give the results of high-resolution x-ray diffraction analysis of InAs-GaAs superlattices grown by MBE at 200 °C. We show that despite a very high density of point defects attributable to the presence of excess arsenic, the as-grown superlattice has high crystal perfection. High-temperature annealing, accompanied by the formation of As clusters and the diffusion of indium, induces significant structural transformations in the GaAs matrix and at the interfaces, and the x-ray diffraction patterns become smeared as a result of these processes.

SAMPLES AND PROCEDURE OF THE INVESTIGATIONS

The InAs-GaAs superlattices were grown by molecular-beam epitaxy in the two-chamber Katun apparatus on semi-insulating GaAs(001) substrates at a temperature of 200 °C. The growth rate was 1 μm/h. The GaAs layers in the superlattice had a thickness of 30 nm. The InAs layers were grown by shutting off the Ga flux and turning on a flux of In. This technique produced InAs layers having a nominal one-monolayer thickness. The superlattice was made up of 30 periods. The total thickness of the InAs-GaAs epitaxial film was approximately 0.9 μm. The grown structure was divided into three parts. One part was left untreated, and the other two were annealed for 15 min, one at a temperature of 500 °C and the other at 600 °C. Annealing took place in the growth chamber of the MBE apparatus with excess arsenic pressure.

The average In concentration and the presence of excess As in the epitaxial films was determined by x-ray spectral microanalysis. The concentration of antistructural As_{Ga} defects was determined by measuring the characteristic optical absorption in the near-infrared region using Martin's calibration.[6] The structure of the samples was monitored by transmission electron microscopy along the cross section.

High-resolution x-ray diffraction analyses of the structural perfection were performed on two-crystal diffractometers. For precise measurements of the mismatch parameters and for assessment of the crystal perfection the measurements were carried out in the open-detector ω-scanning regime. The monochromator-collimator was an asymmetrical germanium crystal, which ensured divergence of the primary beam within angular limits of 1.0–1.2′ for the Cu$K\alpha1$ (004) reflection. Measurements over a broad angular interval to determine the period of the superlattice and estimates of the planarity of the layers and the diffuseness of the interfaces were made in ω–2Θ scanning regimes. In this case the aperture of the detector was confined to a narrow receiving slit to diminish the contribution of diffusely scattered x rays. A precisely oriented Ge(001) crystal, ensuring divergence of the primary beam within angular limits of 8′ for the Cu$K\alpha1$ (004) reflection, was used to generate monochromatized primary radiation. To obtain more precise evaluations of the

 1063-7826/98/010019-07$15.00 © 1998 American Institute of Physics

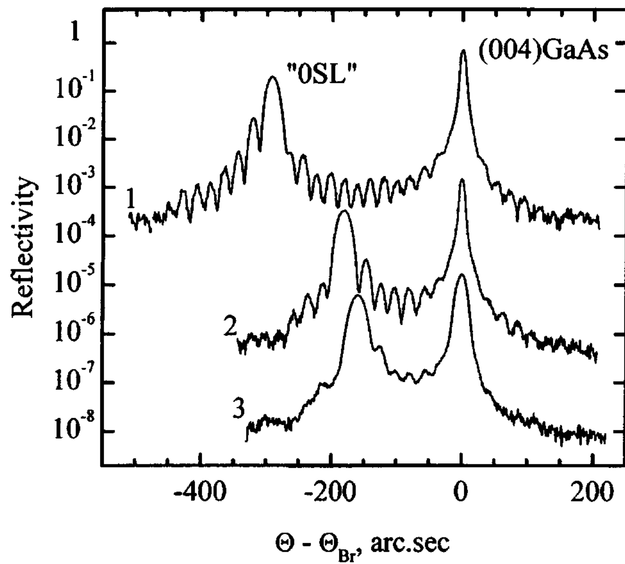

FIG. 1. Diffraction reflection curves near (004)GaAs for InAs-GaAs superlattices grown at low temperature, Cu$K\alpha 1$ radiation. *1*) As-grown superlattice; *2*) annealed at 500 °C; *3*) annealed at 600 °C.

angular and spatial distributions of the diffraction intensity and to determine the type of structural defects and their spatial distribution in the epitaxial structure, the ω curves were measured in addition to the ω–2Θ curves with the detector set in fixed angular positions. To record these curves, the detector with a narrow receiving slit (0.1 mm) was placed in a fixed angular position, and the investigated crystal was rotated near the reflecting position.

The resulting diffraction curves can be used to obtain the distribution of the diffracted intensity in reciprocal space in the direction perpendicular to the diffraction vector **H** [001]. The azimuth of the angular sweep direction was determined by the recording geometry and in our measurements coincided with one of the reciprocal lattice vectors [110]. The preferred type and density of crystal defects can be determined from the shape and parameters of the ω curves, which, in general, are superpositions of the coherent and diffuse components of the diffracted radiation, and because the ω curves correlate with an angular position on the ω–2Θ curves, the spatial positions of defects in the epitaxial structures can be determined quite accurately.

EXPERIMENTAL RESULTS

The x-ray spectral measurements show that an average indium concentration of 1.1 at.% in the layers corresponds to the expected ratio for a superlattice (1 monolayer InAs-30 nm GaAs)$\times$30. The concentration of excess arsenic is $X_{As}=(N_{As}-N_{Ga})/(N_{As}+N_{Ga})\approx 0.3$ at.%, where N_{As} and N_{Ga} are the numbers of As and Ga atoms. This value is in good agreement with the density of antistructural arsenic defects, 0.9×10^{20} cm^{-3}, measured from the optical absorption in the as-grown samples.

Diffraction curves recorded near the (004)GaAs reflection are shown in Fig. 1. The right peaks correspond to reflection from the substrate; and on the left are the so-called "OSL" peaks, which represent reflection from the periodic structure formed by the InAs and GaAs layers. The angular distance between the OSL and substrate peaks is determined by the average strain in the periodic structure, which depends on the thicknesses of the InAs and GaAs layers and the quantity of excess As in the structure. The change in the angular position of the OSL peak after annealing is attributable to the precipitation of excess arsenic in the lattice.[3] After annealing at 500 °C or 600 °C the strain induced by the arsenic excess all but vanishes, and the difference $\Delta\Theta$ between the lattice parameters of the GaAs substrate and the film is associated mainly with the presence of InAs layers in the epitaxial film. By measuring the lattice parameters before and after annealing sessions we were able to determine the average indium concentration in the film, the thickness of the InAs layers, and the initial concentration of excess As. The parameters of the rocking curves before and after annealing and the values of X_{As}, X_{InAs}, and T_{InAs} obtained from an analysis of the curves are summarized in Table I. The results of analyzing the rocking curves exhibit good agreement with the x-ray spectral microanalysis data and optical measurements.

It is evident from Fig. 1 (curve *1*) and the data of Table I that the as-grown sample is characterized by a very pronounced, extended interference pattern on the rocking curve and by high intensity and a small FWHM (full width at half maximum) of the principal peaks. These features are unique evidence of high crystal perfection, good reproduction of the parameters of the epitaxial layer over the entire thickness of the periodic structure, and planarity of the layers and of the structure as a whole.

The shift of the OSL peaks of the superlattice (see Fig.

TABLE I. FWHM, reflection coefficient K_{refl} at the maximum, and distance 2Θ between the principal peaks of the rocking curves, and parameters of the InAs-GaAs superlattice (difference $\Delta a/a_{\perp}$ between the lattice parameters of the substrate and the film, total thickness of the superlattice ΣT_{str}, period of the superlattice T_{SL}, excess arsenic concentration X_{As}, average InAs concentration in the film X_{InAs}, and thickness T_{InAs} of the InAs layers in the superlattice), calculated from x-ray diffraction data for the structures before and after annealing.

Anneal temp., °C	Substrate FWHM, arcsec/K_{refl}	OSL FWHM, arcsec/K_{refl}	$\Delta\Theta$, arcsec	$\Delta a/a_{\perp}$	ΣT_{str}, nm	T_{SL}, nm	X_{As}, %	X_{InAs}, %	T_{InAs}, Å
As-grown	9.00/0.682	20.20/0.195	−280	$2.10\cdot 10^{-3}$	920±20	30.0±1.0	~0.3[a]	1.1±0.1[a]	
500	8.70/0.722	22.90/0.165	−180	$1.35\cdot 10^{-3}$	850±40	27.0±2.0	0.27	0.9	2.45
600	16.50/0.410	24.30/0.155	−160	$1.19\cdot 10^{-3}$	790±80	26.5±3.0	0.34	0.8	2.10

[a]X-ray spectral analysis data.

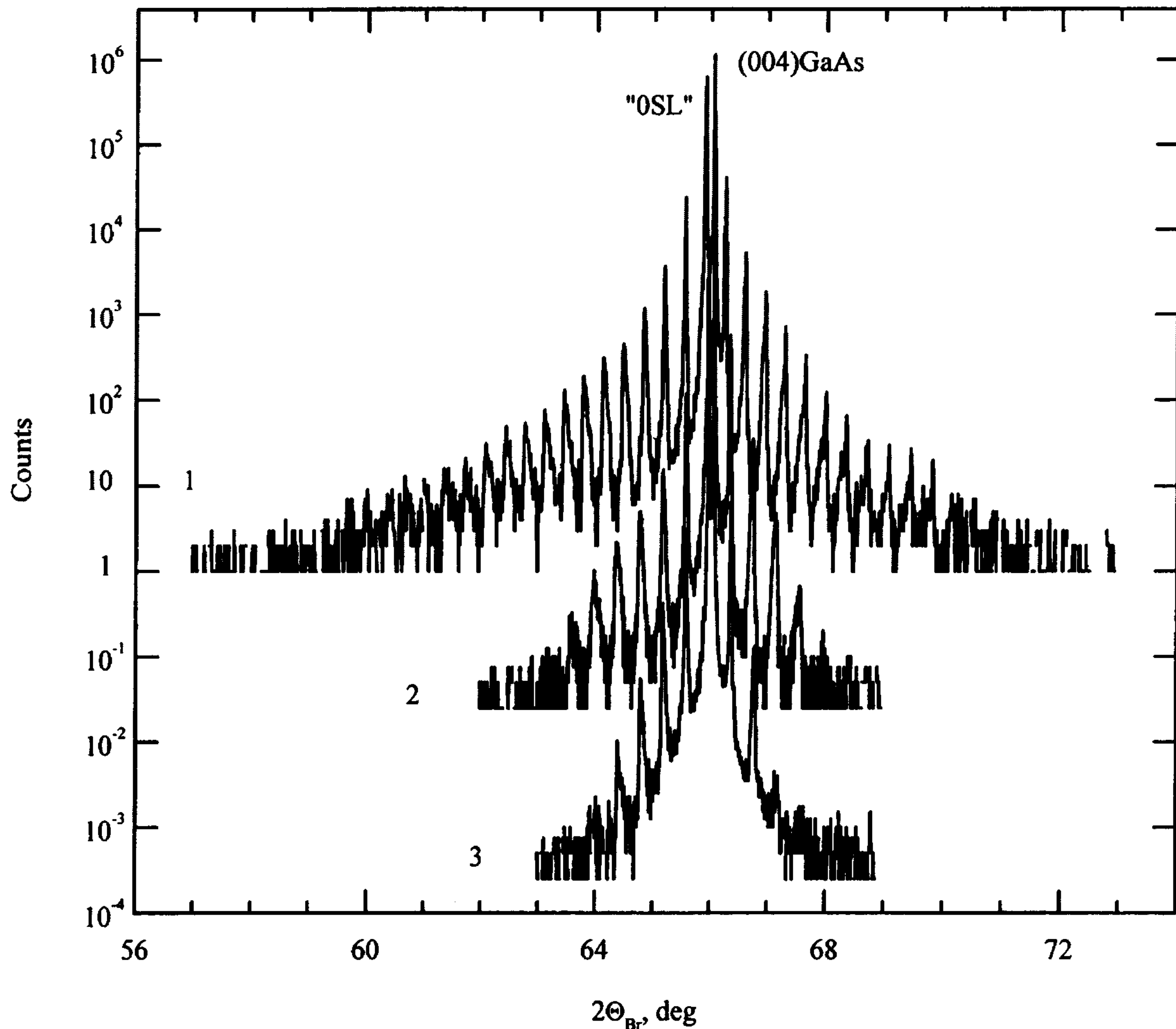

FIG. 2. Coherent ω–2Θ diffraction reflection curves for InAs-GaAs superlattices grown at low temperature, (004) reflection, Cu$K\alpha1$ radiation. *1*) As-grown superlattice; *2*) annealed at 500 °C; *3*) annealed at 600 °C.

1, curves *2* and *3*, and Table I) after annealing at 500 °C and 600 °C indicate a substantial decrease in the average strains in the superlattice due to structural transformation of the excess arsenic. In addition to the shift of the zero peak, there is also a significant change in the shape of the diffraction curves. The interference pattern becomes more diffuse and narrower. These changes are especially conspicuous after annealing at 600 °C, which produces appreciable broadening of the substrate peak and a reduction of its reflection coefficient.

To determine the period of the superlattice and the nature of the structural changes induced by high-temperature annealing, we recorded a series of rocking curves over a broad angular interval in the ω–Θ and ω-scanning regimes. The coherent ω–Θ curves for all the samples are shown in Fig. 2. We see that the previously mentioned changes in the rocking curves after annealing of the samples are also clearly discerned in a broad angular interval. The annealing-induced structural changes smear the interference patterns considerably and suppress the superlattice maxima. Compared with the as-grown curve, the angular width of the diffraction curves decreases by one half after annealing at 500 °C and to a third as much after annealing at 600 °C.

An appreciable increase in the diffuse component of the diffracted radiation could be expected simultaneously with narrowing of the angular interval, due x-ray scattering by As clusters. The formation of As clusters should produce in the diffracting volume of the epitaxial structure new scattering centers distributed nonuniformly in the volume and differing in size. In general, this process should cause the diffuse scattering to increase and, hence, should be detectable from the changes in the shape and parameters of the ω curves.

An analysis of the ω curves shows that diffuse scattering is localized near the (004)GaAs reflection. Figure 3 shows two characteristic ω curves for each of the investigated samples, recorded near the (004)GaAs reflection ($2\Theta \approx 66.20°$) and at a fairly large angular separation from the substrate maximum ($2\Theta \approx 65.48°$). The curves recorded far from the principal maximum have a narrow, coherent peak and essentially no broad diffuse component. Curves recorded near the (004)GaAs reflection ($2\Theta_{max} = 66.06°$) have a perceptible diffuse pedestal in addition to the narrow

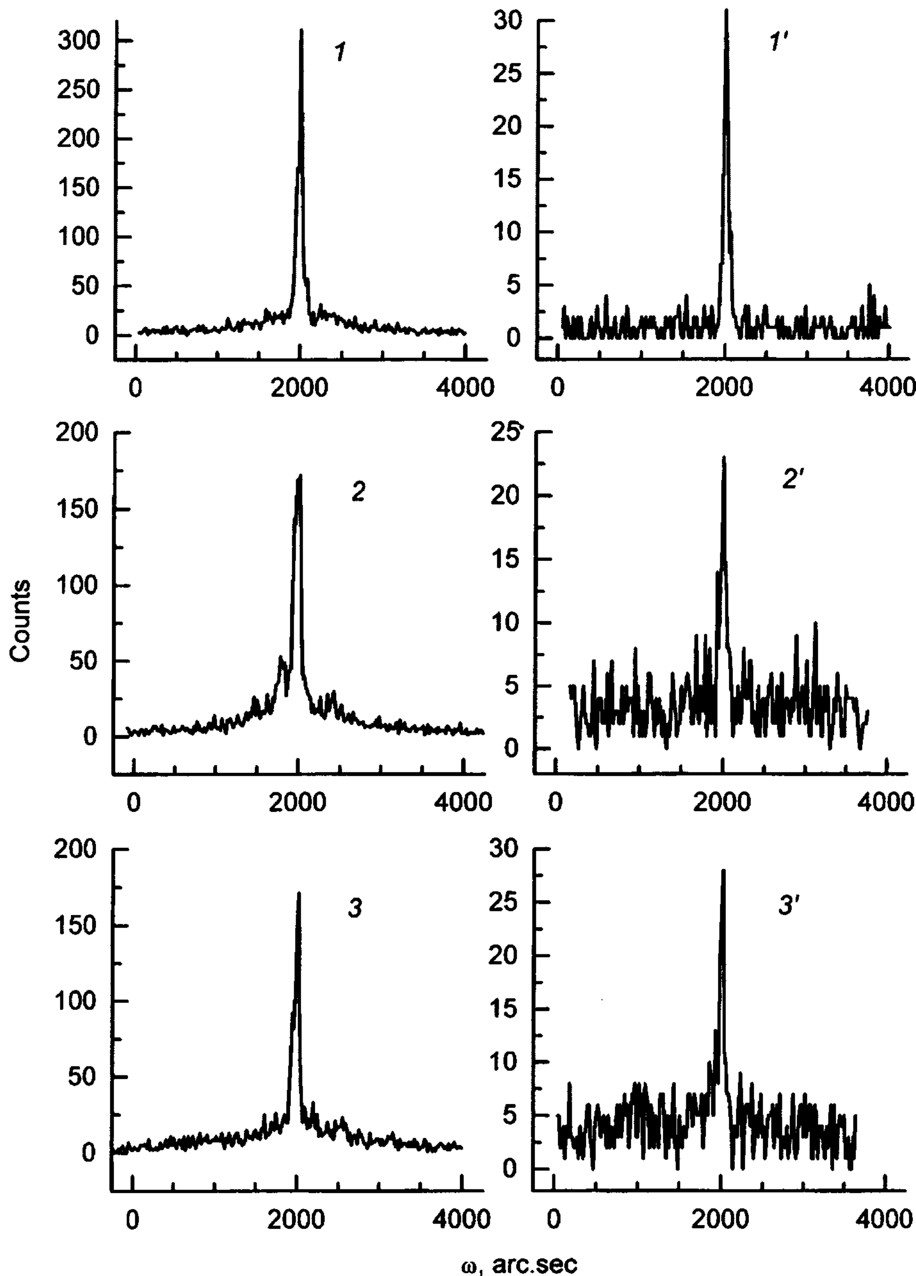

FIG. 3. X-ray ω curves recorded for InAs-GaAs superlattices grown at low temperature, two different detector positions, Cu$K\alpha1$ radiation. *1,1′*) As-grown superlattice; *2,2′*) annealed at 500 °C; *3,3′*) annealed at 600 °C *1–3*) $2\Theta=66.20°$; *1′–3′*) $2\Theta=65.48°$.

coherent peak. This profile of the ω curves is typical of crystals containing shallow structural imperfections of the point-defect and (or) cluster type. We can state with a high degree of probability that larger defects of the dislocation-loop or mismatch-dislocation type are nonexistent in the crystal matrix. The large FWHM of the diffuse component is indicative of small scattering centers, and the extremely low intensity reveals that the scattering centers are few in number, are weak in scattering power, or both. A comparison of the curves for the as-grown and annealed samples shows that the change in the diffuse component after annealing of the structures is insignificant. This result, coupled with the fact that the diffuse-scattering maximum is situated near the coherent substrate peak, justifies the assumption that the strongest contribution to diffuse scattering is from defects in the surface layer of the substrate and at the interface between the substrate and the epitaxial structure. Estimates of the density of defects from the FWHM of the incoherent component show that the density of defects increases from $(3.5-5.0)\times10^9$ cm^{-2} in the as-grown structure and the structure annealed at 500 °C to $(7.0-8.0)\times10^9$ cm^{-2} in the structure annealed at 600 °C. The correlation lengths in the [110] direction, which is perpendicular to the diffraction vector, decrease from 25–30 nm to 20–22 nm, respectively. The slight broadening and decrease in the intensity of the coherent peak for the annealed samples (see Fig. 3) are most likely associated with the decrease in the total width of the interference pattern.

DISCUSSION

It can be stated on the basis of the reported experimental data that an InAs-GaAs periodic structure grown at low temperature has a high crystal perfection, as characterized in the

x-ray diffraction curves by strong, narrow reflection peaks and a broad interference pattern formed by thickness oscillations and the superlattice peaks. Both the individual layers and the structure as a whole have good planarity, and the thicknesses of the layer are well reproduced from one period to the next. The low intensity of the diffusely scattered radiation and the character of its distribution in reciprocal space (see the ω curves in Fig. 3) indicate a comparatively low number density and small size of defects in the structures. The majority of the defects contributing to diffuse scattering are probably localized in a surface layer of the substrate and at the substrate-epitaxial film interface. These defects can be point defects, small clusters, or both together. Extended structural defects of the mismatch-dislocation type are nonexistent in the structures.

Having analyzed our data by the methodological approach proposed in Ref. 7, we can state that a large portion of the excess arsenic occupies space in the cationic sublattice of GaAs during low-temperature epitaxial growth. The InAs layers alternating with GaAs layers form a regular periodic structure with period $T_{SL}=30\pm1$ nm, whose average strain $(+2.1\times10^{-3})$ is determined by the quantity of excess As and the thickness of the InAs layers. The broad interference pattern and the low density and small size of the structural defects lead to the conclusion that the structure as a whole and its arsenic-enriched constituent InAs and GaAs layers have high crystal perfection and good planarity, and the period of the alternating layers is maintained very precisely over the entire thickness of the structure. The characteristic shape of the outlying superlattice maxima suggests the presence of a slight gradation of the period along the thickness of the structure.

Proof that the excess arsenic predominantly takes up positions at the GaAs lattice sites can be found in the results of modeling of the coherent ω–2Θ diffraction curve for the as-grown sample within the framework of the Takagi-Taupin model for an ideal strained crystal. Since the existing computational models cannot correctly incorporate the presence of excess atoms of one group in a sublattice of atoms of another group, we have slightly increased the thickness of the InAs layers in our calculations to compensate for the added strain created by the presence of excess As. This artifice has scarcely any effect on the accuracy of determination of the superlattice period. The calculated curve is shown in Fig. 4. Also shown in the same figure for comparison is the experimental rocking curve for the as-grown sample. Clearly, the calculated and experimental curves exhibit good mutual agreement, both qualitatively and quantitatively. Our calculations enable us to refine the period of the superlattice and the accuracy (uniformity) of its reproduction along the thickness. The postulated existence of a slight gradation of the period along the thickness, based on an analysis of the shape of the outlying superlattice peaks, is corroborated by the results of the calculations.

Since the excess arsenic changes state during annealing (forming clusters, which increase in size as the temperature is raised), one might well expect a sizable increase in diffuse scattering in the annealed samples by comparison with the as-grown case. Our investigations have shown, however, that the diffuse scattering changes very little after annealing. This means that annealing does not produce new defects or significantly increase the density and sizes of existing defects of the kind responsible for diffuse scattering, and scattering by As clusters up to 8 nm in diameter with a density $\sim10^{16}$ cm^{-3} is slight. The weak scattering power of As clusters is probably explained by the fact that the clusters are imbedded in the GaAs lattice without generating large local strains of the surrounding matrix and without producing extended structural defects of the mis-match-dislocation type formed in stress relaxation. This conclusion is confirmed by the results of electron microscope examinations of the samples.

The process of structural transformation appears most likely to take place as follows. In the course of annealing a large portion of the excess arsenic, initially residing in the gallium sublattice, diffuses throughout the crystal and forms small clusters, which are distributed fairly uniformly in the volume of the periodic structure. The absence of any appreciable variations in the general form of the distribution of the diffuse component of the diffracted radiation suggests that an intrinsic crystal structure having parameters compatible with those of the GaAs matrix takes shape in the newly formed As clusters, beginning with very small diameters of the latter. This event probably accounts for the clusters becoming imbedded in the lattice, essentially without the formation of structural defects, and explains why that average lattice parameter of the GaAs layer grown at low temperature relaxes to values characteristic of stoichiometric GaAs, as is clearly evident from the shift of the OSL peak.

It is evident from Fig. 1 and Table I that annealing at 500 °C produces only very slight changes in the reflection coefficient and FWHM of the principal peaks of the rocking curves. Far more substantial changes takes place in these parameters after annealing at 600 °C. The broadening of the substrate peak and the decrease of its reflection coefficient are probably caused by the diffusion of excess arsenic into the substrate.

The insignificance of the increase in the diffuse component of the diffracted radiation for the as-grown samples rules out the possibility of linking the smearing of the interference patterns and suppression of the superlattice maxima, as observed on the corresponding coherent curves (see Figs. 1 and 2, curves *2* and *3*), to incoherent x-ray scattering directly by As clusters. From all appearances the main factor responsible for this effect is a loss of planarity of the epitaxial layers,[8] i.e., an increase in the thickness irregularity of the layers, smearing of the interfaces, and increased roughness of the latter due to the diffusion of indium, as well as the formation of As clusters near the thin InAs layers. It should be noted that, owing to the high density of native point defects, gallium vacancies, in particular, the diffusion of indium in GaAs grown at low temperature is far more rapid than in the stoichiometric material.[9] Data from Ref. 9 have been used to estimate the diffusion smearing of the InAs layers in our investigated superlattices. We have found, however, that the indium diffusion lengths during annealing of the samples, determined by extrapolation of the data from Ref. 9, are several times smaller than the estimates of nonplanarity (irregu-

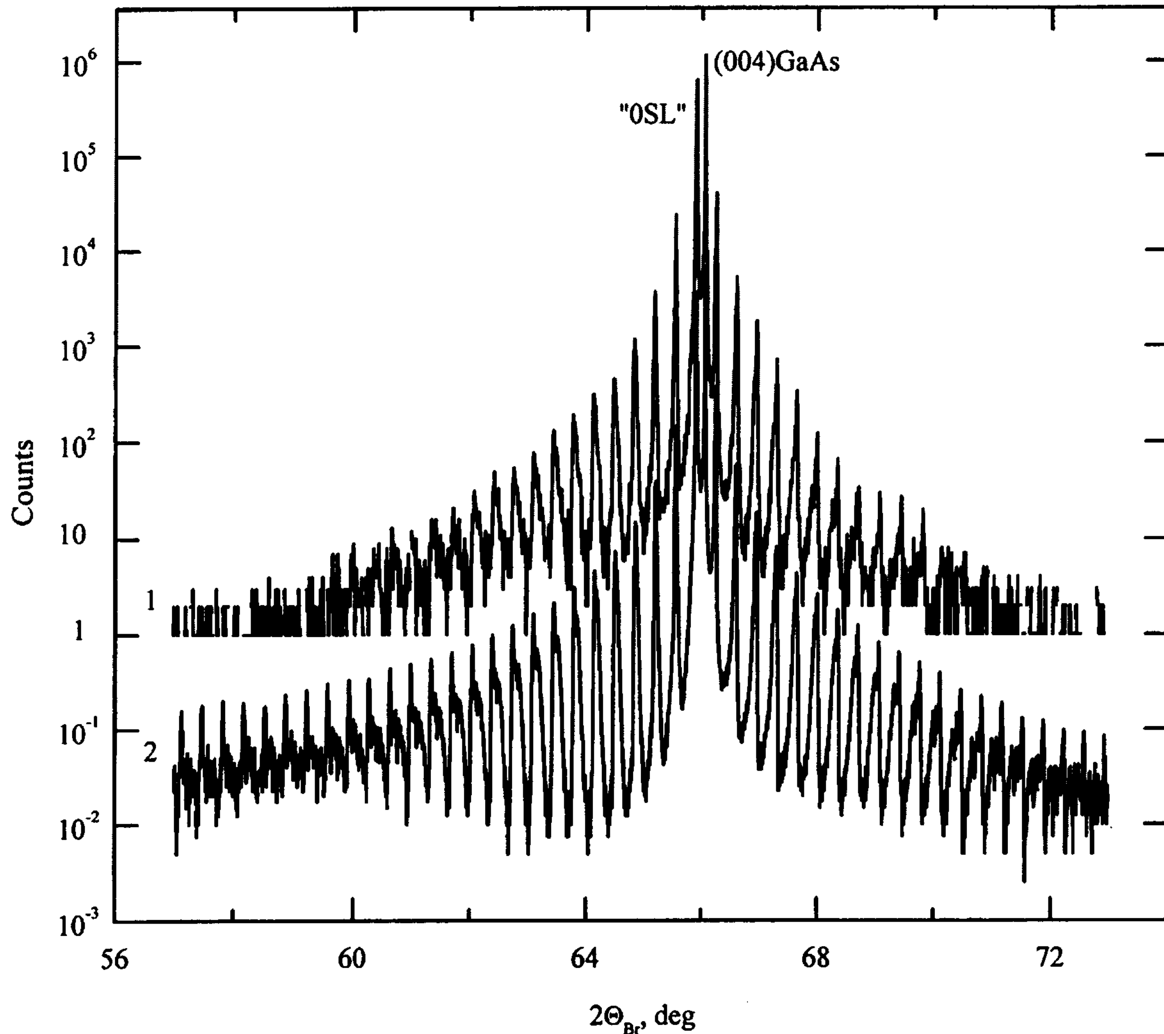

FIG. 4. Diffraction reflection curves for an InAs-GaAs superlattice grown at low temperature, (004) reflection, Cu$K\alpha1$ radiation. *1*) Experimental; *2*) calculated. Calculated parameters of the structure: $T_{SL}=300$ Å, $T_{\mathrm{InAs}}=3$ Å.

larity) of the superlattice period according to data on the widths of the ω–2Θ interference patterns (cf. $\pm T_{SL}$ in Table I). Such a striking difference is possibly associated with the different structure of the samples investigated in Ref. 9; there the superlattice (6-nm $In_{0.2}Ga_{0.8}As$--10-nm GaAs) was grown at standard temperature, and a GaAs layer grown at low temperature on top of this superlattice was used as the source of gallium vacancies. In our situation, on the other hand, both the GaAs layers and the thin InAs layers were grown at low temperature, which necessarily creates a high density of vacancies and, accordingly, a large In-Ga interdiffusion coefficient.

The presence of a periodic deformation potential in the InAs-GaAs superlattice has a significant influence on the spatial distribution of the arsenic clusters formed during annealing.[5] Electron microscope examinations have confirmed that the thin InAs layers are cluster-accumulation centers. The formation of clusters tends to displace the indium and crumble the thin InAs layers. This nonuniform crumbling in combination with diffusive smearing probably accounts for the experimentally observed, anneal-induced changes in the rocking curves. It is obvious that the smearing and crumbling of the InAs layers becomes more pronounced the higher the sample annealing temperature, as has indeed been observed experimentally.

It is evident from the table that the concentrations of excess As and the thicknesses of the InAs layers in the periodic structure, determined from a comparison of the parameters of the rocking curves for the as-grown samples and samples annealed at 500 °C and 600 °C, are very close to the corresponding values obtained by x-ray spectral microanalysis. Nonetheless, it is important to note that to use the parameters of the rocking curves for the sample annealed at 500 °C in such an analysis yields somewhat underestimated values of the excess arsenic concentration. This discrepancy is attributable to the fact that after annealing at 500 °C a small part of the excess arsenic persists in atomic form, as before, and the lattice parameter of such a material is somewhat higher than in the stoichiometric material. Essentially all the excess arsenic enters into clusters after annealing at 600 °C, and the concentration of atomic arsenic is negligible. In this case the lattice constant is slightly smaller than in the stoichiometric material, because of the high density of gallium vacancies and As clusters. According to our estimates,

this deformation is approximately -7.5×10^{-5}. Taking into account the indicated corrections, we can conclude that the concentration of excess As in our investigated InAs-GaAs superlattices is about 0.3%, the average InAs concentration in the epitaxial films is 0.85%, and the average thickness of the InAs layers in the superlattice is 2.28 ± 0.02 Å.

CONCLUSIONS

The reported x-ray diffraction investigations have shown that a 30-period InAs-GaAs superlattice grown by low-temperature molecular-beam epitaxy is highly perfect in spite of the presence of 0.3 at.% excess arsenic. The InAs layers in this superlattice have a thickness of approximately one monolayer, and the irregularity of the period and the deviations from planarity of the layers do not exceed 1 nm. A distinct, broad interference pattern closely approximating the ideal pattern obtained from model calculations is observed on the rocking curves of the superlattice within a broad angular interval. The diffuse scattering intensity is small. An analysis of the x-ray diffraction data leads to the conclusion that the bulk of the excess arsenic atoms trapped in the film during low-temperature epitaxy occupy sites in the cationic sublattice, forming antistructural As_{Ga} defects.

In the course of annealing the excess arsenic forms clusters, many of which accumulate in the thin InAs layers. The formation of clusters tends to smear and degrade the homogeneity of the InAs layers. In addition, the interdiffusion of indium, accelerated by a high density of native point defects, takes place during annealing of the InAs-GaAs superlattice. These phenomena attenuate the superlattice maxima in the annealed samples. We have established that arsenic clusters do not contribute significantly at all to diffuse x-ray scattering, which changes very little in annealing.

The authors are indebted to N. A. Bert and Yu. G. Musikhin for the electron microscope data.

This work has been supported by the Russian Fund for Fundamental Research and the Ministry of Science of Russia (under the programs ''Fullerene and Atomic Clusters'' and ''Physics of Solid State Nanostructures'').

[1] *Molecular Beam Epitaxy and Heterostructures*, edited by L. L. Chang and K. Ploog (Martinus Nijhoff, Dordrecht-Boston, 1985).

[2] M. Kaminska Z. Liliental-Weber, E. R. Weber, T. George, J. B. Kortright, F. W. Smith, B. Y. Tsaur, and A. R. Calawa, Appl. Phys. Lett. **54**, 1831 (1989).

[3] N. A. Bert, A. I. Veĭnger, M. D. Vilisova, S. I. Goloshchapov, I. V. Ivonin, S. V. Kozyrev, A. E. Kunitsyn, L. G. Lavrent'eva, D. I. Lubyshev, V. V. Preobrazhenskiĭ, V. R. Semyagin, V. V. Tret'yakov, V. V. Chaldyshev, and M. P. Yakubenya, Fiz. Tverd. Tela (St. Petersburg) **35**, 2609 (1993) [Phys. Solid State **35**, 1289 (1993)].

[4] T. M. Cheng, C. V. Chang, A. Chin, and J. H. Huang, Appl. Phys. Lett. **64**, 2517 (1994).

[5] N. A. Bert, V. V. Chaldyshev, D. I. Lubyshev, V. V. Preobrazhenskiĭ, and B. R. Semyagin, Fiz. Tekh. Poluprovodn. **29**, 2242 (1995) [Semiconductors **29**, 1170 (1995)].

[6] G. M. Martin, Appl. Phys. Lett. **39**, 747 (1981).

[7] M. Lesczynski, Phys. Rev. B **48**, 17046 (1993).

[8] V. G. Gruzdov, A. O. Kosogov, and N. N. Faleev, Pis'ma Zh. Tekh. Fiz. **20**(14), 1 (1994) [Tech. Phys. Lett. **20**, 517 (1994)].

[9] J. C. Tsang, C. P. Lee, S. H. Lee, C. M. Tsai, and J. C. Fan, J. Appl. Phys. **79**, 664 (1996).

Translated by James S. Wood

Photoluminescence of cadmium telluride recrystallized by nanosecond pulsed laser irradiation

V. N. Babentsov and N. I. Tarbaev

Institute of Semiconductor Physics, National Academy of Sciences of Ukraine, 252028 Kiev, Ukraine
(Submitted January 28, 1997; accepted for publication February 25, 1997)
Fiz. Tekh. Poluprovodn. **32**, 32–35 (January 1998)

The influence of nanosecond pulsed laser irradiation on the morphology and low-temperature photoluminescence of n-type CdTe at energy densities sufficient to melt the material ($0.2-0.5\ \mathrm{J/cm^2}$) is investigated. After recrystallization the material has an ''orange-peel'' appearance. The low-temperature photoluminescence spectrum corresponds to low-grade single-crystalline p-type CdTe containing a large number of dislocations and clusters of point defects. The laser treatment has a long-range effect, significantly altering the impurity-defect system in a way characteristic of $n \rightarrow p$ conductivity conversion at distances greater than 50 μm from the site where laser radiation is absorbed. © *1998 American Institute of Physics.*
[S1063-7826(98)00501-8]

INTRODUCTION

We have previously investigated the influence of pulsed laser radiation with a relatively low pulse energy density (up to $150\ \mathrm{mJ/cm^2}$) on the impurity-defect system of cadmium telluride.[1,2] This type of laser beam can create new defects or anneal existing defects in a CdTe crystal, depending on the prior history of the sample and the pulsed lasing regime.

We have shown that before the CdTe melting threshold (0.2–0.3 J/cm) is reached, a thin layer of amorphous tellurium (of thickness 10–20 nm) is formed on the surface of the crystal, where it eventually crystallizes, producing a polycrystalline film. Beneath this film is a cadmium-depleted layer of material extending to a depth of 30–40 nm and comprising nonstoichiometric $\mathrm{Cd}_x\mathrm{Te}_{1-x}$, where $x=0.3-0.5$.

Situated beneath the nonstoichiometric cadmium telluride is a layer of material in which a dislocation network is formed during stress relaxation.[3] The low-temperature photoluminescence and electrical properties in this region differ substantially from the properties of the as-grown material. In general, they exhibit a tendency to lower the conductivity and to produce new bands in the low-temperature photoluminescence spectrum, which are associated with recombination at complex defects such as nV_{Cd} or $nV_{\mathrm{Cd}}+M_{\mathrm{Cd}}$, where n is the number of solitary vacancies, and M is a group-I impurity. Here we report the results of an experimental study of the influence of nanosecond pulsed laser radiation on the morphology and low-temperature photoluminescence of n-type CdTe at power densities sufficient to melt the material ($0.2-0.5\ \mathrm{J/cm^2}$). We show that after recrystallization of the material its surface layer loses its as-grown mirror quality and acquires a morphology of the ''orange-peel'' type. The low-temperature photoluminescence spectrum observed on it corresponds to single-crystalline p-type CdTe with a high content of dislocations and clusters of point defects.

EXPERIMENTAL PROCEDURE

Samples of n-CdTe were prepared by annealing undoped (specifically, without any special doping procedure) p-CdTe wafers with a hole density $p<10^{15}\ \mathrm{cm^{-3}}$ at a temperature $T_a=500-600\ ^\circ\mathrm{C}$ in an atmosphere of saturation cadmium vapor in a sealed ampoule containing the sample and a weighed portion of cadmium.[4]

After the removal of the surface layer of the annealed wafer to a depth of 100–200 μm by polishing in a solution of bromine in methanol, the remaining wafer comprised n-type material uniformly doped in thickness with an electron density $n=(2-5)\times10^{15}\ \mathrm{cm^{-3}}$.

The orientation of the wafers corresponded to the {111} plane.

Prior to treatment the samples were placed on a holder permitting them to be moved in a straight line perpendicular to the direction of the laser beam at a rate $V=100-200\ \mu\mathrm{m/s}$.

The pulsed-laser irradiation of the sample was performed at room temperature in air using a Nd:YAG laser (operating in the Q-switching regime at a repetition rate of 10 Hz with a pulse duration of 20 ns and an emission wavelength $\lambda=0.63\ \mu\mathrm{m}$) through a slit of width 80 μm situated at a distance of 50–100 μm from the surface of the sample.

With the laser beam focused into a spot of diameter 20 μm, the given pulse repetition rate ensured conditions such that each point of the sample was irradiated by 10–20 pulses at a specified rate of movement of the laser beam along the slit until a strip of the irradiated material was formed. After one strip had been obtained, the slit was shifted in the parallel direction by 100–200 μm, and the treatment was repeated. This procedure produced a series of alternating strips of irradiated and nonirradiated material.

After laser treatment the surface of the sample was examined in an electron microscope (secondary-electron image contrast). The low-temperature photoluminescence spectra

 1063-7826/98/010026-03$15.00 © 1998 American Institute of Physics

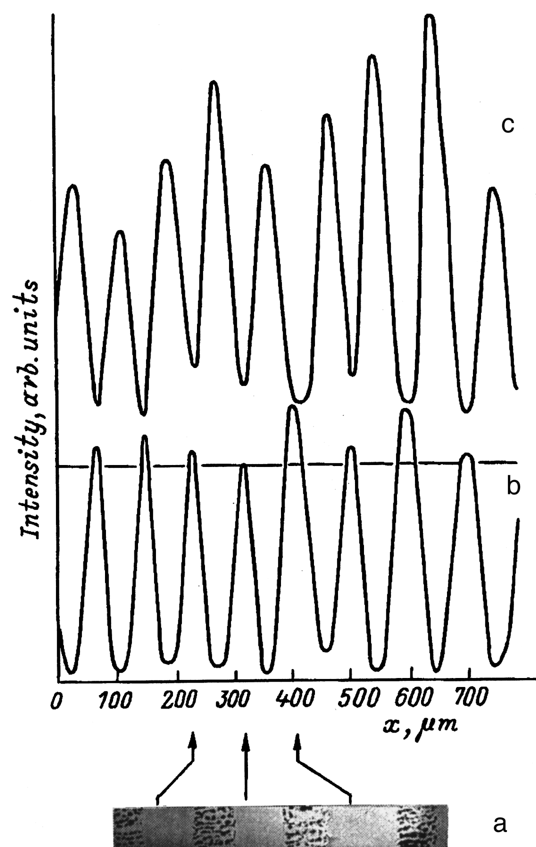

FIG. 1. Spatial distribution of secondary electrons in the electron microscope for the excitation of the surface of a laser-irradiated n-type CdTe sample (a) and intensities of the low-temperature photoluminescence bands at 780 nm (b) and 840 nm (c) in scanning along the coordinate x in the direction perpendicular to the strips of irradiated material.

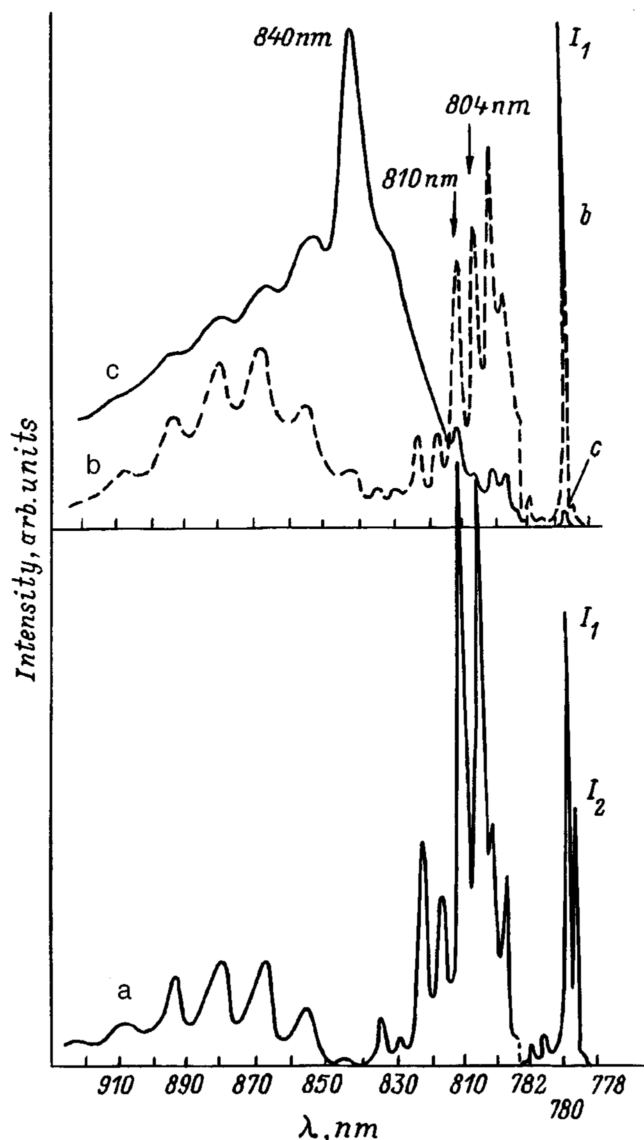

FIG. 2. Low-temperature photoluminescence spectra of CdTe. a) As-grown, untreated n-type material; b) area located half-way between tracks of laser-treated material; c) recrystallized material with orange-peel surface morphology.

were then measured on them (at a temperature $T = 4.2$ K). To obtain the spatial distribution of photoluminescence radiation with a specified wavelength, the photoexcitation zone (40-mW He-Ne laser beam, $\lambda = 632.8$ nm, focused into a spot of diameter 50 μm) was moved along the sample in the direction perpendicular to the laser tracks in such a way as to keep the recorded emission at all times focused onto the entrance slit of the MDR-23 spectral instrument.

EXPERIMENTAL RESULTS AND DISCUSSION

1. Surface morphology

Figure 1a shows secondary-electron micrographs of the surface of a p-type CdTe sample after laser irradiation. The tracks, whose surfaces resemble orange peels, are formed as a result of remelting of the material by the laser beam and its subsequent crystallization in air. Between them are tracks of the untreated surface of as-grown material, which have retained their mirror finish. The treated and untreated tracks on the sample surface have widths of 80–120 μm.

2. Low-temperature photoluminescence

Figure 2a shows the low-temperature photoluminescence spectrum of as-grown n-type CdTe, which contains two exciton lines of comparable intensity in the coupled-exciton region: I_1) line of excitons bound to neutral shallow acceptors (Li_{Cd},Na_{Cd},Cu_{Cd},P_{Te}); I_2) line of excitons bound to neutral shallow donors (Li_i,Na_i,Cu_i) (Ref. 5).

In the region of edge donor-acceptor (D-A) photoluminescence the indicator of n-type conductivity in CdTe is the band with a maximum at 810 mn, which is associated with the phosphorus acceptor state P_{Te} and is dominant in the wavelength interval 800–820 nm (Ref. 4).

After laser irradiation the photoluminescence spectrum changes radically, not only in the zone of the remelted material (orange-peel tracks), but also between these zones (Fig. 2, spectra b and c), i.e., where no remelting of the material has occurred.

The main change in the spectrum of the remelted material in comparison with the as-grown material is a substantial (20- to 40-fold) reduction in the radiation intensity in the region of bound excitons and in the D-A emission region

800–820 nm. Here the photoluminescence spectrum exhibits a new band of dominant intensity with a maximum at 840 nm, which is customarily assumed to be attributable to recombination at complex defects, including cadmium vacancies and atoms of residual impurities of group I metals,[6] which is also induced by plastic deformation of the bulk material or by abrasive treatment of its surface.[7] Most remarkable in this regard is the total disappearance of the I_2 line from the spectrum, an event characteristic of p-type material.

Figures 1b and 1c show profiles of the intensity distribution of the low-temperature photoluminescence bands in the vicinities of 840 nm and 780 nm, obtained by scanning the excitation spot perpendicular to the laser-formed tracks.

The spatial correlation of the extrema of the tracks indicates the interaction of recombination mechanisms in these bands.

Significant changes in the low-temperature photoluminescence spectrum also take place in regions where the material has not remelted as a result of laser heating, i.e., where the intensity of the I_1 is a maximum.

At a point equidistant from adjacent remelted CdTe tracks the I_2 line is essentially nonexistent in the photoluminescence spectrum, and the D-A emission band at 810 nm is no longer dominant in the interval 800–820 nm (Fig. 2, spectrum b). The 804-nm band is dominant in the spectrum, as is typical of p-type material.[4]

We can therefore conclude from the analysis of the low-temperature photoluminescence spectra that the laser heating of n-CdTe material enriched with excess cadmium atoms has the effect of predominantly eliminating cadmium from the material and generating cadmium vacancies.

The same result has been obtained previously[8] in mass-spectrometer measurements of the composition of the flux of atoms ejected during the laser irradiation of cadmium telluride. In the cited work it is shown that once a steady flux has been established, the number of cadmium atoms in the flux is four times the number of tellurium atoms. Consequently, the surface layer of the laser-irradiated material is depleted of cadmium, and a film of amorphous tellurium is formed on the surface.

The cadmium vacancies formed in the surface layer diffuse into the depth and off to the sides of the laser-treated parts of the material. These vacancies are filled with atoms of residual group-I impurities, generating singly charged acceptors, which induce p-type conductivity.

A ''supersaturated solid solution'' of cadmium vacancies condenses in the zones of remelted material, resulting in the formation of dislocation loops and complex defects; on the one hand, this process lowers the quantum yield of radiative recombination and, on the other, produces a new 840-nm band, which is not observed in the photoluminescence of the as-grown, near-stoichiometric cadmium telluride.

Scanning of the photoluminescence excitation point across the pulsed laser-irradiated strips shows that the effect of laser treatment is very far-reaching, and that it propagates along the surface of the sample to distances greater than 50 μm (the intensity profiles of the I_1 line and the 840-nm band are shown in Fig. 1, graphs b and c).

The large range to which the laser treatment extends is very difficult to explain by heat flow propagating from a nanosecond laser pulse. Probably more significant factors in the given situation are the diffusion of cadmium vacancies and the active role of dislocations in this process [the dislocation density is usually $(0.5-1.0)\times10^5$ cm^{-2}].

CONCLUSION

We have shown that:

1) the laser recrystallization of n-CdTe in air produces a material having a low-temperature photoluminescence spectrum characteristic of low-grade (many dislocations, twins, clusters of point defects, etc.) p-type cadmium telluride;

2) irradiation by nanosecond laser pulses has a long-range effect; the change in the photoluminescence spectrum at a point more than 50 μm distant from the laser absorption site indicates a major modification of the impurity-defect system, typical of $n\rightarrow p$ conductivity conversion.

[1] V. N. Babentsov, A. Baĭdullaeva, B. M. Bulakh, S. I. Gorban', P. E. Mozol', and B. K. Dauletmuratov, Fiz.-Khim. Mekh. **12**, 144 (1988).

[2] A. Baĭdullaeva, B. M. Bulakh, B. K. Dauletmuratov, B. R. Dzhumaev, N. E. Korsunskaya, P. E. Mozol', and G. Garyagdyev, Fiz. Tekh. Poluprovodn. **26**, 801 (1992) [Sov. Phys. Semicond. **26**, 450 (1992)].

[3] V. N. Babentsov, A. Baĭdullaeva, A. I. Vlasenko, S. I. Gorban', B. K. Dauletmuratov, and P. E. Mozol', Fiz. Tekh. Poluprovodn. **27**, 1618 (1993) [Semiconductors **27**, 894 (1993)].

[4] N. V. Agrinskaya and V. V. Shashkova, Fiz. Tekh. Poluprovodn. **22**, 1248 (1988) [Sov. Phys. Semicond. **22**, 790 (1988)].

[5] E. Molva, J. P. Chamonal, and J. L. Pautrat, Phys. Status Solidi B **109**, 635 (1982).

[6] V. N. Babentsov, B. M. Bulakh, S. I. Gorban', L. V. Rashkovetskiĭ, and E. A. Sal'kov, Fiz. Tekh. Poluprovodn. **23**, 1560 (1989) [Sov. Phys. Semicond. **23**, 967 (1989)].

[7] V. N. Babentsov, S. I. Gorban', E. A. Sal'kov, and N. I. Tarbaev, Fiz. Tekh. Poluprovodn. **21**, 1724 (1987) [Sov. Phys. Semicond. **21**, 1043 (1987)].

[8] J. J. Dubovski, P. K. Bhat, D. F. Williams, and P. Becla, J. Vac. Sci. Technol. A **4**, 1879 (1986).

Translated by James S. Wood

Filling of dislocation levels in strong electric fields

Z. A. Veliev

Yu. G. Mamedaliev Nakhichevan State University of the Azerbaidzhan Republic, 373630 Nakhichevan, Azerbaidzhan

(Submitted March 18, 1997; accepted for publication May 30, 1997)
Fiz. Tekh. Poluprovodn. **32**, 36–37 (January 1998)

The dependence of the filling factor for occupation of the energy levels of an edge dislocation by electrons on the external electric field is investigated theoretically. An analytical relation is derived for the filling factor. It is established that the dislocation filling factor decreases as the electric field is increased. © *1998 American Institute of Physics.* [S1063-7826(98)00601-2]

1. One cause of the nonlinearity of the current-voltage (I-V) curves of semiconductor crystals containing dislocations is the dependence of the filling factor f of the dislocation electron levels on the external electric field. This dependence is attributable to the independent variations of the electron capture cross section σ and the coefficient of thermal ionization of electrons β in the presence of an electric field. As a result, the filling factor f in arbitrary electric fields exhibits a complex dependence on the field strength $\mathscr{E}$.

Here we investigate the filling factor for occupation of the dislocation energy levels by electrons as a function of the electric field.

2. The steady-state dislocation filling factor is given by the equation

$$\sigma v n(0)(1-f)=\beta f. \qquad (1)$$

Here v is the average electron velocity, and $n(0)$ is the density of free electrons at the top of the dislocation barrier. Consequently,

$$f=[1+\beta/\sigma v n(0)]^{-1}, \qquad (2)$$

and the dependence of σ and β on $\mathscr{E}$ must be known in order to find the electric-field dependence of f.

For specific calculations of these quantities we adopt the edge-dislocation model proposed in Ref. 1, where the potential energy of the elastic field of the dislocations is taken into account together with the electrostatic field:

$$U(r,\theta)=U_0 \ln(R/r)-(Wb/r)\cos\theta+l\mathscr{E}r\cos\theta. \qquad (3)$$

Here $U_0=2e^2/\varepsilon a$, ε is the dielectric constant of the semiconductor, and a is the lattice period along the dislocation,

$$W=G(1-2\nu)/(1-\nu),$$

G is the deformation potential constant, ν is the Poisson ratio, **b** is the dislocation Burgers vector, and R is the radius of the Read cylinder of the charged dislocation. Equation (3) is written in cylindrical coordinates r,θ,z. The z axis is aligned with the dislocation axis, and the electric field vector is parallel to the x axis.

We also use the cascade trapping model developed in Ref. 2 to calculate the capture cross section σ and the coefficient of thermal ionization β of electrons from the dislocation center. The potential well near a dislocation is distorted in an external electric field. The discrete energy levels in this well correspond to negative values of the total energy $|E|\leqslant\Delta$. The quantity Δ is determined from the condition $\partial E/\partial r=0$ for $r=r_s(\mathscr{E})$, where

$$r_s=U_0[(1+4Wbe\mathscr{E}/U_0^2)^{1/2}-1]/2e\mathscr{E}, \qquad (4)$$

$$\Delta=-U_0\ln\{U_0R[(1+4Wbe\mathscr{E}/U_0^2)^{1/2}-1]/2Wb\}+U_0[1+(4Wbe\mathscr{E})/U_0^2]^{1/2}. \qquad (5)$$

The final relations for the capture cross section and the ionization coefficient as functions of the applied field have the form

$$\sigma(\xi)=\beta\left(\frac{2\pi\hbar^2}{mkT}\right)^{3/2}\frac{[(\Delta/kT)^2+\mu]^{\mu}}{v\mu^{\mu+3/2}\mathscr{U}(3/2,\mu+5/2,\mu)}\times\exp(E_D/kT), \qquad (6)$$

$$\beta=\frac{mU_0^2Z_{s0}^2}{4l_0\pi\hbar^3}\exp[-(E_D-\Delta)/kT]\ln(Z_s/a). \qquad (7)$$

Here $\mathscr{U}(x,y,z)$ is the Kummer hypergeometric function, $\mu=(\mathscr{E}/\mathscr{E}_0)^2$ is a parameter characterizing the degree of heating of electrons,

$$\mathscr{E}_0=(6mkT)^{1/2}(mG)^2kT/\pi e\rho s^2\hbar^4,$$

m is the electron mass, ρ is the density of the crystal, s is the sound velocity in the crystal,

$$r_{s0}=Wb/U_0;$$

E_D is the depth of the dislocation level, the quantity l_0 is related to the mean free path l in scattering by acoustic phonons by the equation $l_0=l(kT/2ms^2)$, and k is the Boltzmann constant.

Substituting Eqs. (6) and (7) into (2), we obtain the filling factor in the form

$$f=1+\frac{2}{n_d}\left(\frac{mkT}{2\pi\hbar^2}\right)^{3/2}\frac{\mu^{\mu}Q\left(\frac{3}{2},\mu+\frac{5}{2},\mu\right)}{[(\Delta/kT)^2+\mu]^{\mu}}\times\exp-\left[\frac{E_D-e\varphi(0)}{kT}\right], \qquad (8)$$

where n_d is the density of bulk donors.

In the weak-field limit, when $\mu\ll 1$ and $\mu^{\mu}Q(\frac{3}{2},\mu+\frac{5}{2},\mu)\rightarrow 1$ (see Ref. 3), Eq. (8) assumes the customary form

$$f=\left[1+\exp\left(-\frac{E_D-e\varphi(0)+\eta_0}{kT}\right)\right]^{-1}. \quad (9)$$

where $\eta_0=kT\ \ln(N_c/n_d)$ is the unperturbed chemical potential of electrons in the crystal, and N_c is the effective density of states.

In the strong-field limit, $\mu\gg 1$, Eq. (8) has the form

$$f=\left\{1+\frac{1}{2\pi n_d}\left(\frac{mkT_e}{\hbar^2}\right)^{3/2}\left(\frac{2}{3}\right)^{3/4}\frac{\Gamma\left(\frac{3}{4}\right)}{\sqrt{2}}\times\exp\left[-\frac{E_D-\Delta}{kT}+\frac{3}{2}\left(\frac{\Delta}{kT_e}\right)^2+\frac{e\varphi(0)}{kT}\right]\right\}^{-1}. \quad (10)$$

Here $kT_e=e\mathscr{E}l\delta^{-1}$ is the temperature of the electronic subsystem in the electric field, $\delta=ms^2/kT$ is the quasielastic scattering parameter, and $\Gamma(x)$ is the gamma function.

It is evident from Eq. (10) that f decreases as the electric field is increased. This behavior is attributable to the fact that the depth of the dislocation well decreases in strong electric fields. The ionization process therefore prevails over the trapping process, causing f to decrease.

3. We should mention that the equations for σ and β have been derived on the assumptions that $kT_e\gg\Delta$ and $T_e\gg T$. To these inequalities we also need to add $1<r_s(\mathscr{E})/l\ll\delta^{-1}$, which, on the one hand, is consistent with the cascade trapping model and, on the other, corresponds to the dependence of the distribution function of dislocation-bound electrons on their total energy.

We now estimate the domain of validity of Eqs. (9) and (10) with respect to the electric field. For a Si crystal: $a\simeq 5\times 10^{-10}$ m, $m\simeq 2.4\times 10^{-31}$ kg, $s\simeq 5\times 10^3$ m/s, $\rho\simeq 2.3\times 10^3$ kg/m^3, $G\simeq 10^{-18}$ J, and $\mathscr{E}_0\simeq 10^3$ V/m at $T=300$ K; i.e., Eq. (9) is valid for $\mathscr{E}\ll 10^3$ V/m, and Eq. (10) is valid for $\mathscr{E}>10^3$ V/m.

[1] V. B. Shikin and N. I. Shikina, Phys. Status Solidi A **108**, 669 (1988).

[2] V. N. Abakumov, I. N. Yassievich, and V. I. Perel', Fiz. Tekh. Poluprovodn. **12**, 3 (1978) [Sov. Phys. Semicond. **12**, 1 (1978)].

[3] *Handbook of Special Functions* [in Russian] (Nauka, Moscow, 1978), p. 321.

Translated by James S. Wood

Influence of the intensity of γ irradiation on the photoluminescence of GaAs:Te

V. I. Dubovik, V. A. Bogdanova, N. A. Davletkil'deev, N. A. Semikolenova, and O. A. Shutyak

Institute of Sensor Microelectronics, Siberian Branch, Russian Academy of Sciences, 644077 Omsk, Russia
(Submitted May 5, 1997; accepted for publication May 26, 1997)
Fiz. Tekh. Poluprovodn. **32**, 38–39 (January 1998)

The influence of γ irradiation (^{60}Co) of various intensities ($P_\gamma \approx 1.7-7.5$ kGR/h) on the photoluminescence of GaAs:Te single crystals $[n_0=(1.2-2.3\times 10^{18}$ cm$^{-3}]$ is investigated. Together with the known photoluminescence impurity bands ($h\nu_{max}\approx 1.2$ eV and/or $h\nu_{max}\approx 1.35$ eV) and edge band ($h\nu_{max}\approx 1.51$ eV), new bands are also observed in the spectra at $h\nu_{max}\approx 1.3$ eV and $h\nu_{max}\approx 1.48$ eV. The observed effects are attributed to radiation-stimulated ordering of the donor impurity and deep impurity centers. © *1998 American Institute of Physics.* [S1063-7826(98)00801-1]

A significant increase in the intensities of the photoluminescence edge and impurity bands is observed in gallium arsenide crystals with critical concentrations (n_{cr}) of a Te donor impurity ($3-4\times 10^{18}$ cm^{-3}).[1] An additional band at $h\nu_{max}(90\ \mathrm{K})\approx 1.48$ eV is observed simultaneously with the photoluminescence edge band associated with high-temperature transitions of the ''band-to-tail'' type. This behavior of the photoluminescence bands is assumed to be attributable to defect ordering processes in the impurity sublattice.[1]

We have investigated the influence of γ rays of various intensities on the photoluminescence of GaAs:Te single crystals in the region of ''precritical'' free-carrier densities with a view toward exploring the feasibility of taking GaAs:Te into a state with an ordered distribution of impurity centers. Single crystals of GaAs:Te grown by the Czochralski method[1)] with free-carrier densities $n_0=(1.2-2.3)\times 10^{18}$ cm^{-3} were irradiated from a ^{60}Co γ-ray source ($E_\gamma=1.17$ MeV and 1.33 MeV, $P_\gamma\approx 1.7-7.5$ *kGR/h*, $T_{irr}=300$ K). Prior to photoluminescence recording, the samples were ground (120–150 μm), polished, and etched in H_2SO_4:H_2O_2:H_2O (3:1:1) polishing etchant.

The observation of an impurity band with $h\nu_{max}(90\ \mathrm{K})\approx 1.3$ eV and a shift of the photoluminescence edge band toward the long-wavelength end with $h\nu_{max}(90\ \mathrm{K})\approx 1.48$ eV in the photoluminescence spectrum of γ-irradiated GaAs:Te crystals has been reported earlier[2] (Fig. 1). The investigations showed that these bands appear in the photoluminescence spectra only at certain γ-ray intensities. They could not be detected in the photoluminescence spectra of GaAs:Te crystals $[n_0=(1.2-1.4\times 10^{17}$ cm$^{-3}]$ after high-power irradiation ($P_\gamma\approx 4.6-7.5$ kGR/h). Reversible changes in the intensities and positions of the peaks of the photoluminescence impurity and edge bands with an increase in the absorbed dose of γ rays at $P_\gamma\approx 5.3$ kGR/h were observed for the first time in samples with $n_0=2.3\times 10^{18}$ cm^{-3} (Fig. 2).

We know[1,3] that the composition of the dominant recombination centers changes in GaAs:Te crystals with densities $n_0=1.4-2.3\times 10^{18}$ cm^{-3}, and the impurity band with $h\nu_{max}(90\ \mathrm{K})\approx 1.2$ eV ($V_{Ga}Te_{As}$) is replaced by a band with $h\nu_{max}(90\ \mathrm{K})\approx 1.35$ eV, which is associated with the complex $(V_{Ga}Te_{As})V_{As}$ (Ref. 4). The subsequent γ irradiation of these crystals stimulates radiative impurity ordering processes. In fact, according to the impurity ordering model[5] in GaAs doped with a group-VI impurity, at critical donor densities ($>3\times 10^{18}$ cm^{-3}) Coulomb interaction of (impurity ions-native point defects) complexes and interaction through the deformation potential lead to ordering of the impurity sublattice. In the ordering region of the photoluminescence spectra an additional band-to-band recombination spectral band with $h\nu_{max}<E_g^{opt}$ of the bulk material is observed as a result of the formation of a miniband energy spectrum. The emergence of the 1.3-eV and 1.48-eV bands in the photoluminescence spectra of γ-irradiated samples with $n_0<n_{cr}$ is attributable to the effective interaction of radiative Frenkel defects with deep impurity centers and to the correlative redistribution of the latter.

As a result of γ irradiation at $T=300$ K, Frenkel defects are formed in both sublattices of the crystal:[6]

$$As_{As}\rightarrow As_i+V_{As}, \quad (1)$$

$$Ga_{Ga}\rightarrow Ga_i+V_{Ga}. \quad (2)$$

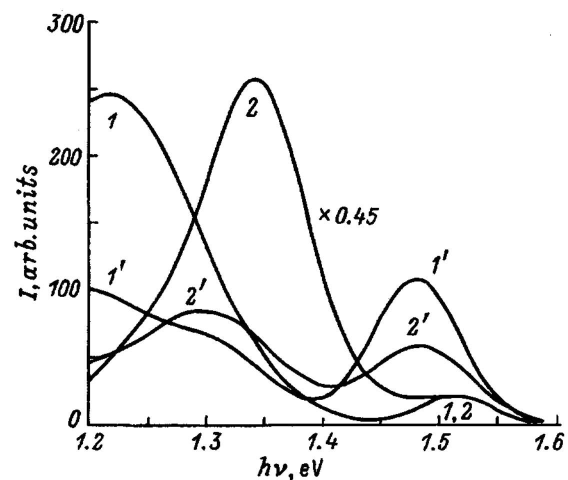

FIG. 1. Photoluminescence spectra of γ-irradiated GaAs:Te, $n_0=1.2\times 10^{18}$ cm^{-3}: *1, 1'*) 2.4 kGR; *2, 2'*) 2.3 kGR; before (1, 2) and after γ-irradiation: *1'*) 3.3 kGR ($P_\gamma\approx 1.7$ kGR/h; *2'*) 38.1 kGR ($P_\gamma\approx 5.3$ kGR/h).

 1063-7826/98/010031-02$15.00 © 1998 American Institute of Physics

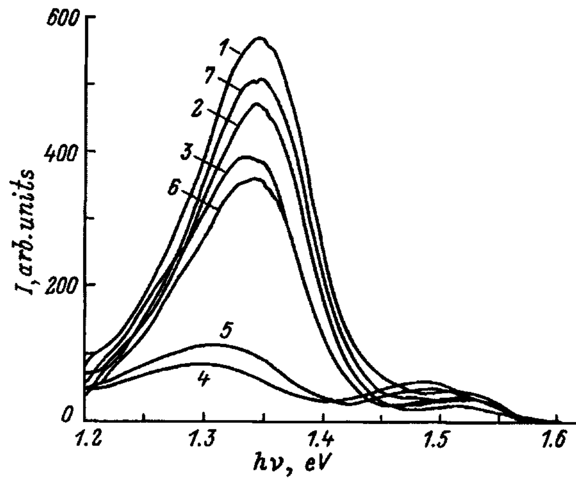

FIG. 2. Photoluminescence spectra of γ-irradiated GaAs:Te, $n_0=1.2\times10^{18}\ \mathrm{cm}^{-3}$, $P_\gamma\approx4.6$ kGR/h. *1)* $D_\gamma=0$; *2)* $D_\gamma=5$ kGR; *3)* 16 kGR; *4)* 38.5 kGR; *5)* 46 kGR; *6)* 57 kGR; *7)* 99 kGR.

It has been established[6–8] that at $T\geqslant300$ K As_i is mobile, and V_{As} is ''frozen'' up to $T\leqslant500$ K. Also mobile is V_{Ga} formed in γ irradiation.[9] As a result, we have V_{Ga} interacting with a $\mathrm{Te}_{\mathrm{As}}$ donor impurity, and As_i interacting with a $(V_{\mathrm{Ga}}\mathrm{Te}_{\mathrm{As}})V_{\mathrm{As}}$ impurity center, thereby increasing the concentration of $V_{\mathrm{Ga}}\mathrm{Te}_{\mathrm{As}}$ complexes:

$$\mathrm{Te}_{\mathrm{As}}+V_{\mathrm{Ga}}\rightarrow V_{\mathrm{Ga}}\mathrm{Te}_{\mathrm{As}}, \qquad (3)$$

$$(V_{\mathrm{Ga}}\mathrm{Te}_{\mathrm{As}})V_{\mathrm{As}}+\mathrm{As}_i\rightarrow V_{\mathrm{Ga}}\mathrm{Te}_{\mathrm{As}}+\mathrm{As}_{\mathrm{As}}. \qquad (4)$$

On the other hand, the reaction of displacement of an interstitial impurity atom by a mobile As_i becomes possible by virtue of the Watkins mechanism:

$$V_{\mathrm{Ga}}\mathrm{Te}_{\mathrm{As}}+\mathrm{As}_i\rightarrow V_{\mathrm{Ga}}+\mathrm{Te}_i+\mathrm{As}_{\mathrm{As}}. \qquad (5)$$

The relation between the values of n_0, P_γ, D_γ, and T_{irr} shift equilibrium toward the reaction (3), (4), or (5), accounting for the change in the intensities of the photoluminescence bands. But the emergence of the band with $h\nu_{\max}(90\ \mathrm{K})\approx1.3$ eV shows that both donor impurities and deep impurity centers are actively drawn into the process of forming radiation defects. The specific form of the recombination centers responsible for this photoluminescence band differs from both $V_{\mathrm{Ga}}\mathrm{Te}_{\mathrm{As}}$ (1.2 eV) and $(V_{\mathrm{Ga}}\mathrm{Te}_{\mathrm{As}})V_{\mathrm{As}}$ (1.35 eV) and is dictated by the interaction of the indicated centers with the mobile components of the reactions (1) and (2) and also by the possibility of the formation of split interstitial defects.[10]

[1)]The crystals were grown at the State Scientific-Research and Design Institute of the Rare Metal Industry (GIREDMET) in Moscow.

[1] V. A. Bogdanova and N. A. Semikolenova, Fiz. Tekh. Poluprovodn. **26**, 818 (1992) [Sov. Phys. Semicond. **26**, 460 (1992)].
[2] V. A. Bogdanova, N. A. Davletkil'deev, V. I. Dubovik, and N. A. Semikolenova, in *Digests of the Second Russian Conference on Semiconductor Physics* [in Russian] (Zelenogorsk-St. Petersburg, 1996), p. 127.
[3] V. A. Bogdanova, V. I. Dubovik, V. V. Prudnikov, and N. A. Semikolenova, in *International Conference on Solid State Devices and Materials* (Osaka, Japan, 1995), p. 1057.
[4] K. D. Glinchuk, V. F. Kovalenko, and A. V. Prokhorovich, Optoélektron. Poluprovodn. Tekh., No. 2, 46 (1991).
[5] V. V. Prudnikov, I. A. Prudnikova, and N. A. Semikolenova, Phys. Status Solidi B **187**, 87 (1994).
[6] V. V. Emtsev and T. V. Mashovets, *Impurities and Point Defects in Semiconductors* [in Russian] (Radio i Svyaz', Moscow, 1981).
[7] *Point Defects in Solids* [Russian translations], collected articles (Mir, Moscow, 1979).
[8] R. D. Dzhafarov, *Radiation-Stimulated Diffusion in Semiconductors* [in Russian] (Énergoatomizdat, 1991).
[9] V. I. Vovnenko, K. D. Glinchuk, and K. Lukat, Fiz. Tekh. Poluprovodn. **14**, 1834 (1980) [Sov. Phys. Semicond. **14**, 1093 (1980)].
[10] P. F. Fewester, J. Phys. Chem. Solids **42**, 883 (1981).

Translated by James S. Wood

Optical characteristics of 1.18-eV luminescence band complexes in *n*-GaAs:Sn(Si): results of a photoluminescence study with polarized resonant excitation

A. A. Gutkin, M. A. Reshchikov, and V. E. Sedov

A. F. Ioffe Physicotechnical Institute, Russian Academy of Sciences, 194021 St. Petersburg, Russia

T. Piotrowski and J. Pultorak

Institute of Electronics Technology, 02-668 Warsaw, Poland

(Submitted July 14, 1997; accepted for publication July 14, 1997)
Fiz. Tekh. Poluprovodn. **32**, 40–46 (January 1998)

Experimental values of the polarization of the low-temperature luminescence from the $V_{Ga}Sn_{Ga}$ and $V_{Ga}Si_{Ga}$ complexes in n-GaAs under conditions of resonant excitation by polarized light propagating along the [110] or [100] crystal axis are compared with expressions obtained in the classical dipole approximation for defects with triclinic or monoclinic symmetry. It is shown that the rotator fraction in the superposition of rotator and oscillator contributions to the emission of the complexes is 17–18%. The direction of the axis of these dipoles, which matches the experimental data, is consistent with the assumption that the effect of the donor on the vacancy orbitals of a hole localized in the complex is lower than that of the Jahn–Teller effect. The resulting symmetry of the complex may be monoclinic or triclinic. In either case, deviation of the optical dipole axis of the complex from the dipole axis of an isolated V_{Ga} vacancy distorted as a result of the Jahn–Teller effect is lower for the $V_{Ga}Sn_{Ga}$ and $V_{Ga}Si_{Ga}$ complexes than for $V_{Ga}Te_{As}$ complexes. This means that the effect of the donor on the electron structure of the $V_{Ga}Te_{As}$ complexes is greater than in the $V_{Ga}Sn_{Ga}$ and $V_{Ga}Si_{Ga}$ complexes. This correlates with the difference in the donor position in these complexes. © *1998 American Institute of Physics.* [S1063-7826(98)01001-1]

1. INTRODUCTION

It is well known that the photoluminescence band with maximum near 1.2 eV in n-GaAs, associated with gallium-vacancy (V_{Ga})—donor (D) complexes (Refs. 1 and 2), can be resonance-excited, i.e., as a result of optical transitions of the electrons from the complexes into the conduction band or to levels lying near its bottom.[3–6] Qualitative regularities of the polarization of this band in the case in which the light causing such transitions is polarized have led to the conclusion that the symmetry of the defects giving rise to its appearance in GaAs doped with Te, Sn, or Si is not higher than monoclinic.[4–6] A more detailed quantitative analysis of the measurements of this polarization has been carried out only for GaAs:Te (Ref. 7). In the present paper such an analysis, which allows one to draw some conclusions about the degree of correspondence of the phenomenological model considered in Ref. 6 with the properties of the defects and to estimate some of their parameters, is carried out for $V_{Ga}D_{Ga}$ complexes in GaAs:Sn and GaAs:Si, which differ from complexes in GaAs:Te by the position of the donor. Results of studies of defects in materials with different donors are compared.

2. DISTORTIONS OF $V_{Ga}D_{Ga}$ COMPLEXES

The initial positions of the components of the complex (V_{Ga} and D_{Ga}) at the sites of the undistorted GaAs lattice correspond to monoclinic symmetry of the defect and can be characterized by the direction of the ⟨110⟩-type axis that joins these components. However, according to the model considered in Ref. 6, at least in the emitting state of the complex, the positions of its components and/or the atoms surrounding them are displaced from the lattice sites in the ideal crystal because of the existence of a distortion associated with the Jahn–Teller distortion of V_{Ga}. This latter distortion is caused by the interaction of a hole, which is localized in the emitting state of the complex on a vacancy orbital, with the F_2-mode of the not-fully symmetric vibrations of the As atoms surrounding the V_{Ga} vacancy. For an isolated V_{Ga} vacancy, the interaction leads to trigonal symmetry of the initially tetrahedral quasimolecule $V_{Ga}As_4$ and gives four equivalent configurations with different directions of the ⟨111⟩-type trigonal axis. In order to allow a qualitative comparison with the experimental data, it was assumed in Ref. 6 that the splitting of the states of the V_{Ga} vacancy in the tetrahedral crystal field exceeds their splitting due to the Jahn–Teller interaction and the influence of the donor. In this case, the Hamiltonian describing the interaction with the F_2 mode and the influence of the donor in the basis of wave functions of the type $Z,\ Y,\ X$ has the form

$$H=d'\begin{pmatrix} 0 & Q_4 & Q_5 \\ Q_4 & 0 & Q_6 \\ Q_5 & Q_6 & 0 \end{pmatrix} + \begin{pmatrix} \beta^* & \left(\alpha-\frac{\beta}{2}\right) & \left(\alpha-\frac{\beta}{2}\right) \\ \left(\alpha-\frac{\beta}{2}\right) & -\frac{\beta^*}{2} & (\alpha+\beta) \\ \left(\alpha-\frac{\beta}{2}\right) & (\alpha+\beta) & -\frac{\beta^*}{2} \end{pmatrix}, \quad (1)$$

where d' is the coupling constant between the hole and the F_2 vibrations; Q_4, Q_5, and Q_6 are the normal coordinates which describe these vibrations and which transforms respectively as X, Y, Z, and α, β, and β^* are parameters which describe the influence of the donor.

It can be assumed that the effect of the donor on the vacancy orbitals is less than that of the interaction with the F_2 mode, as is the case for $V_{Ga}Te_{As}$ complexes in GaAs (see, e.g., Ref. 7). This conclusion follows from a series of experimental data, in particular, the absence of visible alignment of the distortions in the case of uniaxial pressures up to 10 kbar along the [100] direction.[6,8] and also from the proximity of the positions of the photoluminescence bands for complexes involving different donors (Te_{As} Sn_{Ga}, Si_{Ga}, S_{As}), while the Jahn–Teller stabilization energy for $V_{Ga}Te_{As}$ exceeds 200 meV (Ref. 7).

Accordingly, in first-order perturbation theory the influence of the donor in the formation of the $V_{Ga}D_{Ga}$ complex leads to some change in the displacements of the atoms of the $V_{Ga}As_4$ quasimolecule and the energies of the previously equivalent configurations of this molecule.[6] The directions of the resulting displacement of the V_{Ga} vacancy in the complex corresponding to these configurations are indicated by arrows in Fig. 1.

Jahn–Teller configurations *2* and *3* (Fig. 1), in which the hole is localized mainly on the dangling bonds of atoms *2* and *3*, which are initially arranged symmetrically about the donor, are equivalent. If they have lowest energy, then the application of moderate uniaxial pressure to the crystal along the [111] direction under low-temperature conditions should lead to the destruction of the equivalency of these configurations in some of the complexes and to their nonequilibrium population (alignment of the distortions). The latter circumstance should result in a stepped variation of the polarization of the photoluminescence in the case of application of uniaxial pressure at low temperatures. Since such an effect has been observed experimentally in the excitation of complexes as the result of generation of electron–hole pairs and subsequent trapping of holes onto complexes (see, e.g., Ref. 6), it was previously assumed that the indicated configurations of the complex have lowest energy.[6,8] This corresponds to $\beta \geqslant 0$, $\alpha > -\beta/4$ in the Hamiltonian (1) and triclinic symmetry of the complex.[6] However, such a situation is possible only under those conditions in which the potential of the donor core has a minimum near atoms *2* and *3* or can be approximated by a potential of zero radius (a δ-shape potential).[9] Factors which could cause such behavior of the potential are unclear.

It is more natural to assume that the donor core potential repelling the hole decreases monotonically with distance. In this case, only one configuration has lowest energy for zero external deformation, and that is the one corresponding to localization of the hole on a dangling bond of the atom furthest removed from the donor, atom *4* (Fig. 1), which corresponds to $\beta < 0$, $\alpha > \beta/2$ and monoclinic symmetry of the complex.[6] Due to the absence in the complex of equivalent configurations with lowest energy, variation of the direction of distortion in certain groups of the complexes subjected to uniaxial pressure is possible only when this pressure com-

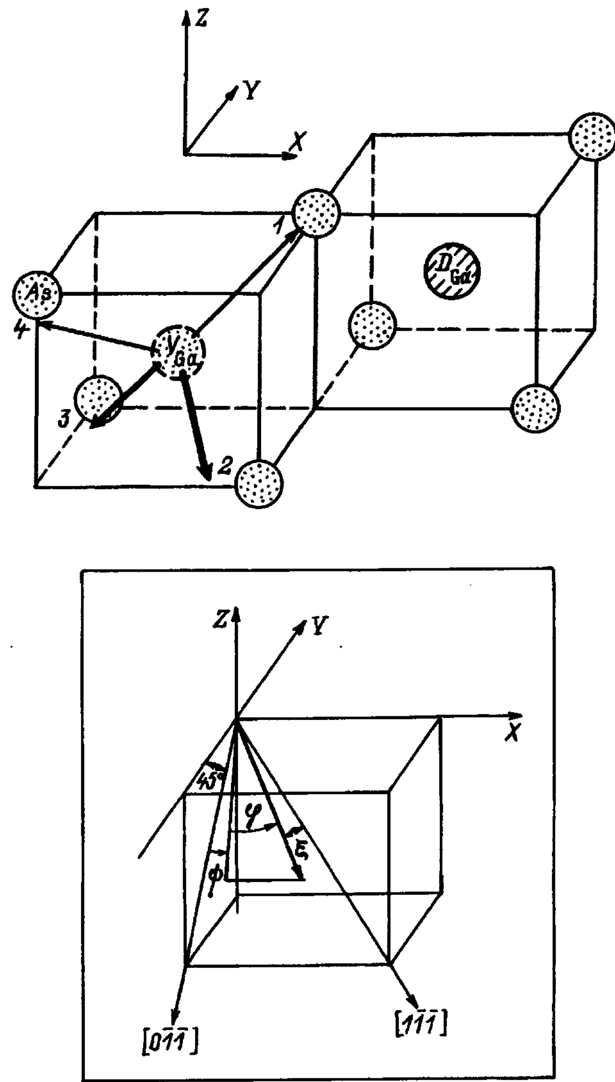

FIG. 1. Schematic diagram of distortion of the V_{Ga} D_{Ga} complex. *1–4*—numbers of the As atoms surrounding the V_{Ga} vacancy. The arrows indicate the directions of the displacement of the V_{Ga} vacancy in configurations *1–4*. X, Y, Z—coordinate system in which Q_4, Q_5, Q_6 transform. The inset shows an example of reckoning of the angles φ, ψ, ξ for an optical dipole of the complex in configuration *2*.

pensates for the increase in energy of the other configurations under the influence of the donor. The stepped growth of the polarization of the photoluminescence band of the $V_{Ga}Sn_{Ga}$ and $V_{Ga}Si_{Ga}$ complexes at 2 K and ~5 kbar pressure in the [111] direction may be associated with such an alignment of the distortions of these complexes.[6] The jump in the polarization of this photoluminescence band near zero pressure[6] should in this case be assigned to uncontrollable defects that possess similar optical properties.[1)] However, direct experimental evidence allowing one to choose between these two variants of the model is still lacking. We will accordingly analyze the results of photoluminescence measurements of complexes under conditions of resonant excitation, allowing for both possibilities. We note that monoclinic configuration 1, which corresponds to localization of a hole mainly on the dangling bond of the atom nearest the donor, atom *1* (Fig. 1), should have the highest energy, and there-

fore we do not consider the variant of the model in which the structure of the complex corresponds to this configuration.

The total energies (W_i) of all the considered configurations of the emitting state of the complex, reckoned from the energy of the initial t_2 state of the V_{Ga} vacancy, can be expressed in first-order perturbation theory in terms of the parameters α and β with the help of the Hamiltonian (1) (Ref. 6)

$$W_1 = -E_{JT} + 2\alpha,$$

$$W_2 = W_3 = -E_{JT} - \frac{2}{3}(\alpha+\beta),$$

$$W_4 = -E_{JT} - \frac{2}{3}(\alpha - 2\beta). \tag{2}$$

Here E_{JT} is the Jahn–Teller stabilization energy, which is

$$E_{JT} = \frac{2d'^2}{3k}, \tag{3}$$

where k is the elasticity coefficient of the F_2 mode of the vibrations.

In the same approximation, the generalized coordinates $Q_{i0}^{(1)}$, $Q_{i0}^{(2)}$, $Q_{i0}^{(3)}$, $Q_{i0}^{(4)}$ ($i=4,5,6$), which correspond to these configurations, are

$$Q_{40}^{(1)} = Q_{50}^{(1)} = Q_{60}^{(1)} = -\frac{E_{JT}}{d'},$$

$$Q_{40}^{(2)} = -\frac{E_{JT}}{d'} + \frac{4\alpha+\beta}{6d'}, \quad Q_{50}^{(2)} = \frac{E_{JT}}{d'} + \frac{\alpha - 2\beta}{3d'},$$

$$Q_{60}^{(2)} = \frac{E_{JT}}{d'} + \frac{2\alpha + 5\beta}{6d'};$$

$$Q_{40}^{(3)} = Q_{50}^{(2)}, \quad Q_{50}^{(3)} = Q_{40}^{(2)}, \quad Q_{60}^{(3)} = Q_{60}^{(2)};$$

$$Q_{40}^{(4)} = Q_{50}^{(4)} = \frac{E_{JT}}{d'} + \frac{2\alpha - \beta}{6d'}, \quad Q_{60}^{(4)} = -\frac{E_{JT}}{d'} + \frac{2\alpha - \beta}{3d'}. \tag{4}$$

The projections of the equilibrium displacements of the vacancy from its site onto the X, Y, and Z axes of real space are proportional respectively to Q_{40}, Q_{50}, and Q_{60}. In the case in which the influence of the donor is negligible ($\alpha=\beta=0$), these displacements in each of the configurations extend along one of the $\langle 111 \rangle$ directions.

3. PHOTOLUMINESCENCE POLARIZATION OF THE SET OF $V_{\mathrm{Ga}}D_{\mathrm{Ga}}$ COMPLEXES IN GaAs

The photoluminescence polarization was determined experimentally as in Refs. 4–7 in an orthogonal scheme in which the directions of the exciting and observed light fluxes coincided respectively with the crystallographic axes [110] and [001] (the [110]–[001] scheme) or [100] and [010] (the [100]–[010] scheme).

The direction of the electric field vector of the exciting light was characterized, as in Ref. 7, by the angle η, reckoned from the axis perpendicular to the directions of exciting and recorded light fluxes. The degree of induced polarization of the photoluminescence, $\rho(\eta)$, is defined by the ratio

$$\rho(\eta) = \frac{I_{\parallel}(\eta) - I_{\perp}(\eta)}{I_{\parallel}(\eta) + I_{\perp}(\eta)}, \tag{5}$$

where $I_{\parallel}(\eta)$ and $I_{\perp}(\eta)$ are the intensities of the photoluminescence with electric field vector of the light wave parallel and perpendicular to the axis from which the angle η is reckoned.

To analyze the experimental data, we calculate $\rho(\eta)$ in the classical dipole approximation describing the optical properties of the defect by a superposition of oscillator and rotator which are incoherent with each other,[11] as was done for $V_{\mathrm{Ga}}\mathrm{Te}_{\mathrm{As}}$ complexes in Ref. 7. Such calculations are valid, in general, for the analyzed centers and do not impose any restrictions on the relationship between the Jahn–Teller effect and the influence of the donor.

As in Ref. 7, we assume that the relative contributions of the rotator (μ) and oscillator ($1-\mu$) to the absorption are equal to their relative contributions to the emission, that the directions of the radiating and absorbing dipoles coincide (single-dipole approximation), and that the intensity of excitation is low, so that the stationary concentration of excited defects is much lower than the concentration of defects with definite orientation of the reference axis. In our study we consider only the case of low temperatures, where only configurations with lowest energy are realized in the ground state of the complex, while in the excited state thermal emission by the complex of holes and reorientation of distortions are impossible. The distribution of the complexes over possible orientations of the reference axis and over configurations with lowest energy is assumed to be uniform since polarization is not observed for nonresonant excitation.

Under these conditions polarization of the photoluminescence under conditions of resonant polarized excitation depends on the absolute values of the direction cosines (a,b,c) of the optical dipole axis of the complex. According to Refs. 6 and 7, this axis is parallel to the displacement of the V_{Ga} vacancy (Fig. 1). For each of the configurations of the complex, we define a, b, c in the local Cartesian coordinate system, whose axes are parallel to the $\langle 100 \rangle$ directions and are chosen such that the projections of the displacements of the vacancy on these axes in the absence of any influence of the donor are positive (see the inset in Fig. 1). The calculations show that the extremal values of the polarization in both experimental schemes correspond to $\eta=0°$ and 90°. In this case, for the [110]–[001] scheme

$$\rho(\eta=0)=\rho_1=\frac{4(a^2b^2+a^2c^2+b^2c^2)(1-2\mu)^2}{(a^2+b^2+2\mu c^2)^2+(a^2+c^2+2\mu b^2)^2+(b^2+c^2+2\mu a^2)^2}, \quad (6)$$

and for the [100]–[010] scheme

$$\rho(\eta=0)=\rho_2=\frac{[(a^2-b^2)^2+(a^2-c^2)^2+(b^2-c^2)^2](1-2\mu)^2}{(a^2+b^2+2\mu c^2)^2+(a^2+c^2+2\mu b^2)^2+(b^2+c^2+2\mu a^2)^2}, \quad (7)$$

and $\rho(\eta=90°)\equiv 0$ for both cases.

The condition $a\neq b\neq c$ corresponds to triclinic centers, and the condition $b=c\neq a$, corresponds to monoclinic centers. As can be seen from expressions (6) and (7), measurement of $\rho(\eta=0)$ in the two indicated experimental schemes allows one to determine the possible values of μ:

$$\mu=\frac{1}{2}-\frac{\pm\sqrt{(3\rho_1+2\rho_2)(3-\rho_2)}-\frac{1}{2}(3\rho_1+2\rho_2)}{4-\rho_1-2\rho_2}. \quad (8)$$

For ease of visualization, it is convenient to express the direction cosines a, b, c in terms of the angles φ and ψ, which are defined in the same system of coordinates as the direction cosines for each configuration (see the inset in Fig. 1)

$$a=\sin\varphi, \quad b=\cos\varphi\cos(45°+\psi),$$
$$c=\cos\varphi\sin(45°+\psi). \quad (9)$$

Thus, substituting relation (9) into Eqs. (6) and (7) we obtain a relation which φ and ψ should satisfy for known value of the ratio ρ_1/ρ_2

$$\cos^2\varphi(4\sin^2\varphi+\cos^2\varphi\cos^2 2\psi)=\frac{4\rho_1/\rho_2}{3\rho_1/\rho_2+2}. \quad (10)$$

This relation, as we will see in the next section, makes it possible to determine the region of possible values of φ and ψ.

4. EXPERIMENTAL RESULTS AND DISCUSSION

We investigated samples cut from several single crystals of n-type GaAs. The n-type GaAs:Sn single crystals were grown by the Czochralski method and had electron concentrations from $\sim 6\times 10^{16}$ to $\sim 10^{18}$ cm^{-3}. The n-type GaAs:Si crystals were grown by the method of directional crystallization and had electron concentration $\sim 10^{18}$ cm^{-3}. In all the samples a photoluminescence band with maximum near 1.2 eV associated with the $V_{\mathrm{Ga}}D_{\mathrm{Ga}}$ complexes was observed at 77 K. The excitation spectra of this band were similar to those observed earlier.[5,6] Its polarization, induced by polarized resonant excitation, was investigated for the above-indicated orientations of the crystal relative to the exciting and observed light fluxes.

The degree of polarization ρ $(\eta=0)$ increased from zero as the photon energy of the exciting light ($\hbar\omega_{\mathrm{exc}}$) was decreased from ~ 1.47 eV and for $\hbar\omega_{\mathrm{exc}}<1.38$ eV essentially ceased to depend on $\hbar\omega_{\mathrm{exc}}$. The latter circumstance indicates that only resonant excitation of the complexes occurs for $\hbar\omega_{\mathrm{exc}}<1.38$ eV. In this case $\rho(\eta=90°)\approx 0$, as one would expect. The distribution of the degree of polarization $\rho(\eta=0)$ over the photoluminescence band for the crystals with high donor concentration was uniform in the energy range 1.16–1.25 eV, where the signal was quite strong (Fig. 2). The values of ρ_1 and ρ_2, measured in this range for $\hbar\omega_{\mathrm{exc}}<1.38$ eV, were assumed to be characteristic of the investigated complexes; they are listed in Table I along with the analogous values[7] for the $V_{\mathrm{Ga}}\mathrm{Te}_{\mathrm{As}}$ complex in GaAs.[2)]

The values of the relative contribution of the rotator to the absorption and emission (μ) [see Eq. (8)] corresponding to these experimental values lie in the range 16–18%. The region of possible angles defined by relation (10), which characterize the direction of the optical dipole axis of the complex for the experimental values of ρ_1/ρ_2 listed in the table, is plotted in Fig. 3 for the triclinic ($\psi\neq 0$) and the monoclinic ($\psi=0$) configurations.

To further refine the possible values of φ and ψ, it is necessary to allow for the fact that the influence of the Jahn–Teller effect on the vacancy orbitals of a hole localized in the investigated complexes exceeds that of the donor member of the complex. This circumstance allows us, for qualitative analysis and estimates, to use expressions obtained in first-order perturbation theory in the quantities α/E_{JT} and β/E_{JT} (see Sec. 2). Below we analyze the experimental results within the framework of each of the two variants of the structure of the $V_{\mathrm{Ga}}D_{\mathrm{Ga}}$ complex indicated in Sec. 2, for which either the triclinic or the monoclinic configuration of the complex is realized at equilibrium at low temperatures.

a) Complex with triclinic symmetry

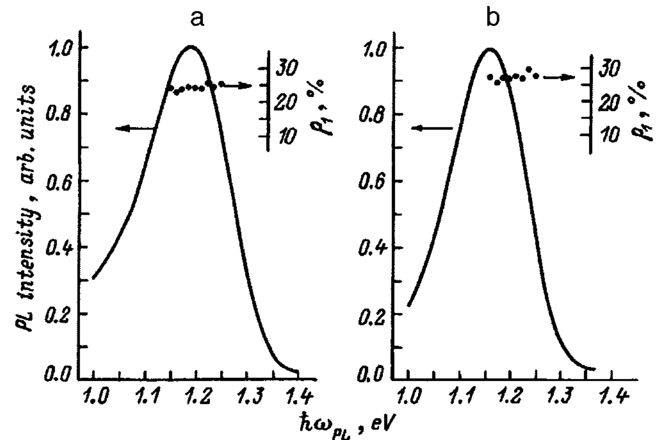

FIG. 2. Photoluminescence and induced polarization spectra (ρ_1) for GaAs:Sn (a) and GaAs:Si (b). The donor concentration in the samples $\sim 10^{18}$ cm^{-3}. $T=77$ K. Photon energy of the exciting light for measurement of the photoluminescence spectra—1.96 eV, and of the induced polarization spectra—1.37 eV.

TABLE I. Degree of polarization of the photoluminescence under conditions of resonant polarized excitation of the vacancy–donor complexes in n-GaAs and possible values of the optical dipole parameters of these defects.

Complex	ρ_1 (%)	ρ_2 (%)	ρ_1/ρ_2	μ	φ and ψ Possible values of φ and ψ	
					triclinic model	monoclinic model
$V_{Ga}Sn_{Ga}$	25–26	4.5–5	5.4 ± 0.4	~0.18	$19°\lesssim\varphi\lesssim35°$ $0°\lesssim\psi\lesssim18°$	$\varphi\approx19°$ $\psi=0$
$V_{Ga}Si_{Ga}$	27–29	5–6	5.2 ± 0.6	~0.17	$19°\lesssim\varphi\lesssim35°$ $0°\lesssim\psi\lesssim18°$	$\varphi\approx19°$ $\psi=0$
$V_{Ga}Te_{As}$ (Ref. 7)	27–29	8–9	3.3 ± 0.3	~0.16	-	$\varphi\approx15°$ $\psi=0$

In this case configurations *2* and *3* have minimum energy and it follows from Eqs. (4) that

$$a=\sin\,\varphi\approx\left(1-\frac{4\alpha+\beta}{6E_{JT}}\right)\frac{1}{\sqrt{3}},$$

$$b=\cos\,\varphi\,\cos(45°+\psi)\approx\left(1+\frac{\alpha-2\beta}{3E_{JT}}\right)\frac{1}{\sqrt{3}},$$

$$c=\cos\,\varphi\,\sin(45°+\psi)\approx\left(1+\frac{2\alpha+5\beta}{6E_{JT}}\right)\frac{1}{\sqrt{3}}, \tag{11}$$

where α and β should satisfy the inequalities[6]

$$\beta\geqslant0,\quad 4\alpha+\beta>0,\quad \alpha,\beta<E_{JT}. \tag{12}$$

Calculations using expressions (10) and (11) show that conditions (12) are satisfied for the experimental value $\rho_1/\rho_2\approx5.2$ only for $19°\lesssim\varphi\lesssim35°$ and the corresponding values of ψ are positive (see Fig. 3). The relative values α/E_{JT} and β/R_{JT}, obtained by solving the three different possible pairs of Eqs. (11) for the above-indicated interval of φ values, differ slightly from each other because of the approximate nature of the equations (Fig. 4).

b) Complex with monoclinic symmetry

In this case configuration *4* has minimum energy (Fig. 1), $\psi=0$, and it follows from Eqs. (4) that

$$a=\sin\,\varphi\approx\left(1-\frac{2\alpha-\beta}{3E_{JT}}\right)\frac{1}{\sqrt{3}},$$

$$b=c=\frac{1}{\sqrt{2}}\cos\,\varphi\approx\left(1+\frac{2\alpha-\beta}{6E_{JT}}\right)\frac{1}{\sqrt{3}}, \tag{13}$$

where the parameters α and β should satisfy the inequalities[6]

$$\beta\leqslant0,\quad 2\alpha-\beta>0,\quad \alpha,|\beta|<E_{JT}. \tag{14}$$

Relation (10) gives $\varphi=\pm19°$ and $\varphi=\pm54°$. Only the value $\varphi=19°$ satisfies conditions (13) and (14). The φ-dependence of the parameter $(2\alpha-\beta)/(6E_{JT})$, obtained separately from the first and second equations in (13), is plotted in Fig. 5. As in the case of the triclinic complex, these values differ from each other for the experimental value $\varphi\approx19°$, because of the approximate nature of Eqs. (13).

The results which we obtained can be used to compare the relative influence of the donor in the $V_{Ga}Sn_{Ga}$, $V_{Ga}Si_{Ga}$, and $V_{Ga}Te_{As}$ complexes. For an isolated vacancy $(\alpha=\beta=\beta^*=0)$, which is subjected only to trigonal distor-

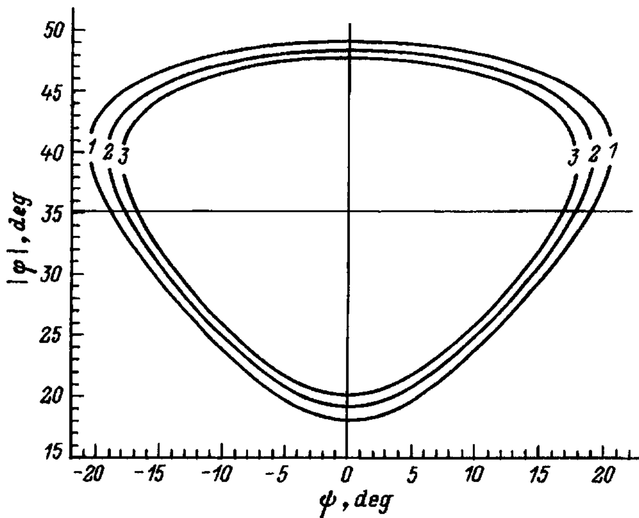

FIG. 3. Possible values of the angles φ and ψ corresponding to prescribed values of ρ_1/ρ_2 for complexes with triclinic symmetry. ρ_1/ρ_2: *1*—4.6, *2*—5.2, *3*—5.8. For complexes with monoclinic symmetry, the possible values of φ correspond to $\psi=0$.

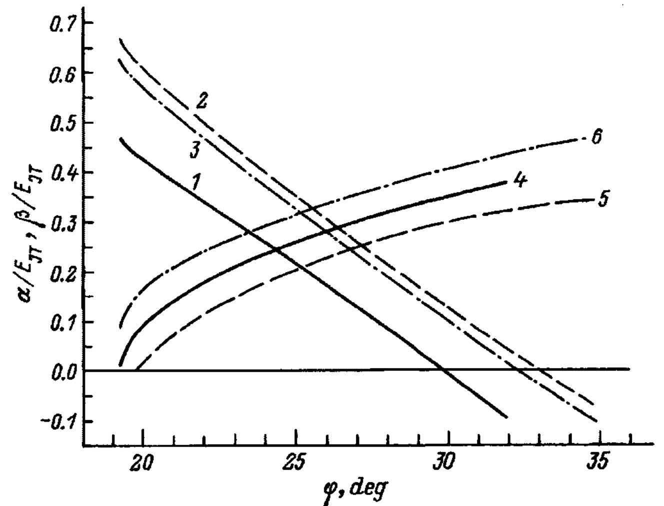

FIG. 4. Values of α/E_{JT} and β/E_{JT} corresponding to $\rho_1/\rho_2=5.2$ in the region of φ values permissible for triclinic configuration of the complex. *1–3*—α/E_{JT}, *4–6*—β/E_{JT}. *1,4;2,5;3,6*—the three pairs of dependences obtained by solving the three different pairs of equations in (11).

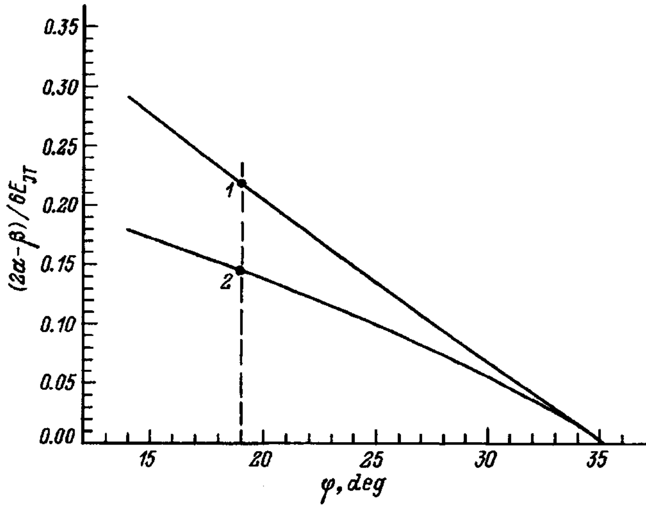

FIG. 5. Values of $(2\alpha-\beta)/6E_{JT}$ for a complex with monoclinic symmetry. The points indicate the values corresponding to $\rho_1/\rho_2=5.2$ for the monoclinic configuration of the complex. *1,2*—two values obtained by solving each of the two equations in (13).

tion as a result of the Jahn–Teller effect, the optical dipole axis coincides with one of the $\langle 111\rangle$ directions. Any deviation of the optical dipole axis from this direction is due to the influence of the donor; therefore, it is natural to estimate the strength of this effect from the absolute value of the angle ξ between the optical dipole axis and the corresponding $\langle 111\rangle$ axis. The angle ξ is related to the angles φ and ψ by the equation

$$\cos\xi=\frac{1}{\sqrt{3}}(\sqrt{2}\cos\varphi\cos\psi+\sin\varphi). \qquad (15)$$

Its absolute value for the $V_{Ga}Sn_{Ga}$ and $V_{Ga}Si_{Ga}$ complexes in the region of ψ values and for the corresponding positive φ values (Fig. 3) is shown in Fig. 6. Figure 6 also plots the value of ξ for $V_{Ga}Te_{As}$ complexes (in the case $\psi=0$). It can be seen that for the $V_{Ga}Sn_{Ga}$ and $V_{Ga}Si_{Ga}$ complexes the value of ξ is lower than for $V_{Ga}Te_{As}$ complexes. This could have been expected since the donor in the $V_{Ga}Te_{As}$ complex is located closer to the vacancy and its effect should therefore be greater.

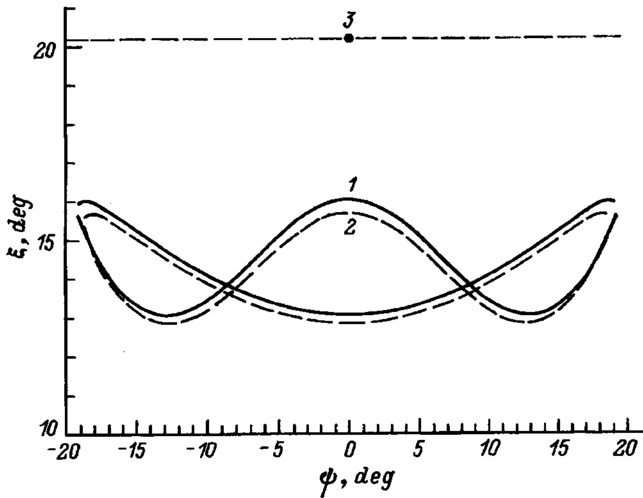

FIG. 6. Possible absolute values of the angle of deviation from the $\langle 111\rangle$ axis of the dipole axis of the $V_{Ga}D$ complex corresponding to the direction of the Jahn–Teller distortion of an isolated V_{Ga} vacancy. *1*—$V_{Ga}Sn_{Ga}$, *2*—$V_{Ga}Si_{Ga}$, *3*—$V_{Ga}Te_{As}$. ρ_1/ρ_2: *1*—5.2, *2*—5.4, *3*—3.3. $\varphi>0$.

5. CONCLUSION

The analysis carried out above of the 1.2-eV photoluminescence band of GaAs:Sn and GaAs:Si crystals with donor concentrations $\sim 10^{17}-10^{18}$ cm^{-3} at low temperatures under conditions of resonant polarized excitation shows that absorption and emission of light by the complexes responsible for this band is approximated in the classical single-dipole approximation by a superposition of a rotator and an oscillator in which the rotator fraction is $\sim 17-18\%$. The directions of the axes of these dipoles matching the experimental polarization values can be chosen such that they correspond to the model of the $V_{Ga}D_{Ga}$ complex, assuming on the basis of a number of other experimental results that the influence of the donor on the vacancy orbitals of a hole localized on the defect is small in comparison with that of the interaction of this hole with the F_2 mode of the vibrations of the initially tetrahedral complex (the Jahn–Teller effect).[6] From this standpoint, the experimental results can be explained in the case in which the minimum total energy of the defect corresponds to one configuration of the complex with monoclinic symmetry and in the case in which it corresponds to two equivalent configurations of triclinic symmetry. In both cases the deviation of the optical dipole axis of the complex from the $\langle 111\rangle$-type axis, which corresponds to the direction of the dipole axis of an isolated vacancy distorted as a result of the Jahn–Teller effect, is smaller for the $V_{Ga}Sn_{Ga}$ and $V_{Ga}Si_{Ga}$ complexes than for the $V_{Ga}Te_{As}$ complexes. This means that the influence of the donor on the vacancy orbitals is greater for $V_{Ga}Te_{As}$ than for $V_{Ga}Sn_{Ga}$ and $V_{Ga}Si_{Ga}$. This is in qualitative agreement with the difference in the position of the donor relative to the vacancy in these complexes.

[1)] We are grateful to Prof. G. D. Watkins, who suggested this explanation and indicated that just the configuration considered in this case is realized in many similar vacancy–donor pairs in II–VI semiconductors (see Ref. 10 and the references cited there).

[2)] For the n-GaAs:Sn samples with donor concentration less than 10^{17} cm^{-3} a weak dependence of ρ_1 on $\hbar\omega_{PL}$ was observed; however, the values of ρ_1 for $\hbar\omega_{PL}\approx 1.2$ eV lie in the limits indicated in the table. The maximum of the photoluminescence band of these samples was shifted toward shorter wavelengths by ~ 20 meV.

[1] E. W. Williams, Phys. Rev. **168**, 922 (1968).

[2] S. Y. Chiang and G. L. Pearson, J. Lumin. **10**, 313 (1975).

[3] I. A. Buyanova, S. S. Ostapenko, and M. K. Sheĭkman, Fiz. Tverd. Tela **27**, 748 (1985) [Sov. Phys. Solid State **27**, 461 (1985)].

[4] N. S. Averkiev, A. A. Gutkin, E. B. Osipov, M. A. Reshchikov, V. E. Sedov, and V. R. Sosnovksiĭ, Fiz. Tekh. Poluprovodn. **25**, 50 (1991) [Sov. Phys. Semicond. **25**, 28 (1991)].

[5] A. A. Gutkin, M. A. Reshchikov, and V. R. Sosnovksiĭ, Fiz. Tekh. Poluprovodn. **27**, 1516 (1993) [Semiconductors **27**, 838 (1993)].

[6] A. A. Gutkin, M. A. Reshchikov, and V. E. Sedov, Fiz. Tekh. Poluprovodn. **30**, 1123 (1996) [Semiconductors **30**, 595 (1996)].

[7] A. A. Gutkin, M. A. Reshchikov, and V. E. Sedov, Fiz. Tekh. Poluprovodn. **31**, 1062, (1997) [Semiconductors **31**, 908 (1997)].

[8] A. A. Gutkin, N. S. Averkiev, M. A. Reshchikov, and V. E. Sedov, in *Defects in Semiconductors 18*, edited by M. Suezawa and H. Katayama-Yoshida (Mater. Sci. Forum, **196-201**, Pt. 1, 1995), p. 231.
[9] N. S. Averkiev, A. A. Gutkin, S. Yu. Il'inskii, M. A. Reshchikov, and V. E. Sedov, Z. Phys. Chem. **200**, 209 (1997).
[10] F. C. Rong, W. A. Barry, J. F. Donegan, and G. D. Watkins, Phys. Rev. B **54**, 7779 (1996).
[11] E. E. Bukke, N. N. Grigor'ev, and M. V. Fok, Trudy FIAN **79**, 108 (1974).

Translated by Paul F. Schippnick

Intrinsic defect states in PbTe single-crystal films grown by laser-modulated epitaxy

S. V. Plyatsko

Institute of Semiconductor Physics, Ukrainian Academy of Sciences, 252650 Kiev, Ukraine
(Submitted March 5, 1997; accepted for publication May 15, 1997)
Fiz. Tekh. Poluprovodn. **32**, 47–49 (January 1998)

The electrical properties of PbTe/KCl(KBr) layers grown by infrared-laser-modulated epitaxy and their dependences on conditions of fabrication (power density of the laser beam W, substrate temperature T_s) have been investigated. It is established that the $R_H(T)$ dependences can be explained within the framework of a two-level model in which one of the levels (E_{d1}) is in the conduction band and the second level E_{d2} is in the band gap. The positions of the energy levels and their density of states depend on the conditions of growth. © *1998 American Institute of Physics.* [S1063-7826(97)00212-3]

The problem of intrinsic defects in PbTe, both in bulk single crystals and in thin films, is not a new one, it has nevertheless been studied insufficiently. In addition, in films the solution of this problem is complicated by the presence of dislocations of a different nature and deformation fields, which can lead to the appearance of new energy states and a shift of the known states under the action of mechanical stresses, especially in the case of hetero-epitaxial growth. It is quite clear that the variety of methods of epitaxial growth used today introduces into this problem the same variety of characteristic features in the behavior of the intrinsic point defects and their energy states.

In the present study PbTe/KCl(KBr) films were grown by laser-modulated epitaxy (LME). The target was sputtered by an infrared laser beam which was interrupted by a mechanical modulator. The lasing time was $\tau_{\text{pulse}}=3\times10^{-3}$ s with pulse repetition frequency $f=20$ Hz. The radiation was introduced with the help of an optical system and a focusing system into a vacuum chamber with residual vapor pressure $P=1\times10^{-6}$ Torr. Laser-modulated epitaxy has the capability of monitoring the thickness of the growing layers, the substrate temperature, and monitoring and controlling the power density of the laser radiation. As the target–source we used a stoichiometric PbTe single crystal with free hole concentration $p_{77}=(3-5)\times10^{18}$ cm^{-3} and mobility $\mu_{77}=1.2\times10^4$ cm^2/(V·s). The source completed a rotational–translational motion during the epitaxy process, which prevented crater formation and any change in the scatter diagram of the sputtered material.

From the analysis which we made of the dependence of the electrical properties on the conditions of growth of PbTe/KCl films by laser-modulated epitaxy it is clear that these properties are determined by electrically active defects of a different kind, which arise in the films during their growth. Depending on the growth temperature, for constant power density of the laser beam at the target $W=8.5\times10^4$ W/cm^2 for the substrate temperature in the neighborhood of $T_s=270$ °C an inversion of the type of conductivity $n\rightarrow p$ is observed, followed by the reverse inversion $p\rightarrow n$ when the epitaxy temperature reaches $T_s=330$ °C. Further increase of the substrate temperature T_s leads to an increase of the electron concentration with a tendency toward saturation at $T_s>400$ °C. Since the films were not doped in this case, the novel electrically active defects arising in the layers are intrinsic and depend, as experimental studies have shown, on the growth temperature T_s and the laser power density W.

Figure 1 plots the temperature dependence of the Hall constant for PbTe/KCl(KBr) films grown under different conditions. It can be seen that these different dependences differ substantially from one other and also from the corresponding dependences of films grown by conventional methods.

In the region of low epitaxy temperatures $80\leqslant T_s\leqslant270$ °C for constant power density ($W=8.5\times10^4$ W/cm^2) of the laser beam at the target, an activation segment is present in the dependence $R_H(T)$, which is associated with the ionization of local states in the conduction band (Fig. 1, curve *1*). Increasing the epitaxy temperature alters the character of this dependence (curves *2*, *3*, and *5*). In the intermediate temperature region ($270\leqslant T_s\leqslant330$ °C), where p-type conductivity is observed, as the hole concentration is varied one observes the usual shift of the inversion temperature for p-PbTe from $T_{\text{inv}}=120$ to 330 K, and in the remaining curve the dependence of $R_H(T)$ is of the usual form (Fig. 1, curve *4*).

In the region of low substrate temperatures T_s the concentration of donor centers, whose level is located in the conduction band, increases with increasing power density at the target and at $W=10^5$ W/cm^2 reaches $N_{d1}=1\times10^{19}$ cm^{-3}.

Together with a change in the concentration N_{d1}, raising the epitaxy temperature results in the appearance and growth of the concentration of donor centers N_{d2}, whose level at 0 K is located in the band gap. Note that the donor centers N_{d2} are also present for low growth temperatures (Fig. 1, curve *5*); however, their concentration does not exceed $N_{d2}\leqslant10^{15}$ cm^{-3}; therefore, the level E_2 is barely seen even at the lowest current-carrier concentrations.

In the region of epitaxy temperatures insignificantly exceeding the temperature of the second inversion $p\rightarrow n$ ($T_s\geqslant330$ °C) in $R_H(T)$ for n-PbTe, both E_1 and E_2 contribute to the conductivity (Fig. 1, curve *2*). With growth of T_s, the density of states at the level E_1 falls, but at the level E_2 it grows (Fig. 2), which also affects the behavior of the Hall constant $R_H(T)$.

 1063-7826/98/010040-03$15.00 © 1998 American Institute of Physics

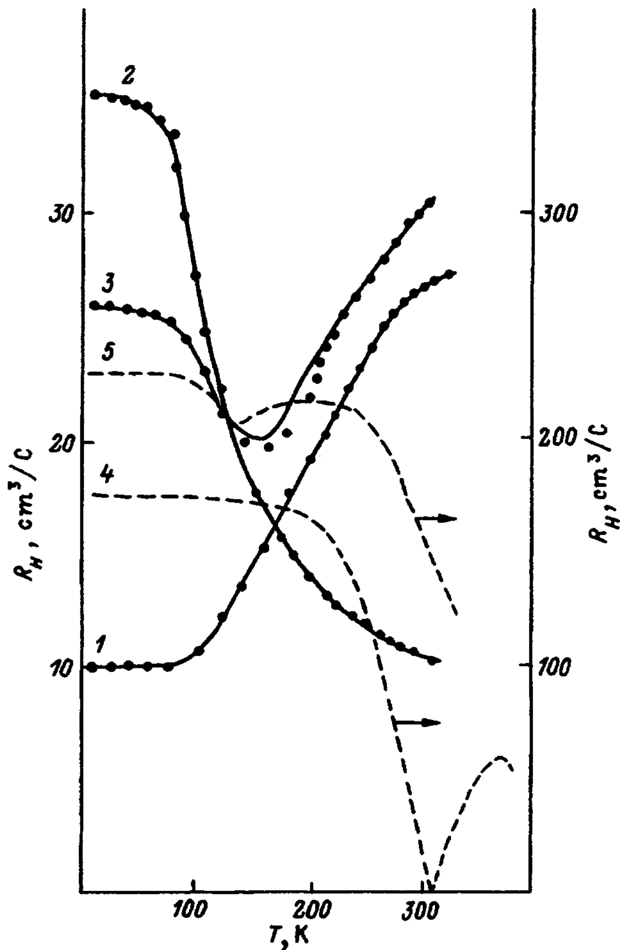

FIG. 1. Temperature dependence of the Hall coefficient of PbTe films grown under different conditions. The points correspond to experiment, the dashed line is the envelope experimental points, the solid lines were calculated. *1*—*n*-PbTe/KCl, $W=5.0\times10^4$ W/cm², $T_s=150$ °C; *2*—*n*-PbTe/KCl, $W=8.5\times10^4$ W/cm², $T_s=335$ °C; *3*—*n*-PbTe/KCl, $W=8.5\times10^4$ W/cm², $T_s=400$ °C; *4*—*n*-PbTe/KCl, $W=8.5\times10^4$ W/cm², $T_s=300$ °C; *5*—*p*-PbTe/KBr, $W=3.5\times10^4$ W/cm², $T_s=150$ °C.

An analysis of the experimental data on the Hall effect, based on the two-level model under the assumption that the form of the wave functions for both levels is of s-type, gave the level positions $E_1=0.075$ eV and $E_2=-0.055$ eV at $T=0$ K. The changes in the level positions E_1 and E_2 with temperature are $dE_1/dT=(4.5\pm0.5)\times10^{-4}T$ and $dE_2/dT=(3.5\pm0.7)\times10^{-4}T$, respectively. The energy level position E_1 also depends on the density of states at that level (Fig. 3), which in turn grows with increasing power density of the laser beam at the target. Such a dependence of the level position on the density of states at it for IV–VI compounds is unusual. Lead telluride is characterized by a large dielectric constant ($\varepsilon\geqslant400$); therefore, the wave functions of the defect states up to $N=2$ at. % overlap weakly, but the localization radius cannot noticeably exceed one or two unit cells; i.e., the wave functions of the impurity defect states are localized in a region on the order of 10–15 Å. In the case of wave-function overlap the energy of the level will be lowered relative to the band, of which it is a detached state. In our case the density of states at the level is significantly lower than 10^{20} cm^{-3}; therefore, one cannot speak of wave-function overlap.

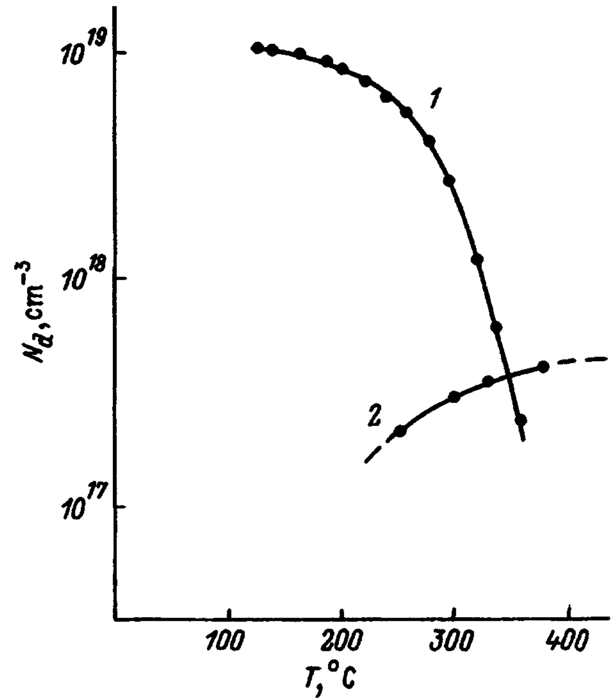

FIG. 2. Dependence of the densities of states N_{d1} and N_{d2} on the epitaxy temperature of PbTe/KCl films for $W=8.5\times10^4$ W/cm² (curves *1* and *2*, respectively).

In our opinion, such behavior of E_1 with increasing power density of the laser beam at the target–source is a result of the fact that the lead ion as a result of the way in which it is built into the lattice occupies an interstitial site and thereby creates a local deformation. In the case of a uniform lead distribution in the lattice the excited elastic fields are proportional to the point defect concentration.[1,2] In films prepared at low epitaxy temperatures, the strains can be significant in contrast to films and crystals grown at high temperatures, where the strains are essentially completely re-

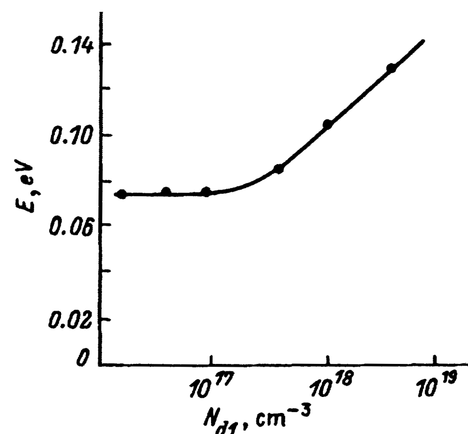

FIG. 3. Dependence of the energy level position E_1 on the density of states N_{d1} at 0 K.

laxed and do not give a noticeable contribution to the electrical properties.

An increase in the elastic deformation entails a change in the energy positions of the defect levels, as is confirmed by experiment. A similar shift of the defect levels in bulk single crystals of PbSnTe takes place when the crystals are irradiated by infrared laser radiation, upon which a change in the current-carrier concentration takes place due to a redistribution of the point defects in the ''cold'' matrix in the field of the electromagnetic wave of the laser radiation.[3–5] This process gives rise to elastic fields which cause the level of the intrinsic defects to change its energy position.

Regarding the charge state of interstitial lead, we note that no previous study touching on this question has given a concrete answer. But despite this fact, the opinion remains in the literature that interstitial lead is found in the singly charged state. However, electron-spin resonance experiment at liquid-helium temperatures have not confirmed this supposition. Therefore, in our opinion, lead, like manganese and europium, at regular lattice sites and at interstitials, is found in the doubly charged state,[5] and does not show up in the electron spin resonance for this reason.

The origin of the level in the band gap is probably attributable to tellurium vacancies. However, it should be noted that the vacancy concentration is determined not only by the condensation temperature, but also by peculiarities of the growth of the films under conditions far from equilibrium, which are realized when using laser radiation to sputter semiconductor target–sources.

In summary, the electrical properties of layers grown on dielectric substrates when using a modulated infrared laser beam to sputter the PbTe source material, are determined mainly by the electrically active, intrinsic point defects, whose concentration and the energy positions of the corresponding levels are determined by the power density of the laser beam at the target and by the epitaxial growth temperature.

[1] Prusin, J. Appl. Phys. **32**, 1876 (1961).
[2] V. A. Panteleev and V. A. Murav'ev, Fiz. Tekh. Poluprovodn. **19**, 682 (1977) [Sov. Phys. Semicond. **19**, 395 (1977)].
[3] F. F. Sizov, S. V. Plyatsko, and S. D. Darchuk, Infrared Phys. **27**, 249 (1987).
[4] Yu. S. Gromovoĭ, L. A. Korovina, S. V. Plyatsko, F. F. Sizov, S. D. Darchuk, and S. A. Belokon', Fiz. Tekh. Poluprovodn. **24**, 250 (1990) [Sov. Phys. Semicond. **24**, 152 (1990)].
[5] Yu. S. Gromovoj, S. V. Plyatsko, and F. F. Sizov, Mater. Lett. **8**, 11–12, 495 (1989).

Translated by Paul F. Schippnick

Manganese-related recombination centers in epitaxial GaAs grown from a bismuth melt

K. S. Zhuravlev, T. S. Shamirzaev,* and N. A. Yakusheva

Institute of Semiconductor Physics, Siberian Branch of the Russian Academy of Sciences, 630090 Novosibirsk, Russia

(Submitted April 1, 1997; accepted for publication May 15, 1997)
Fiz. Tekh. Poluprovodn. **32**, 50–56 (January 1998)

The photoluminescence properties of heavily doped GaAs:Mn layers grown for the first time by liquid-phase epitaxy from a bismuth melt have been studied. Manganese-related centers of radiative and nonradiative recombination, in addition to the manganese substitutional acceptors (manganese replacing gallium), have been observed in this material. It is found that the concentrations of both centers increase with the doping level. A radiative recombination center with strong electron–lattice coupling has been observed for the first time. We believe that the high concentration of this new center may be a result of the growth method used. The ionization energy of this center is found to be equal to 41 meV. © *1998 American Institute of Physics.* [S1063-7826(97)00312-8]

1. INTRODUCTION

Manganese in GaAs, where it replaces gallium atoms (Mn_{Ga}), creates an acceptor with a deep level.[1–11] The ionization energy of this acceptor, found from electrical[1–3] and optical[2,4–11] measurements, is approximately equal to 100 meV, which makes manganese-doped gallium arsenide a promising material for infrared photodetectors.[12] To increase the sensitivity of such detectors, it is necessary to increase the doping level and lower the concentration of background impurities and defects, which function as recombination centers that decrease the lifetime of the holes and, as a consequence, lower the sensitivity of the detector.[12]

Previously it was shown that using bismuth as the solvent when growing GaAs by liquid epitaxy allows one to obtain layers with a low concentration of background impurities and defects[13,14] and a high concentration of impurities built into the gallium sublattice,[15] which gives hope of obtaining by this method GaAs layers with high Mn_{Ga} acceptor concentration and low concentration of unintentionally introduced recombination centers.

In the present paper we examine the photoluminescence of GaAs:Mn layers obtained by liquid-phase epitaxy from a bismuth melt, with the aim of revealing the recombination centers formed in GaAs due to strong manganese doping.

2. EXPERIMENTAL TECHNIQUE

Epitaxial layers were grown from a bismuth melt on semi-insulating GaAs(100) substrates in the temperature interval from 700 to 640 °C by the technique described earlier in Ref. 13. The manganese content in the liquid phase (X_{Mn}) was varied from 4×10^{-5} to 1×10^{-2} atomic fractions. The thickness of the layers was 8–10 μm. All the manganese-doped GaAs layers grown under similar conditions had electron-type conductivity. The concentration of free charge-carriers in the investigated layers was determined from the Hall constant measured by the van-der-Pauw method. The Hall scattering factor for n-type layers was assumed equal to unity, and for the p-type layers was set equal to 2.66 in accordance with calculations carried out in Ref. 16 based on a model that allows for degeneracy at the center of the Brillouin zone of light and heavy holes. Values of the concentrations of free charge-carriers are given in Table I as a function of the manganese content in the melt. Stationary photoluminescence spectra were measured on a setup based on an SDL-1 double monochromator with 600 rulings/mm gratings (focal length 600 mm, spectral resolution no worse than 0.2 meV). Photoluminescence was recorded by a photomultiplier with an $S1$ photocathode working in the photon-counting regime. To excite photoluminescence we used a He–Ne laser with the power density set equal to 100 W/cm^2. When measuring the temperature dependences, the accuracy of the temperature setting was ±0.5 K.

3. EXPERIMENTAL RESULTS

Photoluminescence spectra of GaAs layers with different doping levels, measured at 4.2 K, are shown in Fig. 1. The spectrum of the intentionally undoped layer is dominated by the lines due to exciton recombination (X), and the lines of recombination through the shallow acceptor levels ($e/D,A$). A line is also present in this spectrum with energy position of its maximum equal to 1.408 eV, accompanied by phonon echoes, which is associated with recombination of nonequilibrium charge carriers through the levels of the background manganese acceptor (e, Mn),[5,7 1)] as well as a line due to recombination through the Ga_{As} defect levels.[18] The intensities of these lines are more than two orders of magnitude lower than the intensities of the exciton lines, indicating a low concentration of manganese and Ga_{As} defects in the intentionally undoped layer. In the photoluminescence spectra of the doped layers the (e, Mn) line dominates. As the doping level is increased, its full-width at half-maximum (FWHM) varies from 5 meV in layer 2 (numbering of the layers as in Table I) to 23 meV in layer 8. A shoulder is observed on the high-energy limb of this line, indicated in the figure by the arrow. The presence of a shoulder indicates that the (e, Mn) line is strongly overlapped by an unknown line, which we denote as line D. With continued growth of the manganese concentration, the shoulder on the (e, Mn) line shows up more distinctly, testifying to the growth of the

 1063-7826/98/010043-06$15.00 © 1998 American Institute of Physics

TABLE I.

N fi.	Sample	X_{Mn}, at. frac.	$p_0(n_0)$ cm^{-3} 77 K	295 K
1*	A15-1	0	2.0×10^{14}	2.1×10^{14}
2	MC4-3	4.53×10^{-5}	9.3×10^{13}	7.5×10^{17}
3	MC4-2	2.18×10^{-4}	6.6×10^{14}	2.1×10^{18}
4	MC4-1	5.53×10^{-4}	1.4×10^{15}	2.9×10^{18}
5	MC1	5.89×10^{-4}	1.3×10^{15}	2.8×10^{18}
6	MC2	6.22×10^{-4}	1.4×10^{15}	2.9×10^{18}
7	MC5-3	2.90×10^{-3}	1.9×10^{15}	5.8×10^{18}
8	MC5-2	9.58×10^{-3}	4.0×10^{14}	2.4×10^{18}

*Remark.** sample of n-type conductivity.

relative intensity of the D line. It can also be seen from Fig. 1 that the total photoluminescence intensity and the intensity of the exciton lines fall abruptly as the doping level is increased. This indicates the formation in GaAs:Mn of nonradiative recombination centers, whose concentration grows with increase of the doping level.

The photoluminescence spectra of layer 2 are shown in Fig. 2 for different measurement temperatures. It can be seen from the figure that the spectra are modified as the temperature is raised. Lines associated with exciton recombination disappear and an interband recombination line (BB) appears. The intensity of the (e, Mn) line and its phonon echoes diminish, and the D line begins to dominate in the photoluminescence spectra. It can be seen from the photoluminescence spectrum at 110 K (the temperature at which the D line shows up the most distinctly) that this line has Gaussian shape and its FWHM is equal to 150 meV. As the temperature is raised, this line shifts toward lower energies; however, this shift is not described by the law $\hbar\omega(T)=E_g(T)-E+0.5\cdot kT$ (where E_g is the width of the band gap, E is the binding energy of the charge carrier to the recombination center, and k is the Boltzmann constant), which is valid for lines due to recombination through levels of impurity centers not bound with the lattice,[19,20] e.g., for the (e, Mn) line.[21] The Gaussian shape, large line width, and the temperature dependence of the energy of the maximum all indicate that the D line is associated with transitions through levels of a center strongly bound with the crystal lattice,[19,20,22] which we denote as the R center.

The temperature dependence of the intensity of the interband recombination line and of the total intensity of the strongly overlapping lines D and (e, Mn)[2)] for layers 2 and 7, having different doping levels, is shown in Figs. 3a and 3b. It is clear from Fig. 3a that the intensity of the interband recombination line in the spectra of layer 2 falls as the temperature is increased from 10 to 110 K and grows exponentially with a slope of 20 ± 2 meV as the temperature is raised

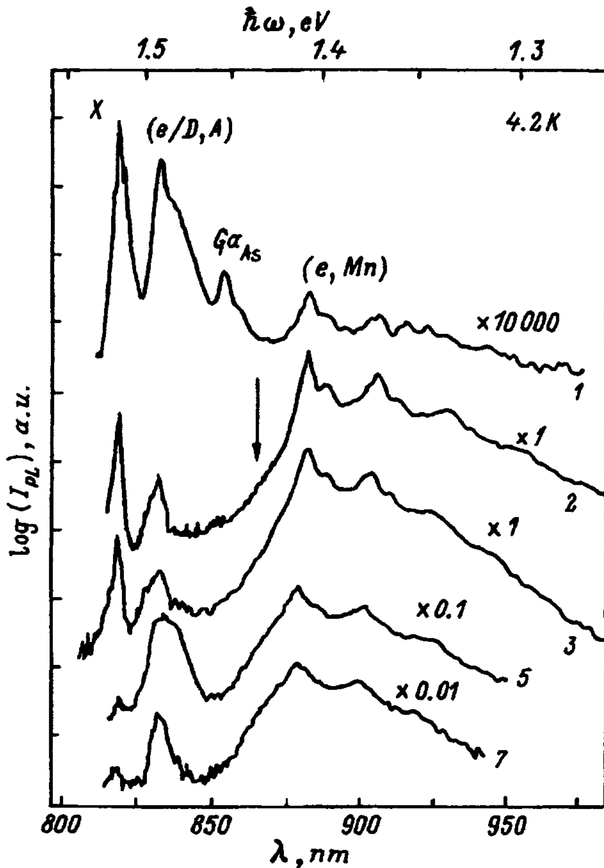

FIG. 1. Photoluminescence spectra of GaAs : Mn layers with different doping levels, measured at 4.2 K. The number labeling each spectrum corresponds to the layer numbers in the table.

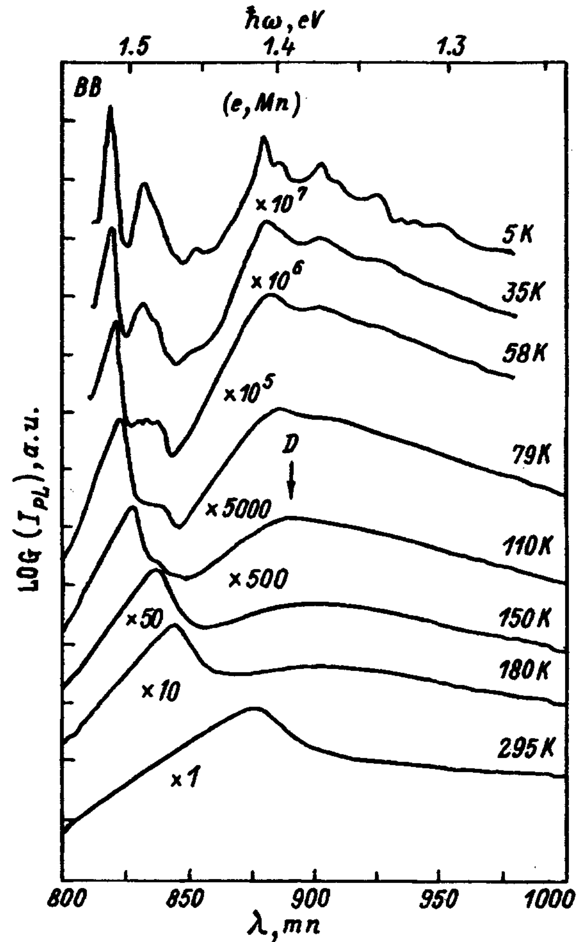

FIG. 2. Photoluminescence spectra of layer 2, measured at different temperatures.

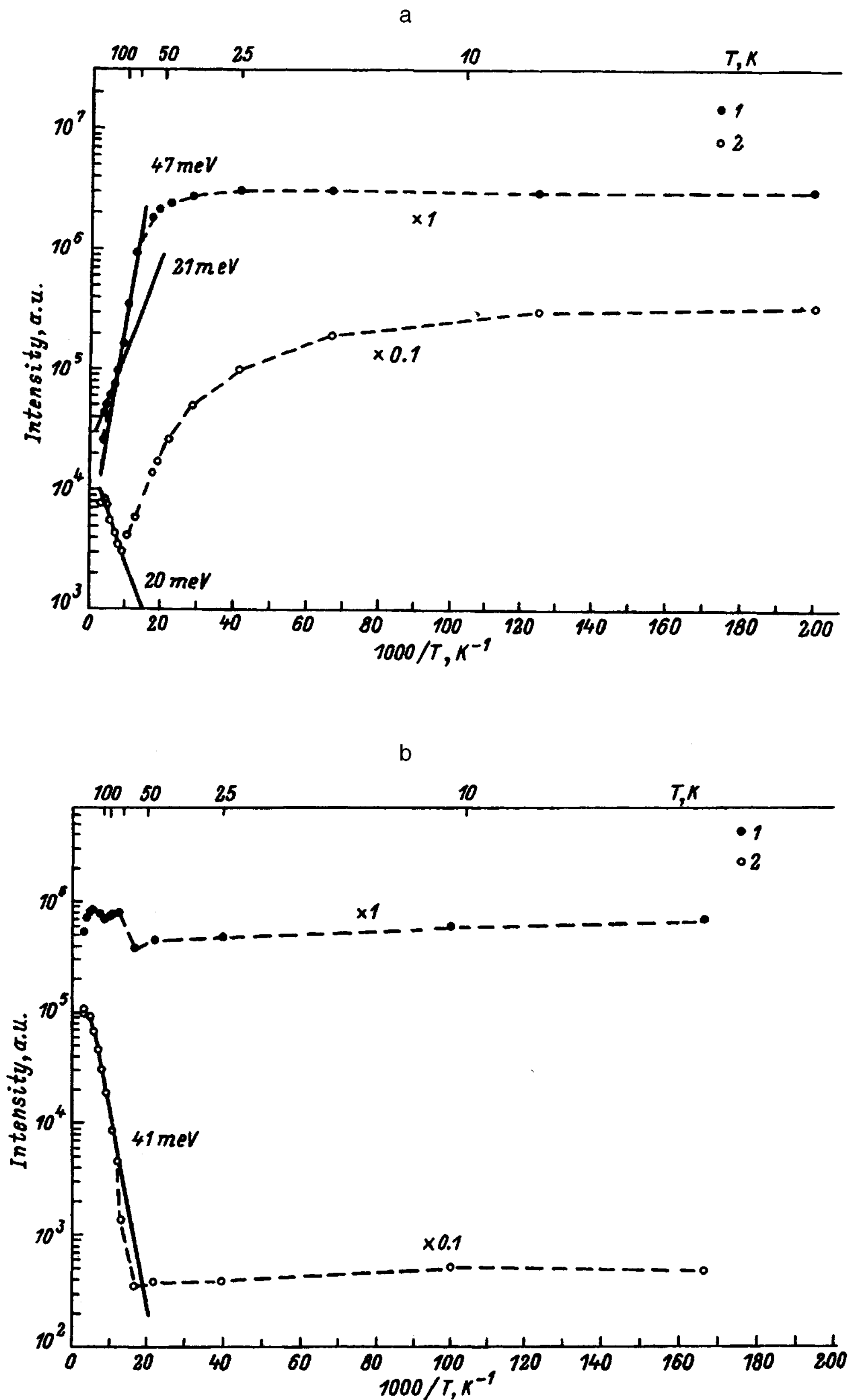

FIG. 3. Temperature dependence of the interband recombination line intensity (*1*) and total intensity of the (*e*, Mn) and *D* lines (*2*): a—for layer 2, b—for layer 7.

further. The total intensity of the (*e*, Mn) and *D* lines remains essentially constant as the temperature is raised from 5 to 60 K and falls exponentially with a slope of 47 ± 2 meV as the temperature is raised from 60 to 110 K. At higher temperatures the decrease of the total intensity of these lines slows down and is described by an exponential with slope

21 ± 2 meV. As the doping level is increased, the nature of the temperature dependence of the line intensities in the photoluminescence spectrum changes. As can be seen from Fig. 3b, the intensity of the interband recombination line in the spectrum of layer 7 remains constant at temperatures from 6 to 60 K, but as the temperature is raised from 60 to 295 K, it grows exponentially by more than two orders of magnitude with a slope of 41 ± 2 meV. The total intensity of the (e, Mn) and D lines in this layer is essentially independent of temperature.

The activation energies of thermal quenching of the total intensity of the (e, Mn) and D lines in the investigated layers are substantially lower than the thermal activation energy of quenching of the individual (e, Mn) line, determined in Refs. 2, 7, and 8, and, consequently, the main contribution to the total intensity of these lines at temperatures above 60 K is due to the D line.

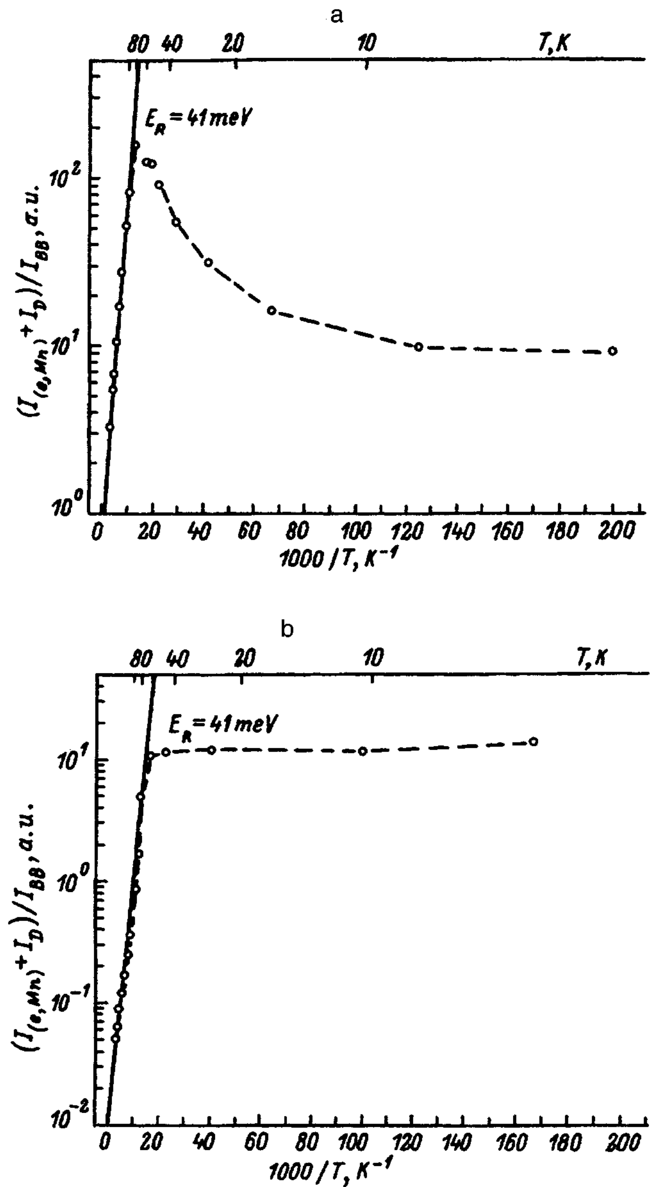

FIG. 4. Temperature dependence of the ratio of the total intensity of the (e, Mn) and D lines to the interband recombination line intensity: a—for layer 2, b—for layer 7.

4. DISCUSSION

It is clear from the experimental data that in strongly manganese-doped GaAs layers obtained by liquid-phase epitaxy from a bismuth melt, in addition to a substitution acceptor, at least two additional centers are formed, one of which is a radiative recombination center, and the other, a nonradiative recombination center.

The nonradiative recombination centers, which appear in GaAs upon strong manganese-doping, were observed earlier in material grown by molecular-beam epitaxy.[11] At the same time, the strongly lattice-bound R center is observed in GaAs :Mn here for the first time and the high concentration of these centers is apparently due to the method of preparation of the layers. It should be noted that the growth of the relative intensity of the D line in the photoluminescence spectra measured at 4.2 K with increase of the doping level indicates that the concentration of the R centers increases with increasing manganese concentration faster than the Mn_{Ga} concentration. This gives grounds to believe that the R center is a complex consisting of components whose concentration increases with increasing doping level. Such components may be manganese atoms as well as intrinsic point defects of the GaAs lattice. An unambiguous determination of the makeup of this center requires additional study.

An analysis of the experimental data within the framework of the Shockley–Reed–Hall model[23] allowed us to determine the binding energy of the holes[3)] at the R center (E_R).

The standard procedure for determining the binding energy of the charge carrier (E) to the recombination center is to fit the experimental temperature dependence of the intensity $I(T)$ of the photoluminescence line associated with the recombination center by a calculated dependence, which, as follows from the model in Ref. 23, can be written in the form

$$I(T) = \partial n \cdot p \cdot N / [(C_n \cdot \partial n + C_p \cdot p)/(C_n \cdot C_p) + (A/C_n)\exp(-E/kT)], \quad (1)$$

where $p = p_0 + \partial p$ is the total concentration of equilibrium and nonequilibrium holes, ∂n is the concentration of nonequilibrium electrons, N is the concentration of centers, C_n and C_p are the coefficients of electron and hole capture by the recombination center, E is the binding energy of a hole at the center, and A is a constant.

To simplify Eq. (1), we divided the expression for the intensity of the photoluminescence line associated with the recombination center R into an expression for the intensity of the interband recombination line, which is proportional to the electron and hole concentrations in the allowed bands, from which we derived the formula

$$I(T)/I_{BB}(T) = (N/B)/(\partial n/C_p + p/C_n + (A/C_n) \times \exp(-E/kT)), \quad (2)$$

where B is the interband recombination coefficient.

It is clear from Eq. (2) that to calculate $I(T)/I_{BB}(T)$ it is necessary to know the temperature dependence of the coefficients of charge-carrier capture by the recombination center

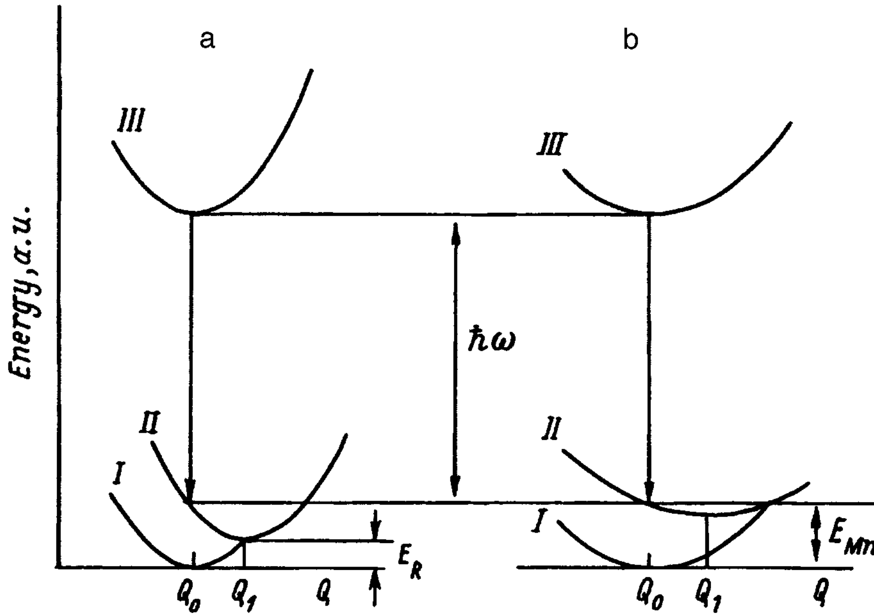

FIG. 5. Possible models of the configuration coordinates: a) for the R centers, and b) for the Mn_{Ga} centers. The vertical axis plots the sum of the electron energy and the vibrational energy of the center, and the horizontal axis plots the configuration coordinate. The states of the system center+electron are: I—electron in the valence band, II—electron trapped at a center, III—electron in the conduction band. E_g and E_{Mn} are the hole binding energy to the R and Mn_{Ga} centers, respectively; $\hbar\omega$ is the energy at the maximum of the lines associated with recombination through the levels of these centers. Q_n and Q_1 are the configuration coordinates of the position of vibrational equilibrium for the center without an electron and for the center having captured an electron, respectively. Emission of a hole from a center in the given model is equivalent to capture of an electron from that center.

and the temperature dependence of the free electron and hole concentrations. It is well known that with increase of the temperature, the charge-carrier capture coefficients can decrease according to a power law,[24] grow exponentially,[24,25] or remain constant.[25] The temperature dependence of charge-carrier capture by the recombination centers present in the investigated material is not known to us, and to simplify the calculations we disregarded the temperature dependence of these coefficients. The hole concentration in the GaAs:Mn layers in the temperature range from 77 to 295 K, as was shown in Refs. 1, 3, and 16, grows exponentially with slope 110 meV. The values we obtained for the free-hole concentrations for the GaAs:Mn layers at 77 and 295 K coincide with the values derived from the expression $p_0 \propto \exp(-110\,\text{meV}/kT)$, and, since in this temperature range $p \approx p_0$, we used this expression to describe the temperature dependence of the hole concentration in the GaAs : Mn layers. In the temperature interval where the ratio $I(T)/I_{BB}(T)$ decreases, the value of the sum of terms $p/C_n + (A/C_n)\exp(-E/kT)$ (which grow as the temperature is increased) in the denominator of expression (2) exceed the value of the term $\partial n/C_p$; consequently, in the determination of the value of E it is possible to ignore this term and rewrite Eq. (2) as follows:

$$I(T)/I_{BB}(T) = (N/B)/(p/C_n + (A/C_n)\exp(-E/kT)). \tag{3}$$

The experimental temperature dependence of the ratio of the total intensity of the D and (e, Mn) lines to the intensity of the interband recombination line for layers 2 and 7 is plotted in Figs. 4a and 4b, respectively.

Fitting Eq. (3) to these dependences in the temperature region above 80 K, where the main contribution to the total intensity comes from the D line, showed that the value of the binding energy of the hole to the R center, E_R, is the same in both layers and equal to 41 ± 2 meV.

The value of E_R obtained is unexpectedly small and at first glance contradicts the available experimental data. Despite the fact that the binding energy of the holes to the center responsible for the D line is more than two times smaller than the binding energy of the holes to the acceptor Mn_{Ga}, when the temperature is increased the D line begins to quench out at higher temperatures than the (e, Mn) line. In addition, the energies of the maxima of these two lines essentially coincide.

To shed light on the reason for this apparent contradiction, we analyzed expression (2). It is clear from this expression that the temperature (Θ), at which the intensity of the photoluminescence line associated with the recombination center begins to decrease abruptly, is determined by the relation between the coefficients of electron and hole capture by this center. Indeed, the photoluminescence line intensity decreases abruptly, beginning with the temperature at which the sum of the terms that increase with increasing temperature in the denominator of expression (2) becomes equal to the term $\partial n/C_p$:

$$\partial n/C_p = p/C_n + (A/C_n)\exp(-E/k\Theta). \tag{4}$$

Substituting in Eq. (4) the values of the binding energy of the holes to the R center and the Mn_{Ga} center and the free-hole concentration, which can be written in the form $p = A[(N_{Mn} - N_d)/N_d]\exp(-110\,\text{meV}/k\Theta)$ (Ref. 16), where N_{Mn} is the concentration of the Mn_{Ga} acceptors and N_d is the concentration of the compensating donors, we can rewrite this formula for the R center as

$$C_n/C_p = (A/\partial n)\{[(N_{Mn} - N_d)/N_d]\exp(-110\,\text{meV}/k\Theta) + \exp(-41\,\text{meV}/k\Theta)\} \tag{4a}$$

and for the Mn_{Ga} center as

$$C_n/C_p = (A/\partial n)(N_{Mn}/N_d)\exp(-110\,\text{meV}/k\Theta). \tag{4b}$$

Substituting the experimentally obtained temperature Θ for the D line in Eqs. (4a) and (4b), which, as is evident from Fig. 3, is approximately equal to 60 K, shows that the (e, Mn) line quenches at a lower temperature if the ratio C_n/C_p for the R center exceeds the corresponding ratio for the Mn_{Ga} center by more than three orders of magnitude.

The coincidence of the energies at maximum for the lines associated with transitions through the levels of centers with substantially different charge-carrier binding energies can be explained within the framework of the model of configuration coordinates, which is used to treat the thermal generation and capture of charge carriers.[24,25] Possible configuration diagrams for the R and Mn_{Ga} centers are shown in Fig. 5. It is clear from the figure that different energy dependences on the configuration coordinates and different displacements of the position of vibrational equilibrium for charge-carrier capture for different recombination centers makes it possible to realize situations having substantially different charge-carrier binding energies, located in the same energy range.

5. CONCLUSIONS

To summarize, we have shown that in strongly manganese-doped GaAs, obtained by liquid-phase epitaxy from a bismuth melt, in addition to the Mn_{Ga} acceptors, two other centers are formed, a radiative recombination center and a nonradiative recombination center. The concentrations of these centers increase with increasing doping level, with the concentration of radiative recombination centers growing faster than the Mn_{Ga} concentration. The radiative recombination center is strongly bound to the crystal lattice and is probably a complex consisting of impurity atoms and/or intrinsic point defects of the GaAs lattice. The ionization energy of the radiative recombination center has been determined to be equal to 41 ± 2 meV.

*E-mail: tim@ns.isp.nsc.ru (T. S. Shamirzaev) Phone: (3832) 357807 (T. S. Shamirzaev)

1)Look and Pomrenke[17] suggested that the line with energy position of its maximum equal to 1.408 eV, present in the photoluminescence spectrum of the intentionally undoped GaAs layer, may be associated with recombination through defect levels. However, traces of manganese which we detected in the undoped sample by x-ray fluorescence spectroscopy indicate that in the investigated layers the line at 1.408 eV is associated with transitions to manganese acceptor levels.

2)The intensity of the (e, Mn) line includes the intensity of its phonon echoes.

3)The available data do not allow us to determine the types of centers; therefore, we make the type of charge carrier specific. E_R is the binding energy of a hole if the center is an acceptor, or of an electron, if the center is a donor. For definiteness, we have assumed that the R center is an acceptor.

1. J. S. Blakemore, W. J. Brown, M. L. Stass, and D. A. Woodbury, J. Appl. Phys. **44**, 3352 (1973).
2. M. Ilegems, R. Dingle, and L. W. Rupp, J. Appl. Phys. **46**, 3059 (1975).
3. P. Kordos, L. Jansak, and V. Benc, Solid-State Electron. **18**, 223 (1975).
4. L. Montelius, S. Nilsson, L. Samuelson, E. Janzén, and M. Ahlström, J. Appl. Phys. **64**, 1564 (1988).
5. T. C. Lee and W. W. Anderson, Solid State Commun. **2**, 265 (1964).
6. W. Schairer and M. Schmidt, Phys. Rev. B **10**, 2501 (1974).
7. P. W. Yu and Y. S. Park, J. Appl. Phys. **50**, 1097 (1979).
8. L. Montelius, S. Nilsson, and L. Samuelson, Phys. Rev. B **40**, 5598 (1989).
9. N. S. Averkiev, A. A. Gutkin, E. B. Osipov, and M. A. Reshchikov, Preprint FTI No. 1201 (A. F. Ioffe Physicotechnical Institute) [in Russian] (Leningrad, 1988).
10. S. J. C. H. M. van Gisbergen, A. A. Ezhevkii, N. T. Son, T. Gregorkiewicz, and C. A. J. Ammerlaan, Phys. Rev. B **49**, 10 999 (1994).
11. F. Fabre, G. Bacquet, J. Frandon, J. Bandet, and R. Taouint, Solid State Commun. **71**, 717 (1989).
12. V. V. Antonov, A. V. Voĭtsekhovskiĭ, M. A. Krivov, E. V. Malisova, É. N. Mel'chenko, V. S. Morozov, M. P. Nikiforova, E. A. Popova, and S. S. Khludkov, in *Doping of Semiconductors* [in Russian] (Nauka, Moscow, 1982), p. 32.
13. N. A. Yakusheva, K. S. Zhuravlev, S. I. Chikichev, O. A. Shegai, Cryst. Res. Technol. **24**, 235 (1989).
14. R. Kh. Akchurin, I. O. Donskaya, S. I. Dulin, and V. B. Ufimtsev, Kristallografiya **33**, 464 (1988) [Sov. Phys. Crystallogr. **33**, 273 (1988)].
15. N. A. Yakusheva, *Abstracts of the Sixth All-Union Conference on the Physico-chemical Foundations of Doping of Semiconductor Materials* [in Russian] (Nauka, Moscow, 1988), p. 51.
16. L. Gouskov, S. Bilac, J. Pimentel, and A. Gouskov, Solid-State Electron. **20**, 653 (1997).
17. D. C. Look and G. S. Pomrenke, J. Appl. Phys. **54**, 3249 (1983).
18. P. W. Yu, Phys. Rev. B **27**, 7779 (1983).
19. D. L. Dexter, in *Solid State Physics*, edited by F. Seitz and D. Turnbull (New York, 1958), Vol. 6, p. 355.
20. K. K. Rebane, *Impurity Spectra of Solids: Elementary Theory of Vibrational Structure* (Plenum Press, New York, 1970).
21. E. W. Williams and H. B. Bebb, *Semiconductors and Semimetals* (Academic Press, New York, 1972), Vol. 8, p. 321.
22. C. C. Klick and J. H. Shulman, *Solid State Physics*, edited by F. Seitz and D. Turnbull (New York, 1957), Vol. 5, p. 97.
23. K. D. Glinchuk, A. V. Prokhorovich, V. E. Rodionov, and V. I. Vovnenko, Phys. Status Solidi A **48**, 593 (1978).
24. B. K. Ridley, *Quantum Processes in Semiconductors*, 2nd ed. (Oxford University Press, New York, 1988).
25. É. M. Alidovich, *Some Questions in the Theory of Luminescence of Crystals* [in Russian] (Gosudarstvennoe Izdatel'stvo Tekhniko-Teoreticheskoĭ Literatury, Moscow, 1956).

Translated by Paul F. Schippnick

Effect of selenium on the galvanomagnetic properties of the diluted magnetic semiconductor $Hg_{1-x}Mn_xTe_{1-y}Se_y$

V. A. Kulbachinskiĭ, I. A. Churilov, P. D. Maryanchuk, and R. A. Lunin

M. V. Lomonosov Moscow State University, 119899 Moscow, Russia
(Submitted February 17, 1997; accepted for publication May 28, 1997)
Fiz. Tekh. Poluprovodn. **32**, 57–60 (January 1998)

The galvanomagnetic properties of single crystals of the diluted magnetic semiconductor $Hg_{1-x}Mn_xTe_{1-y}Se_y$ $(0.01<y<0.1)$ with $x=0.05$ and 0.14 have been investigated in the temperature range 4.2–300 K. Peculiarities of the temperature dependence of the Hall coefficient R_H and its complicated behavior in a magnetic field are quantitatively explained by the existence of three groups of current carriers: electrons and two types of holes with different mobilities for which the temperature dependence of concentration and mobility was obtained. A transition from p-type to n-type conductivity was observed with increase of Se content, alongside with a simultaneous change of sign of the magnetoresistance from negative to positive. © *1998 American Institute of Physics.* [S1063-7826(97)00412-2]

1. INTRODUCTION

Diluted magnetic semiconductors are solid solutions in which one of the components is replaced by an atom of a transition element (M) with uncompensated magnetic moment. Among $A^{II}_{1-x}M_xB^{VI}$ compounds diluted magnetic semiconductors with the composition $Hg_{1-x}Mn_xTe$, $Hg_{1-x}Mn_xSe$ have been relatively well studied.[1–3] It has been found that $Hg_{1-x}Mn_xTe$ has p-type conductivity,[4] while $Hg_{1-x}Mn_xSe$ has n-type conductivity.[5] The type of conductivity is connected with the charge defects appearing in the crystals: vacancies in the mercury sublattice are acceptors in $Hg_{1-x}Mn_xTe$, while mercury atoms at interstitials and vacancies in the selenium sublattice are donors in $Hg_{1-x}Mn_xSe$. It is of interest to study the diluted magnetic semiconductors $Hg_{1-x}Mn_xSe_yTe_{1-y}$. It may be assumed that varying the selenium concentration will produce a particular kind of compensation of the various defects, which could make it possible to regulate the type of conductivity and current-carrier concentration in this quaternary compound. The galvanomagnetic properties of $Hg_{1-x}Mn_xSe_yTe_{1-y}$ were examined earlier as functions of the manganese content in Refs. 6–8, and transitions to the spin-glass state were investigated in Refs. 7 and 8.

We will investigate the galvanomagnetic properties (in the temperature interval 4.2–300 K) of single crystals of the solid solution $Hg_{1-x}Mn_xTe_{1-y}Se_y$ with $x=0.05$ and 0.14 varying the selenium content from $y=0.01$ to $y=0.10$.

2. SAMPLES

Single crystals of $Hg_{1-x}Mn_xTe_{1-y}Se_y$ were grown by the Bridgman technique from chemically pure components. Samples with characteristic dimensions $0.6\times0.6\times5\ mm^3$ were cut from bars by electrical erosion. The manganese content was determined more precisely with the aid of an x-ray microprobe and from measurements of the room-temperature magnetic susceptibility. Both methods gave identical results within the limits of measurement error. The selenium content in the samples was inferred from these data. From the x-ray and microprobe analyses and also the magnetic measurements it was determined that there were no foreign phase inclusions in the samples and that the samples were homogeneous. The homogeneity of the samples was also monitored from measurements of the Hall coefficient R_H along the length of the sample. The difference in values of R_H did not exceed a few percent.

Electrical measurements were performed on freshly etched samples at constant current by the four-contact method. We studied samples of $Hg_{1-x}Mn_xTe_{1-y}Se_y$ with $x=0.05$, 0.14 and $y=0.01$, 0.05, 0.075, 0.10. Some parameters of the single crystals at $T=4.2$ K are listed in Table I.

It is known that the electrical and galvanomagnetic properties of HgTe-based semiconductor solid solutions are significantly affected by the surface region (skin layer).[9] To eliminate this effect, the samples were etched immediately before measurement. Special studies showed that storing the etched samples in air for several days does not alter their electrical properties, in particular, the complicated behavior of the Hall coefficient in a magnetic field at different temperatures; i.e., the skin layer does not affect the results obtained here.

3. MEASUREMENT OF THE GALVANO-MAGNETIC PROPERTIES AND DISCUSSION

As the temperature is lowered, the resistance of all the samples grows, exhibiting activation behavior with activation energy equal to about 30 meV at temperatures above 100 K. The samples with minimum selenium content manifest negative magnetoresistance at temperatures below $T=30$ K, which increases with decreasing temperature. As the selenium content is increased, the negative magnetoresistance decreases and for the selenium content $y=0.10$ even at liquid-helium temperatures the magnetoresistance becomes positive. Figure 1 plots the magnetoresistance $\Delta\rho/\rho_0[\rho(B)-\rho(0)]/\rho(0)$ as a function of the magnetic field B for five samples. The negative magnetoresistance in large magnetic fields can be explained by an increase in the conductivity via the impurity band characteristic of $Hg_{1-x}Mn_xTe$, (Refs. 1–3) as a result of the overlap of the

 1063-7826/98/010049-03$15.00 © 1998 American Institute of Physics

TABLE I. Parameters of $Hg_{1-x}Mn_xTe_{1-y}Se_y$ samples at 4.2 K.

Sample No.	Content		n, 10^{14} cm^{-3}	μ_e, 10^4 cm^2/(V·s)	p_1, 10^{17} cm^{-3}	μ_{p1}, cm^2/(V·s)	p_2, 10^{15} cm^{-3}	μ_{p2}, cm^2/(V·s)
	Mn, x	Se, y						
1	0.14	0.01	0.3	−6.0	2.7	820	9.0	3000
2	0.14	0.05	0.003	−6.0	0.9	130	0.46	4800
3	0.14	0.075	2.5	−3.0	7.8	850	25.0	5300
4	0.14	0.10	1.1	−1.2	42	60	0.52	4100
5	0.05	0.01	5.3	−1.5	2.8	715	7.2	2000
6	0.05	0.10	72.0	−0.56	8.2	80	4.8	5700

Remark: n, p_1, and p_2 are the concentrations of the electrons and two types of holes, respectively; μ_e, μ_{p1}, and μ_{p2} are the corresponding mobilities.

acceptor wave functions in a magnetic field—the so-called magnetic boiling-off of holes.[10–14] As the selenium content is increased, the role of conductivity via the acceptor impurity band is diminished and the samples even change their type of conductivity from p- to n-type; therefore, the negative magnetoresistance is replaced by positive magnetoresistance.

Determination of the mobilities of the various groups of current carriers from the Hall effect. Most complicated is the behavior of the Hall coefficient R_H at different temperatures as a function of the magnetic field. For the sample $Hg_{0.86}Mn_{0.14}Te_{1-y}Se_y$ with a direct band gap at 4.2 K the Hall coefficient is positive ($R_H>0$). As the temperature is increased, the sign of R_H in weak fields changes to negative. Increasing the selenium concentration leads to a growth of the electron concentration and to a change of sign of the Hall coefficient in weak magnetic fields. This effect is manifested more strongly in gapless samples. As an example, Fig. 2 plots the magnetic-field dependence of R_H at different temperatures for the samples $Hg_{0.95}Mn_{0.05}Te_{1-y}Se_y$ with $y=0.01$ and 0.10.

Quantitatively, we were able to satisfactorily describe the $R_H(B)$ data plotted in Fig. 2 only by taking into account three groups of carriers (electrons and two types of holes) with different concentrations and mobilities. The hole conductivity is realized both in the valence band (the first sort of band holes or intrinsic holes) and via the impurity acceptor band (the second sort of holes).[7,8] The Hall coefficient depends on the magnetic field (for the Hall factor for all three groups equal to 1) in the following way:

$$R_H(B)=N/(A^2+N^2B^2), \tag{1}$$

where we have introduced the notation

$$N=en\mu_e^2/(1+\mu_e^2B^2)+ep_1\mu_{p1}^2/(1+\mu_{p1}^2B^2)+ep_2\mu_{p2}^2/(1+\mu_{p2}^2B^2), \tag{2}$$

$$A=en\mu_e/(1+\mu_e^2B^2)+ep_1\mu_{p1}/(1+\mu_{p1}^2B^2)+ep_2\mu_{p2}/(1+\mu_{p2}^2B^2). \tag{3}$$

The calculated curves in Fig. 2 take into account the three indicated groups of carriers. Table I lists the electron and hole concentrations and mobilities at 4.2 K, obtained by fitting the $R_H(B)$ data. Highest are the values of the electron mobility, which is typical of $Hg_{1-x}Mn_xTe$. A characteristic peculiarity is growth of the electron concentration with increase of the selenium content in the samples up to change of

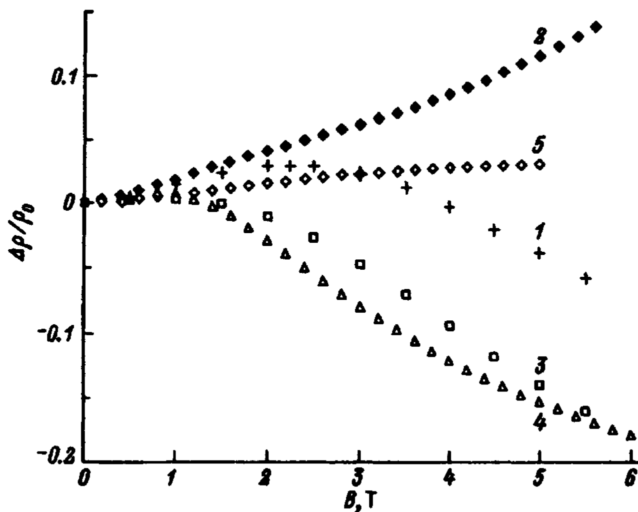

FIG. 1. Dependence of the magnetoresistance $\Delta\rho/\rho_0$ on the magnetic field B at $T=4.2$ K for $Hg_{1-x}Mn_xTe_{1-y}Se_y$ samples with various composition: *1)* $x=0.05$, $y=0.01$; *2)* $x=0.05$, $y=0.1$; *3)* $x=0.14$, $y=0.01$; *4)* $x=0.14$, $y=0.075$; *5)* $x=0.14$, $y=0.10$.

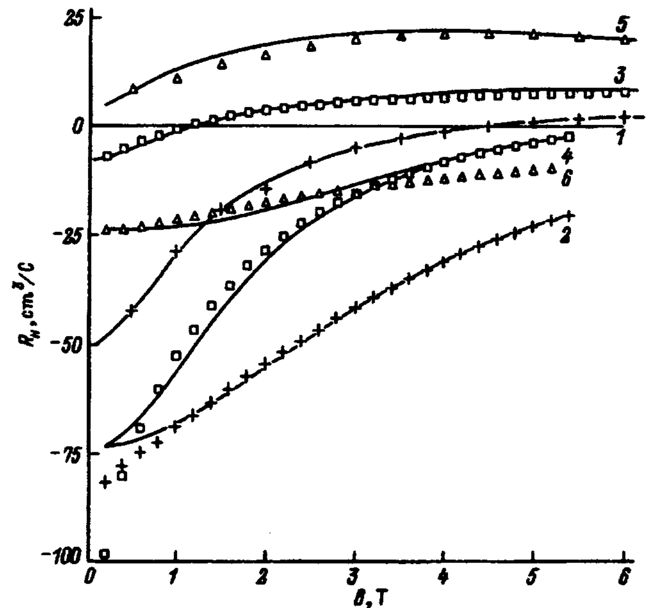

FIG. 2. Dependence of the Hall coefficient R_H on the magnetic field B for $Hg_{0.95}Mn_{0.05}Te_{1-y}Se_y$ samples with $y=0.01$ (curves *1*, *3*, *5*) and $y=0.1$ (curves *2*, *4*, *6*). $T=81$ (*1*), 95 (*2*), 36 (*3*), 4.2 K (*4*).

the type of conductivity from p to n (the samples with $x=0.05$). As the temperature is lowered, the mobilities of all three groups of charge carriers increase.

Determination of the mobilities of the different groups of current carriers from the dependence of the positive magnetoresistance on the magnetic field. To find the mobilities of the different groups of current carriers in the investigated samples, we used the classical magnetoresistance effect. The authors of Ref. 15 proposed a method which transforms the magnetic-field dependences of the resistance into the so-called ''mobility spectrum''—the dependence of the conductivity on the mobility. This method assumes that the concentration of the current carriers n is a continuous function of their mobility $\mu\, n(\mu)$, so that the components of the mobility tensor transverse to the magnetic field can be written in the form of integrals summing the contributions to the conductivity from each group of carriers:

$$\sigma_{xx}(B)=\int_{-\infty}^{+\infty}\frac{s(\mu)d\mu}{1+(\mu B)^2},\quad \sigma_{xy}(B)=\int_{-\infty}^{+\infty}\frac{s(\mu)\mu B d\mu}{1+(\mu B)^2}, \tag{4}$$

where $s(\mu)d\mu=en(\mu)d\mu$ is the contribution to the conductivity at $B=0$ from the carriers having mobility from μ to $\mu+d\mu$; the electrons have negative mobility, and the holes have positive mobility. In the case in which there are N-types of current carriers with discrete concentrations n_i and mobilities μ_i $(i=1...N)$, N peaks appear in the mobility spectrum, whose centers are located at the mobilities μ_i, and whose amplitudes are equal to $en_i\mu_i$. Figure 3 shows the mobility spectrum for the sample $Hg_{0.86}Mn_{0.14}Te_{0.9}Se_{0.1}$ at 79 K. From this figure it can be seen that there are three groups of current carriers with different mobilities: two groups of holes and the electrons. Mobility values obtained from the corresponding spectra for the other samples agree well with the values calculated from the magnetic-field dependence of the Hall coefficient.

4. CONCLUSIONS

In the diluted magnetic semiconductor $Hg_{1-x}Mn_xTe_{1-y}Se_y$ galvanomagnetic effects, in particular, sign inversion of the Hall coefficient with increase of the temperature and its complicated behavior in a magnetic field are thus determined by the electrons and by two groups of holes. With increase of the selenium content, the electron concentration grows and the type of conductivity changes from p to n.

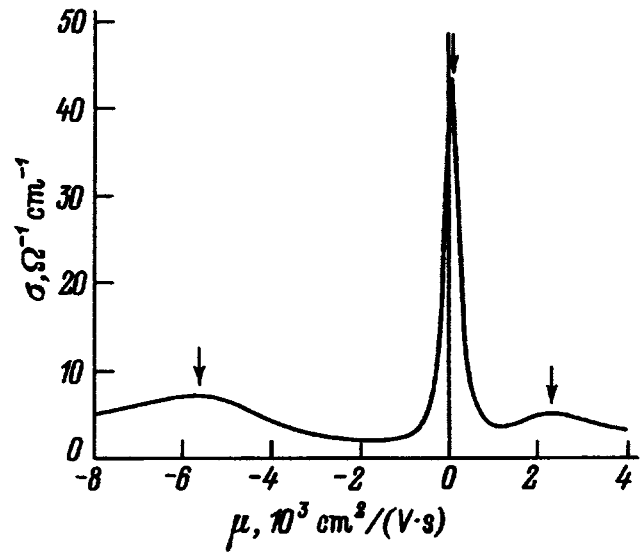

FIG. 3. Mobility spectrum at 79 K for the $Hg_{0.86}Mn_{0.14}Te_{0.90}Se_{0.10}$ sample. The three maxima (indicated by arrows) correspond to the three groups of current carriers (the mobility is negative for the electrons).

[1] J. K. Furdyna, J. Appl. Phys. **64**, R29 (1988).
[2] N. B. Brandt and V. V. Moshchalkov, Adv. Phys. **33**, 194 (1984).
[3] I. I. Lyapilin and I. M. Tsidil'kovskiĭ, Usp. Fiz. Nauk **146**, 35 (1985) [Sov. Phys. Usp. **28**, 349 (1985)].
[4] N. B. Brandt, V. V. Moshchalkov, A. O. Orlov, L. Skrbek, I. M. Tsidil'kovskiĭ, and S. M. Chudinov, Zh. Éksp. Teor. Fiz. **84**, 1059 (1983) [Sov. Phys. JETP **57**, 614 (1983)].
[5] Zh. T. Ismailov, V. A. Kul'bachinskiĭ, S. M. Chudinov, N. P. Gavaleshko, and P. D. Mar'yanchuk, Fiz. Tekh. Poluprovodn. **22**, 375 (1988) [Sov. Phys. Semicond. **22**, 231 (1988)].
[6] K. R. Krylov, N. K. Lerinman, A. I. Ponomarev, L. D. Mar'yanchuk, Fiz. Tekh. Poluprovodn. **28**, 1382 (1994) [Semiconductors **28**, 779 (1994)].
[7] V. A. Kul'bachinskiĭ, P. D. Mar'yanchuk, and I. A. Churilov, Fiz. Tekh. Poluprovodn. **29**, 2007 (1995) [Semiconductors **29**, 1047 (1995)].
[8] V. A. Kulbachinskii, P. D. Maryanchuk, I. A. Churilov, M. Inoue, M. Sasaki, H. Negishi, and Y. Hara, Semicond. Sci. Technol. **10**, 463 (1995).
[9] I. Ivanov-Omskii, N. N. Berchenko, and A. I. Elizarov, Phys. Status Solidi A **103**, 11 (1987).
[10] J. Mycielski, in *Recent Developments in Condensed Matter Physics*, edited by J. T. De Vreese (Plenum, New York, 1981), Vol. 1, p. 725.
[11] L. R. Gawron and J. Trylski, *Lecture Notes in Physics 152, Physics of Narrow Gap Semiconductors, Proceedings of the Lintz Conference 1981*, edited by E. Gornik, H. Heinrigh, L. Palmetshofer (Springer, Berlin, 1982), p. 294.
[12] A. Mycielski and J. Mycielski, J. Phys. Soc. Jpn. **49**, 807 (1989).
[13] W. B. Johnson, J. R. Anderson, and D. R. Stone, Phys. Rev. B **29**, 6679 (1984).
[14] A. B. Davydov, B. B. Ponikarov, and I. M. Tsidilkovskii, Phys. Status Solidi B **101**, 127 (1980).
[15] W. A. Beck and J. R. Anderson, J. Appl. Phys. **62**, 541 (1987).

Translated by Paul F. Schippnick

On $C-V$ profiling near an isotypic heterojunction

V. I. Zubkov, M. A. Melnik, and A. V. Solomonov

St. Petersburg State Electrico-technical University, 197376 St. Petersburg, Russia
(Submitted February 20, 1997; accepted for publication June 3, 1997)
Fiz. Tekh. Poluprovodn. **32**, 61–62 (January 1998)

A method of accurate determination of the majority carrier profile near an isotypic heterojunction is proposed. The method takes into account the different values of the dielectric constants on the two sides of the heterojunction. The carrier profile is first calculated from the $C-V$ characteristic and then corrected according to the maximum of $p(w)$. © *1998 American Institute of Physics.* [S1063-7826(98)01601-9]

Current–voltage characteristics are an effective instrument for determining the profile of the main charge carriers in semiconductors. For isotypic heterojunctions it is possible with the aid of $C-V$ characteristics to determine the carrier concentrations in the enrichment and depletion regions near the heterobarrier and also the magnitude of the built-in charge on the heteroboundary and the magnitude of the band discontinuity.[1,2] In general, the materials on either side of the junction have different dielectric constants. However, this fact is usually disregarded in calculations of the carrier concentration profile from the measured current–voltage characteristic since the coordinate of the heterojunction is not known to start with. Thus, the resulting profile is different from the actual one.

We propose a method for accurately determining the profile of the main charge carriers near an isotypic heterojunction, based on a refinement of the concentration profile initially calculated from the $C-V$ characteristic.

Let us consider an isotypic heterosemiconductor (for definiteness, of $p-p$ type), on one side of which an ohmic contact is placed and on the other, a rectifying barrier. The narrow-band interlayer has a wide band gap E_1 and dielectric constant ε_1, and a wide-band layer, E_2 and ε_2. For a moderate reverse bias the space charge region (SCR) is located entirely in the interlayer near the metal–semiconductor rectifying barrier; therefore, the initial segment of the $C-V$ characteristic is determined by the parameters of the interlayer (E_1, ε_1). As the reverse bias is increased, the edge of the space charge region intersects the heteroboundary, engulfs the space charge region near the heterointerface and moves into the wideband layer (Fig. 1). Here the increment of the capacitance on the right side of the heteroboundary is determined by the parameters of the second layer.

We assume that the heteroboundary is located a distance w_0 from the rectifying barrier. We thus represent the total capacitance of the structure with reverse bias U_r as the sum of the capacitances of two capacitors linked in series

$$C=\frac{C_1C_x}{C_1+C_x}, \tag{1}$$

where C_1 is the capacitance of the narrow-band layer, and C_x is the capacitance of the wide-band semiconductor layer with thickness x.

According to the formula of a planar capacitor

$$C_1=\frac{\varepsilon_1\varepsilon_0 S}{w_0},$$

$$C_x=\frac{\varepsilon_2\varepsilon_0 S}{x}. \tag{2}$$

Here S is the area of the sample. Hence

$$C=\frac{\varepsilon_1\varepsilon_2\varepsilon_0 S}{\varepsilon_1 x+\varepsilon_2 w_0}. \tag{3}$$

If we introduce an effective dielectric constant ε^* such that

$$C=\frac{\varepsilon^*\varepsilon_0 S}{w_0+x}, \tag{4}$$

then the expression for ε^* can be written in the form

$$\varepsilon^*=\frac{w_0+x}{w_0/\varepsilon_1+x/\varepsilon_2}. \tag{5}$$

The quantity ε_2 is obviously close in value to ε_1 if the space charge region is located near the heterojunction and tends to ε_2 as the space charge region moves into the layer bordering the ohmic contact with growth of U_r (Fig. 2).

Now the sequence of determining the exact profile of the main charge carriers in an isotypic heterojunction reduces to the following.

1. The concentration profile of the charge carriers is calculated from the measured $C-V$ characteristic using the usual procedure of numerically differentiating the $C-V$ dependence according to the formulas in Ref. 3:

$$p(w)=-\frac{C^3}{q\varepsilon\varepsilon_0 S^2}\left(\frac{dC}{dU}\right)^{-1},$$

$$w=\frac{\varepsilon\varepsilon_0 S}{C}. \tag{6}$$

We assume $\varepsilon=\varepsilon_1$.

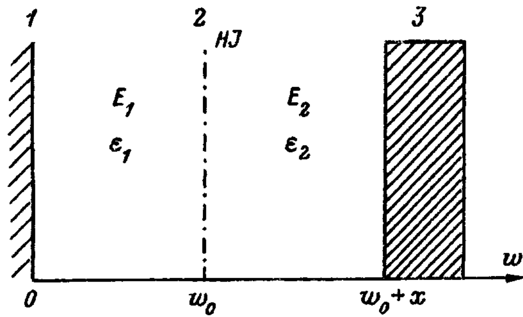

FIG. 1. Schematic diagram of an isotypic heterojunction. The dot–dashed line marks the position of the heterojunction. *1*—Schottky barrier, *2*—space charge region, *3*—quasineutral region.

2. From the obtained dependence $p(w)$ we find the coordinate of the maximum, which corresponds to the peak of the narrow enrichment region of the main charge carriers near the heterojunction.

In the zeroth approximation we can assume this coordinate to be the thickness of the layer w_0. [Numerical calculations based on the solution of the Poisson equation[1,2,4] show that in the case of a narrow-band layer the heterojunction point lies between the extrema of $p(w)$ roughly 10 times closer to the maximum.]

3. For all points $w_i > w_0$ we find x from Eqs. (1) and (2):

$$x_i = \frac{\varepsilon_2 \varepsilon_0 S}{C_i} - \frac{\varepsilon_2}{\varepsilon_i w_0}, \tag{7}$$

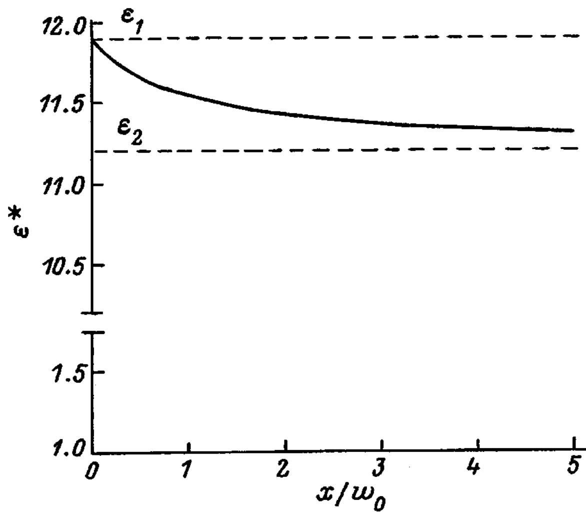

FIG. 2. Dependence of the "effective" dielectric constant on the thickness of the depleted wide-band layer.

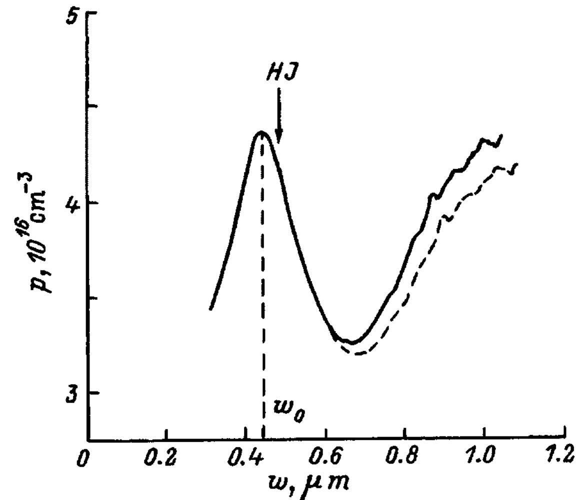

FIG. 3. Initial (dashed curve) and corrected (solid curve) profiles of the main charge carriers near the heterojunction ($\varepsilon_2 < \varepsilon_1$).

and, correspondingly, we calculate ε^* from Eq. (5). For each point $w_i > w_0$ we then recalculate the thickness of the space charge region and the concentration from the equations

$$w_{icorr} = w_0 + x_i, \tag{8}$$

$$p_{icorr} = p_i \cdot \frac{\varepsilon_1}{\varepsilon^*}. \tag{9}$$

The corrected profile $p(w)$ is shown in Fig. 3. For comparison, the profile initially calculated according to Eq. (6), without allowance for the change in ε to the right of the heterojunction, is represented by the dashed line.

The corrected profile corresponds more accurately to the real charge carrier distribution in an isotypic heterojunction than the distribution obtained by "the usual method" [Eq. (6)]. It should be noted that the new profile should be used to compare with the results of modeling the $C-V$ characteristics based on numerical solution of the Poisson equation.

Fax: (812)-234-98-68
E-mail: zubkov@fvleff.etu.spb.ru

[1] J. S. Rimmer, M. Missous, and A. R. Peaker, Appl. Surf. Sci. **50**, 149 (1991).

[2] M. O. Watanabe, J. Yoshida, M. Mashita, T. Nakanisi, and A. Hojo, J. Appl. Phys. **57**, 5340 (1985).

[3] L. S. Berman, *Capacitance Methods of Study of Semiconductors* [in Russian] (Nauka, Leningrad, 1972), p. 104.

[4] M. A. Melnik, A. N. Pikhtin, A. V. Solomonov, V. I. Zubkov, and F. Bugge, *Summaries of the 23rd International Symposium on Compound Semiconductors* (St. Petersburg, Russia, 1996), p. 62.

Translated by Paul F. Schippnick

Impact ionization luminescence of InGaN/AlGaN/GaN *p-n*-heterostructures

A. N. Kovalev and F. I. Manyakhin

Moscow Institute of Steel and Alloys, 119899 Moscow, Russia

V. E. Kudryashov, A. N. Turkin, and A. É. Yunovich

Moscow State (M. V. Lomonosov) University, Department of Physics, 119899 Moscow, Russia

(Submitted May 22, 1997; accepted for publication May 28, 1997)
Fiz. Tekh. Poluprovodn. **32**, 63–67 (January 1998)

The luminescence spectra of InGaN/AlGaN/GaN p-n heterostructures with reverse bias sufficient for impact ionization are investigated. The injection luminescence of light-emitting diodes with such structures was examined earlier. A strong electric field is present in the InGaN active layer of the heterostructures, and for small reverse bias the tunneling component of the current predominates. Avalanche breakdown commences at voltages $V_{\text{th}}>8-10$ V, i.e., $\sim 3E_g$, (E_g is the width of the band gap) in the absence of lightly doped structures. The luminescence spectra have a short-wavelength edge corresponding to the width of the GaN band gap (3.40 eV) and maxima in the region 2.60–2.80 eV corresponding to the maxima of the injection luminescence spectra in the active layer. The long-wavelength edge of the spectra in the region 1.7–1.8 eV may be associated with deep recombination levels. Mechanisms of recombination of the hot electron–hole plasma in the strong electric fields of the p-n heterostructures are discussed. © *1998 American Institute of Physics.* [S1063-7826(98)01701-3]

1. INTRODUCTION

Injection luminescence spectra of high-brightness blue and green light-emitting diodes (LED's) based on InGaN/AlGaN/GaN heterostructures were investigated in Refs. 1–5. It is of interest to investigate the luminescence of these structures under conditions of impact ionization with the aim of obtaining additional information about the mechanisms influencing the properties and efficiency of LED's.

Luminescence under conditions of ionization breakdown in GaN was first studied in the context of $i-n$ and MIS diodes.[6–9] It was shown that under conditions of reverse bias the electrons tunnel from the metal into the n-region of the structure and at a high enough voltage impact ionization and avalanche breakdown enter into the picture.

It follows from spectral and capacitance measurements[3–5] that a strong electric field is present in the active layer of InGaN/AlGaN/GaN based blue LED's.

A heavily doped p-region and a thin active layer distinguish these LED's from earlier structures.[6–9] In the present paper we describe the luminescence spectra of blue LED's at breakdown and we analyze the electrical and luminescence properties of InGaN/AlGaN/GaN based structures with reverse bias.

2. EXPERIMENTAL RESULTS

The luminescence spectra and electrical properties of LED's based on InGaN/AlGaN/GaN structures with a thin InGaN active layer were described in Refs. 1 and 2. We chose blue LED's with known parameters of their injection luminescence spectra for measurement.[2–4] The reverse-bias current–voltage ($I-V$) characteristics of the blue diode (sample 3) are shown in Fig. 1a. The main part of the $I-V$ characteristics can be approximated by two exponentials of the type

$$J \sim \exp(|eV|/E_J) \quad (1)$$

with parameters E_J that vary near the voltages $V=5-7$ V in the range 0.8–0.9 eV. The variation of the slopes in this region is clearly seen on the semilogarithmic derivatives $E_J=dV/d(\ln J)$ (see Fig. 1a). The values of E_J were essentially independent of temperature in the range $T=80-300$ K. This part of the $I-V$ characteristics is determined by the tunneling component of the current. Note that the variations on the reverse-bias branches of the $I-V$ characteristics of GaN diodes near $|V|=5-6$ V were also observed by other authors,[10,11] but were not given any importance.

Impact ionization commences at higher voltages, $|V|>8-10$ V, as can be concluded from the minimum of the capacitance–voltage ($C-V$) characteristics (corresponding to the maximum on the curve $1/C^2=f(V)$ plotted in Fig. 1b). Luminescence was detected at the threshold voltage $V_{\text{th}}\simeq -11$ V. The spectra were recorded at currents $|J|<5$ mA, at which blue diodes do not cease to operate. Radiative recombination served as an indication of generation of minority carriers as a result of impact ionization. The luminescence was visually nonuniform, which is attributable to the microplasma nature of the current.

Breakdown luminescence spectra for three LED's are shown in Fig. 2. Injection luminescence spectra are also shown in this figure. The intensity of the breakdown luminescence was 6–7 orders of magnitude lower than the injection luminescence, as the scales of the ordinate axes show. A wide luminescence band is visible in the region 1.7–3.5 eV. In the high-energy region the edge of the spectrum corresponds roughly to the room-temperature width of the band gap in GaN, $E_g=3.4$ eV.

The shoulder at 3.2 eV corresponds to the energy $E_g-\Delta E_A$, where ΔE_A is the ionization energy of the Mg acceptors. The maxima in the region 2.6–2.8 eV correspond

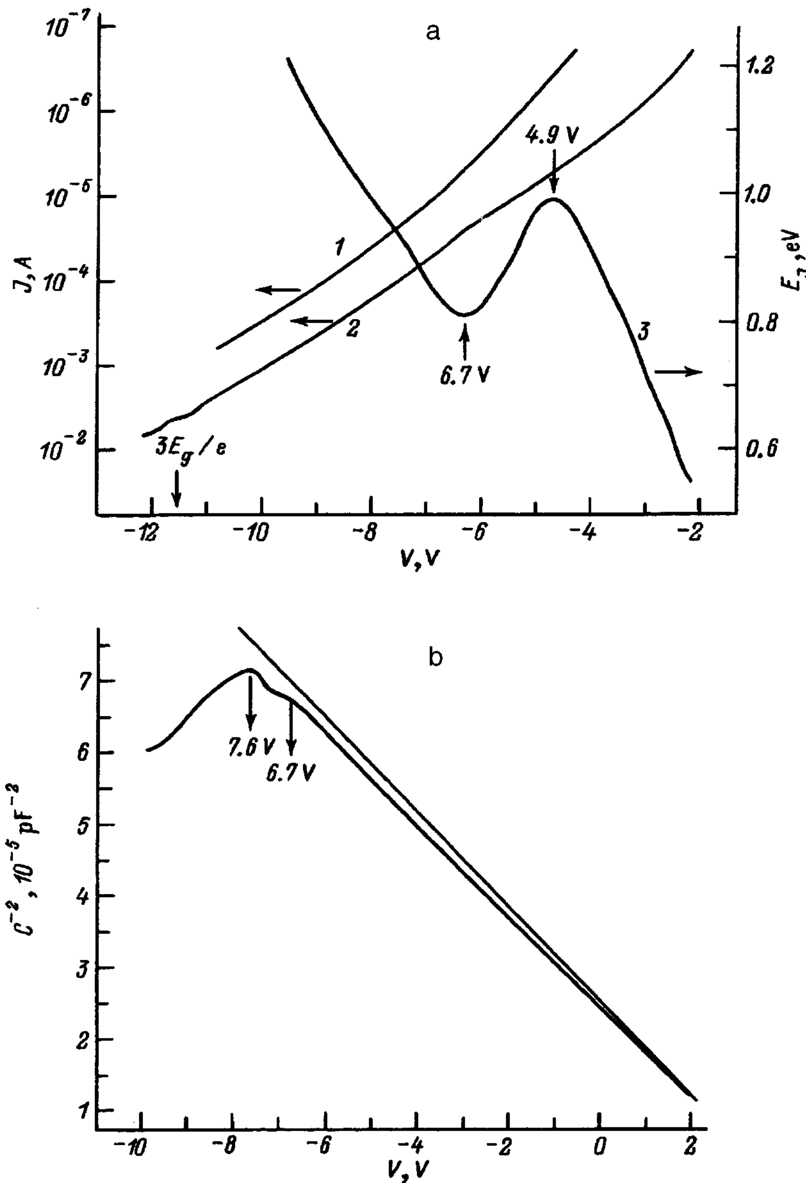

FIG. 1. a—Current–voltage characteristics of a blue LED based on the heterostructure InGaN/AlGaN/GaN (sample 3) with reverse bias, at $T=77$ K (*1*) and 300 K (*2*), and $E_J(V)=dV/d(\ln J)$ at $T=300$ K (*3*). b—capacitance–voltage characteristic of a blue LED based on the heterostructure InGaN/AlGaN/GaN (sample 3) with reverse bias.

to the maxima of the injection luminescence. The wide maxima at 2.2–2.3 eV correspond to the well-known ''yellow band'' in n-GaN, which is associated with donor–acceptor pairs and/or with double donor levels.[12]

The charge density distribution in the lightly doped p-region of the structure was determined from measurements of the dynamic capacitance (this method is described in Ref. 13). The capacitance–voltage characteristics in the coordinates $1/C^2=f(V)$ up to the breakdown have a more complicated form than a linear dependence.

3. DISCUSSION

3.1. To describe the capacitance–voltage and current–voltage characteristics, it is necessary to devise a model of the investigated structures, the charge distribution, and the electric fields. A model energy diagram for these structures with reverse bias is shown in Fig. 3. The InGaN active layer is located between two compensated regions roughly 10 nm in length (from the sides of the n and p regions, respectively). Analysis of the capacitance–voltage measurements indicates the presence of charged walls at the boundaries of the active layer and the compensated regions. The charge concentration in the p region near the heteroboundary is $(1-2)\times10^{18}$ cm^{-3} (thickness 11 nm), and 1×10^{19} cm^{-3} (thickness 1.5 nm) in the n region.

The electric field in the InGaN active layer is large, $\mathcal{E}\simeq10^7$ V/cm; the fields in the adjacent layers $\mathcal{E}\simeq(2-4)\times10^6$ V/cm.

3.2. The tunneling component of the reverse current can be described by the theory of current–voltage characteristics of abrupt, heavily doped p-n-junctions in direct-band semiconductors,[14]

$$J\sim(V-V_k)\exp[B(e|V|/2E_g)],$$

$$B=(\pi/2)^{3/2}(2m_{cv}^*/\hbar^2)^{1/2}(E_g^{3/2}/eE),$$

$$m_{cv}^*=m_c^*m_v^*/(m_c^*+m_v^*), \tag{2}$$

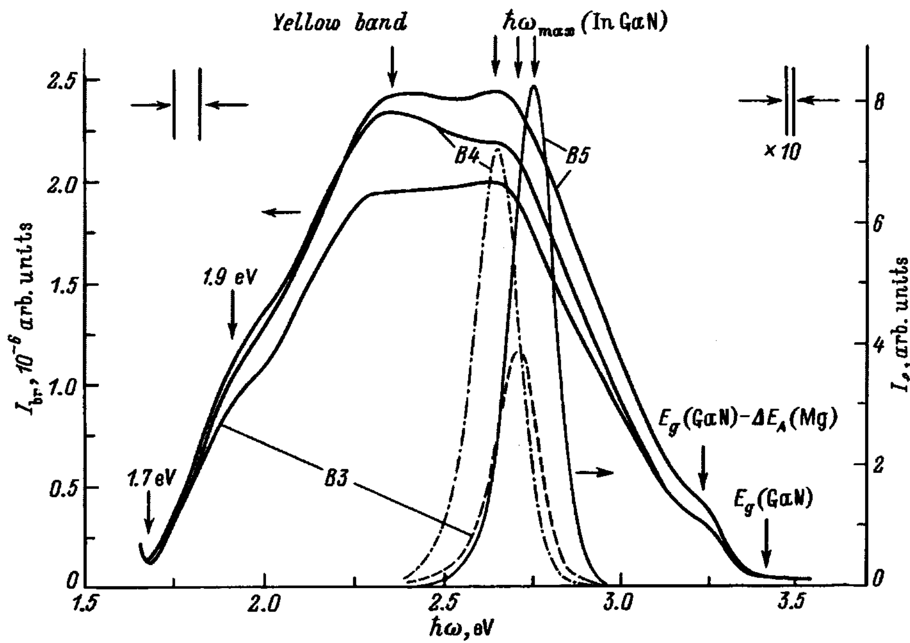

FIG. 2. Luminescence spectra at ionization breakdown (I_{br}) in blue LED's based on InGaN/AlGaN/GaN heterostructures (current $J=-4$ mA, left scale) and injection luminescence spectra (I_f) (current $J=+15$ mA, right scale). B3, B4, B5—different samples.

where V_k is the contact potential difference, E_g is the effective width of the band gap, and m_c^* and m_v^* are the effective masses. Substituting the parameters $m_c^*=0.22m_0$, $m_v^*=0.54m_0$, and $E_g=3.4$ eV, for $V_k=3.2$ eV and $E_J=0.8-0.9$ eV we obtain the following estimate of the electric field in the active region: $E\simeq 2\times 10^7$ V/cm.

3.3. The threshold value of the impact ionization potential is related to the concentration of charged impurities in the p-n junction by the empirical formula[15]

$$V_{\mathrm{th}}=60(E_g/1.1)^{3/2}(N/10^{16})^{-3/4}. \tag{3}$$

Substituting the parameter values $E_g=3.4$ eV and $V_{\mathrm{th}}=11.5$ V, we obtain $N\simeq N_A\simeq 1\times 10^{18}$ cm^{-3}. This value is in agreement with the results of an analysis of the capacitance measurements and an estimate of the electric field distribution.[3,5]

Impact ionization occurs because of electron tunneling from the valence band of the p region into the InGaN active region with subsequent drift into the neighboring quasi-neutral and charged n-regions of the structure. In a strong field they accelerate and acquire an energy $\sim 3E_g$, sufficient for impact ionization.

The impact ionization of the electrons can be assumed to be much larger than the impact ionization of the holes, $\alpha_n \gg \alpha_p$. To estimate α_n, it is necessary to know the mean free path of the electrons λ_{fr} and the effective phonon energy $k\theta$, taking into account the additional high-energy extrema in the conduction band. The extremum between the Λ and M points amounts to 5.5 eV, and at the Γ point, it is 5.6 eV (Ref. 16). It can be assumed that the variations of the current–voltage characteristic slopes at $|V|=5-6$ V are associated with the probability that electrons reach the extrema at the Γ point with large effective masses, and that transitions to the indirect extrema are less probable. The problem of hot electrons in GaN is still far from being solved.

3.4. The low efficiency of breakdown luminescence can be explained by assuming that the electron–hole pairs are separated by the electric field after a time $w/v_T\simeq 10^{-13}-10^{-14}$ s (the thermal velocity of the electrons is $v_T\simeq 2\times 10^7$ cm/s), and only a few electrons reach the outer boundary of the n space charge region and recombine in the neutral region. If the radiative times are on the order of 10^{-9} s, then only a small fraction of the pair can radiatively recombine in the structure.

The spectral maxima in the region 2.2–2.3 eV, which are associated with the radiative recombination of donor–

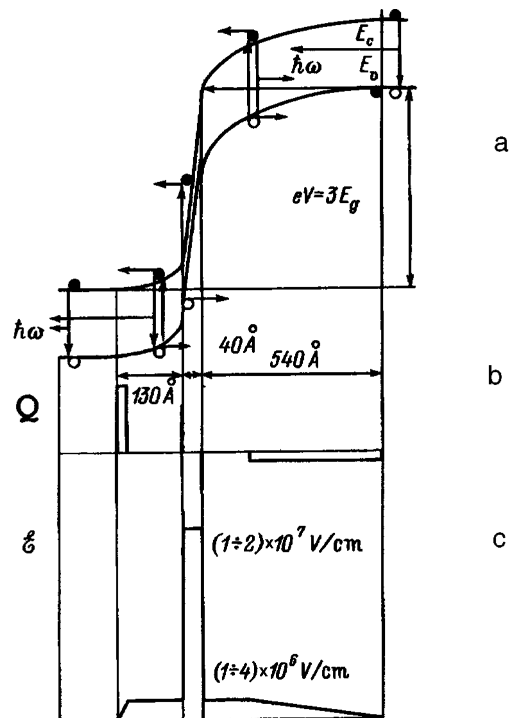

FIG. 3. Model energy diagram (a), distribution of electric charges Q (b) and fields $\mathscr{E}$ (c) in InGaN/AlGaN/GaN-based p-n heterojunctions.

acceptor pairs and/or double donors, were observed earlier in n-GaN (Refs. 12 and 17). This is evidence that a large part of the radiative recombination takes place because of electrons that are created near the n region of the structure. This recombination is a consequence of some structural defects; strong electric fields and impact ionization are concentrated near the defects.

The shoulder at 3.2 eV may be associated with the optical transition to the Mg acceptor. Thus, some of the holes created by impact ionization can recombine with electrons in the p region of the structure.

4. CONCLUSIONS

1. In blue LED's based on InGaN/AlGaN/GaN p-n heterostructures, breakdown luminescence has been observed at reverse biases $|eV| \simeq 11-12 \simeq 3E_g$, which are sufficient for impact ionization, and the intensity is 6–7 orders of magnitude less than the intensity of injection luminescence. The high-energy edge of the spectra corresponds to the width of the GaN band gap (3.4 eV).

2. In the InGaN active layer of InGaN/AlGaN/GaN heterostructures with reverse bias, a strong electric field, up to 10^7 V/cm is created, while the fields in the adjacent layers reach $(2-4)\times 10^6$ V/cm. For reverse biases less than 10 V, the tunneling component of the current predominates and electron tunneling gives rise to impact ionization at biases $\gtrsim 3E_g/e$. The salient points of the current–voltage characteristics near 5–6 V are due to electron transitions to higher-lying extrema of the GaN conduction band.

3. The low efficiency of breakdown luminescence is due to separation of the electrons and holes by the strong electric fields. The wide band of the electroluminescence spectra (2.14–3.4 eV) corresponds to recombination of charge carriers mainly at the outer boundaries of the space charge region.

We wish to thank Dr. Sh. Nakamura for samples which he kindly provided for study at MSU. We also thank K. G. Zolin for help with this work.

[1] S. Nakamura, M. Senoh, N. Iwasa, T. Yamada, and T. Mukai, Jpn. J. Appl. Phys. **34 Pt. 2**, L1332 (1995).
[2] K. G. Zolina, V. E. Kudryashov, A. N. Turkin, A. E. Yunovich, and S. Nakamura, MRTS Int'l. J. Nitride Semicond. Res., 1/11; http://nsr.mij.mrs.org/1/11.
[3] A. N. Kovalev, V. E. Kudryashov, F. I. Manyachin, A. N. Turkin, K. Zolina, A. E. Yunovich, *Abstracts of the 23rd International Symposium on Semiconductor Compounds*, ISCS-23 (St. Peterburg, Russia, 1996), Abstr. 03.P3.04.
[4] K. G. Zolina, V. E. Kudryashov, A. N. Turkin, and A. É. Yunovich, Fiz. Tekh. Poluprovodn. **31**, 1055 (1997) [Semiconductors **31**, 901 (1997)].
[5] A. E. Yunovich, A. N. Kovalev, V. E. Kudryashov, F. I. Manyachin, A. N. Turkin, and K. Zolina, *Abstracts of MRS Fall Meeting* (Boston, 1996), Symp. N, Abstr. N9-37, 347 (1996).
[6] J. I. Pankove, E. A. Miller, and J. E. Berkeyheiser, J. Lumin. **5**, 84 (1972); **6**, 482 (1973).
[7] J. I. Pankove and M. Lampert, Phys. Rev. Lett. **33**, 361 (1974).
[8] L. N. Mikhaĭlov, Yu. K. Shalabutov, M. D. Shagalova, V. G. Sidorov, and L. N. Vasilishchev, Fiz. Tekh. Poluprovodn. **9**, 1808 (1975) [Sov. Phys. Semicond. **9**, 1189 (1975)].
[9] V. A. Dmitriev, N. I. Kuznetsov, K. G. Irvine, and C. H. Carter, Jr., *MRS Symposium Proceedings*, Vol. **395, p.** 909 (1996).
[10] R. P. Vaudo, I. D. Goepfert, T. D. Moustakas, D. M. Beyea, T. J. Frey, and K. Meehan, J. Appl. Phys. **79**, 2779 (1996).
[11] R. J. Molnar, R. Singh, and T. D. Moustakas, Appl. Phys. Lett. **66**, 268 (1995).
[12] D. M. Hoffmann, D. Kovalev, G. Steude, D. Volm, B. K. Meyer, C. Xavier, T. Monteiro, E. Pereira, E. N. Mokhov, H. Amano, and I. Akasaki, *MRS Symposium Proceedings*, Vol. **395, p.** 619 (1996).
[13] F. I. Manyakhin, Izmer. Tekh. **11**, 49 (1996).
[14] G. E. Pikus, *Theory of Semiconductor Devices* [in Russian] (Nauka, Moscow, 1965), p. 347.
[15] S. M. Sze, *Physics of Semiconductor Devices* (Wiley, New York, 1969) [Vol. 1, p. 111 of the Russian edition (1984)].
[16] W. E. Carlos, J. A. Freitas, M. Azif Khan, D. T. Olson, and J. N. Kuznya, Phys. Rev. B **48**, 17 878 (1993).
[17] F. A. Ponce, MRS Bull. **22**, 51 (1997).

Translated by Paul F. Schippnick

Calculation of the Schottky barrier height at the early stage of formation of the (silicon carbide)-(metallic submonolayer) contact

S. Yu. Davydov, A. A. Lebedev, and S. K. Tikhonov

A. F. Ioffe Physicotechnical Institute, Russian Academy of Sciences, 194021 St. Petersburg, Russia

(Submitted June 5, 1997; accepted for publication June 24, 1997)
Fiz. Tekh. Poluprovodn. **32**, 68–71 (January 1998)

The position of the local and quasi-local states of metal atoms (alkali metals, group-III metals, the copper group) adsorbed on the surface of $6H$-SiC are calculated within the framework of the extended Anderson–Halstane model of the semiconductor density of states. The results of these calculations are compared with the experimental data on Schottky barriers. © *1998 American Institute of Physics.* [S1063-7826(98)01801-8]

The presence in SiC of a wide band gap Δ, whose magnitude for different polytypes can vary from 2.4 eV (type $3C$) to 3.33 eV (type $2H$),[1] makes this material very attractive in the design of high-temperature, high-frequency, and high-power microelectronic devices.[2] It is therefore not surprising that in recent years interest in SiC–metal film contacts has grown, both among experimenters[3–8] and theoreticians.[7,9–11]

Recently, in a study of the formation of the Schottky barrier at a metal–semiconductor contact, Davydov[12] proposed an approach based on a generalization of a model of the density of states of a semiconductor, ρ, proposed by Halstane and Anderson.[13] The initial model[13] is extraordinarily simple

$$\rho(\omega)=\begin{cases}\rho & \text{for} \quad |\omega|>\Delta/2,\\ 0 & \text{for} \quad |\omega|\leq\Delta/2,\end{cases} \tag{1}$$

where $\rho=$const and ω is the energy. Here and in what follows, it is assumed that the zero energy coincides with the center of the band gap. We call this model of the density of states the ''defect-free'' model (DFM). If impurity states or states on defects are present inside the gap, then the expression for $\rho(\omega)$ must be changed accordingly. Thus, for example, in Ref. 12 it was assumed that at the center of the gap there exists a band of defect states of width $\delta<\Delta$ with density of states γ. We call this model the ''defect'' model (DM). General properties of the DFM and DM (position of the local and quasilocal levels located in the region of the gap, and their occupancy as functions of the model parameters) were investigated in Ref. 12, and the local states of atoms of alkali metals and metals of the Cu group and group III on a GaAs surface were calculated within the framework of the DFM. Comparison of the calculated results with experiment shows completely satisfactory agreement. In the present paper we consider adsorption of the same atoms on SiC.

All expressions needed for calculation are given in Ref. 12, so we do not repeat them here. Let us discuss only the parameters of the model. We consider adsorption on the $6H$-SiC polytype. We assume the width of the band gap Δ to be equal to 3.06 eV and the electron affinity χ to be equal to 4.4 eV (Ref. 8). For the DM we take $\delta/\Delta=0.2$ and $\gamma=\rho$. The position of the energy level of the adsorbed atom (adatom) E_a relative to the center of the gap is

$$E_a=-I+(\chi+\Delta/2), \tag{2}$$

where I is the ionization potential of the atom, whose values we take from Ref. 14. The half-width of the quasilevel of adatom $\Gamma=\pi\rho V^2$, where V is the matrix element describing

TABLE I. Input parameters and results of calculations of the positions of the local states and their filling for the intrinsic semiconductor $6H$-SiC ($E_F=0$) in relative units ($\Delta=1$, $\delta=0.2$).

Na	K	Rb	Cs	Ag	Au	Cu	Al	Ga	In		
E_a:		0.24	0.52	0.57	0.67	−0.54	−1.08	−0.59	−0.02	−0.02	0.05
Γ:		0.39	0.29	0.22	0.19	0.62	0.69	0.79	1.06	1.46	0.82
	ω^*	0.16	0.36	0.41	0.47	−0.29	−0.46	−0.28	−0.01	−0.01	0.02
DFM	n_b	0.08	0.04	0.03	0.02	0.15	0.23	0.17	0.14	0.17	0.12
	n_a	0.08	0.04	0.03	0.02	0.62	0.39	0.58	0.57	0.52	0.61
	$-\omega_1^*$	0.11	0.10	0.10	0.10	0.34	0.47	0.34	0.18	0.19	0.16
	ω_i^*	−0.09	−0.10	−0.10	−0.10	0.10	0.10	0.10	0	0	−0.01
DM	ω_2^*	0.23	0.23	0.43	0.48	0.10	0.10	0.10	0.18	0.18	0.18
	n_b	0.06	0.04	0.03	0.03	0.15	0.25	0.18	0.16	0.19	0.13
	n_i	0.07	0.03	0.02	0.01	0.03	0.01	0.02	0.03	0.02	0.04
	n_a	0.21	0.07	0.05	0.04	0.53	0.38	0.50	0.37	0.36	0.34

Remark. DFM—defect-free model, DM—defect model; E_a and n_a are the energy position and degree of filling of the level of the adsorbed atom (2); $\omega*$, ω_1^*, and ω_2^* are the energies of the local levels, ω_i^* is the energy of the quasilocal level; $n_a=n_b+n_1$ in the DFM, $n_a=n_b+n_1+n_i$ in the DM, where n_b and n_i are the contributions of the valence band and the defect band, n_1 is the contribution of the local states with energy $\omega*$ in the DFM and with energy ω_1^* in the DM.

 © 1998 American Institute of Physics

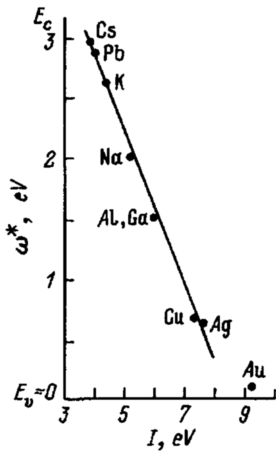

FIG. 1. Position of the local levels of the adatoms, ω^* relative to the top of the valence band of $6H$-SiC, plotted as a function of the ionization potential I (E_v is the top value of the valence band, E_c is the bottom value of the conduction band), calculated in the defect-free model.

the interaction of the metal atom with the semiconductor (for details, see Ref. 12), can be estimated by the expression:

$$\Gamma = \frac{\pi}{2} t_a, \tag{3}$$

where t_a is the matrix element of the interaction of nearest neighbors for atoms in the bulk of the semiconductor, which, as in Ref. 12, we equate to the corresponding universal Harrison matrix element.[15,16] The input parameters and calculated results are presented in Table I in relative units ($\Delta = 1$).

Let us first discuss the calculated results for the DFM. Figure 1 plots the results of calculation of the position of the local levels of the adatom in the band gap (for convenience the quantity ω^* is given in eV reckoned from the top of the valence band of $6H$-SiC). It follows from this graph that the dependence of ω^* on the ionization potential of the adatom, I, is linear except for Au, which is attributable to the very large value of $I = 9.23$ eV for Au, which differs sharply from the ionization potential of the previous element, $I_{\mathrm{Ag}} = 7.58$ eV. Figure 2 plots the experimental values of the Schottky barrier height Φ_{Bp} taken from Refs. 3–7, from

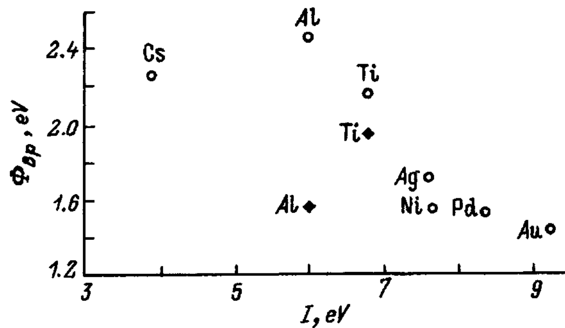

FIG. 2. Height of the Schottky barrier Φ_{Bp} for $p-6H$-SiC, plotted as a function of the ionization potential of the adatom, I, (according to the data of Refs. 3–7 for adsorption on Si; results for Al and Ti, denoted by rhombuses, correspond to an annealed system).

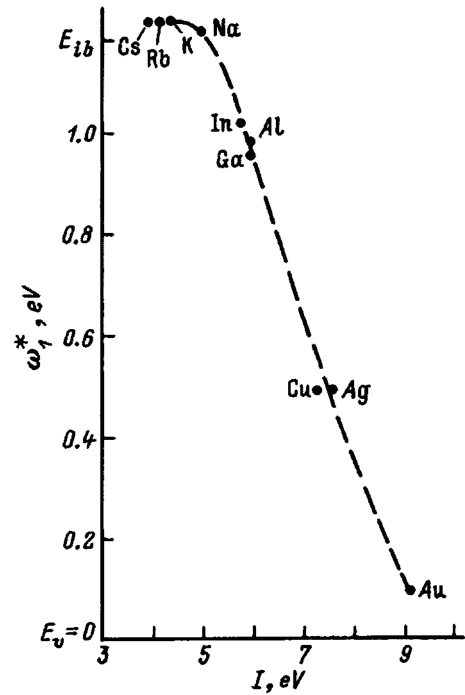

FIG. 3. Position of the local levels of the adatoms, ω_1^*, relative to the top of the valence band, plotted as a function of the ionization potential I, calculated in the defect model; E_{ib} is the bottom value of the defect band.

which it is evident that Φ_{Bp} decreases with growth of I. Unfortunately, it is possible to directly compare the experimental results with the calculation only for Cs, Ag, Au, and Al. For these adatoms the dependence $\Phi_{Bp}(I)$ is also nearly linear (if we draw a straight line from Cs to Au, then the point corresponding to Al is located just between the values

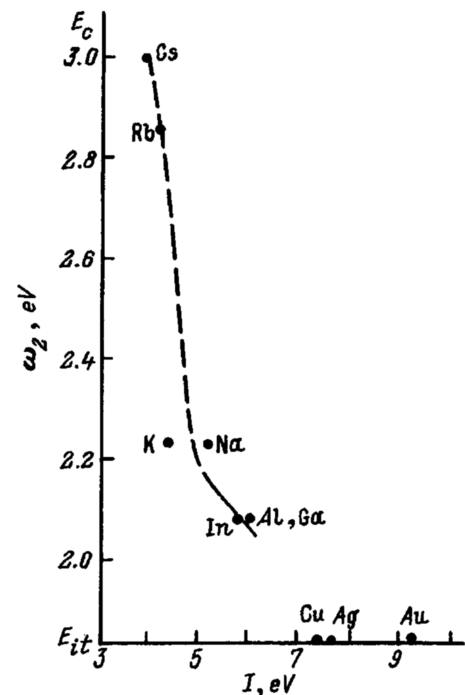

FIG. 4. Same as in Fig. 3, but for the energy level ω_2^*; E_{it} is the top value of the defect band.

of Φ_{Bp} for the annealed and unannealed systems), but it is shallower than the calculated dependence $\omega^*(I)$. (Physical reasons for comparing the depth of the local levels of the adatom in the band gap and the height of the Schottky barrier forming for small coatings are discussed in Refs. 12, 17–20).

The table also lists the occupation numbers of the adatoms, n_a, and separately the contribution to n_a from the valence band, n_b (for details, see Ref. 12). The quantity n_a is equal to n_0+n_1, where n_1 is the contribution from the *filled* local state, which for the case of an intrinsic semiconductor (Fermi energy $E_F=0$) is nonzero for atoms of the group Cu, Al, and Ga ($\omega^*<0$). In the remaining cases the local states are located above the center of the gap and do not contribute to n_a. Note that we fix the position of the Fermi level at the center of the gap only in the calculation of the occupation numbers. In the comparison of the calculated values of ω^* with the results of the Schottky barrier (Φ_{Bp}) experiment it is assumed, as in Refs. 12, 17–20, that for certain (very small) coatings the Fermi level is stabilized in the region of energies corresponding to the energy of the local state (pinning).

Let us turn now to the results for the defect model, setting $\delta/\Delta=0.2$ (the ratio of the width of the defect band to the width of the band gap). Results of calculations of the positions of the local levels $\omega^*_{1,2}$ are plotted in Figs. 3 and 4. Here there are two branches of local states, lying above and below the defect band. In the case of the defect model, as in the foregoing case of the defect-free model, a falling dependence of $\omega^*_{1,2}(I)$ is observed. For the defect model ''sticking'' of the levels of a specific group of adatoms (alkali metals for the lower branch and metals of the Cu group for the upper branch) to the edge of the defect band is characteristic. Note, however, that such ''sticking'' levels can be an artifact of theory, which arises as a result of the step-like approximation of the density of states of the semiconductor spectrum (see Ref. 12).

In both the defect and defect-free cases the population of the adatoms of the alkali-metal adatoms is small, whereas for metals of group-III and the Cu group the occupation numbers $n_a \cong 0.5$. Consequently, for all the cases under consideration, the adatoms enter as donors. Calculation of the occupation numbers of adatoms is of interest in connection with the concentration dependences of the Schottky barrier height, which we intend to address in a future paper.

In conclusion, we note that the completely different approaches to the calculation of the Schottky barrier height which we used in Refs. 9 and 10 and in this paper, lead to qualitatively the same results.

This work was carried out with partial support of the University of Arizona.

[1] V. I. Gavrilenko, A. M. Grekhov, D. V. Korbutyak, and V. G. Litovchenko, *Optical Properties of Semiconductors: Handbook* [in Russian] (Naukova Dumka, Kiev, 1987).

[2] *Proceedings of the Fifth Conference on Silicon Carbide and Related Materials*, edited by M. G. Spencer *et al.* [Inst. Phys. Conf. Ser., No. 137 (Bristol–Philadelphia, 1993)].

[3] J. R. Waldrop and R. N. Grant, Appl. Phys. Lett. **56**, 557 (1990).

[4] J. R. Waldrop, R. N. Grant, Y. C. Wang, and R. F. Davis, J. Appl. Phys. **72**, 4757 (1992).

[5] J. R. Waldrop and R. N. Grant, Appl. Phys. Lett. **62**, 2685 (1993).

[6] J. R. Waldrop, J. Appl. Phys. **75**, 4548 (1975).

[7] V. van Elsbergen, T. U. Kampen, and W. Mönch, J. Appl. Phys. **79**, 316 (1995).

[8] A. N. Andreev, A. A. Lebedev, and M. G. Rastegaeva, F. M. Snegov, A. L. Syrkin, V. E. Chelnokov, and L. N. Shestopalov, Fiz. Tekh. Poluprovodn. **29**, 1828 (1995) [Semiconductors **29**, 955 (1995)].

[9] S. Yu. Davydov and S. K. Tikhonov, Fiz. Tverd. Tela **37**, 2221 (1995) [Phys. Solid State **37**, 1212 (1995)].

[10] S. Yu. Davydov, A. A. Lebedev, and S. K. Tikhonov, Fiz. Tekh. Poluprovodn. **30**, 597 (1996) [Semiconductors **30**, 640 (1996)].

[11] W. Mönch, in *Control of Semiconductor Interfaces*, edited by I. Ohdomari *et al.* (Elsevier, Amsterdam, 1994), p. 169.

[12] S. Yu. Davydov, Fiz. Tekh. Poluprovodn. **31**, 1236 (1997) [Semiconductors **31**, 1062 (1997)].

[13] F. D. M. Halstane and P. W. Anderson, Phys. Rev. B **13**, 2553 (1976).

[14] *Handbook of Physical Quantities*, edited by I. S. Grigor'ev and E. Z. Meĭlizov (Energoatomizdat, Moscow, 1991).

[15] W. A. Harrison, *Electronic Structure and Properties of Solids* [Russian translation] (Mir, Moscow, 1983).

[16] W. A. Harrison, Phys. Rev. B **27**, 3592 (1983).

[17] W. Mönch, Europhys. Lett. **7**, 275 (1988).

[18] W. Mönch, Rep. Prog. Phys. **53**, 221 (1990).

[19] J. E. Klepeis and W. A. Harrison, J. Vac. Sci. Technol. B **6**, 1315 (1988).

[20] J. E. Klepeis and W. A. Harrison, Phys. Rev. B **40**, 5810 (1989).

Translated by Paul F. Schippnick

Photoelectric properties of *n*-CdS/*p*-InP heterojunctions

V. M. Botnaryuk, L. V. Gorchak, and I. I. Diaconu

Moldovan State University, 277069 Kishinev, Moldova

V. Yu. Rud'

St. Petersburg State Technical University, 195251 St. Petersburg, Russia

Yu. V. Rud'

A. F. Ioffe Physicotechnical Institute, Russian Academy of Sciences, 194021 St. Petersburg, Russia
(Submitted July 24, 1996; accepted for publication June 10, 1997)
Fiz. Tekh. Poluprovodn. **32**, 72–77 (January 1998)

The polarization method for studying photoactive absorption is used to investigate the photoconversion processes in CdS/InP heterojunctions as a function of the orientation of the indium phosphide substrate. The results of these investigations demonstrate the sensitivity of the photoelectric processes to several factors, including the crystallographic orientation of the p-type InP substrate and the optical quality of the CdS layer. The induced photopleochroism coefficient of these heterojunctions increases proportionally to the square of the angle of incidence ($P_I \sim \Theta^2$). Such CdS/InP heterojunctions can be employed as polarization-photosensitive devices. © *1998 American Institute of Physics.* [S1063-7826(98)02001-8]

The photosensitivity of heterojunction structures based on direct-gap semiconductor compounds, viz., indium phosphide [$E_g \approx 1.26$ eV (Refs. 1 and 2)] and cadmium sulfide [$E_g \approx 2.53$ eV (Refs. 3 and 4)] have attracted the attention of researchers for a long time in regard to achieving highly efficient conversion of the energy of solar radiation into electrical energy.[5–10] The binary compounds InP and CdS have different types of crystal structures (under normal conditions InP has a sphalerite structure, and CdS has a wurtzite structure[3,4,9]) and exhibit a high degree of lattice mismatch Δa: 4.7% when the cubic modifications are joined, 13.95% and 34.67% when a wurtzitic phase of CdS is joined to InP in different crystallographic directions at $T = 300$ K. Despite the unfavorable matching conditions observed when n-type CdS layers are deposited on single-crystal InP substrates, a solar radiation conversion coefficient as high as 18% along with high radiation stability has been achieved in recent years in such heterojunctions on areas ≈ 0.5 cm^2 (Ref. 10). In this paper we present the results of the first experimental studies of the photoelectric properties of heterojunctions obtained by depositing n-type CdS layers on differently oriented indium phosphide substrates with p-type conduction.

EXPERIMENTAL METHOD

Layers of n-type CdS were deposited on single-crystal p-InP substrates in the form of wafers oriented in the (100) and (111) planes. In the latter case the layers were deposited on plane A or B. This enabled us to subsequently evaluate the role of the polarity of the sphalerite lattice[1] in the deposition processes. The concentration of free holes in the zinc-doped InP substrates was $\approx 3 \times 10^{18} - 4 \times 10^{18}$ cm^{-3} at $T = 300$ K, while the regime used to deposit the CdS layers provided an electron concentration $\approx 10^{18} - 10^{19}$ cm^{-3} in them at $T = 300$ K. The CdS layers were deposited by the vapor-phase method in a flow-through system with the use of hydrogen at a temperature in the range 700−730 °C. The time of the process usually did not exceed 60 min. It was established for identical technological parameters of the CdS growth process that changes in the orientation of the InP substrates from (100) to (111) reproducibly resulted in reduction of the thickness of the layers deposited. For example, the n-CdS layers on the (100) plane usually had a thickness of 4–5 μm after a deposition time of ≈ 30 min at $\approx 700 - 750$ °C, while the thickness of the layers deposited on the (111)A and (111)B planes did not exceed 0.5–1 μm. This attests to a decrease in the deposition rate as a result of alteration of only the crystallographic orientation of the substrates, while the influence of their polarity on the thickness of the layers has not yet been mentioned in the literature. It should also be stressed that the outer plane of the CdS layers on InP(111) substrates was highly perfect, while the surface of the CdS layers on InP(100) substrates was generally rough and was characterized by diffuse reflections.

After the n-CdS layers were deposited, the free surface of the p-InP substrates was covered by a continuous layer of Ag, which played the role of an ohmic contact, by thermal sputtering in a vacuum. A contact grid was deposited on the outer plane of the n-CdS layers by thermally sputtering indium through a mask. Then the n-CdS/p-InP structures were mounted on a Fedorov stage, which permitted variation of the spatial orientation of the photoreceptive layer of the heterojunction relative to a beam of incident natural or linearly polarized radiation to an angular accuracy no poorer than 30′.

The current-voltage characteristics, as well as the angular and spectral dependences of the relative photoconversion quantum efficiency η, were investigated on the n-CdS/p-InP structures obtained with mean dimensions of the n-CdS photoreceptive plane $\approx 5 \times 5$ mm^2.

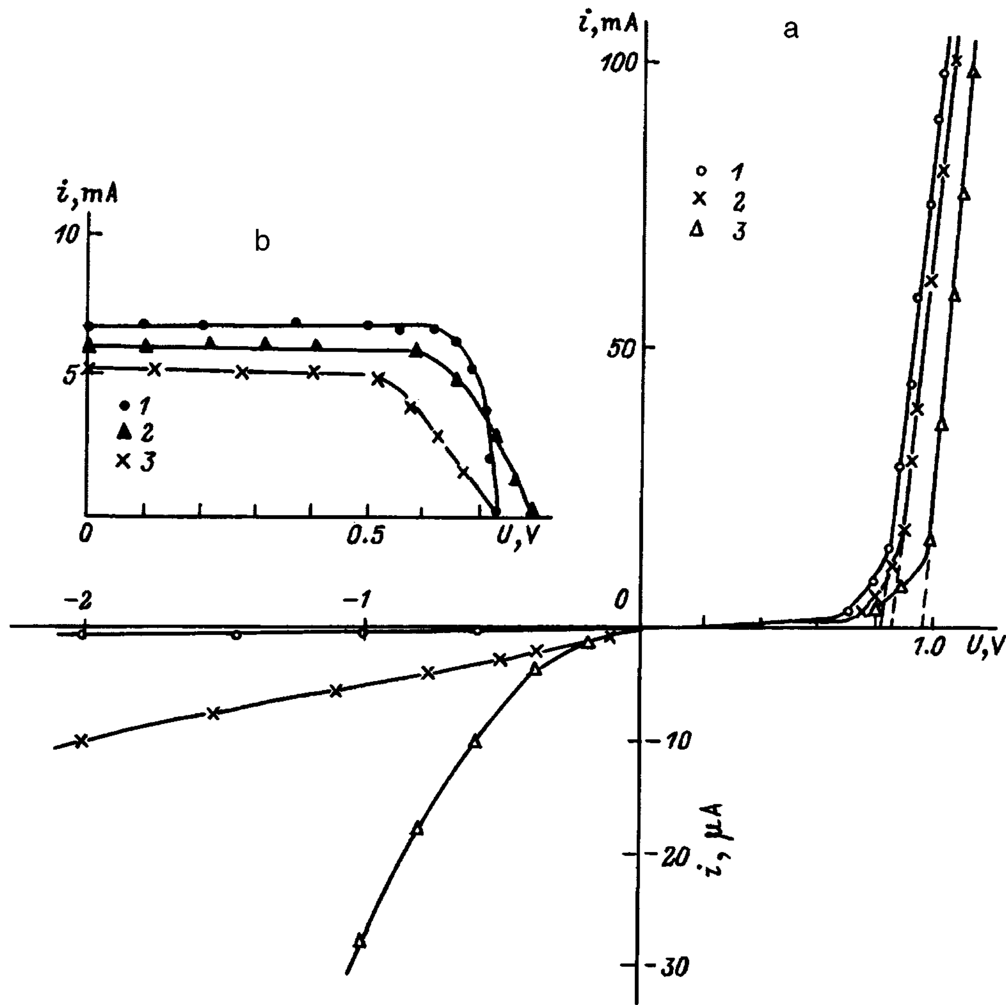

FIG. 1. Stationary current-voltage (a) and load (b) characteristics of n-CdS/p-InP structures at $T=300$ K as a function of the orientation of the InP substrate: *1* — (100), *2* — (111) B, *3* — (111) A.

EXPERIMENTAL RESULTS AND DISCUSSION

1. The stationary and load current-voltage characteristics for typical heterostructures obtained by depositing n-CdS layers on different crystallographic planes of InP are shown in Fig. 1a, and their photoelectric parameters are presented in Table I. Under a forward bias greater than the cutoff voltage $U>U_0$ the current in the heterojunctions varies with the voltage according to the linear law

$$I=\frac{1}{R_0}(U-U_0),$$

where R_0 is the residual resistance. It can be seen from Table I that the minimum value of R_0 is provided when n-CdS layers are deposited on the InP(100) plane. The residual resistance was found to be dependent on the polarity of the InP(111) plane and was greatest when the (111)A orientation was used. The values of the cutoff voltage U_0 in these heterojunctions are in satisfactory agreement with the saturation photovoltage U_{xx}^{∞} and therefore can be taken as the values of the contact potential difference φ_B in these heterojunctions. No clear-cut relationship between φ_B and the crystallographic orientation of the substrates was established. As follows from Table I, the maximum short-circuit current i_{sc}, fill factor β of the load characteristics (Fig. 1), and current photosensitivity S_i are attained when CdS layers are deposited on the InP (100) plane. The minimum reverse current i_r is ensured specifically in this deposition geometry (Fig. 1, Table I). When we go over to the deposition of CdS on the

TABLE I. Photoelectric properties of n-CdS/p-InP structures at $T=300$ K.

Orientation of p-InP	(100)	(111) A	(111) B
d_{InP}, mm	0.4	0.4	0.4
d_{CdS}, μm	4	1	1
R_0, Ω	11	59	13
U_0, V	0.82	0.85	0.96
i_r, μA ($U=1$ V)	0.5	26	5
i_{sc}, mA ($L=20$ mW/cm^2)	14	10	9
U_{xx}^{∞}, V ($L=20$ mW/cm^2)	0.74	0.8	0.75
β ($L=20$ mW/cm^2)	0.83	0.62	0.75
S_i, mA/W	45	10	20
$\delta_{1/2}$, eV	1.09	0.93	1.2
$\Delta\hbar\omega_m$, eV	1.5–1.85	1.5–1.6	1.55–1.6
$i_{65^\circ}^p/i_{0^\circ}^p$		1.2	1.3

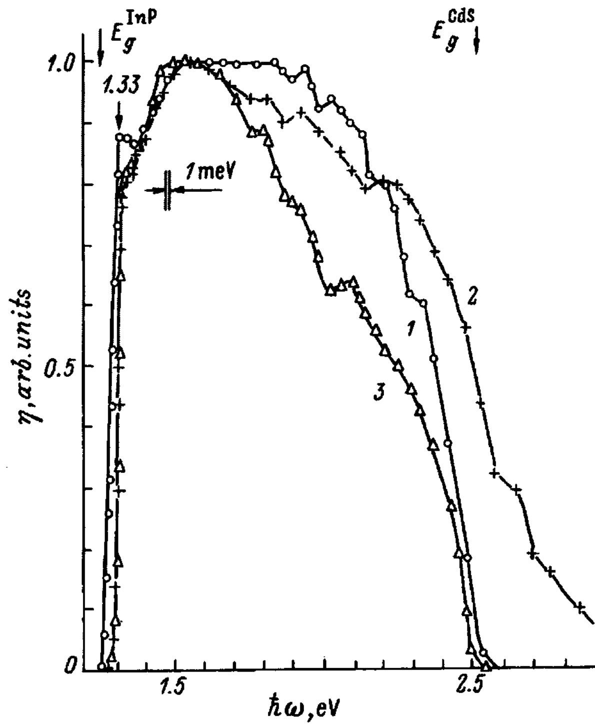

FIG. 2. Spectral dependence of the relative photoconversion quantum efficiency of n-CdS/p-InP structures at $T=300$ K. Illumination by natural radiation on the CdS side. Crystallographic orientation of the substrate: *1* — (100), *2* — (111) B, *3* — (111) A. Thickness of the CdS layer, μm: *1* — 4, *2*, *3* — 1; $\Theta=0°$.

InP (111) plane, there is an increase in the reverse current, which is most pronounced for the InP (111)A substrates. The increase in the reverse currents, as well as the lowering of the fill factor and the current sensitivity, attest to deterioration of the quality of the heterojunction with respect to photosensitivity processes. It should also be stressed that the dependence of the photoelectric properties of the heterojunctions on the polarity of the InP (111) plane discovered in the case of deposition on this plane can be an indication of the higher chemical activity of the (111) A plane with dangling indium bonds, which cause an increase in the residual resistance and lowering of the current photosensitivity of the heterojunctions.

2. The spectral dependences of η calculated as the ratio of the short-circuit photocurrent to the number of incident quanta of unpolarized radiation for typical heterojunctions with various crystallographic orientations of the InP substrates are presented in Fig. 2. It is seen that the photosensitivity of these heterojunctions is observed in the range between the gap widths E_g^{InP} and E_g^{CdS}. The appearance of the ''window effect'' reflects the formation of heterojunctions that are sharp and fairly perfect with respect to photoconversion processes. The long-wavelength photosensitivity limit is virtually identical for all of them, since it is determined by the beginning of the interband absorption in indium phosphide at $\hbar\omega > 1.26$ eV (Fig. 2). The short-wavelength limit of η in the heterojunctions obtained is adjacent to E_g^{CdS} and is caused by localization of the photoexcitation region at the surface of the n-CdS layer, which results in removal of this region from the space-charge layer and ultimately in a drop in η. It also follows from Fig. 2 that the spectral photosensitivity range for the heterojunctions investigated is determined only by the nature of the contacting semiconductors, while the variation of the crystallographic orientation of the InP substrates is manifested, perhaps, only in the spectral contour of the photoconversion quantum efficiency at $\hbar\omega > 1.5$ eV, at which the absorption of radiation is localized in the vicinity of the heterojunction on the side of the CdS layer. The earliest short-wavelength drop and the lowest half-width of the $\eta(\hbar\omega)$ spectra at half-maximum $\delta_{1/2} \approx 0.93$ eV are obtained in the heterojunctions (see Table I) with (111) A substrates, while an increase in the short-wavelength photosensitivity appears when we go over to substrates with the (111) B and (100) orientations. This finding can be attributed primarily to improvement of the heterojunction. The broadest maximum photosensitivity range $\Delta\hbar\omega_m$, which extends from 1.5 to 1.9 eV (see Table I), is characteristic of the heterojunctions based on substrates with the (100) orientation, attesting to the highest perfection of these structures. As can be seen from Fig. 2, when CdS layers are grown on InP wafers with the (111) orientation, preference should be given to the growth of CdS layers on InP with dangling bonds of the phosphorus atoms on the surface to improve the photosensitivity in the spectral range $\hbar\omega > 1.6$ eV.

3. When the heterojunctions obtained were illuminated by linearly polarized radiation along a normal to the n-CdS receptive plane, their short-circuit photocurrent was independent of the spatial orientation of the electric vector **E** of the light wave; therefore, when the angle of incidence $\Theta=0°$, the polarization indicatrix of the photocurrent i_φ degenerates into a straight line (Fig. 3, curve *1*). As soon as the angle of incidence of the linearly polarized radiation differs from $\Theta=0°$ (Fig. 3, curves *2* and *3*), a periodic dependence of the photocurrent on the azimuthal angle φ between **E** and the plane of incidence (PI) of the linearly polarized radiation appears and obeys the relation

$$i_\varphi = i^p \cos^2\varphi + i^s \sin^2\varphi,$$

where i^p and i^s are the photocurrents in the $\mathbf{E}\parallel$PI and $\mathbf{E}\perp$PI polarizations, respectively. The inequality $i^p > i^s$ is maintained the entire photosensitivity range of the heterojunctions with different crystallographic orientations of the InP substrates; here the ratio i^p/i^s increases with increasing Θ at $\hbar\omega=$const (Fig. 3).

The lack of a dependence of i_φ on the azimuthal angle φ for $\Theta=0°$ allows us to draw the important conclusion that the photoactive absorption in the heterojunctions obtained here remains isotropic even when the crystallographic orientation of the InP substrate is varied. Passage to oblique incidence of the linearly polarized radiation gives rise to induced photopleochroism,[11]

$$P_I = \frac{i^p - i^s}{i^p + i^s},$$

in the heterojunctions obtained, which increases with the angle of incidence according to a $P \sim \Theta^2$ law (Fig. 4). These dependences are linearized in $\sqrt{P_I}$-versus-Θ coordinates, are

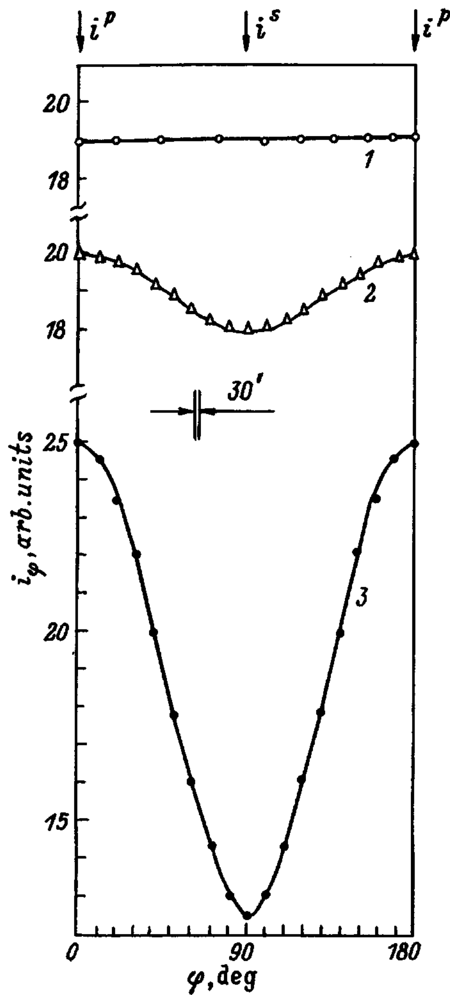

FIG. 3. Polarization indicatrices of the short-circuit photocurrent of an n-CdS/p-InP structure at $T = 300$ K as a function of the angle of incidence of linearly polarized radiation onto the CdS receptive plane. $\hbar\omega = 1.4$ eV; Θ, deg: *1* — 0, *2* — 30, *3* — 70.

identical over the entire photosensitivity range of the heterojunctions, and do not display any sensitivity to changes in the orientation of the InP substrate. These findings are attributed to the fact that under oblique incidence of the linearly polarized radiation the induced photopleochroism is determined mainly by the refractive index n of the semiconductor on which the radiation impinges.[11,12] In accordance with Ref. 12, the experimental $P_I(\Theta)$ curves give $n \approx 2.5$ for the heterojunctions obtained here, which coincides with the known value of this parameter for CdS.[13] This allows us to assume that the photoelectric anisotropy[11] of the heterojunctions induced by oblique incidence of the linearly polarized radiation does not depend on the orientation of the InP substrate and is determined entirely by the nature of the CdS layer growing on the substrate.

At the same time, as follows from Fig. 4, the photocurrent of the heterojunctions in linearly polarized radiation exhibited an explicit dependence on the quality of the outer surface of the CdS layer, through which the radiation enters these structures. For specularly smooth n-CdS, which can be grown reproducibly on InP substrates oriented in the (111) plane, the angular dependences of the photocurrents $i^p(\Theta)$ and $i^s(\Theta)$ are consistent with the Fresnel relations for the amplitude transmission coefficients of linearly polarized radiation through the air–CdS interface.[14] More specifically, i^s decreases monotonically with increasing Θ, while i^p at first increases, then passes through a maximum near the pseudo-Brewster reflection angle, and only then begins to decrease. For the heterojunctions with the (111) A and (111) B substrate orientations there is a distinct maximum on the $i^p(\Theta)$ curves in the vicinity of $\Theta \approx 65°$ (Figs. 4a and 4b), and the photocurrent ratio $i^p_{65°}/i^p_{0°}$ reaches 1.2–1.3 (see Table I), attesting to a significant decrease in the losses due to reflection in the $\mathbf{E}\|$PI orientation. This decrease was greatest in the heterojunctions with substrates having the (111) B crystallographic orientation, pointing out again the higher optical quality of the CdS layers grown specifically in this geometry.

In the case of the heterojunctions with the (100) substrate orientation, as is seen from Fig. 4c, the photocurrents i^p and i^s maintained the dependence on the polarization expressed by the inequality $i^p > i^s$ and displayed a monotonic decrease at $\Theta > 0°$. Such a phenomenon was previously noted in polarization studies of the photosensitivity of GaP/Si structures and was attributed to deterioration of the optical quality of the GaP layers.[15] On this basis the character of the $i^p(\Theta)$ curves for the heterostructures on InP (100) substrates can also be attributed to deterioration of the optical quality of the surface of the CdS layer when such a substrate orientation is used. Therefore, polarization studies of the photocurrent of CdS/InP heterojunctions can find application as a new, quick, diagnostic test of the optical quality of the receptive surface of finished photoconverters.

4. In the case of oblique incidence of the linearly polarized radiation, the η^p and η^s spectral contours maintain the principal features of the photoactive absorption of such heterojunctions when they are illuminated by unpolarized radiation (Fig. 1). The transition from $\mathbf{E}\|$PI to $\mathbf{E}\perp$PI polarization causes parallel descent of the entire η^s curve relative to η^p in accordance with the polarization dependence of the amplitude transmission coefficients of a light wave through an air–CdS layer interface; here the relation $\eta^p > \eta^s$ is satisfied over the entire sensitivity range at $\Theta = \text{const}$.

The spectral dependences of the polarization difference in the photoconversion quantum efficiency $\Delta\eta = \eta^p - \eta^s$ clearly display a window effect with respect to the polarization photosensitivity. In fact, as is seen in Fig. 5, in heterojunctions with different orientations of the InP substrate $\Delta\eta \neq 0$ in the range between E_g^{InP} and E_g^{CdS}. The observed differences in the spectral contour of $\Delta\eta$ can be attributed to features of the photogeneration and separation of nonequilibrium charge carriers in these heterojunctions. Variation of the substrate orientation then permits regulation of the spectral distribution of $\Delta\eta$. For example, to ensure maximum polarization quantum efficiency in the range $\hbar\omega > 1.6$ eV, preference should be given to the deposition of CdS layers on InP substrates with the (111) B orientation.

The induced photopleochroism coefficient in CdS/InP heterojunctions is nearly constant in the entire photosensitivity range (Fig. 5), in agreement with the conclusions in Refs. 11. In addition, as can be seen from Fig. 5, the value of P_I in the heterojunctions obtained is insensitive to changes in the

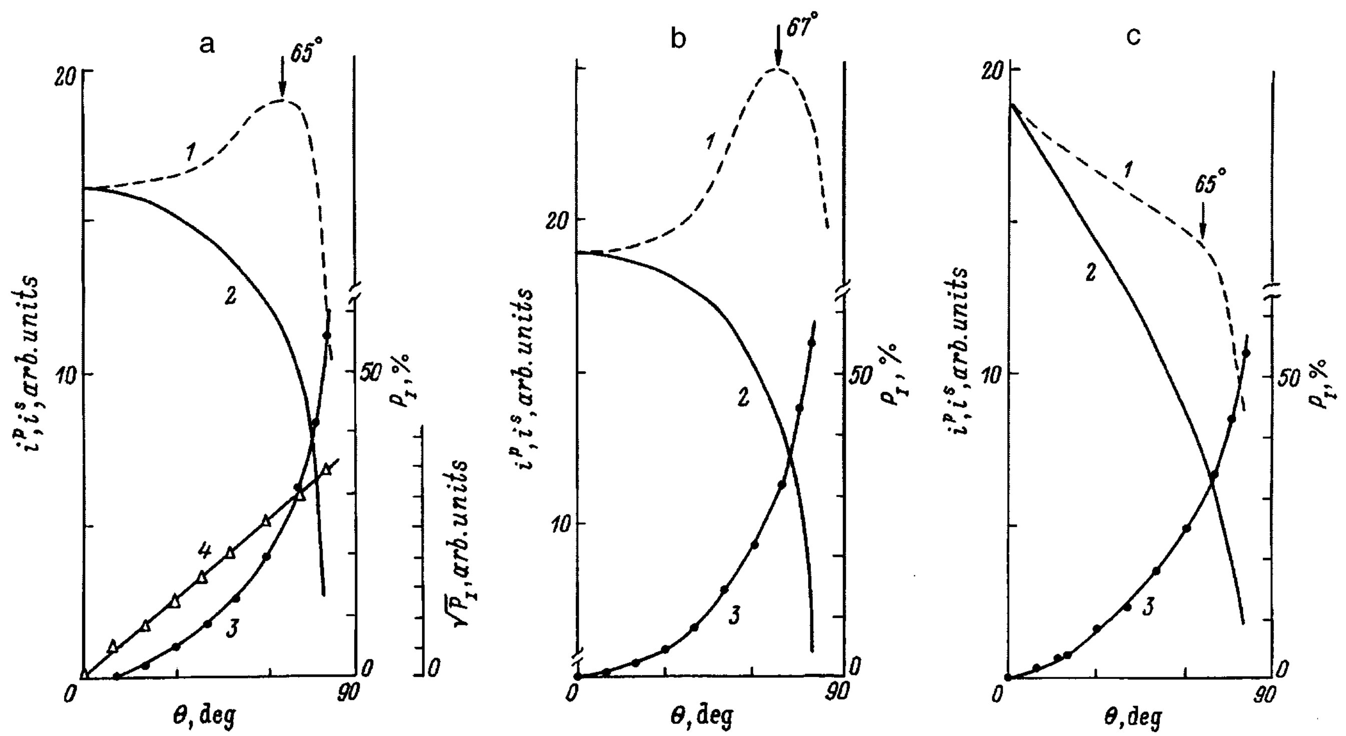

FIG. 4. Dependence of the short-circuit photocurrents i^p (*1*) and i^s (*2*), the induced photopleochroism coefficient $P_I(\Theta)$ (*3*), and $\sqrt{P_I}(\Theta)$ on the angle of incidence of linearly polarized radiation onto the CdS receptive plane of n-CdS/p-InP structures at $T=300$ K. Substrate orientation: a — (111) B, b — (111) A, c — (100). $\hbar\omega=1.33$ eV.

orientation of the InP substrate. This allows us to conclude that the induced photopleochroism is determined in our case only by the nature of the semiconductor through which the linearly polarized radiation enters the active region of each structure, and that in this sense it is a fundamental parameter of the heterojunction.

Since the azimuthal photosensitivity Φ is proportional to the product of the polarization difference in the quantum

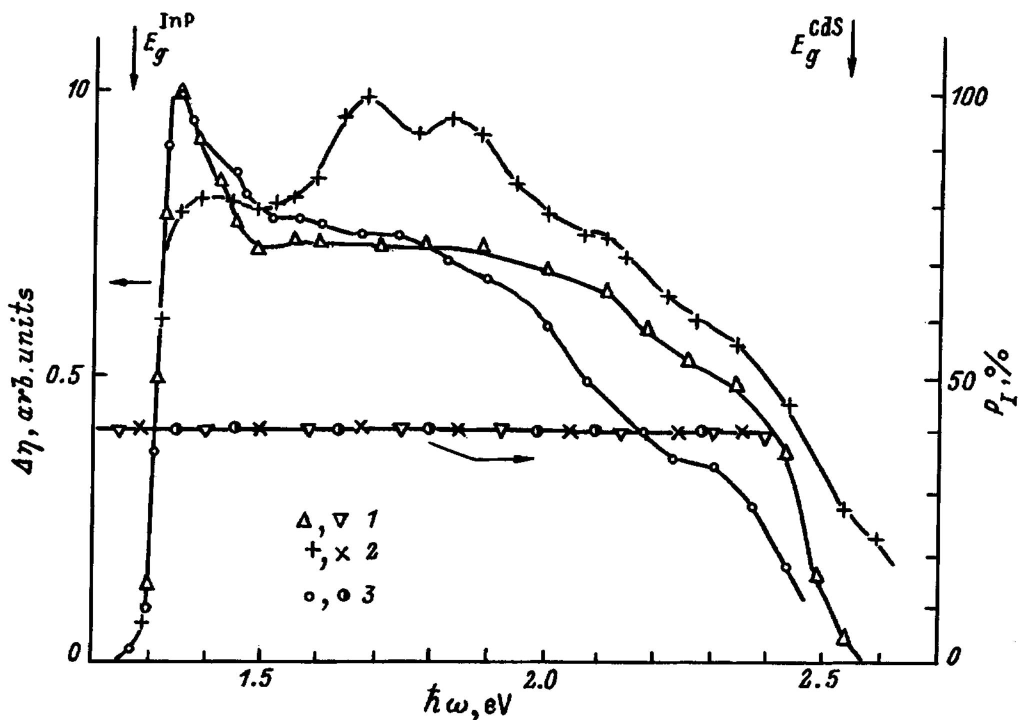

FIG. 5. Spectral dependence of the polarization difference in the quantum efficiency and of the induced photopleochroism coefficient of n-CdS/p-InP structures at $T=300$ K. $\Theta=75°$. Crystallographic orientation of InP: *1* — (100), *2* — (111) B, *3* — (111) A.

efficiency and the photopleochroism coefficient [$\Phi \sim \Delta \eta \times P_I$ (Ref. 11)], it can also be concluded on the basis of the data in Fig. 5 that the spectral dependence of Φ for the heterojunctions obtained is determined only by $\eta(\hbar \omega)$. Therefore, solar elements based on CdS/InP heterojunctions in a semifilm implementation can be employed as broad-band photoanalyzers of linearly polarized light without any additional technological operations. The switching from a polarization-insensitive photodetection mode to a polarimetric mode is accomplished by simply altering the angle of incidence of the linearly polarized light in the photoreceptive plane of the heterojunction.

[1] C. Hilsum and A. C. Rose-Innes, *Semiconducting III–V Compounds*, Pergamon Press, Oxford (1961) [Russian trans., IL, Moscow (1963)].

[2] O. Madelung, *Physics of III–V Compounds*, Wiley, New York (1964) [Russ. trans., Mir, Moscow (1967)].

[3] *Physics and Chemistry of II–VI Compounds*, M. Aven and J. S. Prener (eds.), North-Holland, Amsterdam; Interscience, New York (1967) [Russian trans., Mir, Moscow (1970)].

[4] P. I. Baranskiĭ, V. P. Klochkov, and I. V. Potykevich, *Semiconductor Electrons. A Handbook* [in Russian], Naukova Dumka, Kiev (1975).

[5] J. L. Shay, S. Wagner, K. Bachman, and E. Buehler, J. Appl. Phys. **47**, 614 (1976).

[6] S. Wagner, J. L. Shay, K. Bachman, and E. Buehler, J. Appl. Phys. Lett. **26**, 229 (1975).

[7] A. Yoshikawa and Y. Sakai, Solid-State Electron. **20**, 133 (1977).

[8] K. Ito and T. Ohsawa, Jpn. J. Appl. Phys. **14**, 1259 (1975).

[9] A. V. Simashkevich, *Heterojunctions Based on II–VI Semiconductor Compounds* [in Russian], Kishinev (1980).

[10] V. M. Botnaryuk, L. V. Gorchak, C. M. Grigorjeva, M. B. Kogan, T. A. Kozyneva, L. L. Lyubashevskaya, C. V. Russu, and A. V. Simashkevich, Sol. Energy Mater. **20**, 359 (1990).

[11] Yu. V. Rud', Izv. Vyssh. Uchebn. Zaved. Fiz. **29**, 68 (1986).

[12] G. A. Medvedkin and Yu. V. Rud', Phys. Status Solidi A **67**, 333 (1981).

[13] *Physicochemical Properties of Semiconductor Materials* [in Russian], Nauka, Moscow (1978).

[14] G. S. Landsberg, *Optics* [in Russian], Moscow (1976).

[15] Yu. V. Zhilyaev, N. Nazarov, V. Yu. Rud', Yu. V. Rud', and L. M. Fedorov, Fiz. Tekh. Poluprovodn. **27**, 1610 (1993) [Semiconductors **27**, 890 (1993)].

Translated by P. Shelnitz

Photoelectric properties of structures based on $TlInS_2$ single crystals

S. Iida and N. Mamedov

Nagaoka University of Technology, Nagaoka, Niigata 940-21, Japan

V. Yu. Rud'

St. Petersburg State Technical University, 195251 St. Petersburg, Russia

Yu. V. Rud'

A. F. Ioffe Physicotechnical Institute, Russian Academy of Sciences, 194021 St. Petersburg, Russia
(Submitted July 24, 1996; accepted for publication June 10, 1997)
Fiz. Tekh. Poluprovodn. **32**, 78–81 (January 1998)

The photovoltaic effect in heterocontacts of various types, viz., In/$TlInS_2$, InSe/$TlInS_2$, and GaSe/$TlInS_2$, is investigated. The relative photoconversion quantum efficiency of these structures is studied as a function of the energy of the incident photons and the polarization plane of linearly polarized light. It follows from photosensitivity measurements that the photosensitive structures obtained can be employed as broad-band and selective photosensors of optical radiation. © *1998 American Institute of Physics.* [S1063-7826(98)02101-2]

Thallium indium disulfide, $TlInS_2$, is one of numerous ternary compounds which forms layered crystals with a monoclinic structure under normal conditions (space group C_{2h}^6 at $T=300$ K) and which undergoes a sequence of first- and second-order phase transitions as the temperature is lowered.[1–3] Materials of this class have been classified on the basis of their fundamental properties as ferroelectric semiconductors and have been actively investigated to reveal the features of the set of phase transitions that control electrical and optical processes in layered Tl–III–VI_2 crystals.[3–7] The study of the physical properties of these interesting objects has heretofore been focused exclusively on homogeneous crystals which have a high resistivity ($\rho=10^9-10^{12}\ \Omega\cdot$cm at $T=300$ K) and which exhibit only hole conduction,[5,7] which, of course, makes it possible to create photosensitive structures on their basis. In this paper we report how this problem was overcome in the case of $TlInS_2$ single crystals and examine the results of the first experimental investigations of the spectral photosensitivity dependences of such structures.

The original material $TlInS_2$ was synthesized by fusing stoichiometric quantities of TlS and InS placed in an evacuated quartz cell. Single crystals were obtained by directed crystallization of the $TlInS_2$ melt using a vertically oriented crucible. The crystallization rate, $\simeq 1$ mm/h, was determined by the rate of descent of the crucible, which had a conical bottom with an angle $\simeq 30°$ to provide conditions for the nucleation of a single crystal. The $TlInS_2$ single crystals grown had a tetragonal structure with unit-cell parameters that correspond to the known values for this compound.[7] The structures were fabricated from plane-parallel wafers with an area measuring 3×3 mm and a thickness equal to 0.1 mm, which were prepared by splitting an ingot along a cleavage plane and had a uniform yellowish orange color. As a rule, the cleavage planes had specularly smooth surfaces, which permitted their employment in the fabrication of structures without any additional treatment of the $TlInS_2$ surface.

The fabrication of the photosensitive structures was based on the method of forming a contact with metals or semiconductors of different atomic compositions, which is widely employed for new materials, especially in the stage in which the methods to regulate their physical properties have not yet been determined. In the case of $TlInS_2$, as our first investigations of the contact phenomena showed, a photosensitive barrier is formed by bringing one of these wafers into direct optical contact with a cleavage plane of similar perfection on a layered InSe semiconductor ($\rho_\perp=10^3\ \Omega\cdot$cm with $n\simeq 10^{13}-10^{14}$ cm^{-3}) having n-type conduction, as well as by the thermal sputtering of pure indium in a vacuum. The design of the structures obtained, which exhibit a pronounced photovoltaic effect, and the geometry of their illumination by unpolarized radiation, are presented in Figs. 1–3, near the respective typical spectral dependences of the relative photoconversion quantum efficiency η of these structures.

1. The photovoltaic effect observed in the surface-barrier In/$TlInS_2$ structures is characterized by positive polarity of the photovoltage on the semiconductor, which does not depend on the energy of the incident photons or localization of the light probe on the surface of the structure. This circumstance allows us to assume that separation of the photogenerated charge carriers occurs only in the active region of these structures appearing on the metal–semiconductor interface. As can be seen from Fig. 1, when the system is illuminated on the side of the barrier contact, photosensitivity is observed in the broad spectral range from 1.5 to 3.5 eV. The long-wavelength portion of the spectral $\eta(\hbar\omega)$ curves at $\hbar\omega<2.1$ eV follows a Fowler law $\eta\sim(\hbar\omega-\Phi)^2$ and can therefore be attributed to photoemission (Fig. 1). The barrier height Φ determined from these curves lies in the range 1.2–1.3 eV for different In/$TlInS_2$ structures.

At $\hbar\omega>2.35$ eV a sharp exponential increase in the photosensitivity occurs in the short-wavelength region of the $\eta(\hbar\omega)$ spectra of the surface-barrier structures. A slope $s=d(\ln\eta)/d(\hbar\omega)\approx 35$ eV^{-1} can be assigned to this increase. As is seen in Fig. 1, the exponential increase in the quantum

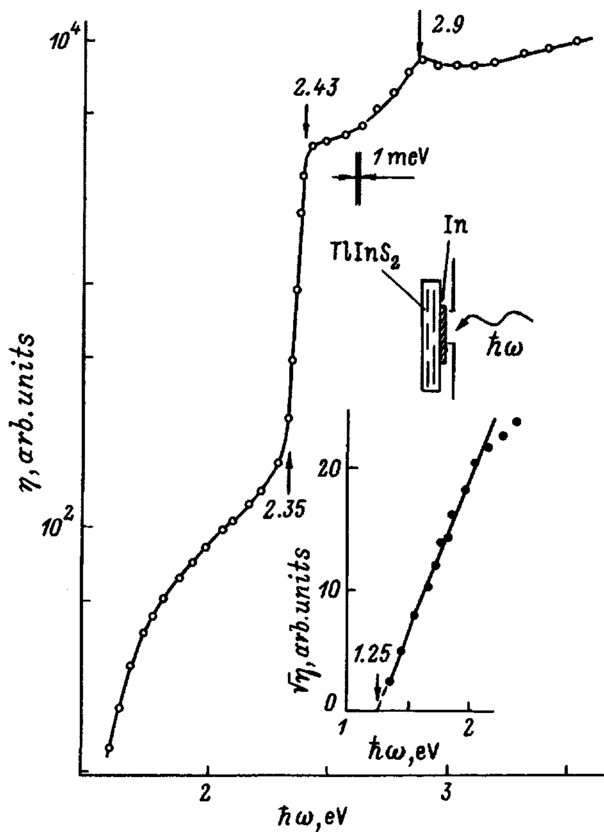

FIG. 1. Spectral dependence of η for an In/$TlInS_2$ surface-barrier structure at $T=300$ K.

efficiency ends at $\hbar\omega \approx 2.43$ eV with the formation of a distinct step, whose energy position agrees well with the literature value of the gap width of $TlInS_2$.[7] It should be stressed that the energy position of the step is also reproduced quite faithfully on the $\eta(\hbar\omega)$ curves of all the In/$TlInS_2$ structures that we obtained and can, therefore, be associated with the appearance of interband optical transitions in $TlInS_2$, which can be classified as direct transitions, with consideration of Ref. 8, on the basis of the high values obtained for the slope. This hypothesis is also supported by the fact that illumination of surface-barrier structures on the side of the $TlInS_2$ wafer produced a sharp short-wavelength photosensitivity limit with $\eta \to 0$ in the photosensitivity spectra at $\hbar\omega > 2.38$ eV, which is caused by a rapid rise in the optical absorption and an increase in the distance between the layer where the nonequilibrium charge carriers are photogenerated and the active region by amounts exceeding the diffusion length of photoelectrons in the semiconductor.

The fact that the photosensitivity at $\hbar\omega > 2.43$ eV continues to increase as long as the structures are illuminated on the side of the barrier contact (Fig. 1) also permits drawing a conclusion that the collection of charge carriers photogenerated on the semiconductor surface is highly efficient and, therefore, that surface recombination plays the major role. This provides for broad-band photoconversion in In/$TlInS_2$ barriers. It should also be stressed that the maximum on the $\eta(\hbar\omega)$ curves in the vicinity of $\hbar\omega \approx 2.9$ eV is reproduced in all the structures investigated and probably reflects features of the band spectrum of $TlInS_2$. This assumption is consistent with the similarity of the $\eta(\hbar\omega)$ curves for the In/$TlInS_2$ structures (Fig. 1) and the photoconductivity spectra of another compound of this class, $TlGaS_2$ (Ref. 4).

The voltaic photosensitivity of In/$TlInS_2$ surface-barrier structures in the short-wavelength spectral range $\hbar\omega > 2.43$ eV at $T=300$ K is at the level of 100 V/W and can be utilized in the development of broad-band photoconverters of natural radiation that are not sensitive to radiation with a photon energy below 2.3 eV.

Polarization studies of the photoconversion quantum efficiency of In/$TlInS_2$ surface-barrier structures during illumination along a normal to the $a-b$ plane[4] by linearly polarized light show that there is virtually no natural photopleochroism[9] in the entire photosensitivity range of these structures. Therefore, the photoactive absorption observed in these structures when they are illuminated along a normal to the $TlInS_2$ cleavage plane is isotropic, in agreement with the results in Ref. 2.

2. Heterostructures fabricated by direct application on a contact[10–12] from $TlInS_2$ and substances of different nature, viz., InSe [$E_G \approx 1.23$ eV (Ref. 13)] and GaSe [$E_G \approx 2.0$ eV (Ref. 13)], exhibited, just as the In/$TlInS_2$ structures considered above, a photovoltaic effect, which predominated when the structures were illuminated on the $TlInS_2$ side. In these cases the ternary compound acted as a broad-band window. Over the entire photosensitivity range of these diverse heterostructures, the semiconductor was positively charged, and the sign of the photovoltage did not depend on their illumination geometry or the photon energy, in agreement with the genesis of their active region.

In the case of a contact formed by GaSe and $TlInS_2$ wafers with very similar electrical resistivities, the photosensitivity in the range between their gap widths turned out to be similar and relatively weakly dependent on the photon energy (Fig. 2, curve *1*). As the resistivity of GaSe decreases, the contribution of the narrow-band component to the photosensitivity begins to drop (Fig. 2, curve *2*), but the long-wavelength and short-wavelength limits for η are maintained, since they are determined by the fundamental absorption in the contacting phases. The long-wavelength increase in η, which is exponential and has a slope $s \approx 38$ eV^{-1}, corresponds to direct interband transitions in GaSe,[10,13] while the short-wavelength drop is caused by reduction of the optical transmission in the $TlInS_2$ wafer as a result of direct interband transitions, in agreement with the results of the investigations of the $\eta(\hbar\omega)$ curves of the In/$TlInS_2$ structures (Fig. 1). The $\eta(\hbar\omega)$ curves of the GaSe/$TlInS_2$ heterostructures also reveal how the relative contribution of the photoactive absorption associated with the introduction of lattice defects increases as the resistivity of GaSe decreases.

With the increase in the difference between the gap widths of the components of the heterostructures based on $TlInS_2$, the spectral photosensitivity range expands toward longer wavelengths in accordance with the decrease in E_G of the narrow-band component. In fact, the long-wavelength maximum of η at $\hbar\omega = 1.25$ eV and the long-wavelength increase in photosensitivity are now determined by the inter-

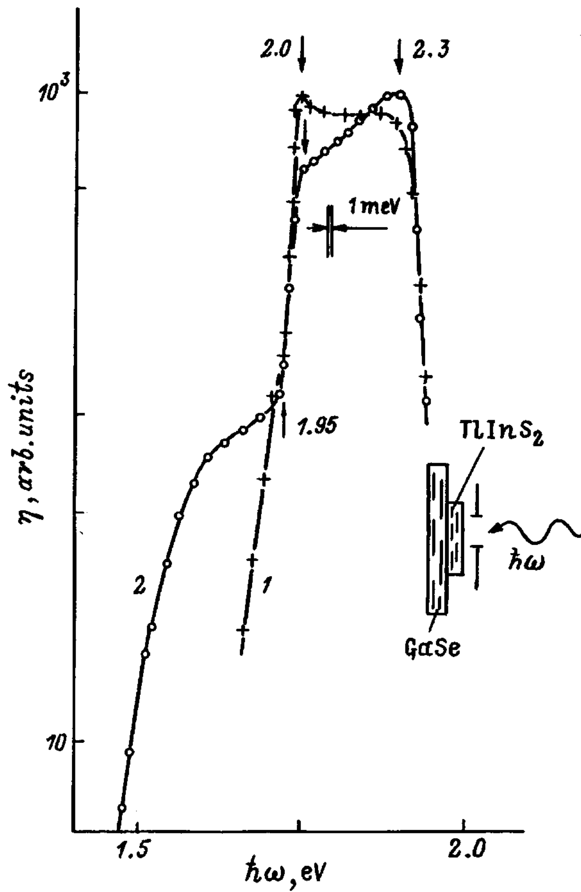

FIG. 2. Spectral dependence of the relative photoconversion quantum efficiency η of GaSe/$TlInS_2$ heterostructures at $T = 300$ K (ρ_{GaSe}, $\Omega \cdot$cm: *1* — 10^9, *2* — 10^7; $\rho_{TlInS_2} = 10^{10}$ $\Omega \cdot$cm).

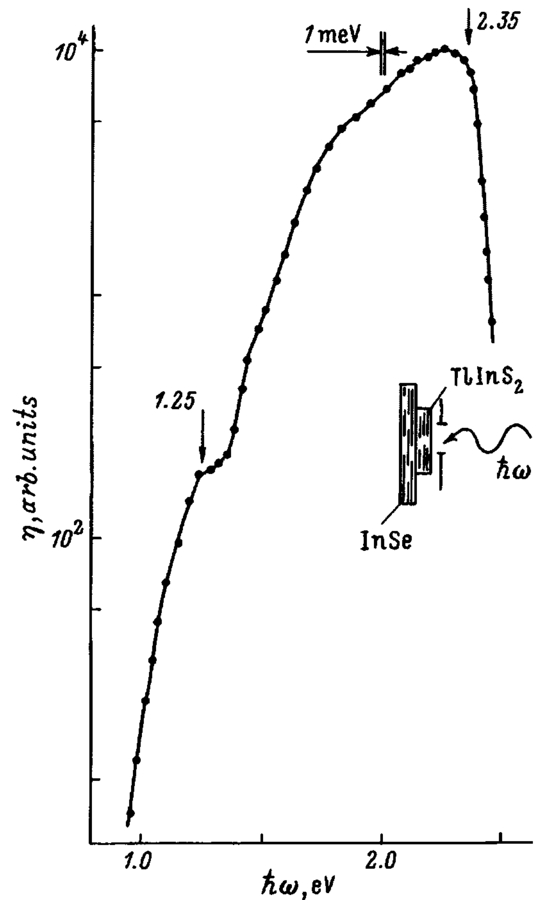

FIG. 3. Spectral dependence of η for InSe/$TlInS_2$ heterostructures at $T = 300$ K.

band transitions in InSe (Fig. 3), while the energy position of the short-wavelength limit for η remains the same as in the case of the GaSe/$TlInS_2$ heterocontact (Fig. 2). For this reason, the total width of the spectral photosensitivity band $\delta_{1/2}$ was found to be significantly higher for the InSe/$TlInS_2$ heterostructure than for GaSe/$TlInS_2$ (see Table I). In accordance with the significantly lower resistivity of InSe in comparison to $TlInS_2$, the active region of such structures is localized mainly in the wafer of the ternary compound. As a result of this displacement, the contribution of the photoactive absorption by thallium indium disulfide becomes decisive (Fig. 3).

As is seen from Table I, a comparable contribution of the photoactive absorption, which can be measured in terms of the ratio between the photoconversion efficiencies at energies near the gap widths of the contacting phases η_1/η_2, is provided only by the GaSe/$TlInS_2$ system (see Table I). As is seen from Table I, the highest values of the maximum voltaic photosensitivity, i.e., $S_U \approx 500$ V/W at $\hbar\omega \approx 2.0-2.3$ eV and $T = 300$ K, were also obtained for this system. In the case of the InSe/$TlInS_2$ heterostructures, the photosensitivity band degenerates into a maximum near the gap width of $TlInS_2$ due to the strong difference between the doping levels of the contacting phases.

Natural photopleochroism is not observed for any of the heterocontacts obtained or for the In/$TlInS_2$ structures. This rule provides some basis to conclude that the direction of the normal to the $TlInS_2$ cleavage plane, as in layered binary InSe and GaSe semiconductors,[10] is photoisotropic.

Thus, the different types of heterocontacts obtained on the basis of $TlInS_2$ can find application as photoconverters of natural radiation, whose spectral contour is controlled by the nature of the narrow-band component.

In conclusion, we also point out that the problem solved herein of fabricating different types of photosensitive structures based on ternary Tl–III–VI_2 compounds (in the example of $TlInS_2$) opens up new possibilities for studying the contribution of various structural phase transitions in photo-

TABLE I. Photoelectric properties of structures based on $TlInS_2$ at $T = 300$ K.

Heterocontact component	$\hbar\omega$, eV	S_U, V/W	$\delta_{1/2}$, meV	s, eV^{-1}	η_1/η_2 [a]
In	>2.43	100		33	
InSe	2.25	150	540		50
					0.9
GaSe	2.0–2.3	500	360	38	1.7

[a]The quantity η_1/η_2 is the ratio between the photoconversion efficiencies of the heterostructure components near the gap widths. Here η_1 corresponds to $TlInS_2$, and η_2 corresponds to GaSe (2 eV) or InSe (1.25 eV).

sensitivity processes and, possibly, for discovering new phase transitions in these substances.

[1] K. R. Allakhverdiev, F. M. Salaev, F. A. Mikhaĭlov, and T. S. Mamedov, Pis'ma Zh. Éksp. Tekh. Fiz. **56**, 153 (1992) [JETP Lett. **56**, 149 (1992)].
[2] A. A. Volkov, Yu. G. Goncharov, G. V. Kozlov, K. R. Allakhverdiev, and R. M. Serdali, Fiz. Tverd. Tela (Leningrad) **25**, 3583 (1983) [Sov. Phys. Solid State **25**, 2061 (1983)].
[3] N. T. Mamedov, N. A. Dzhavadov, and S. T. Kargramanova, Jpn. J. Appl. Phys. **32–33**, 763 (1993).
[4] M. Moronashi, N. Mamedov, and S. Iida, Cryst. Res. Technol. **31**, 189 (1996).
[5] C. H. Karakotsou, M. Hanias, A. N. Anagnostoupoulos, K. Kambas, and G. Bleris, Cryst. Res. Technol. **31**, 41 (1996).
[6] B. R. Gadzhiev, M.-G. Yu. Seidov, and V. R. Abdurakhmanov, Fiz. Tverd. Tela (St. Petersburg) **38**, 3 (1996) [Phys. Solid State **38**, 1 (1996)].
[7] S. N. Mustafaeva, M. M. Asadov, and V. A. Ramazanzade, Fiz. Tverd. Tela (St. Petersburg) **38**, 14 (1996) [Phys. Solid State **38**, 7 (1996)].
[8] Yu. A. Valov, A. A. Lebedev, K. Ovezov, V. D. Prochukhan, and Yu. V. Rud', Pis'ma Zh. Tekh. Fiz. **2**, 1042 (1976) [Sov. Tech. Phys. Lett. **2**, 410 (1976)].
[9] Yu. V. Rud', Izv. Vyssh. Uchebn. Zaved. Fiz. **8**, 68 (1986).
[10] N. M. Mekhtiev, Yu. V. Rud', and É. Yu. Salaev, Fiz. Tekh. Poluprovodn. **12**, 1566 (1978) [Sov. Phys. Semicond. **12**, 924 (1978)].
[11] N. N. Konstantinova, M. A. Magomedov, V. Yu. Rud', and Yu. V. Rud', Fiz. Tekh. Poluprovodn. **26**, 558 (1992) [Sov. Phys. Semicond. **26**, 317 (1992)].
[12] I. V. Bodnar, V. Yu. Rud', and Yu. V. Rud', Fiz. Tekh. Poluprovodn. **28**, 2137 (1994) [Semiconductors **28**, 1175 (1994)].
[13] *Physicochemical Properties of Semiconductor Substances. A Handbook* [in Russian], Nauka, Moscow (1978).

Translated by P. Shelnitz

Temperature anomalies of the work function and relaxation of the surface conductivity of *n*-type Si in the presence of structural defects

N. I. Bochkareva and A. V. Klochkov

A. F. Ioffe Physicotechnical Institute, Russian Academy of Sciences, 194021 St. Petersburg, Russia
(Submitted 13 August 1996; accepted for publication 2 June 1997)
Fiz. Tekh. Poluprovodn. **32**, 82–88 (January 1998)

The temperature behavior of the high-frequency conductivity of surface electron channels in Schottky diodes based on high-resistivity p-type Si containing near-surface, oxidation-induced stacking faults is studied. It is shown that the reversible temperature-induced changes in the surface band bending and the work function of Si have a stepwise character in the temperature range 80–300 K. It is concluded that the surface concentration of free electrons increases during cooling from 180 to 80 K at temperatures which are characteristic of the ordering of water dipoles. These effects are associated with structuring of the water adsorbed on the Si–SiO_2 interface and with the ordered orientation of the water dipoles on the surface in response to the loss of their rotational mobility. © *1998 American Institute of Physics.* [S1063-7826(98)02201-7]

Temperature anomalies of the surface potential and the surface conductivity have previously been observed in the temperature range 80–160 K.[1–10] These anomalies indicate that the surface concentration of free electrons tends to increase as the temperature is lowered. Maxima have been discovered at 90 K on plots of the temperature dependence of the conductivity in electron surface channels in Ge and Si,[2–4] and minima have been discovered for surface hole channels in Ge.[5] These effects have been attributed to the adsorption of oxygen or water vapor,[1] restructuring of the surface,[5] structural changes,[7] and elastic stresses on the Si–SiO_2 interface.[6] Low-temperature anomalies of the rf conductivity of surface electron leakage channels were observed in Refs. 4 and 9 in $p-n$ junctions and Schottky barriers in Ge. In the presence of growth dislocations or microdefects, these anomalies had the form of sharp maxima or steps on plots of the temperature dependence of the conductivity of the channels. It is known that the adsorption of water is accompanied by surface downward band bending and the formation of enriched layers on n-type Ge and inversion layers on p-type Ge, with which the formation of electron leakage channels in barrier structures is usually associated.[1] It has been theorized that reversible low-temperature changes in the surface conductivity of Ge are caused by the structural disorder of the adsorbed water and can take place in other semiconductor materials.[11] It would be of interest to carry out such studies on Si for the purpose of ascertaining the character and nature of the temperature anomalies in the surface conductivity. The interest in such research is also due to the manifestations of these effects in the high-frequency and pulsed characteristics of barrier structures. Their study can provide information regarding the mechanism of the influence of the surface on the characteristics of device structures, as well as a key for elucidating the mechanism of the influence of adsorbed water on the surface properties of Si.

The present research was devoted to an experimental study of the features of the temperature behavior of the work function and the surface conductivity of n-type Si and elucidation of the factors causing these features using measurements of the valve photo-emf and the rf conductivity of surface electron channels through the space-charge region of Schottky barriers on n-type Si.

SAMPLES AND EXPERIMENTAL METHOD

Most of the investigations were performed on n-type Si containing surface oxidation-induced stacking faults (OSF's). It is known that the activity of OSF's is due to dislocations that bound the stacking faults. The penetration depth of OSF's into the bulk of a crystal can be made small compared with the width of the space-charge region in order to rule out the possibility of charge exchange between the deep levels of dislocations during measurements of the high-frequency conductivity and to avoid unequivocal interpretations of the measurement results. This specified the choice of the starting material, viz., dislocation-free n-type Si with a resistivity equal to 2 $k\Omega \cdot cm$.

In this work we used Si wafers with OSF's introduced according to the method described in Refs. 12 and 13 by oxidizing wafers with a ''mildly'' damaged (100) surface in dry oxygen at 1050 °C for 1 h. Oxidation-induced stacking faults with a length of ~ 3 μm, which lie in (111) planes and are bounded by Frank dislocations with a Burgers vector $b=(1/3)[111]$, were located on the damaged surface at a depth $d<1$ μm.[13] After removal of the oxide layer in HF, Au–n-Si(OSF) Schottky barriers were created on this surface by sputter-depositing a semitransparent layer of Au with a diameter of 3 mm (Fig. 1). We note that in the Au–n-Si(OSF) test samples the width of the space-charge region (w) exceeds the penetration depth of the OSF's already in the absence of a reverse voltage. For example, when the height of the surface barrier $\varphi=0.1-0.4$ eV, $w=7-15$ μm, and $w>d$. Ohmic contacts were created by chemically depositing Ni.

To test the influence of adsorbed water on the work function at low temperature, we measured the valve photo-emf in Au–n-Si(OSF) samples, as well as in Au–n-Si and Au–por-Si/n-Si samples, which were obtained by chemically depositing a semitransparent layer of Au on a surface of

 © 1998 American Institute of Physics

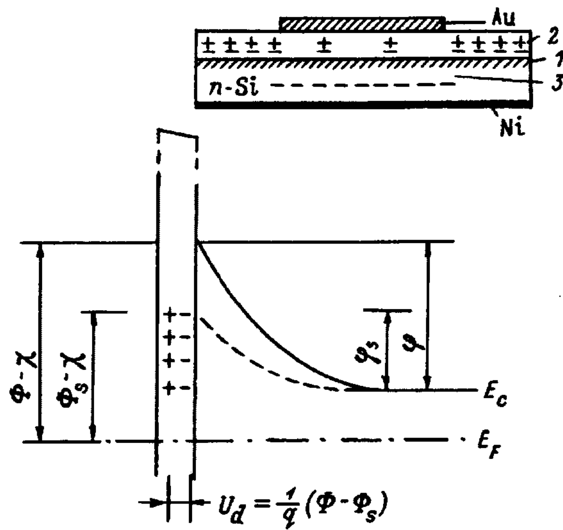

FIG. 1. Schematic representation of a Au–n-Si(OSF) barrier structure and model of a surface barrier in the presence of water dipoles. *1* — OSF, *2* — native oxide film, *3* — space-charge region. The dashed line in the band diagram shows the lowering of the Schottky barrier on the periphery of a Au–Si contact under the influence of adsorbed water, which results in the appearance of surface leakage in Si. Here χ is the electron affinity.

n-Si (with a resistivity $\rho = 2\ \Omega \cdot \mathrm{cm}$) or on a layer of porous silicon (por-Si) deposited on an n-type Si substrate, respectively. It was expected that the influence of the adsorption of water on the surface band bending in n-type Si would be enhanced when Schottky barriers are created in aqueous solutions of HF.[14] In addition, por-Si with its developed porous surface is known as a strong adsorbent containing micropores with diameters ~ 90 Å. Adsorbed water can be present in the form of a particular phase component in pores of such diameter. For example, neutron diffraction revealed the presence of supercooled water at a temperature in the range $T = 246 - 273$ K and grains of hexagonal ice (I_h), cubic ice (I_c), as well as disordered solid water, at $T < 243$ K in SiO_2 microscopic voids with a mean void diameter of 50 Å (Ref. 15) or 90 Å (Ref. 16).

The rf conductivity of the Schottky diodes was measured using a complex-conductivity bridge and a BCI-280 boxcar integrator. The relaxation of the rf conductivity and the capacitance was investigated by deep-level transient spectroscopy (DLTS). The transient capacitance or conductivity was measured with time delays t_1 and t_2 of the gating pulse following switching of the reverse voltage: $U_1 \rightarrow U_2$, where $U_2 > U_1 > 0$. The temperature curves of the transient capacitance $\Delta C(T)$, where $\Delta C = C(t_2) - C(t_1)$, and of the conductivity $\Delta \widetilde{G}(T)$, where $\Delta \widetilde{G} = \widetilde{G}(t_2) - \widetilde{G}(t_1)$ (the relaxation spectra), as well as the other experimental characteristics, were recorded on an H307/n $X - Y$ recorder.

EXPERIMENTAL RESULTS

The value of the leakage current in the Schottky diodes investigated at 300 K and $U = 1$ V was 10^{-9} to 10^{-5} A. Upon cooling a decrease in the leakage current was observed in most of the diodes, and an increase was observed in some of them.

Figure 2 presents the temperature dependence of the capacitance $C(T)$, the rf conductivity $\widetilde{G}(T)$, and the static conductivity $G(T)$ of a Au–n-Si(OSF) diode. The plots of $C(T)$, $\widetilde{G}(T)$, and $G(T)$ are reversible and have inflection points near the same temperatures. The plots of $\widetilde{G}(T)$ for small reverse voltages (curves *3* and *4*) have a minimum near 180 K. We note that $\widetilde{G} \simeq G$ at relatively large voltages ($U = 8$ V) (curves *5* and *6*), but $\widetilde{G} \gg G$ at small voltages.

Typical relaxation spectra of the transient capacitance and the transient conductivity observed in Au–n-Si(OSF) are shown in Fig. 3. The capacitance spectrum contains five peaks at temperatures $T_{\max}$, which we have designated A_1, A_2, B, C, and D. Two shoulders, which are denoted by B_1 and B_2, are also noted on the low-temperature slope of peak B.

Figure 4 presents the corresponding Arrhenius plots for the capacitance relaxation time τ in $\log \tau = f(1/T)$ coordinates. The activation energies ΔE determined from them, which characterize the peaks of the spectrum, are listed in Table I, which, for comparison, also presents the activation energies E_a characterizing the most distinct peaks that were previously observed by various investigators in dislocation Si containing OSF's[12] and were combined into groups A, B, C, and D in Ref. 17. A comparison of the results shows that peaks A_2, B, C, and D in our spectra are comparable to the previously observed peaks $A - D$, which were associated with charge exchange between the deep levels of dislocations and point defects that decorate dislocations. In Ref. 12 peaks $A - D$ were observed on the Schottky barriers in epitaxial layers of Si(P) (with a doping level $N_d = 2 \times 10^{15}$ cm^{-3}) containing OSF's measuring 3.6 μm, whose penetration depth ($d < 0.9$ μm) exceeded the width of the space-charge region ($d > w$). As we have already noted, $w > d$ in the high-resistivity samples of Au–n-Si(OSF) investigated already in the absence of a reverse voltage. When the reverse voltage was switched to a higher level, the edge of the space-charge region in the bulk of the crystal passed through a region where there were no OSF's. Thus, the observed relaxation of the capacitance is not associated with charge transfer between deep levels.

This conclusion is also confirmed by the similarity between the transient capacitance spectra and the transient conductivity spectra, whose peaks are characterized by the same activation energy values (Fig. 3, curves *1* and *2*).

The temperature dependences of the valve photo-emf $U_{\mathrm{oc}}(T)$ (Fig. 5) were measured with uniform illumination of the entire area and with illumination of only the central region of the sample by an incandescent lamp.

The Au–n-Si(OSF) samples exhibit a nonlinear dependence of $U_{\mathrm{oc}}(T)$ under uniform illumination (Fig. 5, curve *1*); the nonlinearity is stronger at the low- and high-temperature edges. When only the central region is illuminated, the slope of the plot of $U_{\mathrm{oc}}(T)$ decreases (curve *2*). The plots of $U_{\mathrm{oc}}(T)$ for the Au–n-Si (curves *3–4*) and Au–por-Si (curve *5*) samples take on a bell-shaped form with a maximum in the range $180 - 200$ K.

We note that inflection points are observed on the $U_{\mathrm{oc}}(T)$, $C(T)$, $\widetilde{G}(T)$, and $G(T)$ curves at the same tempera-

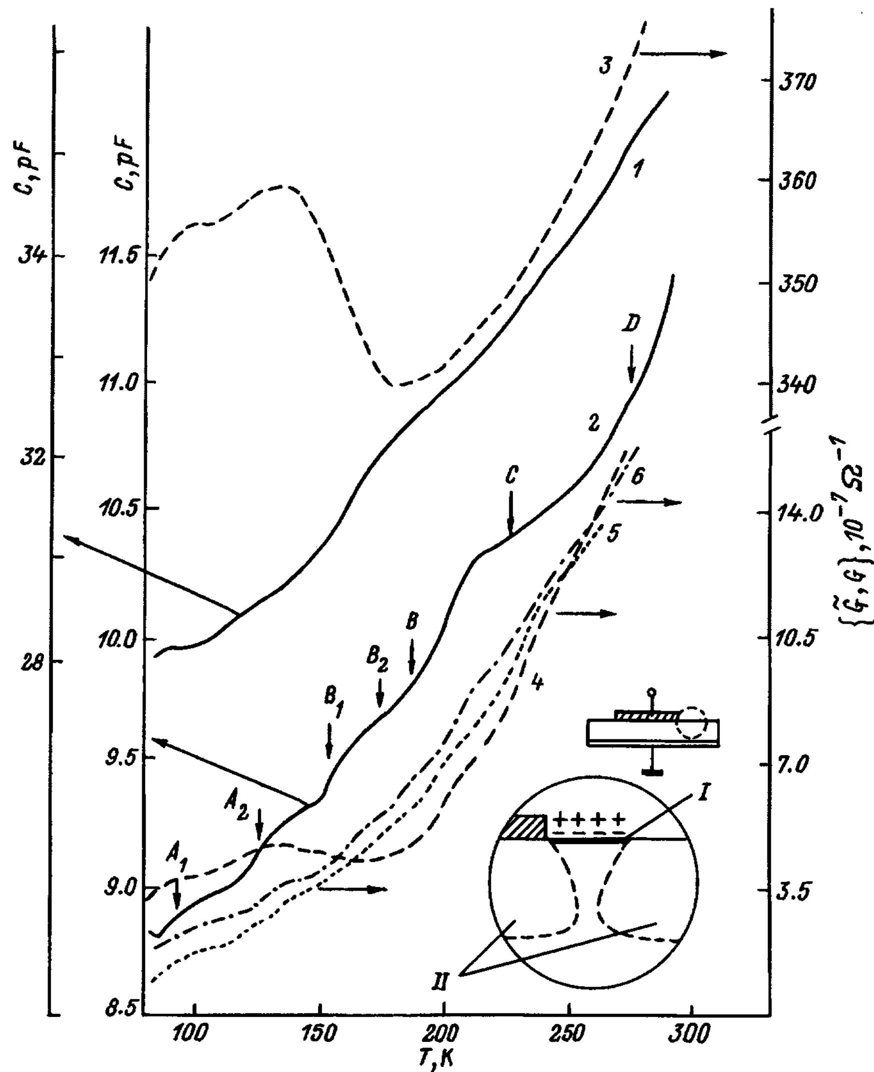

FIG. 2. Temperature dependence of the capacitance (*1*, *2*), the high-frequency conductivity (*3–5*), and the static conductivity (*6*) of Au–n-Si(OSF) diodes. U, V: *1*, *3* — 0.3; *4* — 4; *2*, *5*, *6* — 8. $f = 160$ kHz. The values of T_{max} for the peaks of the capacitance spectrum presented in Fig. 3 are marked. The inset illustrates one of the possible configurations of a surface leakage channel on an open surface: *I* — electron-enriched layer, *II* — space-charge region of a near-surface barrier.

tures as the peaks in the spectra. This indicates that the temperature behavior of the electrical characteristics investigated has basically one cause.

DISCUSSION

Temperature behavior of the valve photo-emf and the work function. In the case of a high density of surface states, the Fermi level on the surface (E_{fs}) is pinned, and the work function (Φ) does not depend on the position of the Fermi level in the bulk (E_f) or, consequently, on the temperature.[18] The surface band bending increases almost linearly with decreasing temperature (when $dE_f/dT \simeq \text{const}$): $\varphi(T) = E_{fs} - E_f(T)$. Under intense illumination the valve photo-emf approximates φ/q (q is the charge of the electron), and a linear temperature dependence of the photo-emf can be expected.

The observed features of the temperature dependence of the valve photo-emf indicate the presence of conducting

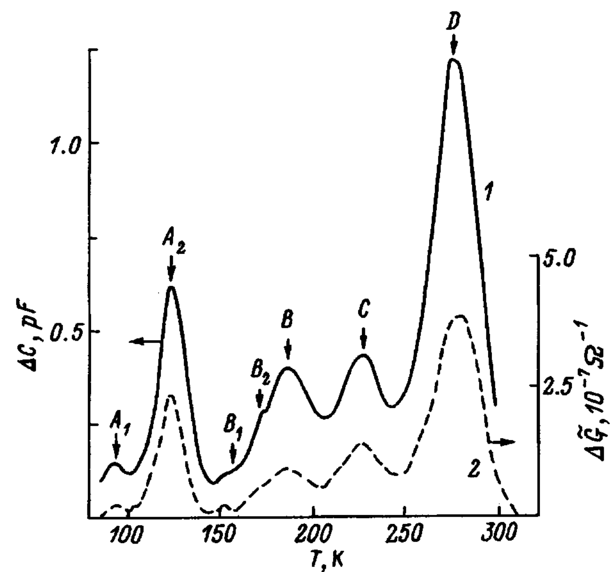

FIG. 3. Relaxation spectra of the transient capacitance (*1*) and the conductivity (*2*) of Au–n-Si(OSF) diodes. $U_1 \rightarrow U_2$, V: *1* — (0→8), *2* — (4→8). $t_1 = 2$ ms, $t_2 = 10$ ms. $f = 160$ kHz.

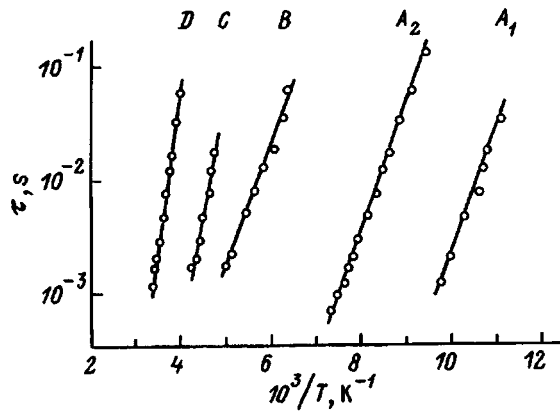

FIG. 4. Arrhenius plots for the capacitance relaxation time of Au–n-Si(OSF) diodes. The corresponding peaks of the relaxation spectra are indicated, and the activation energies are listed in Table I.

channels in the space-charge region of the Schottky barrier. In fact, if there are no leakage channels,

$$qU_{\text{oc}}(T)=\varphi(T)-kT\ \ln\frac{SqvN_d}{4J_{\text{sc}}},$$

where v is the electron thermal velocity, N_d is the donor concentration, J_{sc} is the short-circuit photocurrent, and S is the area of the barrier. When the illuminated area, S_{ph}, is diminished (here $J_{\text{sc}}\sim S_{\text{ph}}$), an increase in the slope of the $U_{\text{oc}}(T)$ curve by $(k/q)[\ln(S/S_{\text{ph}})]$ should be observed.

However, if there are leakage channels through the space-charge region, for example, on the periphery of the barrier, on the open surface (Fig. 2), the photo-emf decreases as the channel conductivity G increases. Since the internal resistance of a Schottky barrier, R_b $[R_b\simeq\exp(-U_{\text{oc}}/kT)]$, increases rapidly with decreasing U_{oc}, the character of the temperature behavior of $G(T)$ can be seen more clearly when the periphery of the barrier is blackened and J_{sc} is diminished. The slope of the plot of $U_{\text{oc}}(T)$ is then determined by the temperature variation of the surface band bending (φ_s) in the channel. As the temperature is lowered, the slope of the plot $U_{\text{oc}}(T)$ increases if in the region of the channel the surface Fermi level moves away from the conduction band, and the work function (Φ_s) increases ($d\Phi_s/dT<0$), whereas if $d\Phi_s/dT>0$, the surface Fermi level approaches the conduction band, and the work function decreases or changes sign. The necessary conditions for a decrease in U_{oc} during cooling include a decrease in the height of the surface barrier ($d\Phi_s/dT>dE_f/dT$ and, accordingly, $d\varphi_s/dT>0$) and an increase in the surface electron concentration $n_s(T)$ in the channel.

It follows from Fig. 5 that the Schottky barriers have leakage channels, and that the surface band bending and the work function undergo stepwise variation with the temperature at their sites. For example, when the Au–n-Si(OSF) samples are cooled from 300 to 80 K and uniformly illuminated, the increase in the photo-emf amounts to $\Delta U_{\text{oc}}=0.26$ V and is close to $\Delta E/q=0.3$ V. However, the plot of $U_{\text{oc}}(T)$ is nonlinear and has inflection points, and when the periphery of the barrier is darkened, its slope decreases, pointing out a nonmonotonic decrease in Φ_s during cooling. It follows from Fig. 5 that in the Au–n-Si and Au–por-Si samples the photo-emf drops at $T<180$ K due to the nonmonotonic decrease in Φ_s.

The increase in the photo-emf observed in all the samples as the temperature is lowered from 280 to 200 K indicates an increase in Φ_s. For example, in the Au–n-Si samples $\Delta U_{\text{oc}}=0.20-0.25$ V, and Φ_s varies in the range 0.10–0.15 eV when the shift in the Fermi level, $\Delta E_f=0.1$ eV, is taken into account.

Complex rf conductivity and relaxation spectra. The correspondence observed between the temperature dependence of the rf conductivity $\tilde{G}(T)$ and the capacitance $C(T)$ of Au–n-Si(OSF) diodes (Fig. 2) is evidence that the ac channel conductivity has not only an active component, but also a reactive component.

Let us consider the structure of a leakage channel (Fig. 2). The potential ''well'' in a Schottky barrier is the source of the leakage channel, the barrier is the gate, and the neutral region of Si beyond the edge of the space-charge region is the drain. This structure is similar to the structure of a unipolar drift transistor with a vertical n-channel and a Schottky gate short-circuited to the source. According to Refs. 19–21, the conductivity of such a conducting channel of nonuniform width increases as the reverse voltage rises as a result of the overlap of the channel by the space-charge region and the lowering of the barrier by the longitudinal electric field. The dominance of one of these processes specifies the character of the dependence of the channel current on the voltage, i.e., whether it is sublinear (a current-voltage characteristic of the pentode type) or superlinear (a current-voltage characteristic of the triode type).

The portions of the channel near the source and the drain provide for internal feedback in the channel and the transient processes associated with recharging of the transfer capacitance C_s of the channel, which are slow compared with the Maxwell relaxation. The instantaneous RC relaxation time of the channel is $\tau_s=C_s/g$, and $\tau_s>12\tau_m(L/a)^2$, where τ_m is the dielectric relaxation time, $g=g(\varphi,U)$ is the transconductance, and $a=a(\varphi,U)$ and $L=L(\varphi,U)$ are the effective width and length of the channel.[21]

The jump in the channel current following a pulsed increase in the reverse voltage is accompanied by decay, which slows with the passage of time. This is attributed to the ohmic voltage drop across the region near the source and the corresponding narrowing of the channel near the source, which causes a further increase in the voltage drop and nar-

TABLE I. Comparison of the parameters of the relaxation time constant $\tau=\tau_0\exp(\Delta E/kT)$ obtained in the present work with data from Ref. 17.

Spectral peaks	$T_{\max}$, K	ΔE, eV	τ_0, s	E_a, eV (Ref. 17)
A_1	93	0.22	10^{-13}	
A_2	125	0.22	2×10^{-11}	0.18−0.19
B	185	0.21	5×10^{-9}	0.27−0.29
B_1	~153			
B_2	~173			
C	226	0.43	10^{-13}	0.37−0.52
D	273	0.54	10^{-13}	0.54−0.68

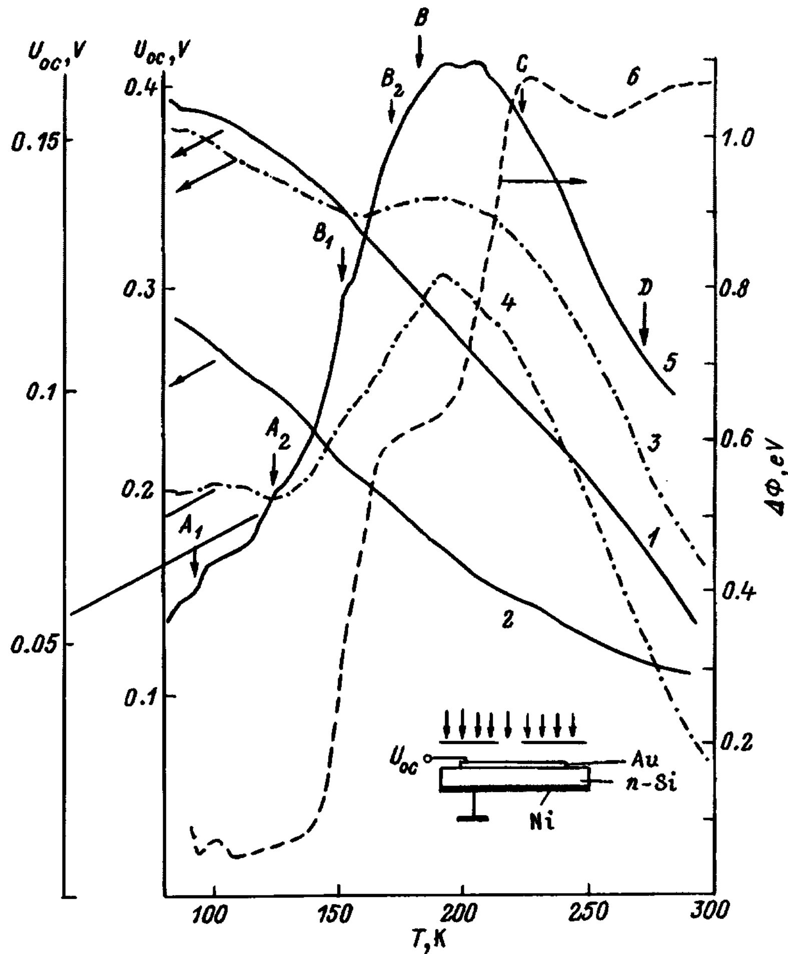

FIG. 5. Temperature dependence of the photo-emf U_{oc} of Au–n-Si(OSF) (*1*, *2*), Au–n-Si (*3*, *4*), and Au–*por*-Si (*5*) diodes and variation of the work function $\Delta\Phi$ of Cu in the H_2O/Cu system (*6*) from Ref. 24. *1*, *3*, *5* — uniform illumination; *2*, *4* — illumination by a spot with a diameter of 2 mm. The values of T_{max} for the peaks of the capacitance spectrum presented in Fig. 3 are marked. Inset – diagram of the experiment.

rowing of the channel (and an increase in τ_s). All these factors lead to a relatively slow decrease in the channel conductivity.[21]

The modulation of the channel conductivity with τ_s leads to a phase shift between the voltage and the channel current. As a result, the rf channel conductivity has both active and reactive components. In capacitance measurements the reactive channel current is summed in the external circuit with the bias current through the barrier capacitance. This also influences the value of the measured capacitance and its temperature dependence.

It follows from Figs. 2 and 5 that at voltages which are small in order of magnitude the rf conductivity of the Au–n-Si(OSF) diodes is close to the static conductivity of a leakage channel in the Au–n-Si diodes, and their temperature dependences are also similar. This confirms that the temperature dependence of the rf conductivity reflects temperature-induced changes in the conductivity of the source region. Since the conductivity of this region is determined by the surface electron concentration n_s, the temperature behavior of $\widetilde{G}(T)$ at small U reflects the temperature behavior of $n_s(T)$ and attests to the nonmonotonic variation of n_s with the temperature.

Let us estimate the characteristic scale of the relaxation time τ_s. At small values of U the ratio $\widetilde{G}/G$ amounts to $\sim 10-5\times 10^3$, depending on the temperature. Hence, it follows that after the voltage is switched to a higher level, the decrease in the current from its value at $t=1$ μs (the frequency $f=160$ kHz, and $1/2\pi f=1$ μs) to the stationary value amounts to $\sim 10-10^3$. A decrease in the current and, accordingly, in the conductivity and the ratio a/L by $10-10^2$ corresponds to an increase in $\tau_s\sim(L/a)^2$ to $0.1-10^2$ ms.

Let us consider the influence of the drain region on the character of the transient process in a channel. Since the field on the space-charge region of the Schottky barrier decreases linearly with the distance x from the barrier, i.e., since $E_b(x)\sim(1-x/w)$, after an instantaneous increase in U, the channel should expand toward the drain during recharging of the transfer capacitance, relaxing toward a stationary distribution $a(x)\sim(1-x/w)^{-1}$. As a result, the decay of the current and the decrease in the conductivity following the initial jump in the current give way to a rise in the current and an increase in the conductivity. According to Ref. 21, when the voltage increment ΔU is small, the transconductance $g\sim\Delta U[w_g/w(U)]$, where $w_g=\varphi\varepsilon/q^2 n_s$ (ε is the dielectric constant), and then $\tau_s=C_s/g\sim n_s$. Also, if $n_s\sim\exp(\Delta E/kT)$, then $\tau_s\sim\exp(\Delta E/kT)$ and increases with increasing n_s. This

can also account for the temperature correspondence of the behavior of $\widetilde{G}(T)$ and the peaks in the relaxation spectrum.

Influence of adsorbed water on the temperature dependence of the work function. According to the theories that have been devised,[1,14,22] the pinning of the Fermi level on the surface of n-type Si is effected by acceptor states of the dangling bonds of three-coordinated Si atoms. When these surface states are filled by electrons, a surface barrier forms. Dangling Si bonds are also the dominant sites for the adsorption of water. The attachment of water molecules to dangling Si bonds results in their passivation, which is accompanied by a decrease in the height of the surface barrier. It is also assumed that adsorbed water can produce a donor effect, which is also a cause of the formation of electron leakage channels in barrier structures. Molecules of adsorbed water and their fragments (H and OH radicals) can form hydrogen bonds with neighboring water molecules and with dangling bonds of oxygen atoms from the local environment.[14]

An analysis of the results obtained and the literature data[22–25] reveals that stepwise changes in the surface potential are observed at 90, 130, 185, 220, and 273 K, as well as at 153 and 173 K, which are characteristic of water and coincide with the temperatures for the loss of the rotational mobility of water dipoles in bulk[23] and two-dimensional[24] phases of water, as well as in clusters of water adsorbed in SiO_2 voids,[22] and the temperatures of the ordering of water dipoles in groups of molecules of crystallized water.[25] In the case of the low-temperature adsorption of water, which has been thoroughly studied on metals, a loss of mobility accompanied by an increase in the work function (Fig. 5, curve *6* from Ref. 24) occurs at the same temperatures as in the H_2O/SiO_2 system.[22]

These results can be explained on the basis of the following qualitative model. When water is absorbed on a Si surface, it undergoes structuring with the formation of clusters in the form of nuclei or fragments of low-temperature crystalline and amorphous phases of water/ice as the temperature is lowered from 273 to 180 K. When the rotational mobility is lost, the water dipoles are oriented in the adsorption field of the Si surface. Enhancement of their preferential orientation normal to the surface occurs during cooling from 300 to 80 K in several steps at temperatures that are characteristic of water. The water dipoles immobilized on the surface neutralize the dangling Si bonds. The ordered orientation of the water dipoles is accompanied by an increase in the positive bound charge on the $Si-SiO_2$ interface, as well as the free charge of electrons on the Si surface. The latter can be associated with the existing donor-like states and possibly with the donor properties of the water dipoles themselves.

The loss of mobility is accompanied by a stepwise increase in the surface electron concentration and a decrease in the work function. The increase in the work function at temperature in the range $280-200$ K can be attributed to an increase in the number of lateral hydrogen bonds.

The increase in the number of crystallization nuclei on a defective surface with a large number of dangling Si bonds [in samples of Si(OSF) associated with the emergence of dislocations on the surface[14]] leads to structural disorder of the adsorbed water and the formation of tiny amorphous clusters or water monomers. A large fraction of the water dipoles maintain their rotational mobility down to 90 K and neutralize surface states only after cooling to lower temperatures.

According to this model, the activation energies $\Delta E = 0.22$, 0.43, and 0.54 eV determined from the Arrhenius plots of $\tau(T) = \tau_0 \exp(\Delta E/kT)$ can be assigned to the energies for the cleavage of one, two, and three hydrogen bonds.

CONCLUSIONS

An analysis of the results obtained in this work provides evidence that the temperature-induced changes in the surface band bending on a real n-type Si surface have a stepwise character, which corresponds to a nonmonotonic decrease in the work function of Si during cooling from 300 to 80 K and an increase in the surface concentration of free electrons at temperatures which are characteristic of water groupings. This results in the formation of surface electron leakage channels, which are manifested in the high-frequency and pulsed characteristics of the diodes investigated.

It is postulated that these effects are associated with the structuring of water adsorbed at the $Si-SiO_2$ interface and orientation of the water dipoles by the surface when their rotational mobility is lost.

We thank D. V. Tarkhin for the n-type Si crystals with OSF's provided for this research.

[1] A. V. Rzhanov, *Electronic Processes on Semiconductor Surfaces* [in Russian], Nauka, Moscow (1971).
[2] T. Ando, A. B. Fowler, and F. Stern, Rev. Mod. Phys. **54**, 437 (1982).
[3] M. S. Kagan and E. G. Landsberg, Fiz. Tekh. Poluprovodn. **8**, 125 (1974) [Sov. Phys. Semicond. **8**, 78 (1974)].
[4] N. I. Bochkareva, Fiz. Tekh. Poluprovodn. **25**, 537 (1991) [Sov. Phys. Semicond. **25**, 323 (1991)].
[5] G. A. Katrich and D. I. Moiseev, Fiz. Tverd. Tela (Leningrad) **27**, 2588 (1985) [Sov. Phys. Solid State **27**, 1553 (1985)].
[6] S. I. Kirillova, M. D. Moin, V. E. Primachenko, S. V. Svechnikov, V. A. Chernobaĭ, and I. N. Dubrov, Fiz. Tekh. Poluprovodn. **26**, 1399 (1992) [Sov. Phys. Semicond. **26**, 784 (1992)].
[7] S. I. Kirillova, V. E. Primachenko, O. V. Snitko, and V. A. Chernobaĭ, Poverkhnost' (11), 74 (1991).
[8] S. I. Kirillova, V. E. Primachenko, and V. A. Chernobaĭ, Fiz. Tekh. Poluprovodn. **30**, 118 (1996) [Semiconductors **30**, 68 (1996)].
[9] N. I. Bochkareva and S. S. Ruvimov, Fiz. Tekh. Poluprovodn. **26**, 872 (1992) [Sov. Phys. Semicond. **26**, 492 (1992)].
[10] N. I. Bochkareva, J. Heydenreich, S. Ruvimov, R. Scholz, K. Scheerchmidt, and L. M. Sorokin, Solid State Phenom. **32–33**, 565 (1993).
[11] H. I. Bochkareva, Fiz. Tekh. Poluprovodn. **28**, 290 (1994) [Semiconductors **28**, 175 (1994)].
[12] J. Kaniewski, M. Kaniewska, and A. R. Peaker, Appl. Phys. Lett. **60**, 359 (1992).
[13] Yu. S. Lelikov, Yu. T. Rebane, S. S. Ruvimov, D. V. Tarkhin, A. A. Sitnikova, and Yu. G. Shreter, Fiz. Tverd. Tela (St. Petersburg) **34**, 1513 (1992) [Sov. Phys. Solid State **34**, 804 (1992)].
[14] V. S. Vavilov, V. F. Kiselev, and B. N. Mukashev, *Defects in Silicon and on Its Surface* [in Russian], Nauka, Moscow (1990).
[15] M.-C. Bellisent-Funel, J. Lal, and L. J. Bosio, J. Chem. Phys. **98**, 4246 (1993).
[16] J. C. Dore, M. Dunn, and P. Chieux, J. Phys., Colloq. **48**, C1-457 (1987).
[17] P. Omling, E. R. Weber, L. Montelius, H. Alexander, and J. Michel, Phys. Rev. B **32**, 6571 (1985). P. Omling, E. R. Weber, L. Montelius, H. Alexander, and J. Michel, Phys. Rev. B **32**, 6571 (1985).
[18] G. E. Pikus, *Principles of the Theory of Semiconductor Devices* [in Russian], Nauka, Moscow (1965).
[19] A. Blicher, *Field-Effect and Bipolar Power Transistor Physics*, Academic

Press, New York (1981) [Russian trans., Énergoatomizdat, Leningrad (1986)].
[20] S. M. Sze, *Physics of Semiconductor Devices*, 2nd ed. Wiley-Interscience, New York (1969) [Russian trans., Énergiya, Moscow (1973)].
[21] J. Nishizawa, T. Terasaki, and J. Shibata, IEEE Trans. Electron Devices **ED-22**, 185 (1975).
[22] V. F. Kiselev, *Surface Phenomena in Semiconductors and Insulators* [in Russian], Nauka, Moscow (1970).
[23] G. P. Johari, A. Hallbrucker, and E. J. Mayer, J. Chem. Phys. **95**, 2955 (1991).
[24] A. Spitzer, A. Ritz, and H. Luth, Surf. Sci. **152/153**, 543 (1989).
[25] N. D. Gavrilova, Yu. P. Kozlova, A. M. Kozlov, and A. N. Izrailenko, Fiz. Tverd. Tela (Leningrad) **26**, 2884 (1984) [Sov. Phys. Solid State **26**, 1744 (1984)].

Translated by P. Shelnitz

Commensurate and incommensurate indium phases on a (111)A InAs surface

Yu. G. Galitsyn, V. G. Mansurov, I. I. Marahovka,* and I. P. Petrenko

Institute of Semiconductor Physics, Siberian Branch of the Russian Academy of Sciences, 630090 Novosibirsk, Russia
(Submitted March 17, 1997; accepted for publication April 29, 1997)
Fiz. Tekh. Poluprovodn. **32**, 89–94 (January 1998)

Adsorption phases of indium on a (111)A InAs surface are investigated. Three phases are detected: $(2\times2)_a$, (1×1), and the (0.77×0.77) incommensurate phase. The (0.77×0.77) incommensurate phase is modeled as a densely packed (111) layer of In (fcc) crystal situated in epitaxial relation to the InAs substrate: $\langle110\rangle_{\mathrm{In}}\|\langle110\rangle_{\mathrm{InAs}}$. Reasons for the realization of the fcc crystal structure are analyzed. It is shown that the incommensurate phase is spatially modulated by the periodic potential of the substrate. A comparison of our data on indium adsorption onto (111) InAs with the data in the literature on indium adsorption onto (111) Si, Ge reveals the importance of relaxation of the elastic strains in the formation of two-dimension adsorption-induced superstructures. © *1998 American Institute of Physics.*
[S1063-7826(97)00512-7]

A study of the interaction of metal atoms with a superconductor surface would be of great scientific interest and, besides, such studies are driven by technological requirements.

Adsorption of metal atoms induces on the surface of a semiconductor ordered two-dimensional structures. These structures can be commensurate, incommensurate, or exist in various epitaxial relations to the substrate lattice. The wide spectrum of arising surface reconstructions not only makes adsorption systems extremely attractive for research in the physics and chemistry of surface phase transitions, but also highlights the unique complexity of the interaction in the adsorbate–substrate system.

At present, the most widely used phase is the $(\sqrt{3}\times\sqrt{3})R30°$ phase, arising in the adsorption both of trivalent metals (Al, Ga, In) and a number of other metals (Pb, Ag, Au, Bi, etc.) on (111) surfaces of Si and Ge crystals.[1–9]

It is well known that the reason for reconstruction of ideal (111) faces in Si and Ge is saturation of dangling bonds by intrinsic adatoms and dimers in Si, and adatoms in Ge. For example, in the (7×7) superlattice in Si the density of dangling bonds is is 2.58 times smaller than in the ideal (1×1) unreconstructed surface. Adatoms in Si and Ge are distributed over the T_4 sites and form (2×2) subcells in (7×7) and (2×8) reconstructions, respectively.[10] During adsorption adatoms are replaced by metal atoms. However, instead of a (2×2) reconstruction, a $(\sqrt{3}\times\sqrt{3})R30°(\alpha)$ reconstruction is realized, which leads to complete saturation of the dangling bonds by the metal atoms at the minimum filling density $\theta=1/3$.

As the adatom density is increased, the densely packed $(\sqrt{3}\times\sqrt{3})R30°(\beta)$ phases are formed.[1,3–5,7] The interaction of the adatoms in the adsorbed layer becomes important and conditions arise for the realization of incommensurate phases. For Pb on (111) Si, as the filling density is increased from 1 to 1.5 to 2 monolayers, incommensurate phases arise with the distance between the adatoms equal to 3.46, 3.43, 3.41 Å respectively.[1] A still more ''compressed'' incommensurate phase of Pb on (111) Si was observed in Ref. 3, where the closest distance between the Pb adatoms was 3.35 Å. It is surprising that the closest distance between the Si atoms in the (111) plane is 3.84 Å, and for crystalline Pb it is 3.50 Å, but the densely packed Pb $(\sqrt{3}\times\sqrt{3})R30°(\beta)$ phase is realized, in which the distance between the Pb atoms is 3.35 Å.

Adsorption of metal atoms on the (111) surface of III–V crystals has received significantly less attention. The main reconstruction of an atomically clean (111)A face of these crystals is the $(2\times2)_v$ vacancy structure.[11] Saturation of dangling bonds (i.e., repulsion of the dangling-bond electronic states from the band gap: empty orbitals into the conduction band and filled orbitals into the valence band) is also a motive force of reconstruction here. In InAs, of the four In atoms in the (2×2) unit cell one is removed leaving a vacancy and three dangling As bonds in the second layer. Transfer of three electrons from the three dangling bonds of the cations to the three dangling bonds of the anions with subsequent relaxation of the atoms into sp^2-hybridization of the cation and s^2p^3-hybridization of the anion leads to a stable $(2\times2)_v$ reconstruction. As a result, the (111)A face becomes similar to the relaxed (110) face.[10] Theoretical estimates indicate that on (111)A GaAs the formation of a cation vacancy is exothermal[12] (it may be surmised that this is also true for InAs), i.e., they confirm the high stability of this reconstruction. The static phase diagram (the diagram in the absence of epitaxial growth), which we determined from RHEED data for (111)A InAs, is similar to the phase diagram of (111)A GaAs (Ref. 13). In the temperature region 200–550 °C and the As_4 pressure region from 10^{-9} Torr to 5×10^{-6} Torr there exists only one reconstruction: the $(2\times2)_v$ vacancy reconstruction. The (111)A face is incommensurate to the arsenic molecules (As_4,As_2). We have not observed any adsorption phases of arsenic. On the other hand, for the (111)B face various phases of arsenic exist.[13]

On the $(2\times2)_v$ reconstructed surface there are no intrinsic adatoms; therefore, adsorption of metal atoms onto this face, in contrast to adsorption onto Si or Ge, has a different character. Here reasons for the formation of the

 © 1998 American Institute of Physics

$(\sqrt{3}\times\sqrt{3})R30°$ phase are absent. Taking into account the chemical inertness of the (111)A surface with $(2\times2)_v$ reconstruction, at low temperatures of metal-atom deposition onto the surface one can expect disordered adsorption whereas at relatively high temperatures they will form three-dimensional clusters or droplets. For example, In condenses into three-dimensional islands on (110) GaAs already at room temperature, starting from $\theta=0.2$ monolayer.[14] Our data, however, on In adsorption onto InAs (111)A present a more complicated picture: along with the formation of three-dimensional indium islands, two-dimensional ordered phases are also formed (the $(2\times2)_a$ commensurate adsorption phase and the (0.77×0.77) incommensurate, densely packed phase).

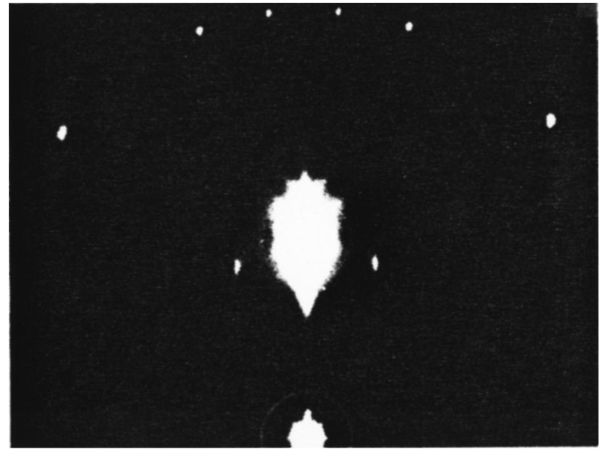

FIG. 1. RHEED pattern of the initial (111)A InAs surface with $(2\times2)_v$ reconstruction, azimuth [112]. $E_p=11$ keV.

EXPERIMENT

Surface-phase studies were carried out in a Riber molecular-beam epitaxy system with residual pressure 10^{-10} Torr equipped for reflection high-energy electron diffraction (RHEED, 7–15 keV). The RHEED patterns were analyzed with the aid of a ''Photon–micro'' video system. The procedure of chemical preparation of the samples before loading them into the chamber is described in previous papers.[15,16] The indium flux was calibrated by the standard oscillation technique for homo-epitaxial growth of InAs (001). Complete filling ($\theta=1$) corresponded to 6.3×10^{14} atoms/cm^2, which is equal to the number of indium surface atoms on an ideal unreconstructed InAs (111)A face. The surface temperature was determined with the help of a calibrated W–W/Re thermocouple.

RESULTS

To obtain one or another adsorption phase, the following cycle is commonly used: deposit a certain quantity of atoms onto the surface, anneal the sample at high temperatures, cool to room temperature. Phase diagrams for adsorption systems, as a rule, give only a qualitative picture of the nature of the phase transformations. Many surface phases in fact are metastable. To achieve true thermodynamic equilibrium usually requires prolonged annealing at some temperature.

To obtain indium adsorption phases, we started with the $(2\times2)_v$ reconstruction and the three-dimensional indium clusters coexisting with it on the surface. It should be noted that in the process of thermal cleaning of the surface in vacuum and preparation of the $(2\times2)_v$ reconstruction, formation of indium clusters is unavoidable due to decomposition of two-to-three surface layers damaged by chemical processing.

Let us briefly characterize diffraction from such a surface. On an atomically smooth (111)A InAs surface with $(2\times2)_v$ reconstruction, resonant scattering shows up clearly in the diffraction patterns.[15,16] As indicators of such scattering we may cite the resonance parabolas appearing in the background intensity, the high contrast of the pattern, and the abrupt increase of the intensity of the mirror reflection under resonant conditions of excitation. In Fig. 1 the resonance parabolas are plainly visible. In resonant scattering, the electron moves along the surface, but along the normal to the surface (transverse motion) it is found in one of the stationary states (a surface or bulk Bloch state) of the one-dimensional, laterally averaged scattering potential.[17]

Let us consider adsorption of indium onto this surface. In order to obtain the $(2\times2)_a$ adsorption phase, we also deposited approximately 10 monolayers of indium onto the $(2\times2)_v$ surface at a temperature of $T=300-350$ °C. At this temperature indium forms liquid three-dimensional clusters on the surface, but the RHEED pattern does not change. The sample must then be cooled to room temperature and kept at this temperature for not less than three hours. During this time the background resonance parabolas gradually disappear, and as a result diffuse background scattering increases and pattern contrast decreases. The ordinary (nonresonant) pattern with fractional point reflections arranged around the Laue circle appears. The characteristic dimensions of the phase domains and terrace widths do not change. The diffraction pattern of this new phase (the $(2\times2)_a$ phase) is shown in Fig. 2. The kinetics of formation of the $(2\times2)_a$ phase can be easily followed from ''quenching'' of the resonance parabola (Fig. 3). This ''quenching'' demonstrates the modification of the spectrum of states of the transverse motion of the electron caused by the change in the surface composition accompanying the phase transition $(2\times2)_v\rightarrow(2\times2)_a$. We observed a similar quenching of resonances during cesium adsorption to a (111)A InAs surface with $(2\times2)_v$ reconstruction.[16] The $(2\times2)_a$ phase cannot be obtained by direct deposition of indium onto the surface at room temperature. In our experiments a well-controlled indium flux deposited not less than 0.1 monolayer per second whereas formation of the $(2\times2)_a$ phase took 3–3.5 h, i.e., the process of phase formation is limited by kinetic factors.

The densely packed, incommensurate (0.77×0.77) phase is obtained by annealing a sample with the $(2\times2)_a$ adsorption phase at a temperature of 250–300 °C (Fig. 4). The transition from the $(2\times2)_a$ phase to the incommensurate (0.77×0.77) phase proceeds via the intermediate commensurate (1×1) phase. The intermediate phase can also be

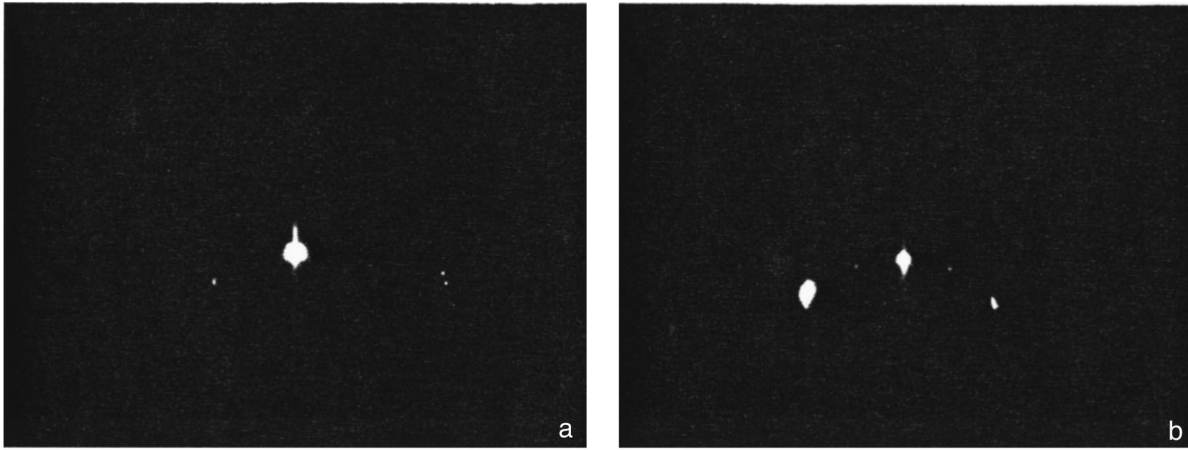

FIG. 2. RHEED pattern of the $(2\times2)_a$. $E_p=10$a adsorption phase. a)—azimuth $[\bar{1}12]$, b)—azimuth [110].

obtained by depositing indium on the vacancy phase from an external source up to complete filling ($\theta=1$) in the temperature range from room temperature down to 200 °C. During such deposition the (1/20) reflection disappears. In our opinion, the formation of the (1×1) adsorption phase is connected with the annihilation reaction of the In cation vacancy with the In adatom. This reaction leads to reverse rehybridization of the bonds of the surface atoms so that they revert to sp^3-hybridization. On each indium surface atom there again appears a half-filled dangling bond. Of course, such a surface will be unstable to saturation of dangling bonds by indium adatoms, supplied either from surface clusters or by an external source. At the given temperature the density of the lattice gas (mobile In adatoms) is governed by equilibrium with the condensed phase (In clusters).

Note also that the intermediate (1×1) phase, as a rule, arises when preparing densely packed phases from less dense

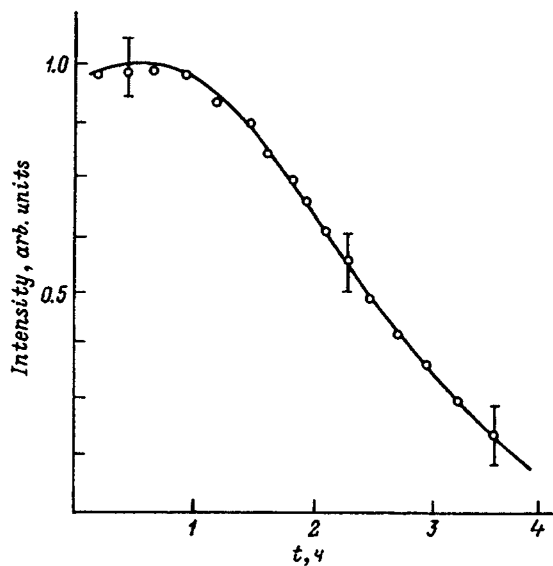

FIG. 3. ''Quenching'' of the phonon resonance parabola during the transition $(2\times2)_v\rightarrow(2\times2)_a$. The intensity of the parabola was measured at its intersection with the $(11)_{InAs}$ column in the $[\bar{1}12]$ azimuth. $T=25$ °C.

phases. As an example, it is observed during the transition $(\sqrt{3}\times\sqrt{3})R30°(\alpha)\rightarrow(1\times1)\rightarrow(\sqrt{3}\times\sqrt{3})R30°(\beta)$ of Pb phases on (111) Si and Ge surfaces.[1,3,8]

The fundamental reflections of the two-dimensional (0.77×0.77) phase, i.e., the (10) and $(\bar{1}0)$ reflections, show up near the possible location of the (4/30) and $(\bar{4}/30)$ columns for diffraction from (111)A InAs; however, exact measurements give

$$P=(10)_{InAs}/(10)_{In}=0.77\pm0.01,$$

which allows us to identify them as reflections of a new incommensurate phase. Besides the fundamental reflections, in this phase satellite reflections with scattering vectors

$$\mathbf{q}_t=\mathbf{g}_s-\mathbf{g}_a,$$

are distinctly observed, where $\mathbf{g}_a$ is the two-dimensional inverse lattice vector of the adsorbed In layer, $\mathbf{g}_s$ is the two-dimensional inverse lattice vector of the InAs substrate.

At around 350 °C the densely packed layer of In atoms melts, drops of liquid indium are formed, and the stable vacancy phase $(2\times2)_v$ appears, with a clearly manifested resonance. Note that the melting temperature of this phase is significantly higher than the melting temperature of crystalline indium ($T_m=157$ °C). On the other hand, the temperature of incongruent decomposition of the (111)A InAs surface is around 520 °C. This implies a strong interaction between the adsorbate and the substrate.

By cooling the sample once again to room temperature and holding it at this temperature for 3 h, it is possible to regain the $(2\times2)_a$ phase and reproduce all the phase transitions.

DISCUSSION

The adsorption phase $(2\times2)_a$. The phase transition $(2\times2)_v\rightarrow(2\times2)_a$ takes place at low temperatures and, consequently, the density of the lattice gas, i.e., of the mobile indium atoms on the surface is not large. On the other hand, noting that the (1×1) intermediate phase is formed from the $(2\times2)_v$ phase only for $\theta=1$, we take as the existence region

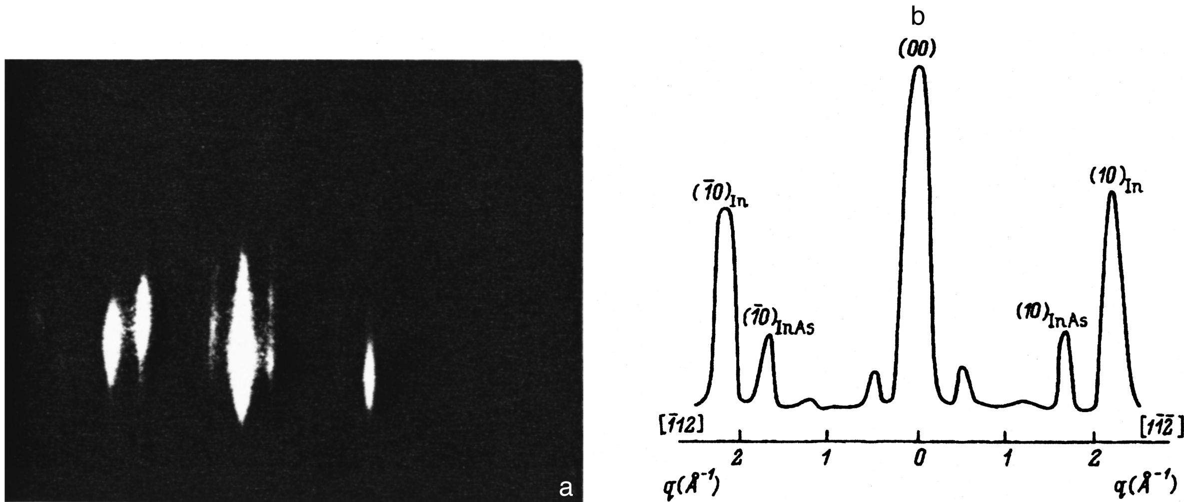

FIG. 4. a) RHEED pattern of the (0.77×0.77) phase, azimuth [110]. b) profiles of the intensity of the reflections in the [110] azimuth. The profiles were measured parallel to the projection of the edge of the sample on the diffractometer screen; reflections of the (0.77×0.77) phase and the fundamental InAs reflections are denoted $(10)_{In}$ and $(10)_{InAs}$, respectively.

of the $(2\times2)_a$ adsorption phase the interval of filling densities $\theta<1$, i.e., it is not densely packed. The stability of the $(2\times2)_a$ phase is low: an irreversible phase transition to the (1×1) phase occurs already at $T=90$ °C. Hence it follows that in the transition $(2\times2)_v\rightarrow(2\times2)_a$ the In adatoms, as they diffuse over the surface, attach themselves near vacancy sites, ''decorating'' the vacancy phase; however, annihilation of the vacancy by the adatom and rehybridization of bonds does not take place.

Note that for indium on (111) surfaces with filling densities $\theta<0.5$ the superstructure (2×2) is more characteristic than $(\sqrt{3}\times\sqrt{3})R30°$. For example, it is well known that indium on (111) Ge with $\theta<0.5$ forms structures with large periods of the type $m\times2\sqrt{3}$, where $m=13,12,11,10$ (Ref. 8). These structures consist of several (2×2) subcells with antiphase boundaries (boundaries 180° out of phase). In essence, indium adsorption here also decorates the (2×8) reconstruction.[8] We think that in the given system the appearance of antiphase boundaries is a consequence of partial relaxation of elastic strains in germanium created by adsorption of indium. In InAs the elastic constants are significantly smaller than in germanium (Ref. 10). There are no factors contributing to the formation of antiphase boundaries since no relaxation of elastic energy is gained here. Therefore the simple adsorption phase $(2\times2)_a$ is realized.

The incommensurate phase (0.77×0.77). As we have already noted, for the reflections of this phase we have

$$P=(10)\text{InAs}/(10)\text{In}=(11)\text{InAs}/(11)\text{In}=0.77\pm0.01$$

this coincides exactly with the ratio 2.85 Å/3.71 Å$=0.77$, where 3.71 Å is the distance between the rows of atoms in the (111) InAs plane arrayed along equivalent azimuths ⟨110⟩; 2.85 Å is the distance between the rows of atoms in the (111) plane of the tetragonal crystal In (fct), arrayed along the four azimuths $[10\bar{1}]$, $[\bar{1}01]$, [011], and $[0\bar{1}\bar{1}]$. Due to tetragonal distortion of the indium crystal $(c/a=1.076)$ the distance between the rows of atoms arrayed along the two other azimuths [110] and $[\bar{1}\bar{1}0]$ is equal to 2.96 Å. For these azimuths we should have $P=2.96$ Å/3.71 Å$=0.8$. Experimentally, however, we do not observe a difference in P for any of the azimuths. For all of the azimuths $P=0.77\pm0.01$. Consequently, the incommensurate phase represents the (111) plane of the face-centered cubic crystal In (fcc). In order to ''obtain the transition'' (111)In$(fct)\rightarrow$(111)In(fcc) it is necessary to stretch the bonds in the [110] direction from 3.25 to 3.29 AA and compress them in the $[\bar{1}12]$ direction (normal to the [110] direction) from 3.38 to 3.29 Å (see Fig. 5). However, in this process the largest distance between the rows of atoms, equal to 2.85 Å and characteristic for In (fct), is preserved.

It is interesting to compare our data with the data on indium adsorption on (111) Ge of Ref. 8. The authors of this paper identified the diffraction reflections produced by indium adsorption with $\theta>1$ as reflections from the (111) plane of the In (fct) crystal. However, they did not provide any proofs of tetragonal distortion of the (111) In plane. From the diffraction patterns presented in Ref. 8, it is possible to determine the ratio $P=(10)_{Ge}/(10)_{In}$. We find $P=0.82\pm0.01$. This value corresponds exactly to the ratio 3.29 Å/4.00 Å$=0.82$, where 3.29 Å is the interatomic distance for the (111) In (fcc) plane as determined by us (see Fig. 5); 4.00 Å the interatomic distance in the (111) Ge plane. Most probably, the authors of Ref. 8 observed the (111) In (fcc) plane. Precisely for this reason they were able to conclude that this plane is found in epitaxial relation with the (111) Ge plane, and the azimuths—in the relation $\langle110\rangle_{In}\|\langle110\rangle_{Ge}$ (Ref. 8). If tetragonal distortion were present, then parallel arrangement of all the azimuths would be impossible.

It is well known that tetragonal distortion of indium crystal is a consequence of instability of the fcc structure to splitting of the set of inverse vectors {002} (Ref. 18). In the In (fcc) structure the inverse vectors **g** from the set {002} are located close to the point q_0, where the Fourier transform of the pseudopotential of the indium atom as a function of the

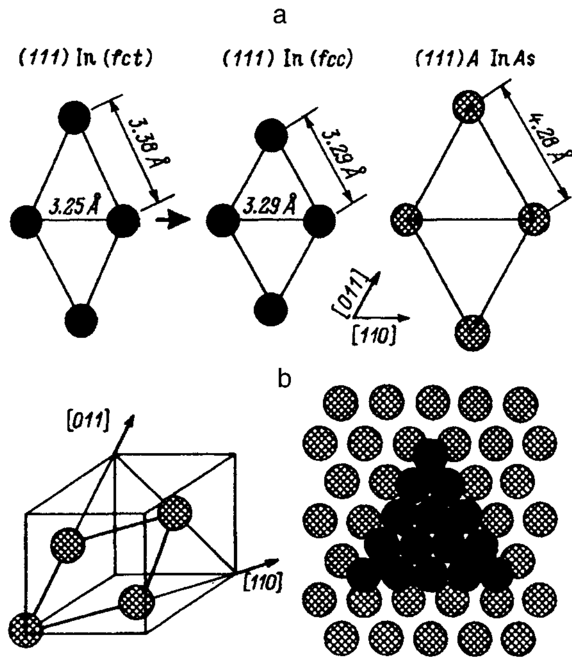

FIG. 5. a) Diagram of the structural transition (111)In(fct)→(111)In(fcc). b) Structural model of the (0.77×0.77) phase on a (111)A InAs surface.

inverse vector **q** passes through 0, i.e., $V(q_0)=0$. It was shown in Ref. 18 that a diminution of the energy band structure of the In (fcc) crystal takes place if some of the {002} inverse vectors decrease somewhat and the others increase, i.e. the vectors **g** "withdraw" from the point q_0. This then leads to a tetragonal distortion of the indium crystal structure. We, however, are dealing here with the two-dimensional (111) In plane, for which the set of inverse vectors {002} is absent; consequently, possible reasons for tetragonal distortion are also absent.

As noted above, besides the main reflections of the (0.77×0.77) phase we also observe a number of other reflections (satellite reflections) in the diffraction pattern. It is natural to explain the satellite reflections (as in the case of the melting temperature of the phase) in terms of a substantial interaction between the incommensurate indium phase and the substrate lattice. Under this assumption, the atomic positions of both of the lattices will be modulated by the periodicity of the other. Since the substrate is more rigid than the layer of adsorbate, it is mainly the atomic positions of the adsorbate that will be modulated.

If we denote the position of the jth indium adatom as $\mathbf{R}_j$, in the absence of an interaction the position of the jth atom will be

$$\mathbf{R}_j+\mathbf{U}_j,$$

where $\mathbf{U}_j$ is the small displacement of the adatom when acted upon by the periodic potential of the substrate. Expanding the periodic potential in the inverse vectors $\mathbf{g}_s$ of the substrate gives

$$V_s(\mathbf{r})=\sum_{g_s} V_g e^{i\mathbf{g}_s\mathbf{r}}. \tag{1}$$

Assuming linear dependence of the displacement on the substrate potential, we have

$$\mathbf{U}_j=\sum_{g_s} U_g e^{i\mathbf{g}_s\mathbf{R}_j}. \tag{2}$$

The scattering amplitude for scattering through the vector **q** is defined in the usual way:

$$\begin{aligned} A(\mathbf{q}) &= \sum_j e^{-i\mathbf{q}(\mathbf{R}_j+\mathbf{U}_j)}=\sum_j F_j e^{-i\mathbf{q}\mathbf{R}_j}(1-i\mathbf{q}\mathbf{U}_j+\dots) \\ &= NF(\mathbf{q})\Bigg[\sum_{\mathbf{g}_a}\delta(\mathbf{q}_t-\mathbf{g}_a) \\ &\quad -i\sum_{\mathbf{g}_a}\sum_{\mathbf{g}_s}\mathbf{q}U_g\delta(\mathbf{q}_t-(\mathbf{g}_a-\mathbf{g}_s))\Bigg], \end{aligned} \tag{3}$$

where N is the number of indium adatoms taking part in the scattering, $F(q)$ is the scattering amplitude of the adatom, $\delta(x)$ is the Dirac delta function, $\mathbf{q}_t$ is the component of the scattering vector parallel to the surface.

The first term of expression (3) defines the principal diffraction reflections of the incommensurate (0.77×0.77) phase. The second term represents the satellite reflections appearing for $\mathbf{q}_t=\mathbf{g}_a-\mathbf{g}_s$.

According to the diffraction data, the incommensurate (0.77×0.77) phase is found in the following epitaxial relation with the (111)A surface: $\langle 110\rangle_{\mathrm{In}}\|\langle 110\rangle_{\mathrm{InAs}}$. If we decrease the shortest distance between indium atoms in this phase by 2.4%, then the commensurate, densely packed (3×3) indium phase will appear. On the other hand, in the epitaxial relation $\langle 110\rangle_{\mathrm{In}}\|\langle 112\rangle_{\mathrm{InAs}}$ to obtain the commensurate phase $(2\sqrt{3}\times 2\sqrt{3})$ it would be necessary to lengthen the In–In bonds in the (0.77×0.77) phase by 11.3%. Therefore, the incommensurability is less for the epitaxial relation $\langle 110\rangle_{\mathrm{In}}\|\langle 110\rangle_{\mathrm{InAs}}$ and a greater relaxation of elastic energy is realized here.

Some relaxation of incommensurate elastic energy could be achieved if the densely packed phase (0.77×0.77) were realized by domains tilted relative to the substrate by small angles α satisfying the following relations:

$$m\mathbf{b}_1=n_1\mathbf{a}_1+n_2\mathbf{a}_2,$$

$$\sin\alpha=\sqrt{3}n_2/2(n_1^2+n_2^2+n_1n_2)^{1/2},$$

where $\mathbf{b}_1$ and $\mathbf{b}_2$ are the vectors of the unit cell of the adsorbate, $\mathbf{a}_1$ and $\mathbf{a}_2$ are the vectors of the unit cell of the substrate, and m, n_1, and n_2 are integers. In fact, such a tilting of the domains is equivalent to transformation of the incommensurate phase into the long-period commensurate structure. For example, in our case for $m=30$, $n_1=23$, $n_2=1$ we have $\alpha=2.1°$, and for $m=17$, $n_1=13$, $n_2=1$ we have $\alpha=4°$, etc. However, we have not observed any domains tilted by small angles in our experiments. On the other hand, when indium is adsorbed ($\theta>0.6$) on (111) Si and Ge the series of commensurate phases $(\sqrt{31}\times\sqrt{31})R\pm 9°$ and $(\sqrt{61}\times\sqrt{61})R30°\pm 4°$ is formed.[7,8] Here again, as we believe, substantial differences in the elastic constants of InAs and Si, Ge are manifested. In systems with strong bonds relaxation of the elastic strains upon adsorption of indium

leads to the creation of long-period domain superstructures either with antiphase boundaries or with tilting of the domains by small angles.

To summarize, we have detected for the first time and characterized three different adsorption phases of indium on the (111)A surface of InAs: the commensurate phases $(2\times2)_a$ and (1×1), and the incommensurate phase (0.77×0.77). On the basis of an analysis of the diffraction data we have proposed a structural model of the incommensurate (0.77×0.77) phase as a densely packed (111) layer of In (fcc), existing in epitaxial relation with the substrate: $\langle110\rangle_{\mathrm{In}}\|\langle110\rangle_{\mathrm{InAs}}$. We have analyzed the reasons for the realization of the (fcc) structure and not the usual indium crystal structure: (fct). We have shown that the incommensurate phase is spatially modulated by the periodic substrate potential. At high temperatures the indium adatoms condense into three-dimensional islands. A comparative analysis of our data on indium adsorption onto a (111) InAs surface and the data in the literature on indium adsorption onto (111) Si, Ge surfaces reveals the importance of relaxation of the elastic strains in the formation of two-dimensional adsorption-induced superstructures.

The authors thank the Russian Fund for Fundamental Research for support of this work (Grant No. 96-03-33916-a).

*E-mail: marah@isp.nse.ru

[1] E. Canz, I. Hwang, F. Xiong, S. Theiss, and J. Golovchenko, Surf. Sci. **257**, 259 (1991).
[2] R. Shioda, A. Kawarn, A. Baski, C. Quate, and J. Nogami, Phys. Rev. B **48**, 4895 (1993).
[3] H. Weitering, D. Heslinga, and T. Hibma, Phys. Rev. B **45**, 5991 (1992).
[4] D. M. Cornelison, C. S. Chang, and I. S. Tsong, J. Vac. Sci. Technol. A **8**, 3443 (1990).
[5] J. J. Lander and J. Morrison, Surf. Sci. **2**, 553 (1964).
[6] H. Hirayama, T. Tatsumi, and N. Aizaki, Surf. Sci. **193**, L47 (1988).
[7] T. Aiyama and Sh. Ino, Surf. Sci. **82**, L585 (1979).
[8] T. Ichikawa, Surf. Sci. **111**, 227 (1981).
[9] M. Bertucci, L. Lay, M. Manneville, and R. Kern, Surf. Sci. **85**, 471 (1979).
[10] W. Monch, *Semiconductor Surfaces and Interfaces* (Springer, Berlin, 1993), p. 180.
[11] J. M. Thornton, P. Unsworth, M. D. Jackson, P. Weightman, and D. A. Woolf, Surf. Sci. **316**, 231 (1994).
[12] D. J. Chaki, Phys. Rev. Lett. **52**, 1911 (1984).
[13] D. A. Woolf, D. J. Westwood, and R. H. Williams, Appl. Phys. Lett. **62**, 1370 (1993).
[14] D. E. Savage and M. G. Lagally, J. Vac. Sci. Technol. **4**, 943 (1986).
[15] Yu. G. Galitsyn, V. G. Mansurov, and V. I. Poshevnev, Poverkhnost', No. 4, 25 (1993).
[16] Yu. G. Galitsyn, V. G. Mansurov, and V. I. Poshevnev, Poverkhnost', No. 8–9, 81 (1994).
[17] S. L. Dudarev and M. J. Whelan, Int. J. Mod. Phys. B **10**, 133 (1996).
[18] V. Heine and D. Weaire, Phys. Rev. **152**, 603 (1966).

Translated by Paul F. Schippnick

Formation of InAs quantum dots in a GaAs matrix during growth on misoriented substrates

A. F. Tsatsul'nikov, B. V. Volovik, N. N. Ledentsov, M. V. Maksimov, A. Yu. Egorov, A. E. Zhukov, A. R. Kovsh, V. M. Ustinov, Chao Chen, P. S. Kop'ev, and Zh. I. Alfërov

A. F. Ioffe Physicotechnical Institute, Russian Academy of Sciences, 194021 St. Petersburg, Russia

V. N. Petrov and G. É. Tsirlin

Institute of Analytical Instrumentation, Russian Academy of Sciences, 198103 St. Petersburg, Russia

D. Bimberg

Institute für Festkörperphysik, Technische Universität Berlin, D-10623 Berlin, Germany

(Submitted 29 May 1997; accepted for publication 3 June 1997)
Fiz. Tekh. Poluprovodn. **32**, 95–100 (January 1998)

The formation of InAs quantum dots grown by submonolayer migration-enhanced molecular-beam epitaxy on GaAs(100) surfaces with various misorientation angles and directions is investigated. It is shown for the deposition of 2 monolayers (ML) of InAs that increasing the misorientation angle above 3° along the [010], [0$\bar{1}\bar{1}$], and [011] directions leads to the formation of several groups of quantum dots differing in geometric dimensions and electronic structure. © *1998 American Institute of Physics.* [S1063-7826(98)02401-6]

1. INTRODUCTION

Great importance has recently been attached in semiconductor physics to structures with quantum dots (QD's), i.e., objects having bounds in all three spatial directions. The most widely used method to obtain such objects utilizes the influence of the spontaneous transformation of a stressed (In, Ga)As layer on an (Al, Ga)As surface into an array of homogeneous islands.[1–3] The use of these QD's as the active region of semiconductor injection lasers permitted the creation of lasers with high-temperature stability and a low threshold current density and the generation of laser output with a power of the order of 1 W in a cw regime at room temperature.[4–6] Improvement of the characteristics of QD lasers calls for reduction of the size dispersion of the QD's, which would lead to narrowing of the photoluminescence (PL) line. There are several techniques to controllably influence the dimensions of QD's, viz., the formation of equilibrium QD's,[7] the vertically self-organized growth of QD'S,[8,9] and the deposition of QD's on misoriented surfaces.[10–12]

In the present work we investigated the optical properties of InAs quantum dots deposited on a GaAs(100) surface misoriented along different crystallographic directions. Misorientation of the surface leads to the appearance of terraces, whose dimensions depend on the misorientation angle. The appearance of such terraces has an influence on the energetics of the surface, which can ensure better orientational ordering of the QD's.[13] In addition, the degree and direction of misorientation strongly influence the lateral dimensions of the QD's formed.[10,11] Our investigations demonstrate the existence of several metastable groups of QD's of different size following the deposition of an InAs layer on a misoriented GaAs surface. The formation and dimensions of such QD's are determined by the misorientation angle and direction, as well as by the quantity of InAs deposited.

2. EXPERIMENT

The growth experiments were performed on a Riber-32 molecular-beam epitaxy system on vicinal substrates of semi-insulating GaAs(100) with different misorientation angles and directions. Several samples with different misorientation angles and directions were simultaneously pasted onto a molybdenum sample holder using indium. The growth processes were carried out with constant rotation of the sample holder for the purpose of reducing the influence of nonuniformity of the molecular flows and the temperature field of the holder heating element. After removal of the oxide layer in the growth chamber in a stream of As, a GaAs buffer layer with a thickness of 300 nm was grown at a substrate temperature $T_s = 630\,°C$. In our case this temperature corresponds to the point of the (2×4) to (3×1) surface reconstruction transition and was selected on the basis of considerations for improving the electrical and optical parameters of the layers.[14] After the buffer layer, a superlattice consisting of five GaAs/$Al_{0.3}Ga_{0.7}As$ (2 nm/2 nm) pairs of layers was grown for the purpose of eliminating the possibility of the diffusion of nonequilibrium carriers into the semi-insulating substrate with a high concentration of deep-level impurities (Cr). Next, a GaAs layer with a thickness of 7 nm was grown, and the temperature of the sample in the stream of As was lowered to $T_s = 470\,°C$ [the point of the (2×4) to (2×2) surface reconstruction transition]. The active layer was grown in a submonolayer migration-enhanced epitaxy regime[11] involving the cyclic deposition of In (in the absence of a stream of As) in the amount needed for the deposition of

 © 1998 American Institute of Physics

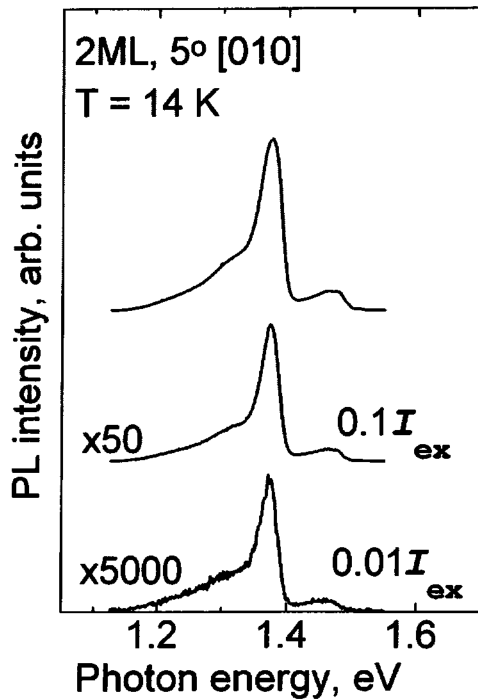

FIG. 1. Photoluminescence spectra of structures with 2 ML of InAs deposited on a substrate misoriented by 5° along the crystallographic directions indicated in the figure.

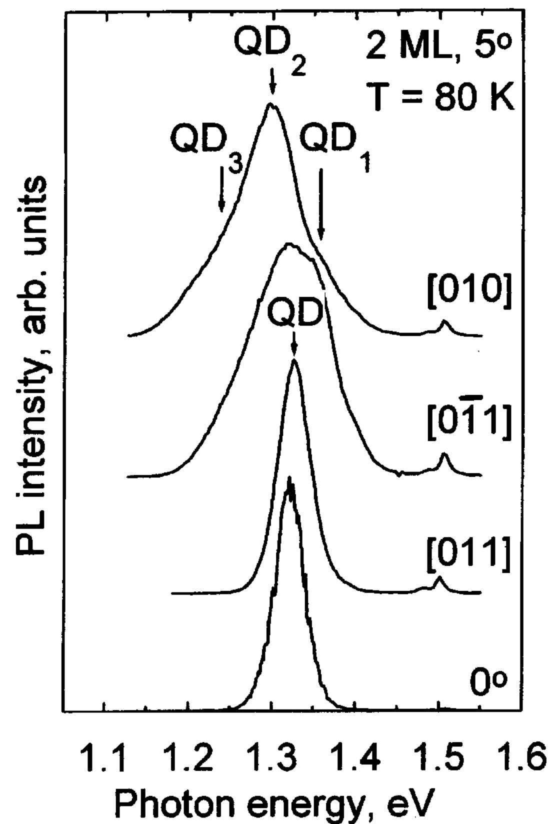

FIG. 2. Photoluminescence spectra of a sample with 2 ML of InAs deposited on a substrate misoriented by 5° relative to the [010] direction for various intensities of the exciting light I_{ex}.

0.5 ML of InAs followed by holding for $2-30$ s in a stream of As. The total nominal thickness of the InAs layer amounted to 2 or 3 ML (four or six deposition cycles). After completion of the procedure for growing the active layer, a layer of GaAs with a thickness of 7 nm was grown at the same temperature. Then, the temperature $T_s = 630$ °C was established, and a layer of GaAs with a thickness of 7 nm was grown. Afterwards a superlattice consisting of five $GaAs/Al_{0.3}Ga_{0.7}As$ (2 nm/2 nm) pairs of layers was grown for the purpose of eliminating the possibility of recombination. During the growth of the superlattices, the surface of the sample was held in a stream of As for 20 s after each GaAs layer. The As pressure in the growth chamber was maintained constant at the 4×10^{-6} Torr level in all the experiments. The values of the precalibrated flows of Ga, Al, and In were established such that the growth rates of GaAs, AlGaAs, and InAs were equal to 0.5, 0.68, and 0.1 ML. The growth rates were measured using a system for observing oscillations of a reflection high-energy electron diffraction (RHEED) specular reflection[15] with a primary beam energy equal to 10 keV.

The photoluminescence was excited by an Ar^+ laser and detected by a cooled photomultiplier. The PL investigations were performed in a closed-cycle liquid-helium temperature cryostat.

3. RESULTS AND DISCUSSION

Figure 1 presents the PL spectra of structures containing an InAs layer with a thickness of 2 ML grown on an exactly oriented (100) substrate (sample 2-0) and substrates misoriented by 5° along various crystallographic directions. As is seen from this figure, the spectra of the samples grown on substrates with misorientation along the [010], $[0\bar{1}\bar{1}]$, and [011] directions (below referred to as samples 2-5[010], 2-5 $[0\bar{1}\bar{1}]$, and 2-5[011]) are different. Misorientation along the [010] and $[0\bar{1}\bar{1}]$ directions results in the appearance of three PL lines, which are designated in Fig. 1 as QD_1, QD_2, and QD_3. Under these conditions the spectrum of sample 2-5[011] displays only a single line QD, whose position coincides with the band in the PL spectrum of sample 2-0. A decrease in the intensity of the exciting light at $T=14$ K (when the heat-induced release of the carriers from the localized states is basically suppressed) does not cause a significant change in the form of the PL spectrum of sample 2-5[010] (Fig. 2). This is evidence that lines QD_1, QD_2, and QD_3 are associated with recombination through different objects.

An increase in the effective thickness of the InAs deposited to 3 ML causes line QD_3 to become dominant in the PL spectrum (Fig. 3). Its position (at 1.24 eV) nearly coincides with the position of line QD_3 in the spectrum of the samples with 2 ML of InAs. We assume that band QD_3 is caused by recombination through the equilibrium quantum dots for migration-enhanced epitaxy.[7] At the same time, in the spectrum of structure 3-0 (the lower curve in Fig. 3), which was grown on an exactly oriented substrate, band QD_3 is weakly expressed, and short-wavelength line QD, which is associated with QD dots of small size, is the principal band. Thus,

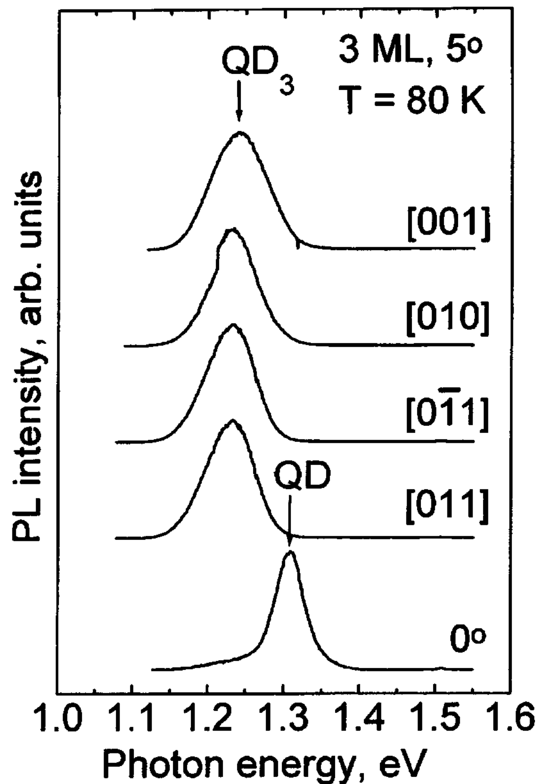

FIG. 3. Photoluminescence spectra for structures with 3 ML of InAs deposited on a substrate misoriented by 5° along the crystallographic directions indicated in the figure.

misorientation leads to an increase in the probability of equilibrium QD's, in agreement with the data obtained using scanning tunneling microscopy in Ref. 12. Figure 4 shows the PL spectra of structures 2-5[010], 2-5[$0\overline{11}$], and 2-5[011] measured at a different temperature (the short-wavelength shift of each curve is specified by the corresponding temperature change in the GaAs gap width). As is seen from this figure, band QD_1 is dominant in the spectra of samples 2-5[010] and 2-5[$0\overline{11}$] at low temperature. Raising the temperature to about 70 K results in a drop in the intensity of this band, and band QD_2 becomes the principal line in the spectrum. A further increase in the temperature causes line QD_3 to become dominant. All the lines exhibit a long-wavelength shift of the maximum with increasing temperature, which is typical of PL caused by QD's. Line QD_1 is also dominant in the spectrum of sample 2-5[011] at low temperatures. Increasing the temperature to about 100 K results in the predominance of band QD_2 in the spectrum. Band QD_3 is absent from the spectrum of this structure. Thus, the results obtained provide evidence that equilibrium QD's did not form in sample 2-5[011] under these conditions.

The positions of the maxima of lines QD_1, QD_2, and QD_3 for the structures investigated are listed in Table I. As we see, the positions of bands QD_1 and QD_2 for samples 2-5[010] and 2-5[$0\overline{11}$] coincide. At the same time, line QD_3 in the spectrum of structure 2-5[$0\overline{11}$] is shifted to a shorter wavelength by about 30 meV in comparison to the same line in the spectrum of structure 2-5[010], attesting to a decrease in the dimensions of the QD's causing this line in sample 2-5[$0\overline{11}$]. Sample 2-5[011] displays a short-wavelength shift of line QD_2 and a long-wavelength shift of band QD_1, which also attest to changes in the dimensions of the QD's when they form on a GaAs surface of this orientation.

To investigate the nature of the appearance of lines QD_1 and QD_2 we studied the photoluminescence excitation spectra and the variation of the shape of the PL spectrum as the energy of the exciting line is varied (Fig. 5) for sample 2-5[010]. As is seen from the excitation spectrum of line QD_2, when the excitation energy closely approximates the recording energy, a significant drop in the PL intensity oc-

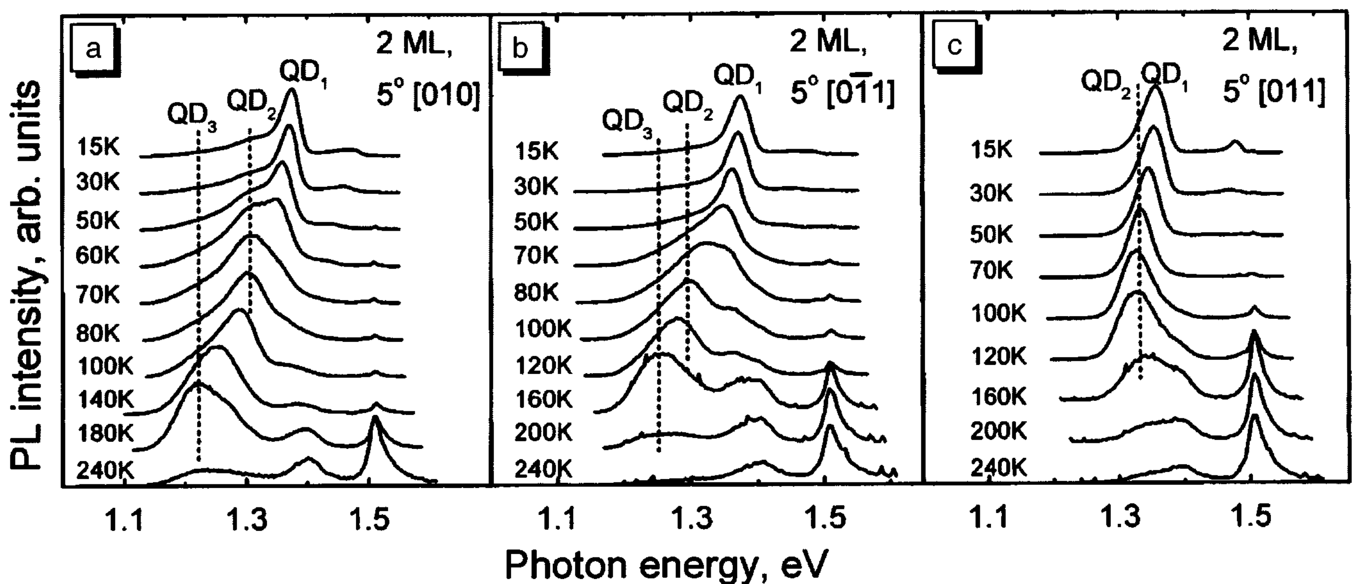

FIG. 4. Photoluminescence spectra of structures with 2 ML of InAs deposited on a substrate misoriented by 5° relative to various directions: a — [010], b — [$0\bar{1}1$], c — [011]. The measurement temperature is indicated near the curves.

TABLE I.

Misorientation angle, deg	Terrace length L, Å	Misorientation direction	Position of lines in spectra QD_1, meV	QD_2, meV	QD_3, meV
3	60	[010]	–	1.32	–
5	35	[010]	1375±5	1300±5	1220±5
		$[0\bar{1}\bar{1}]$	1373±5	1300±10	1250±5
		[011]	1355±5	1325±5	–
7	23	[010]	1376±5	1292±5	1261±5

curs. Such PL behavior is typical of QD's and is due to the δ-type density of states in QD's. Photoluminescence appears when the energy of the exciting light is in resonance with excited states in the QD's. In addition, this points out the absence of the transfer of nonequilibrium carriers between QD's at low temperature. The excitation spectrum of band QD_2 contains a maximum, which shifts in response to variation of the recording energy in such a manner that the energy difference between the position of that maximum and the recording energy remains constant. It amounts to about 30 meV, which corresponds to the energy of an LO phonon in InAs. Moreover, decreasing the energy of the exciting light to values that are smaller than the gap width of GaAs causes line QD_2 to become dominant in the spectrum. Such PL behavior is probably stipulated by the phonon mechanism of carrier trapping in QD's. If the binding energy of an electron in the QD's with which band QD_2 is associated is smaller than the energy of an LO phonon in InAs, it can lead to slower carrier trapping in such QD's when electron-hole pairs are excited by light with an energy greater than the GaAs band width. Upon resonant excitation electron-hole pairs are generated directly in excited states of the QD's. This also causes a change in the intensity of line QD_2.

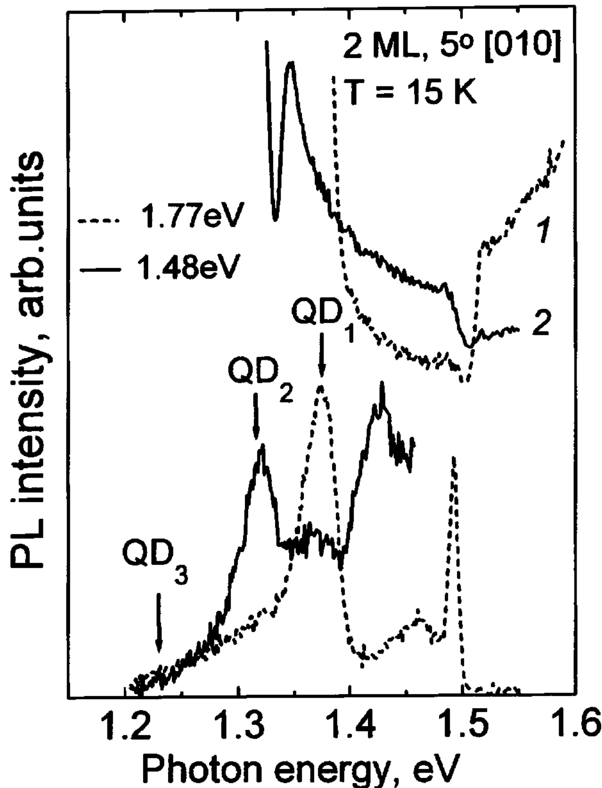

FIG. 5. Photoluminescence excitation spectra (upper curves) and photoluminescence spectra (lower curves) of sample 2-5[010] for excitation by light with different wavelengths. The recording energies of excitation spectra *1* and *2* coincide with the maxima of lines QD_1 and QD_2, respectively.

To study the influence of misorientation on the PL we also investigated structures with different misorientation angles, i.e., with different terrace lengths. The spectrum of the sample with 2 ML of InAs and 3° misorientation (sample 2-3[010]) contains only one line, which is shifted by about 10 meV to a longer wavelength relative to the band of the QD's in the sample grown on an exactly oriented substrate (Fig. 6). Increasing the misorientation angle to 5° along the [010] and $[0\bar{1}\bar{1}]$ directions, as we have already shown above, results in splitting of the PL line into three bands. A further increase in the misorientation angle to 7° (sample 2-7[010]) does not cause any change in the spectral positions of lines QD_1 and QD_2 (Fig. 7). Thus, the dimensions of the QD's, with which these bands are associated, apparently remained nearly constant. At the same time, a considerable shift of line QD_3 toward higher photon energies is observed. A similar short-wavelength shift in response to an increase in the degree of misorientation was observed for the PL lines in the spectra of the samples with 2 ML of InAs misoriented along the [011] direction and for the samples with 3 ML of InAs misoriented along the $[0\bar{1}\bar{1}]$ and [010] directions. Table I presents the positions of the maxima of lines QD_1, QD_2, and QD_3 for structures with various degrees of misorientation and values of the terrace length L. It is seen from this table that as soon as the terrace length becomes less than 60 Å, the PL lines split into three bands in the case of misorientation along the [010] direction. This can be attributed to the fact that the terrace length becomes smaller than the length of the base of the QD's. Increasing the degree of misorientation leads to a considerable shift of band QD_3 to a shorter wavelength, which is apparently attributable to alteration of the geometric dimensions of the QD's with which this line is associated.

Thus, it has been shown that increasing the misorientation angle leads to alteration of the dimensions of the QD's obtained. Misorientation along the [010] and $[0\bar{1}\bar{1}]$ directions has the strongest influence. When 2 ML of InAs are deposited on a GaAs surface misoriented along these directions, groups of QD's of different size form. However, the formation of QD's of identical size can be controlled by

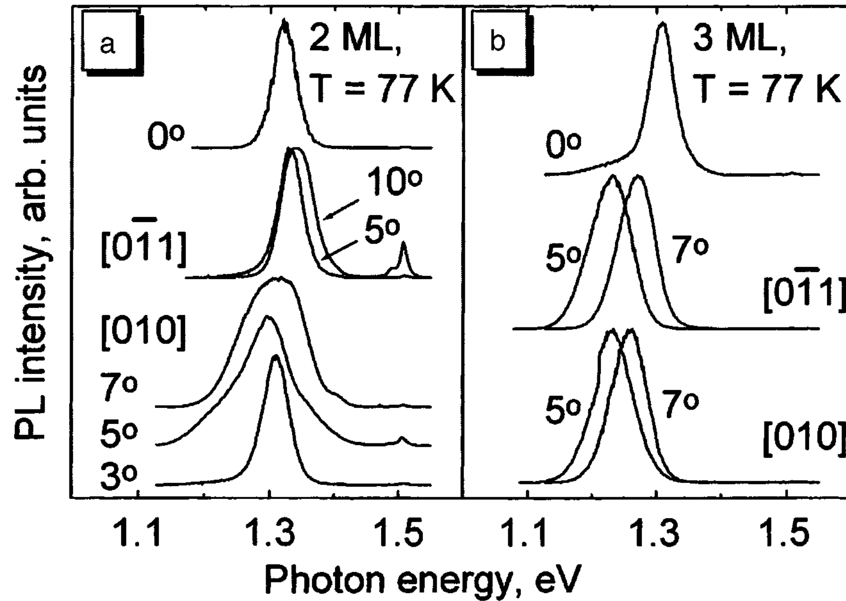

FIG. 6. Photoluminescence spectra of structures with different thicknesses of the InAs layer in monolayer units: a — 2, b — 3. The measurement temperature, direction, and misorientation angle are indicated in the figures.

selecting the misorientation angle and direction. Since the QD's formed in the case of the deposition of 2 ML of InAs are promising for employment in injection lasers,[4] the results obtained attest to the possibility of narrowing the amplification spectrum of such lasers.

We wish to thank D. N. Demidov and N. P. Korneeva for their assistance in performing the experiments on growing the structures.

This work was carried out with partial support from the Russian Foundation for Fundamental Research (Grants 95-02-05084-a, 96-02-17824, and 95-618), INTAS (Grant 94-1028), the Volkswagen Foundation, and the Physics of Solid-State Nanostructures Scientific Program.

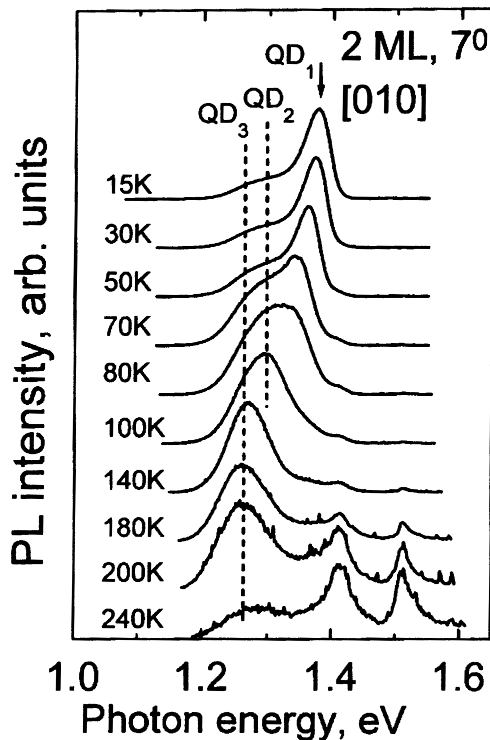

FIG. 7. Photoluminescence spectra of structures with 2 ML of InAs misoriented by 7° along the [010] direction. The temperature at which the spectra were measured is indicated near the curves.

[1] L. Goldstein, F. Glass, J. Y. Marzin, M. N. Charasse, and G. Le Roux, Appl. Phys. Lett. **47**, 1099 (1985).

[2] P. M. Petroff and S. P. Den Baars, Superlattices Microstruct. **15**, 15 (1994).

[3] M. Moison, F. Houzay, F. Barthe, L. Leprince, E. Andre, and O. Vatel, Appl. Phys. Lett. **64**, 196 (1994).

[4] Zh. I. Alferov, N. A. Bert, A. Yu. Egorov, A. E. Zhukov, P. S. Kop'ev, A. O. Kosogov, I. L. Krestnikov, N. N. Ledentsov, A. V. Lunev, M. V. Maksimov, A. V. Sakharov, V. M. Ustinov, A. F. Tsatsul'nikov, Yu. M. Shernyakov, and D. Bimberg, Fiz. Tekh. Poluprovodn. **30**, 351 (1996) [Semiconductors **30**, 194 (1996)].

[5] Zh. I. Alferov, N. Yu. Gordeev, S. V. Zaĭtsev, P. S. Kop'ev, I. V. Kochnev, V. V. Komin, I. L. Krestnikov, N. N. Ledentsov, A. V. Lunev, M. V. Maksimov, S. S. Ruvimov, A. V. Sakharov, A. F. Tsatsul'nikov, Yu. M. Shernyakov, and D. Bimberg, Fiz. Tekh. Poluprovodn. **30**, 357 (1996) [Semiconductors **30**, 197 (1996)].

[6] Yu. M. Shernyakov, A. Yu. Egorov, A. E. Zhukov, S. V. Zaĭtsev, A. R. Kovsh, I. L. Krestnikov, A. V. Lunev, N. N. Ledentsov, M. V. Maksimov, A. V. Sakharov, V. M. Ustinov, Chao Chen, P. S. Kop'ev, Zh. I. Alferov, and D. Bimberg, Pis'ma Zh. Tekh. Fiz. **23**(4), 51 (1997) [Tech. Phys. Lett. **23**, 149 (1997)].

[7] N. N. Ledentsov, M. Grundmann, N. Kirstaedter, O. Schmidt, R. Heitz, J. Bohrer, D. Bimberg, V. M. Ustinov, V. A. Shchukin, A. Yu. Egorov, A. E. Zhukov, S. Zaitsev, P. S. Kop'ev, Zh. I. Alferov, S. S. Ruvimov, P. Werner, and U. Gosele, in *Modulated Semiconductor Structures (MSS-7)*, invited paper.

[8] Q. Xie, A. Madhukar, P. Chen, and N. Kobayashi, Phys. Rev. Lett. **75**, 2542 (1995).

[9] A. Yu. Egorov, A. E. Zhukov, P. S. Kop'ev, N. N. Ledentsov, M. V. Maksimov, V. M. Ustinov, a. f. tsatsul'nikov, N. A. Bert, A. O. Kosogov, D. Bimberg, and Zh. I. Alferov, Fiz. Tekh. Poluprovodn. **30**, 1682 (1996) [Semiconductors **30**, 879 (1996)].

[10] A. Sasaki, Thin Solid Films **267**, 24 (1995).

[11] G. É. Tsyrlin, A. O. Golubok, S. Ya. Tipisev, N. N. Ledentsov, and G. M. Gur'yanov, Fiz. Tekh. Poluprovodn. **29**, 1697 (1995) [Semiconductors **29**, 884 (1995)].
[12] G. E. Cirlin, V. N. Petrov, N. K. Polykov, V. N. Demidov, N. P. Korneeva, A. O. Golubok, S. Ya. Tipissev, V. G. Dubrovskii, G. M. Guryanov, M. V. Maximov, N. N. Ledentsov, and D. Bimberg, in *Proceedings of the International Symposium ''Nanostructures: Physics and Technology,''* St. Petersburg, Russia (1996), p. 375.
[13] G. E. Cirlin, G. M. Guryanov, A. O. Golubok, S. Ya. Tipissev, N. N. Ledentsov, P. S. Kop'ev, M. Grundmann, and D. Bimberg, Appl. Phys. Lett. **67**, 97 (1995).
[14] V. V. Gubanov, G. M. Gur'yanov, N. N. Ledentsov, V. N. Petrov, Yu. B. Samsonenko, and G. É. Tsyrlin, Pis'ma Zh. Tekh. Fiz. **19**(21), 73 (1993) [Tech. Phys. Lett. **19**, 695 (1993)].
[15] G. M. Gur'yanov, V. N. Demidov, N. P. Korneeva, V. N. Petrov, Yu. B. Samsonenko, and G. É. Tsyrlin, Zh. Tekh. Fiz. **67**(8) , 111 (1997) [Tech. Phys. **42**, 956 (1997)].

Translated by P. Shelnitz

Exciton polaritons in long-period quantum-well structures

M. R. Vladimirova, E. L. Ivchenko, and A. V. Kavokin

A. F. Ioffe Physicotechnical Institute, Russian Academy of Sciences, 194021 St. Petersburg, Russia
(Submitted 29 May 1997; accepted for publication 3 June 1997)
Fiz. Tekh. Poluprovodn. **32**, 101–107 (January 1998)

The distribution of the normal frequencies in the complex plane for the exciton polaritons in a finite periodic quantum-well structure is analyzed by matrix-theory methods. Relations governing the sums of the normal frequencies for polariton modes that are even and odd relative to the center of the structure are derived. It is shown in an anti-Bragg structure, whose period equals a quarter of the optical wavelength at the excitonic resonance frequency ω_0, that the sets of the natural frequencies corresponding to even and odd solutions transform into one another upon reflection relative to the vertical line $\omega=\omega_0$. Approximate analytical expressions are found for the natural frequencies of the ''long-lived'' and ''short-lived'' polariton modes. The relation between the shape of the optical reflection spectrum and the set of natural frequencies of the system is elucidated. © *1998 American Institute of Physics.*
[S1063-7826(98)02501-0]

The exciton-photon interaction in bulk crystals is known to lead to the formation of mixed excitations of exciton polaritons, which propagate to infinite distances without damping when the interaction of the exciton with phonons and static defects is ignored. The picture of the formation of exciton polaritons in infinite periodic quantum-well structures or superlattices differs in details, but as in homogeneous materials, the term radiative damping is not introduced. The concept of an exciton polariton undergoes significant changes in a structure with a single quantum well. An exciton excited in an ideal quantum well in a state with a two-dimensional wave vector $\mathbf{k}_\parallel=(k_x,k_y)$ such that $k_\parallel<(\omega_0/c)n_b$ can annihilate with the emission of light into a barrier (ω_0 is the resonant frequency of the exciton, c is the speed of light in a vacuum, and n_b is the refractive index in the barrier material). The frequency of a quasi-two-dimensional exciton is renormalized slightly when the interaction with photons is taken into account, and thus the main result reduces to the appearance of radiative damping in the exciton. It is noteworthy that, unlike the radiative damping of excited levels of isolated atoms, to which the emission of light in a broad solid angle contributes, the radiation of an exciton in a quantum well at a frequency ω consists of two light waves with the wave vectors $\mathbf{k}=(k_x,k_y,\pm k_z)$, where $k_z=[(\omega/c)^2n_b^2-k_x^2-k_y^2]^{1/2}$, since the components of the wave vector remain unchanged in the plane of the interface. An exciton with $k_\parallel>(\omega_0/c)n_b$ induces an electromagnetic field in barriers, whose amplitude decreases with increasing distance into the bulk of the right-hand or left-hand barrier. The inverse influence of this field on the exciton leads to renormalization of the resonant frequency, but does not create a new recombination channel. In this paper we examine the radiative properties of an exciton in a finite periodic quantum-well structure, where excitons in neighboring wells are isolated from one another sufficiently well so that the tunneling effects can be ignored. Such structures have been studied extensively by experimental methods and can be characterized as an intermediate case between a single quantum well and an infinite superlattice. Just as in a single well, in the case under consideration an exciton can recombine with the emission of a photon $(k_x,k_y,\pm k_z)$. However, the radiative recombination rate and the frequency of the light emitted depend on the re-reflection and interference of light in the multilayer structure. In terms of quantum electrodynamics, the excitons in different quantum wells are coupled by the electromagnetic field. As in a system of N coupled pendulums, N natural frequencies generally appear in a system of N quantum wells. Since the possibility of radiative recombination of an exciton is maintained, these frequencies are complex.

The optical properties of finite, long-period structures with identical quantum wells were considered in Ref. 1 and in a group of papers[2–7] appearing thereafter. The case of a resonant Bragg structure with a period $d=\pi(\omega_0 n_b/c)^{-1}$ was analyzed in detail in Ref. 1. It was shown in this case that the spectrum of the natural frequencies ω_i is highly degenerate: the natural frequencies for $N-1$ modes coincide and are equal to $\omega_0-i\Gamma$, where Γ is the nonradiative damping; i.e., these modes are radiation-inactive, and the frequency for one mode equals $\omega_0-i(N\Gamma_0+\Gamma)$, where Γ_0 is the radiative damping of an exciton in a single well, i.e., such an exciton has a radiative lifetime that is N times smaller than in a single quantum well. The real and imaginary parts of the natural frequencies were calculated in Ref. 7 as a function of the period of a CdTe/CdZnTe structure containing 10 quantum wells. The characteristic solutions of the exciton-polariton problem in a structure with a finite number of equidistant quantum wells were analyzed in that paper from the standpoint of parity. In addition, the laws governing the relative arrangement of the natural frequencies of exciton polaritons on the complex plane were investigated, and approximate analytical expressions for the frequencies of long-lived and short-lived modes were derived.

Equation for the natural frequencies in the transfer-matrix formalism

In the transfer-matrix formalism the dielectric polarization is eliminated from the wave equation using the material

relation, and the relation between the electric field amplitudes for the incident wave and the transmitted wave is established. Let us consider a structure consisting of N equidistant quantum wells arranged at a distance d from one another. The transfer matrix through a layer of thickness d with a quantum well in the middle can be written in the form[1,8]

$$\hat{T}=\frac{1}{t}\begin{bmatrix}(t^2-r^2)e^{ikd} & r\\ -r & e^{-ikd}\end{bmatrix}, \tag{1}$$

where r and t are, respectively, the reflection and transmission coefficients at the center of the well

$$r=\frac{i\Gamma_0}{\omega_0-\omega-i(\Gamma+\Gamma_0)},\quad t=1+r. \tag{2}$$

Here and below, the difference between n_b^2 and the background dielectric constant of the well material is disregarded, and normal incidence of light onto the structure is considered. The eigenvalues of this matrix can be represented in the form[8] $\lambda_\pm=e^{\pm iQd}$, and the eigenvectors can be represented as

$$\hat{C}_\pm=\begin{bmatrix}1\\ a_\pm\end{bmatrix},\quad a_\pm=\frac{r}{e^{-ikd}-te^{\pm iQd}}. \tag{3}$$

The quantity Q has the meaning of the wave vector of light at the frequency ω in an infinite periodic structure and satisfies the dispersion relation[9]

$$\cos Qd=G(\omega),\quad G(\omega)=\cos kd-\sin kd\frac{\Gamma_0}{\omega_0-\omega-i\Gamma}. \tag{4}$$

For a structure containing a finite number N of quantum wells, the spectrum of natural frequencies is found from the homogeneous boundary conditions, which signify the absence of an external wave impinging on the structure from the left or the right and which are equivalent to the relation $a_+e^{iNQd}=a_-e^{-iNQd}$. After substituting the expression (3) for the coefficients $a_\pm$ into this relation and performing several additional transformations, we obtain a transcendental equation for finding N complex natural frequencies of the system

$$te^{ikd}=\frac{U_{N-1}(G)}{U_{N-2}(G)}, \tag{5}$$

where the $U_n(x)=(1-x^2)^{-1/2}\sin[(n+1)\arccos x]$ are Chebyshev polynomials of the second kind of degree n (see, for example, Ref. 10), and the argument G is defined according to (4).

The amplitude optical reflection and transmission coefficients for a system of N quantum wells enclosed between homogeneous unbounded barriers are expressed in terms of $a_\pm$ and Q in the following manner:

$$r_N=\frac{a_+a_-(1-e^{2iNQd})}{a_-a_+e^{2iNQd}},\quad t_N=\frac{(a_--a_+)e^{iNQd}}{a_--a_+e^{2iNQd}}. \tag{6}$$

The reflection and transmission coefficients are defined in planes shifted by $d/2$ to the left from the center of the extreme left-hand well and by $d/2$ to the right from the center of the extreme right-hand well, respectively.

It follows[1] from the symmetry of the system that its intrinsic excitations are either even or odd relative to the center of the structure $z=0$. In particular, the dielectric polarization P (or the electric field E) of a normal excitation satisfies one of the following conditions: $P(-z)=\pm P(z)$ or $E(-z)=\pm E(z)$. The natural frequencies for the even solutions are poles of the sum $r_N(\omega)+t_N(\omega)$, and those for the odd solutions are poles of the difference $r_N(\omega)-t_N(\omega)$. Hence it follows that the numerator of the fraction $r_N\mp t_N$ should vanish for the even and odd solutions, respectively, and the conditions

$$U_{N-1}(G)=\pm(t/r) \tag{7}$$

are imposed on these solutions. We note that among the $2N$ roots of the two equations (7) only half are natural frequencies of the heterostructure and satisfy Eq. (5).

Equations (5) and (7) enable us to establish the relations between the natural frequencies for two structures with the same value of N and with periods d_1 and d_2 that satisfy the condition

$$k(d_1+d_2)=\pi. \tag{8}$$

The obvious equalities $\cos kd_2=-\cos kd_1$ and $\sin kd_2=\sin kd_1$ lead to the identity $G^*(\omega,d_1)=-G(2\omega_0-\omega^*,d_2)$. Comparing Eqs. (5) for the two structures and taking into account the relations $t^*(\omega)=t(2\omega_0-\omega^*)$, $\exp(-ikd_1)=-\exp(ikd_2)$, $U_n(-x)=(-1)^nU_n(x)$, and $U_n^*(x)=U_n(x^*)$, we conclude that the sets of natural frequencies $\{\omega_i(d_1)\}$ and $\{\omega_j(d_2)\}$ can be reduced to the relation

$$\omega_j(d_2)=2\omega_0-\omega_i^*(d_1). \tag{9}$$

We denote the natural frequencies for the even and odd solutions as $\omega_i^{(+)}(d)$ and $\omega_{i'}^{(-)}(d)$, where $i,i'=1,\ldots,N/2$ for even N and $i=1,\ldots,(N+1)/2$, $i'=1,\ldots,(N-1)/2$ for odd N. Using Eqs. (7), we rewrite relations (9) in terms of the even and odd solutions

$$\omega_j^{(\pm)}(d_2)=\begin{cases}2\omega_0-\omega_i^{(\pm)*}(d_1) & \text{if } N \text{ is odd},\\ 2\omega_0-\omega_i^{(\mp)*}(d_1) & \text{if } N \text{ is even}.\end{cases} \tag{10}$$

An anti-Bragg structure with $kd=\pi/2$ is a special case. Substituting the values $d_1=d_2=\pi/2k$ into (10), we find for such a structure that the sets of the frequencies $\omega_i^{(+)}$ and $\omega_{i'}^{(-)}$ for odd N are distributed separately on the complex plane symmetrically relative to the vertical straight line $\omega=\omega_0$, and that the set of $\omega_{i'}^{(-)}$ for even N is obtained from the set of $\omega_i^{(+)}$ as a result of reflection relative to the straight line $\omega=\omega_0$. We note that Eqs. (9) and (10) were derived without consideration of the dispersion of the wave vector $k=(\omega/c)n_b$, i.e., under the assumption that $Nn_b|\omega-\omega_0|d/c\ll 1$.

Figure 1 shows the complex energies of the exciton polaritons for three structures with $N=10$ and with periods that satisfy the condition $kd=\pi/4$ (a), $kd=\pi/2$ (b, an anti-Bragg

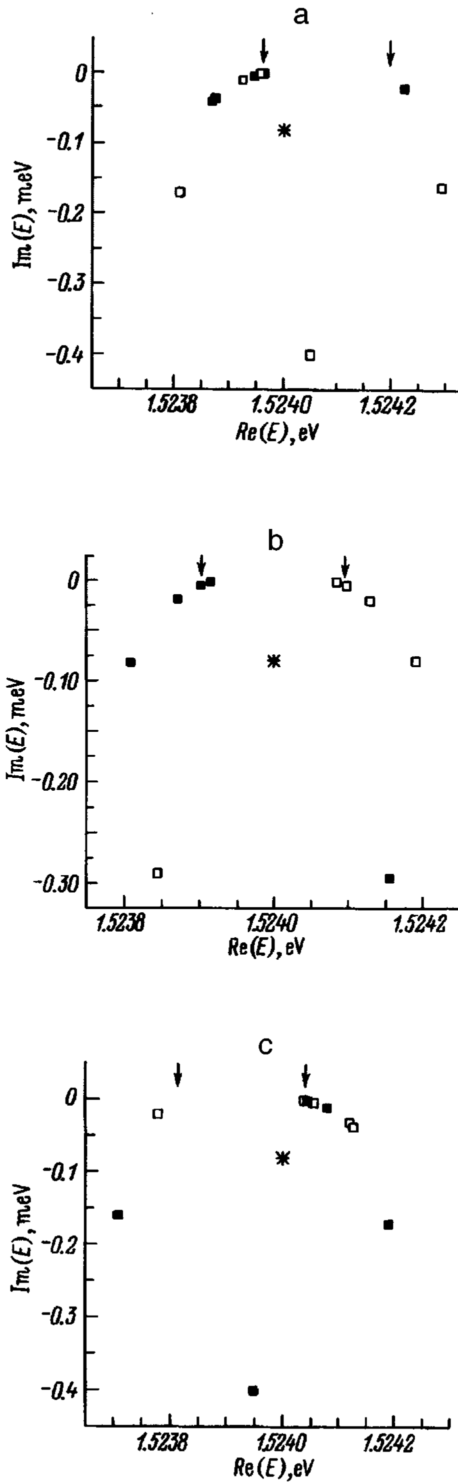

FIG. 1. Complex eigenenergies for exciton polaritons in a structure with ten quantum wells and a period $d=d_A/2$ (a), $d=d_A$ (b), or $d=3d_A/2$ (c), where d_A is the period of the anti-Bragg structure. The nonradiative damping Γ of the exciton was set equal to zero. Unfilled and filled squares — even and odd solutions, respectively; asterisk — eigenenergy of an exciton in a single quantum well. The arrows indicate the edges of the gap in an infinite periodic heterostructure determined according to (15).

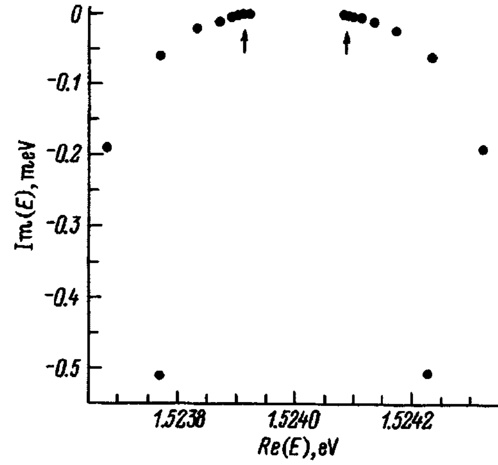

FIG. 2. Complex eigenenergies for exciton polaritons in an anti-Bragg structure ($d=d_A$) with 20 quantum wells for $\Gamma=0$. The arrows show the edges of the gap in an infinite periodic heterostructure.

structure), or $kd=3\pi/4$ (c). The even and odd solutions are denoted by different symbols. The parameters of the heterostructure selected for the calculation are characteristic of the GaAs/GaAlAs system: the excitation energy of a quasi-two-dimensional exciton in a single quantum well $\hbar\omega_0=1.524$ eV, the radiative damping $\hbar\Gamma_0=0.08$ meV, the refractive index in the barrier $n_b=3.64$, and the difference between n_b and the background refractive index in the well material was ignored. For simplicity, the nonradiative damping was set equal to zero, and to take it into account, it is sufficient to shift all the points in Fig. 1 by $-i\Gamma$. In accordance with (10), the points in Fig. 1c are obtained from Fig. 1c by reflection relative to the straight line at $\hbar\omega_0$ and switching the parity symbol, and the complex energies of the polaritons in the anti-Bragg structure (Fig. 1b) are arranged symmetrically relative to this line. The arrangement of the eigenenergies for an anti-Bragg structure with 20 wells is shown in Fig. 2.

Equation for the eigenfrequencies in the coupled-oscillator approach

In this approach the natural frequencies are found from the equation

$$\det\|A_{lm}-\omega\delta_{lm}\|=0,$$

$$A_{lm}=(\omega_0-i\Gamma)\delta_{lm}-i\Gamma_0 e^{ik|l-m|}, \tag{11}$$

which is fully equivalent to Eq. (5). Since the trace of any square matrix is equal to the sum of its eigenvalues, the following constraint can be imposed on this sum:

$$\sum_{j=1}^{N}\Omega_j=0, \quad \Omega_j=\omega_j-\omega_0+i(\Gamma+\Gamma_0). \tag{12}$$

According to Gerschgorin's circle theorem,[11] the eigenvalues of a complex square matrix a_{lm} of order n lie in a closed region of the complex plane $z=z'+iz''$ formed by the circles

$$|z-a_{ll}|\leq\sum_{m\neq l}|a_{lm}|.$$

Hence it follows that the natural frequencies of a system of N quantum wells are localized in a circle, whose center is at the point $\omega_0-i(\Gamma+\Gamma_0)$ and whose radius equals $(N-1)\Gamma_0$. Taking into account the symmetry of the system, we obtain

relations which govern the sums of the roots for the even and odd solutions taken separately. For this purpose, we number a sequence of N quantum wells from $m=-n$ to $m=n$, excluding zero for an even $N=2n$ and including the value $m=0$ for an odd $N=2n+1$, and we pass from a basis of single-well exciton states $|m\rangle$ to $|m\rangle_{\pm}=(|m\rangle \pm |-m\rangle)/\sqrt{2}$ $(m=1,\ldots,n)$ if N is even or to $|m\rangle_{\pm}$ $(m=1,\ldots,n)$, $|0\rangle_{+}\equiv|0\rangle$ if N is odd. In the new basis the matrix $\hat{A}$ transforms into the quasidiagonal matrix

$$\hat{A}=\begin{bmatrix} \hat{A}^{(+)} & 0 \\ 0 & \hat{A}^{(-)} \end{bmatrix}.$$

The eigenvalues of the matrices $\hat{A}^{(\pm)}$ specify the set of the frequencies $\omega_j^{(\pm)}$ for the even and odd solutions, respectively. The diagonal elements of these matrices can be easily calculated: $A_{mm}^{(\pm)}=\tilde{\omega}_0 \mp i\Gamma_0\eta^{2m-1}$, if N is even or $A_{00}^{(+)}=\tilde{\omega}_0$ and $A_{mm}^{(\pm)}=\tilde{\omega}_0 \mp i\Gamma_0\eta^{2m}$ if N is odd, where $\tilde{\omega}_0=\omega_0-i(\Gamma+\Gamma_0)$ and $\eta=e^{ikd}$. Summing them separately, we obtain

$$\sum_{j=1}^{n}\Omega_j^{(+)}=-\sum_{j=1}^{n}\Omega_j^{(-)}$$

$$=-i\Gamma_0\eta\frac{1-\eta^{2n}}{1-\eta^2} \quad \text{for} \quad N=2n, \tag{13}$$

$$\sum_{j=1}^{n+1}\Omega_j^{(+)}=-\sum_{j=1}^{n}\Omega_j^{(-)}$$

$$=-i\Gamma_0\eta^2\frac{1-\eta^{2n}}{1-\eta^2} \quad \text{for} \quad N=2n+1.$$

Relations (20) from Ref. 1 enable us to find the frequencies $\Omega_j^{(\pm)}$ for $N=1-4$:

$$\Omega_1^{(+)}=0 \quad (N=1); \quad \Omega_1^{(\pm)}=\mp i\Gamma_0\eta \quad (N=2);$$

$$\Omega_{1,2}^{(+)}=-\frac{i}{2}\Gamma_0\eta(\eta\pm\sqrt{\eta^2+8}), \quad \Omega_1^{(-)}=i\Gamma_0\eta^2(N=3);$$

$$\Omega_{1,2}^{(+)}(\eta)=\Omega_{1,2}^{(-)}(-\eta)=-\frac{i}{2}\Gamma_0\eta[1+\eta^2$$

$$\pm\sqrt{(1+\eta^2)^2+4(1+2\eta)}] \quad (N=4).$$

It is easy to see that these frequencies satisfy identities (12) and (13).

Approximate expressions for the natural frequencies

An analysis of Figs. 1 and 2 shows that several polariton modes have a small radiative damping, while there are individual polariton states characterized by increased radiation activity. Approximate analytical expressions for the natural frequencies can be derived for these two types of exciton polaritons in quantum-well structures.

We, first of all, note that, according to (4), in an infinite periodic quantum-well heterostructure the dispersion of normal light waves has the form

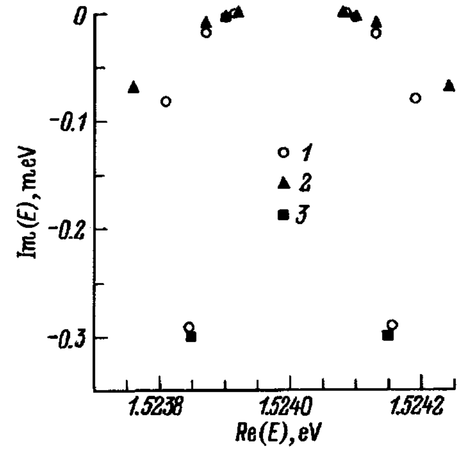

FIG. 3. Complex natural frequencies for exciton polaritons in an anti-Bragg structure ($d=d_A$) with ten quantum wells: *1* — exact calculation, which is also presented in Fig. 1(b); *2* — calculation based on Eqs. (14) and (17); *3* — calculation based on the approximate equation (18).

$$\omega=\omega_0-i\Gamma+\frac{\sin kd}{\cos Qd-\cos kd}\Gamma_0. \tag{14}$$

When $\Gamma=0$, the spectrum has a gap lying between the values

$$\omega=\omega_0-\Gamma_0\tan(kd/2) \quad \text{for} \quad Q=\pi/2 \quad \text{and}$$

$$\omega=\omega_0+\Gamma_0\cot(kd/2) \quad \text{for} \quad Q=0. \tag{15}$$

The arrows in Figs. 1 and 2 show the edges of the gap for exciton polaritons, which are assigned by the expressions $\omega_0+(1\pm\sqrt{2})\Gamma_0$ in a structure with a period equal to 1/4 of the optical wavelength, $\omega_0\pm\Gamma_0$ in an anti-Bragg structure, and $\omega_0+(\pm\sqrt{2}-1)\Gamma_0$ if the period is equal to 3/4 of a wavelength.

In a structure with a finite number of quantum wells the permissible values of the product Qd, which is defined according to (4), are assigned by Eq. (5) which can be represented with consideration of (14) in either of the equivalent forms

$$\frac{\sin NQd}{\sin(N-1)Qd}=\frac{i\sin kd}{1-\exp(-ikd)\cos Qd}$$

or

$$\tan NQd=-i\frac{\sin kd\sin Qd}{1-\cos kd\cos Qd}. \tag{16}$$

For a large number of quantum wells, $N\gg1$, there are solutions of this equation with $|Q|d\ll1$ or $\pi-|Q|d\ll1$ which allow expansion in powers of N^{-1}:

$$Qd\approx\pi\frac{j}{N}\left(1-\frac{i}{N}\cot\frac{kd}{2}\right) \quad \text{for} \quad \frac{j}{N}\ll\left|\sin\frac{kd}{2}\right|, \tag{17}$$

$$Qd\approx\pi\left(\frac{j}{N}-i\frac{N-j}{N^2}\tan\frac{kd}{2}\right) \quad \text{for} \quad \frac{N-j}{N}\ll\left|\cos\frac{kd}{2}\right|,$$

where $j=1,\ldots,N$. In Fig. 3 the circles and triangles show the eigenvalues of the energy for exciton polaritons in an anti-Bragg structure with ten wells, which were calculated from the exact formula (5) and from formulas (14) and (17).

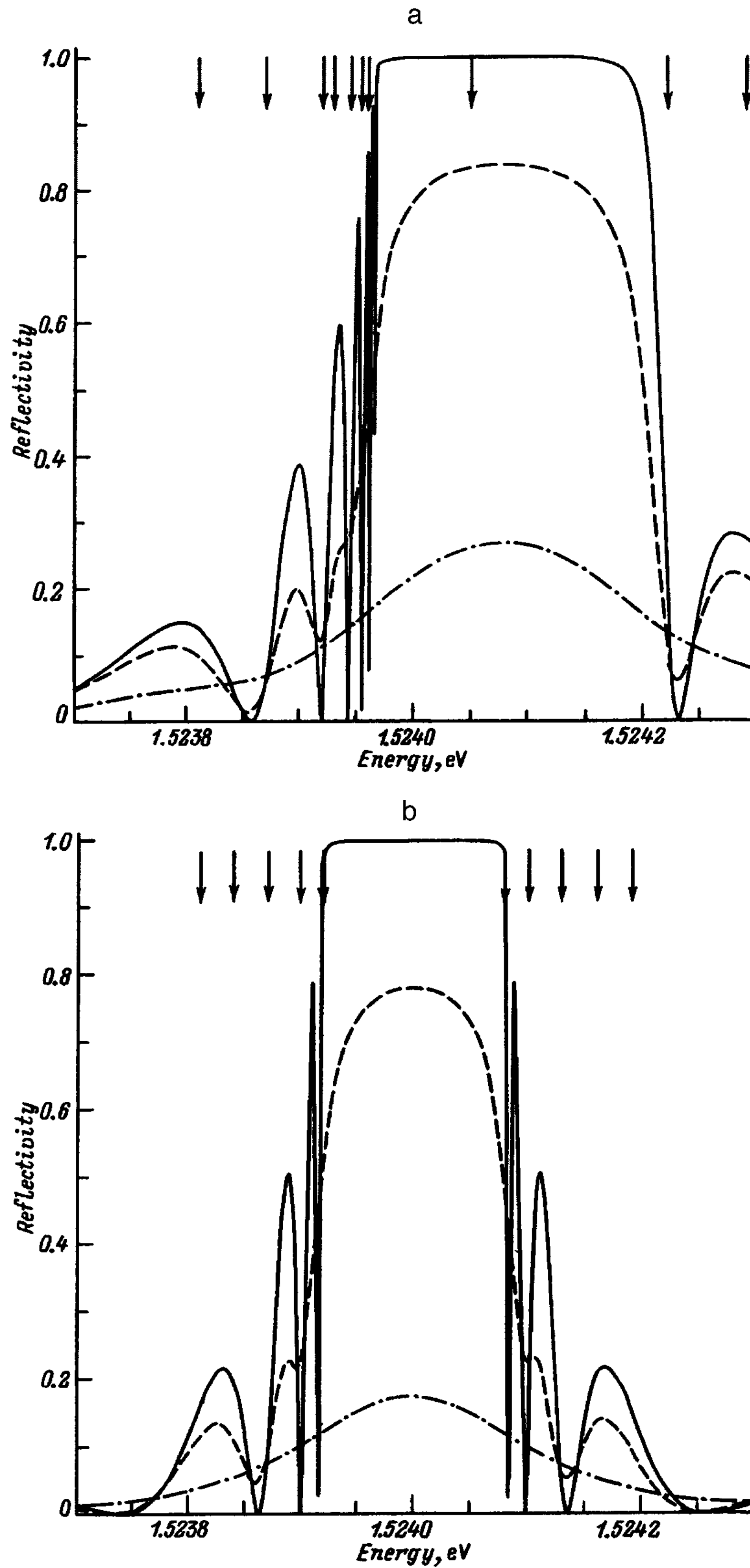

FIG. 4. Optical reflection spectra of a system of ten quantum wells with a period $d = d_A/2$ (a) or $d = d_A$ (b), where d_A is the period of the anti-Bragg structure. Solid curves — calculation without allowance for the nonradiative damping, dashed lines — for $\hbar\Gamma = 0.01$ meV, dot-dashed lines — for $\hbar\Gamma = \hbar\Gamma_0 = 0.08$ meV. The arrows show the real energies of the polariton modes that satisfy Eq. (5).

It is seen that the difference between the exact and approximate values is insignificant for at least four solutions.

We introduce the notation δ for the ratio $\Gamma_0/(\omega_0-\omega-i\Gamma)$. According to (4), for solutions which satisfy the condition $|\delta|\ll 1$ we have $Qd\approx kd+\delta$, and when $|\sin kd|\gg|\delta|$, the equation for the natural frequencies can be written in the form

$$\cot N(kd+\delta)=i\left(1+\frac{\delta^2}{2\sin^2 kd}\right). \tag{18}$$

In the limit $N\to\infty$, the imaginary part of the natural frequency of an exciton polariton that has increased radiation activity tends to the value $-\Gamma-\Gamma_0(N/p)$, where p satisfies the equation $pe^p=2|\sin kd|N$. The squares in Fig. 3 show the radiation-active solutions calculated from the approximate formula (18).

Reflection spectra

Figure 4 presents the reflection spectra $R(\omega)=|r_N(\omega)|^2$ calculated for a structure with $N=10$ and $(\omega_0/c)\sqrt{\varepsilon_b}d=\pi/4$ (a) and $\pi/2$ (b). To facilitate the analysis, the calculation was performed with allowance for the real nonradiative damping of the exciton and for $\Gamma=0$. It is seen that within the band gap the reflection coefficient for an infinite heterostructure with ten wells is close to 100% when $\Gamma=0$. The fine structure outside of this spectral region is consistent with the real values of the natural frequencies for weakly damped polariton modes. Consideration of the nonradiative damping obliterates the fine structure of the reflection spectrum, and the information regarding the distribution of the natural frequencies is lost.

In conclusion, we note that periodic structures with quantum wells offer a unique possibility for regulating the radiative characteristics of excitons, without altering the quantum wells themselves, by varying only the distance between them. A single, optically active mode with a short lifetime (a Bragg structure) can be generated or N nondegenerate polariton modes with different frequencies and lifetimes can be obtained. We have shown that, regardless of the value of N, only a restricted number of these modes have radiative damping exceeding the radiative damping of an exciton in a single well, while the remaining modes are long-lived.

This work was supported by the Nanostructures Program of the Russian Ministry of Science, INTAS Grant 93-3657-Ext, and the Volkswagen Foundation.

[1] E. L. Ivchenko, A. I. Nesvizhskiĭ, and S. Ĭorda, Fiz. Tverd. Tela (St. Petersburg) **36**, 2118 (1994) [Phys. Solid State **16**, 17 (1994)].

[2] L. C. Andreani, Phys. Lett. A **192**, 99 (1994); Phys. Status Solidi B **188**, 29 (1995).

[3] D. S. Citrin, Sov. J. Coord. Chem. **89**, 139 (1994); Phys. Rev. B **49**, 1943 (1994).

[4] Y. P. Kochereshko, G. R. Pozina, E. L. Ivchenko, D. R. Yakovlev, A. Waag, W. Ossau, G. Landwehr, R. Hellmann, and E. O. Göbel, Superlattices Microstruct. **15**, 471 (1994).

[5] T. Stroucken, A. Knorr, C. Anthony, Schulze , P. Thomas, S. W. Koch, M. Koch, S. T. Cundiff, J. Feldmann, and E. O. Göbel, Phys. Rev. Lett. **74**, 2391 (1995).

[6] M. Hübner, J. Kuhl, T. Stroucken, A. Knorr, S. W. Koch, R. Hey, and K. Ploog, Phys. Rev. Lett. **76**, 4199 (1996).

[7] Y. Merle d'Aubigne, A. Wasiela, H. Mariette, and T. Dietl, Phys. Rev. B **54**, 14 003 (1996).

[8] V. A. Kosobukin, Fiz. Tverd. Tela (Leningrad) **34**, 3107 (1992) [Sov. Phys. Solid State **34**, 1662 (1992)].

[9] E. L. Ivchenko, Fiz. Tverd. Tela (Leningrad) **33**, 2388 (1991) [Sov. Phys. Solid State **33**, 1344 (1991)].

[10] S. Paszkowski, *Numerical Applications of Chebyshev Polynomials and Series* [Russian trans. from the Polish], Nauka, Moscow (1983).

[11] M. Marcus and H. Minc, *A Survey of Matrix Theory and Matrix Inequalities*, Allyn and Bacon, Boston (1964) [Russian trans., Nauka, Moscow (1972)].

Translated by P. Shelnitz

Interimpurity light absorption in thin wires of III–V-type semiconductors

A. P. Dzhotyan, É. M. Kazaryan, A. S. Chirkinyan

Erevan State University, 375049 Erevan, Armenia

(Submitted May 20, 1996; accepted for publication June 2, 1997)
Fiz. Tekh. Poluprovodn. **32**, 108–110 (January 1998)

A study has been performed of interimpurity light absorption in weakly doped thin wires of III–V type semiconductors with Kane charge-carrier dispersion law with the one–dimensional random distribution of the impurities taken into account. The dependence of the absorption curve is analyzed: the location of the absorption maxima corresponding to transitions from the acceptor ground level to the ground level and first excited level of the donor as well as their edges and half-widths are found. It is shown that the nonparabolicity of the charge-carrier dispersion law leading to transitions between the impurity ground states causes an abrupt detachment of this absorption line from the remaining lines. © *1998 American Institute of Physics.* [S1063-7826(97)00712-6]

Interband impurity absorption of light in thin III–V superconductor wires was investigated earlier in Ref. 1 with the concrete band structure of the semiconductor taken into account. This study also considered transitions of the electron from the valence band to the discrete donor levels. Further study of impurity absorption in wires requires a consideration of the contribution of transitions between the discrete impurity levels, i.e., the discrete levels of the acceptors and donors. In the solution of this problem in the present paper we restrict the treatment to a weakly doped semiconductor with acceptor concentration $n_A \ll n_D$ (n_D is the donor concentration), where the nearest-neighbor approximation holds.[2] Here we approximate the wire potential (with circular cross section of radius R) by an infinite two-dimensional potential well, and along the z axis we assume that the one-dimensional band structure is preserved. As in Ref. 1, we adopt the Kane charge-carrier dispersion law[3] and employ the two-band approximation ($m_c = m_v = \mu$, m_c is the electron mass, m_v is the hole mass), in which this law is completely analogous to the relativistic law.[4]

To consider interimpurity transitions in a thin wire, it is necessary to determine the wave functions and energy spectrum of the bound states of the hydrogen-like impurity. Assuming that the Bohr radius a of the bound impurity state in a massive sample ($a = \hbar^2\chi/\mu Z e^2$, where Z is the charge of the impurity center, and χ is the dielectric constant of the crystal) is greater than R, the Wannier equation of the impurity problem decomposes into two equations: the first describes the motion of a noninteracting electron and hole in the quantum-well plane, and the second describes the motion of the Coulomb-bound electron–hole pair with Kane dispersion law of the charge carriers along the z axis. In an account of correlation of these motions, the true interaction potential of the electron–hole pair is obtained by averaging the transverse Coulomb motion over the wave functions. Note that taking this correlation into account is of fundamental importance for wires with a quadratic dispersion law[5] since it eliminates difficulties associated with the instability of the ground state of the one-dimensional hydrogen-like atom. At the same time, for III–V wires it is not necessary: the relativistic derivation of the dispersion law ensures the existence of the ground state even for the singular potential $V(z) = -e^2/\chi|z|$ (Ref. 4).

In this treatment of the problem, the total wave functions describing the ground state ($n=0$) and the excited states ($n=1,2,3\ldots$) of an electron localized on a singly ionized donor [with its center at the point $(\boldsymbol{\rho}, z)$ in cylindrical coordinates with the z axis along the axis of the wire, the center of the acceptor is located at the point $(\boldsymbol{\rho}-\boldsymbol{\rho}_0,\ z-z_0)$], have the form

$$\Psi_{D0} = \left[\frac{2b_i^{|m|}}{\alpha a}\right]^{1/2} \frac{1}{\sqrt{S}} \frac{J_{|m|}(\lambda_i^{|m|}\rho/R)}{J_{|m|+1}(\lambda_i^{|m|})} \times \exp(im\varphi)\exp\left(-\frac{b_i^{|m|}z}{\alpha a}\right) U_c(z), \tag{1}$$

$$\Psi_{Dn} = \left[\frac{2(b_i^{|m|})^3}{a^3 n^3 (n+1)^2}\right]^{1/2} \frac{1}{\sqrt{S}} \frac{J_{|m|}(\lambda_i^{|m|}\rho/R)}{J_{|m|+1}(\lambda_i^{|m|})} \times \exp(im\varphi) z\ \exp\left(-\frac{b_i^{|m|}z}{na}\right) L_n^1\left(\frac{2bi^{|m|}z}{na}\right) U_c(z), \tag{2}$$

$$\mathscr{E}_{n,i}^{|m|} = \left[\frac{\mu^2 s^4 + \hbar^2 s^2 (\lambda_i^{|m|})^2/R^2}{1+\alpha^2/(n+t)^2}\right], \tag{3}$$

where $\lambda_i^{|m|}$ is the ith root of the mth Bessel function $J_{|m|}$; s is the nonparabolicity parameter governing the "interaction" of the bands ($E_g = 2m_n s^2$, where m_n is the electron mass at the bottom of the conduction band, and E_g is the width of the band gap). The quantity $\alpha = e^2/\chi\hbar s$ plays the role of the effective fine-structure constant (for InSb $s \approx 10^8$ cm/s, $\alpha \simeq 0.2$), and the quantity $\lambda_s = \alpha a = \hbar/\mu s$ entering into expression (1) for the ground-state wave function is the analog of the Compton wavelength $\lambda = \hbar/m_0 c$ in the case of a Kane semiconductor[4]). As can be seen from Eq. (1), the localization radius of an electron bound to a hydrogen-like impurity center in a thin wire in the ground state is narrower than λ_s by the factor $b_i^{|m|} = [\mu^2 s^4 + (\hbar^2 s^2/R^2)(\lambda_i^{|m|})^2]^{1/2}\mu s^2$. This is because of the boundedness of transverse motion of charge carriers with Kane dispersion law in a wire: S is the cross-

 © 1998 American Institute of Physics

sectional area of the wire, $L_n^1(x)$ is the Laguerre polynomial of order n, $U_c(z)$ is the Bloch amplitude, and $t=(1/2)\pm(1/2)(1-4\alpha^2)^{1/2}$ (Refs. 1 and 4).

The coefficient of interband light absorption is calculated by the standard technique[6] invoking Eqs. (1)–(3) and smallness of the quantity $q_\perp R$, where $q_\perp$ is the photon momentum in the plane perpendicular to the z axis (for InSb with $R\simeq 10^{-6}$ cm $q_\perp R\simeq 0.1$).

Thus, for the optical matrix element of the transition of an electron between impurity ground states ''suspended'' from wire subbands with identical numbers $i=i'$, $m=m'$ (the contribution of the remaining terms is negligible since it is proportional to the square of the small parameter $q_\perp R$, Ref. 7) near $\mathbf{k}=0$, using Eq. (1), we find

$$P_{DA}=\frac{2eA_0}{m_0c}p_{cv}(z_0)\cos\beta\frac{b_i^{|z|}z_0}{\alpha a}\exp\left(-\frac{b_i^{|m|}z_0}{\alpha a}\right), \tag{4}$$

where

$$p_{cv}(z_0)=\frac{i\hbar}{\Omega_0}\int_{\Omega_0}U_{c(z)}U_v(z-z_0)dz,$$

Ω_0 is the volume of the one-dimensional unit cell, A_0 is the amplitude of the vector potential $\mathbf{A}$ of the incident light wave, and β is the angle between $\mathbf{A}$ and the z axis.

For transitions of the electron between the ground states of the donor and acceptor with energies

$$\mathscr{E}_i=-E_g+|\mathscr{E}_{A\,0,i}^{|m|}|-e^2/\chi z_0,\quad \mathscr{E}_f=-|\mathscr{E}_{D\,0,i}^{|m|}|$$

(measured from the bottom of the conduction band) we obtain the following expression for the absorption:

$$\alpha_0(\omega,z_0)=\frac{16\pi^2e^2\cos^2\beta}{m_0^2nc\omega a^2\alpha^2}\sum_{i,m}|p_{cv}(z_0)|^2(b_i^{|m|})^2z_0^2\times\exp\left(-\frac{2b_i^{|m|}z_0}{\alpha a}\right)\delta\left(\frac{e^2}{\chi z_0}-\frac{e^2}{\chi z_1}\right), \tag{5}$$

where $z_1=e^2/\chi(\hbar\omega-\widetilde{E}_g)$, and $\widetilde{E}_g=E_g-|\mathscr{E}_{D\,0,i}^{|m|}|-|\mathscr{E}_{A\,0,i}^{m}|$.

The above expression for $\alpha_0(\omega,z_0)$ must be averaged over the random impurity distribution in the semiconductor. It is not hard to find the probability of finding the nearest acceptor to the given donor within the interval z_0, z_0+dz_0. In the nearest-neighbor approximation this probability has the form of the one-dimensional Poisson distribution

$$W(z_0)dz_0=Sn_A e^{-Sn_Az_0}dz_0. \tag{6}$$

Averaging $\alpha_0(\omega,z_0)$ over distribution (6) and multiplying by the donor concentration, we finally obtain the expression for the absorption coefficient:

$$\alpha_0(\omega)=\frac{16\pi^2\beta_A\beta_D\chi\cos^2\beta}{m_0^2nc\omega a^2S}\sum_{i,m}|p_{cv}(z_1)|^2(b_i^{|m|})^2\times\left(\frac{\omega_D}{\omega-\Omega_{0,i}^{|m|}}\right)^4\exp\left[-\frac{\beta_A\omega_D}{\omega-\Omega_{0,i}^{|m|}}-\frac{2b_i^{|m|}\omega_D}{\alpha(\omega-\Omega_{0,i}^{|m|})}\right], \tag{7}$$

where $\omega_D=e^2/\chi a\hbar$, $\Omega_{0,i}^{|m|}=\widetilde{E}_g/\hbar$, $\beta_A=n_ASa$, and $\beta_D=n_DS_a$.

For transitions from the acceptor ground level to the first excited donor level, using expressions (1)–(3) and (6), we obtain the following expression for the absorption:

$$\alpha_1(\omega)=\frac{16\pi^2\beta_A\beta_D\chi\alpha\cos^2\beta}{m_0^2nc\omega S}\sum_{i,m}|p_{cv}(z_2)|^2|b_i^{|m|}|^2\times\left(\frac{\omega_D}{\omega-\Omega_{1,i}^{|m|}}\right)^4\exp\left[-\frac{\beta_A\omega_D}{\omega-\Omega_{1,i}^{|m|}}-\frac{2b_i^{|m|}\omega_D}{(\omega-\Omega_{1,i}^{|m|})}\right], \tag{8}$$

where $\Omega_{1,i}^{|m|}=[E_g-|\mathscr{E}_{D1,i}^{|m|}|-|\mathscr{E}_{A0,i}^{|m|}|]/\hbar$, and $z_2=a\omega_D/(\omega-\Omega_{1,i}^{|m|})$.

1. DISCUSSION

Interimpurity light absorption in a thin semiconductor wire begins from transitions of the electron between the ground ($n=0$) hydrogen-like levels of the infinitely separated acceptor–donor pair associated with the lowest wire subbands ($i=i'=1$, $m=m'=0$) of the corresponding bands. These transitions, as follows from Eq. (7), correspond to the main impurity peak with absorption edge at the frequency

$$\Omega_{0,1}^0=[E_g-|\mathscr{E}_{D0,1}^0|-|\mathscr{E}_{A0,1}^0|]/\hbar,$$

where $\mathscr{E}_{D0,1}^0$ and $\mathscr{E}_{A0,1}^0$ are the ground-state energies of the donor and acceptor, respectively.

Note that the very existence of this peak in a thin semiconductor wire is due to the nonparabolicity of the charge-carrier dispersion law, which eliminates the instability of the ground state of the one-dimensional Coulomb problem, in analogy with the relativistic problem.[4] For InSb with $E_g=0.23$ eV, $\Omega_{0,1}^0\approx 10^{14}\mathrm{s}^{-1}$.

As a result of the random distribution of the donor–acceptor pairs, this peak has finite width, and its maximum, as follows from Eq. (7), is reached at the frequency

$$\omega_{0,1}^0=\Omega_{0,1}^0+\omega_D/2\alpha+\beta_A\omega_D/4. \tag{9}$$

The second term in expression (9) describes the frequency shift of the main absorption peak due to overlap of the wave functions of the donor and acceptor ground states. This overlap is substantial in our case for z_0 values α^{-1} times smaller than in the two-dimensional ($2D$) (Ref. 8) and three-dimensional ($3D$) case and, correspondingly, for larger values of the quasimomenta. The concentration shift of the peak described by the third term in expression (9) is proportional to the parameter β_A and for values of $\beta_A\sim 0.1$ is two orders of magnitude smaller than the shift described by the second term in expression (9). The half-width of the peak $\delta\omega\approx\omega_D/2\alpha$.

The total absorption coefficient $\alpha_0(\omega)$, as can be seen from expression (7), takes the form of several separate peaks due to transitions of the electron between the discrete levels of the hydrogen-like impurity formed below the bottom of each quantization subband in the wire.

The peaks of the curve $\alpha_0(\omega)$ following after the main one, with absorption edges $\Omega_{0,i}^{|m|}$ shifted toward shorter wavelengths, arise as a result of transitions of the electron between the impurity ground states suspended under the subbands with indices i and m in the wire. To estimate the

quantities $\Omega_{0,i}^{|m|}$ it is convenient to use the asymptotic expansion of the energies of the impurity ground states $\mathscr{E}_{D0,i}^{|m|}$ and $\mathscr{E}_{A0,i}^{|m|}$ (3) for small values of α, which gives

$$\Omega_{0,i}^{|m|} \approx 2\alpha\sqrt{\mu^2 s^4 + \frac{\hbar^2 s^2 (\lambda_i^{|m|})^2}{R^2}}.$$

The peaks of $\alpha_0(\omega)$ are arranged in the order of the roots of the Bessel functions[9] $\Omega_{0,1}^0 < \Omega_{0,1}^1 < \Omega_{0,1}^2 < \Omega_{0,2}^0 < \Omega_{0,1}^3 < \Omega_{0,2}^1$, which reflect the specific character of quantization of the charge-carrier spectrum in a thin wire with circular cross section. Their maxima are reached at the frequencies

$$\omega_{0,i}^{|m|} = \Omega_{0,i}^{|m|} + \omega_D/2\alpha + \beta_A \omega_D/4,$$

and their half-widths are equal to the half-width of the main peak.

For a wire with radius $R \simeq 10^{-6}$ cm the distance between two neighboring maxima for InSb is equal roughly to ω_D ($\omega_D \simeq 10^{12}$ s^{-1}), and the intensity of the peaks falls as ω^{-1}.

The transitions of the electron from the acceptor ground state $(n=0,\ i=1,\ m=0)$ to the first excited donor state $(n=1,\ i=1,\ m=0)$ correspond to the peak with absorption edge at the frequency

$$\Omega_{1,1}^0 = [E_g - |\mathscr{E}_{D1,1}^0| - |\mathscr{E}_{A0,1}^0|]/\hbar,$$

which is substantially shifted away from $\Omega_{0,1}^0$ toward shorter wavelengths. For the above-indicated parameter values $\Omega_{1,1}^0 \approx 3 \times 10^{14}$ s^{-1}.

[1] A. P. Dzhotyan, É. M. Kazaryan, and A. S. Chirkinyan, Fiz. Tekh. Poluprovdn. **30**, 1085 (1996) [Semiconductors **30**, 575 (1996)].
[2] G. M. Dohler, Phys. Status Solidi B **45**, 705 (1971).
[3] E. O. Kane, J. Phys. Chem. Solids **1**, 249 (1957).
[4] H. N. Spector and J. Lee, Am. J. Phys. **53**, 248 (1985).
[5] S. A. Artyunyan and É. M. Kazaryan, Izv. Akad. Nauk Arm. SSR, Fiz. **12**, 16 (1977).
[6] A. I. Anselm, *Introduction to the Theory of Semiconductors* [in Russian] (Moscow, 1978).
[7] É. M. Kazaryan and A. A. Kirakosyan, Sb. VIMI Riport [in Russian], B4 (1975).
[8] A. A. Kirakosyan and É. A. Sarkisyan, Izv. Akad. Nauk Arm. SSR, Fiz. **19**, 129 (1984).
[9] E. Jahnke, F. Emde, and F. Lösch, *Tables of Higher Functions*, 6th ed. (McGraw-Hill, New York, 1960).

Translated by Paul F. Schippnick

Characterization of GaAs/ $In_xGa_{1-x}As$ quantum-dot heterostructures by electrical and optical methods

V. Ya. Aleshkin, D. M. Gaponova, S. A. Gusev, V. M. Danil'tsev, Z. F. Krasil'nik, A. V. Murel, L. V. Paramonov, D. G. Revin, O. I. Khrykin, and V. I. Shashkin

Institute for Microstructure Physics, Russian Academy of Sciences, 603600 Nizhny Novgorod, Russia
(Submitted March 3, 1997; accepted for publication June 7, 1997)
Fiz. Tekh. Poluprovodn. **32**, 111–116 (January 1998)

Results of electrical and optical studies of GaAs/$In_xGa_{1-x}As$ heterostructures are reported. The aim of these studies was to identify the quantum dots and develop a technology of their growth by spontaneous transformation of an $In_xGa_{1-x}As$ layer. The surface charge at the depth of the quantum dots and their surface density as a function of the deposition time of this narrow-band material are estimated by $C-V$ profiling. A photoluminescence study of the quantum dots revealed peculiarities of the filling of their electron states at various excitation levels. The influence of Coulomb interactions on the optical properties of the quantum dots is discussed.
© *1998 American Institute of Physics.* [S1063-7826(97)00912-5]

A number of studies have been dedicated in recent years to the study of strained GaAs/$In_xGa_{1-x}As$ heterostructures. Of especial interest is the possibility of fabricating high-quality quantum layers and quantum dots based on them. The formation of quantum dots as a result of self-organization in strained heterostructures is a possible alternative to lithographic methods of creating such objects. The first studies of quantum-dot heterolasers based on GaAs/ $In_xGa_{1-x}As$ structures confirm this possibility.[1,2] Once an understanding of self-organization processes is formed, factors are found facilitating the attainment of homogeneous size and shape of the quantum dots and their ordered arrangement in the layer(s). In this paper we report the results of optical and capacitance studies of arrays of quantum dots in GaAs/$In_xGa_{1-x}As$ heterostructures grown by metalloorganic chemical vapor deposition (MOCVD).

1. TECHNOLOGY

GaAs/$In_xGa_{1-x}As$ heterostructures were grown epitaxially in the gaseous medium H_2-$Ga(CH_3)_3$–$In(CH_3)_3$–AsH_3 in an atmospheric-pressure vertical reactor with inductive heating of the substrate. We used both semi-insulating and low-resistance GaAs substrates disoriented 2° relative to the [100] plane in the (110) direction. The growth temperature was varied in the range 450–600 °C for InGaAs and 550–650 °C for GaAs.

It was found that for small rates of growth using MOCVD, $v<40$ nm/min, surface diffusion of the adatoms was substantial, which favors layered growth. Growth rates in the range $v\sim 15-40$ nm/min turned out to be optimal for growth of quantum-dot structures. For growth rates in the range 70 nm/min$<v<100$ nm/min the surface of the layers turns out to be nonplanar. In layers grown at higher rates of growth $v>100$ nm/min, three-dimensional islands of the solid solution $In_xGa_{1-x}As$ are formed, observed on a JEM-2000 electron microscope on platinum–carbon replicas. For $x>0.4$ even at low rates of growth, regardless of the state of the GaAs surface, such islands form due to strong lattice mismatch of the heterolayers. This promotes normal rather than layered growth.

The examined structures were epitaxial n-GaAs layers of thickness 0.5 μm with electron concentrations in the range $(1.5-3)\times 10^{17}$ cm^{-3}. An $In_xGa_{1-x}As$ layer was built into these layers at a distance of 0.15 μm from the surface, whose parameters were controlled by the duration and rate of deposition. Table I lists the parameters of samples grown under different conditions, whose electrical and optical characteristics are discussed below.

2. $C-V$ PROFILING

Measurements of the capacitance–voltage characteristics of the Schottky barrier to the heterostructure allows one to determine the surface charge σ for the populated electron states in the solid solution $In_xGa_{1-x}As$. For the investigated capacitance–voltage characteristics a diode with a Schottky barrier 500 μm in diameter was formed on the surface of the structure by thermal sputtering of aluminum through a metal mask. The capacitance–voltage characteristics were measured at frequencies of 1 MHz, 10 kHz, and 1 kHz with an E7-12 admittance meter and an E7-14 admittance meter. The measurements were performed at 300, 80, and 4.2 K.

The GaAs layers had the following electrical characteristics. The electron mobility for a dopant impurity concentration of 2×10^{17} cm^{-3} was 4500 cm^2/(V·s). The concentration of deep levels, estimated from measurements at 300 and 80 K of the $C-V$ profiles, did not exceed $(1-2)\times 10^{16}$ cm^{-3}.

The built-in $In_xGa_{1-x}As$ depletes the adjacent regions of carriers. A plateau was observed in the capacitance–voltage characteristics which is characteristic of structures with quantum wells or dots,[1)] where the capacitance remains nearly constant, which has to do with overstepping of the edge of the depleted region by the quantum layer.[3] Typical $C-V$ characteristics are shown in the inset in Fig. 1, which shows the dependence $1/C^2(V)$ for sample H153, measured at a frequency of 1 MHz at temperatures of 300, 80, and 4.2 K. Lowering the temperature leads to a sharper definition

TABLE I.

Sample number	Mole fraction x	Layer thickness $In_xGa_{1-x}As$, nm	Growth rate $In_xGa_{1-x}As$, nm/min	Growth time, s
H128	0.15	5	30.5	
H135	0.38	5	26	
H138	0.66	2.5	36	
H149	1		5	2
H150	1		5	4
H151	1		5	8
H152	1		5	16
H153	1		5	32
H155	1		5	12
H156	1		5	64
H158	1		5	96

of the characteristic segments of the capacitance–voltage characteristic because of the decrease in the smearing associated with the Debye screening length. The calculated concentration profile (without allowance for the quantum-mechanical peculiarities of nanostructures) is shown in Fig. 1. The electron concentration peak falls into the region of the potential well and the depleted layers are located near this peak. Below we will discuss the relative variation of these quantities as functions of the InAs deposition time.

The InAs deposition time InAs t_{dep} in the examined series of samples was varied from 2 s to 96 s. For the obtainable sensitivity of finding the density of electronic states in the solid solution, where the latter is determined by the carrier concentration in the GaAs epitaxial layer, the minimum deposition time at which the concentration peak could be discerned was 4 s (for sample H150). In this case the height of the N_{CV} peak is equal to 0.1×10^{17} cm^{-3} at 80 K.

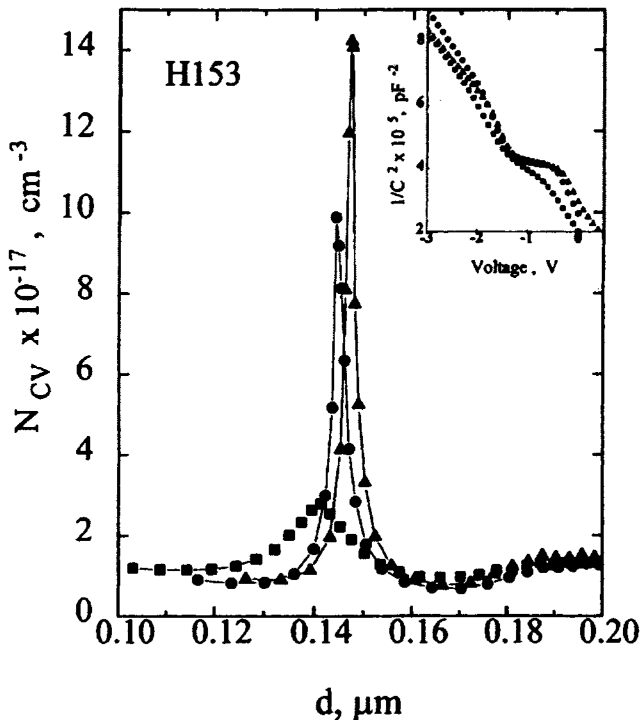

FIG. 1. Concentration profile $N_{CV}(d)$, calculated from the $C-V$ characteristics for sample H 153, d is the depth from the surface of the structure, $T=300$ (■), 77 (●), 4.2 K (▲).

It is possible to determine σ in the region of the InAs layer from the magnitude of the nearly constant capacitance step in the $C-V$ characteristic (see inset in Fig. 1)[3] or by integrating the peak $N_{CV}(x)$. The value of σ can be used to estimate the surface density N_s of the InAs quantum dots (the following sections present experimental confirmation that quantum dots are indeed formed in the examined series of samples) by noting that $\sigma=2eN_s\beta$, where $\beta\leqslant1$ is the quantum states filling factor.

3. OPTICAL MEASUREMENTS

Optical diagnostics of the heterostructures were obtained by photoluminescence (PL), photoconductivity (PC), and interband absorption. For photoluminescence, a continuous He–Ne laser or pulsed LTI-404 laser operating at 532 nm was used as the excitation source. The excitation power was 10 W/cm^2 in the continuous regime and was varied from 10^3 to 10^6 W/cm^2 in the pulsed regime. The photoluminescence signal was passed through an MDR-23 monochromator and detected by an FÉU-62 liquid-nitrogen cooled photomultiplier. In the pulsed regime the output signal of the photomultiplier was passed through a strobe-integrator and averaged. Interband absorption was measured on a BOMEM DA-36 Fourier spectrometer. The photoconductivity was investigated in the transverse-current-flow geometry. In this case, as the tunable source we used radiation from a quartz halogen lamp passed through a monochromator. A nickel layer, semitransparent to the probe light and forming a Schottky barrier, was deposited on the surface of the sample. The second contact was the low-resistance n^+-GaAs substrate. To make the $In_xGa_{1-x}As$ layers fall within the depleted region, reverse bias was applied to the sample. The measurements were made at 77 and 4.2 K.

The objective was to identify the quantum-well and quantum-dot structures from peculiarities of their optical properties, based on the substantial differences in their density of states. Photoluminescence measurements of sample H128 (width of the layer of solid solution 5 nm) demonstrated the high quality of the quantum-well structures. The half-width of the photoluminescence peak did not exceed 6 meV at 77 K (Fig. 2) and 2.8 meV at 4.2 K. In some of the runs, to decrease the effect of inhomogeneity of the region from which photoluminescence was observed, we decreased the size of the laser spot from 50 to 20 μm, which caused the half-width of the photoluminescence peak of sample H128 to decrease to 3.8 meV at 77 K. This figure shows the interband absorption spectrum in which the narrow exciton absorption line associated with the quantum well is clearly visible.

The nature of the photoluminescence from the quantum well at high pump levels reflects filling of the upper levels in the quantum well by photoexcitation carriers.[6] With increase of the excitation power, the main photoluminescence line from the quantum well broadens toward higher energies; luminescence corresponding to transitions between subsequent quantum-well levels then appears. As the quantum well is filled by photocarriers, the GaAs photoluminescence peak also begins to grow. Figure 3 shows photoluminescence

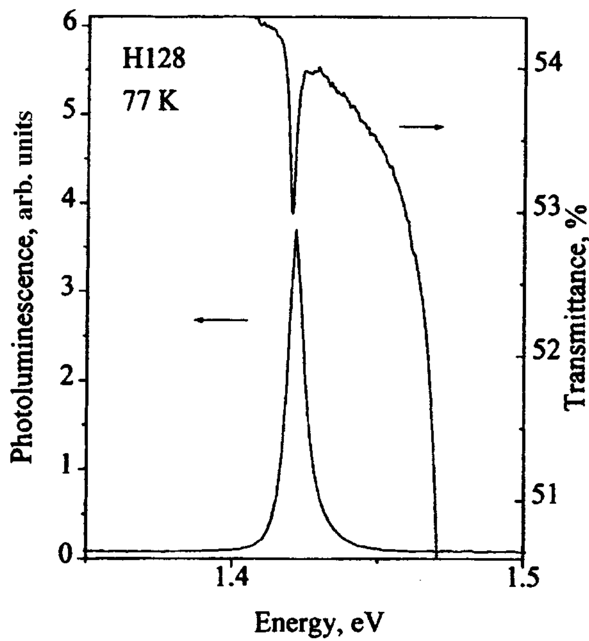

FIG. 2. Transmittance and photoluminescence spectra for sample H128.

spectra for a series of power levels of the exciting laser and the photoconductivity spectrum of sample H135 with an $In_{0.38}Ga_{0.62}As$ quantum well of width 5 nm. According to theoretical calculations, the two plateaus (1.3–1.36 eV and 1.39–1.46 eV) in the photoconductivity spectrum correspond to transitions between the first electron quantum-well level and first hole quantum-well level and between the second hole level and the conductivity band, respectively. Features in the photoluminescence and photoconductivity spectra are well aligned in energy.

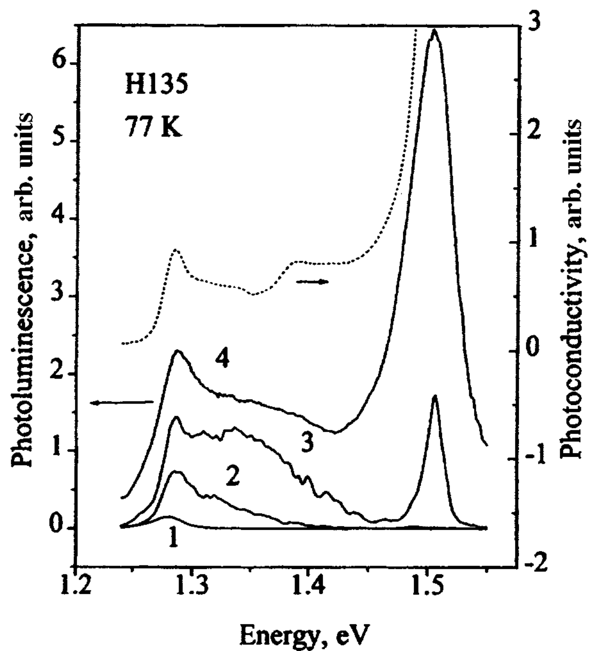

FIG. 3. Photoluminescence and photoconductivity spectra for sample H135 for different levels of excitation, W/cm^2: *1* — 10^3, *2* — 10^4, *3* — 10^5, *4* — 10^6.

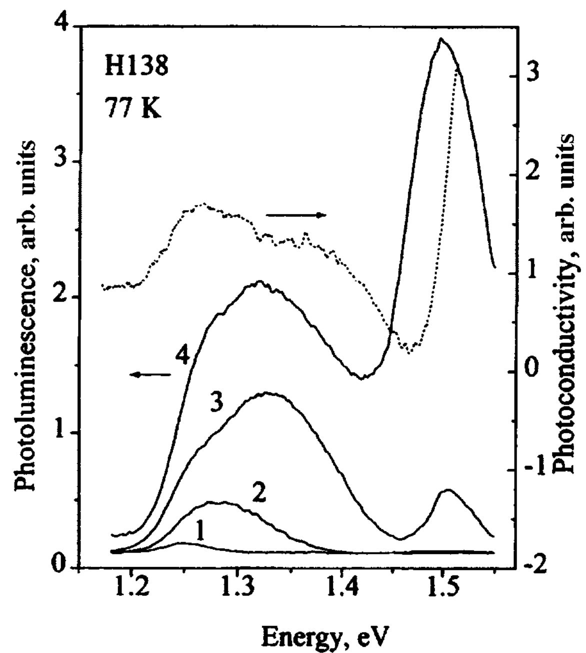

FIG. 4. Photoluminescence and photoconductivity spectra for sample H138 for different levels of excitation, W/cm^2: *1* — 10^3, *2* — 10^4, *3* — 10^5, *4* — 10^6.

As was noted in Sec. 1, at high growth rates or values of $x > 0.4$ nanometer-sized islands were observed on the surface of the solid solution in an electron microscope. These islands are imbedded predominantly on the steps separating the terraces.[2)] These formations were identified as $In_xGa_{1-x}As$ quantum dots arising as a result of strong lattice mismatch of GaAs and the solid solution. In the photoluminescence spectra of such objects the peaks were observed to be shifted toward higher energies in comparison with the calculated position determined from the conditions of fabrication. Thus, for example, based on the growth regimes of sample H138, the width of the $In_{0.66}Ga_{0.34}As$ solid solution can be estimated to be 2.5 nm under conditions of layered growth, which corresponds to the position of the photoluminescence peak at 1.16 eV. The measurements gave a different value—1.25 eV (spectrum *1* in Fig. 4). Similarly to how we proceeded with the quantum wells, we inferred filling levels of the electronic states in the quantum dots at high excitation levels (samples with $x > 0.4$) from the photoluminescence spectra. Figure 4 shows typical photoluminescence spectra for the quantum dots for a series of pump levels overlaid by the photoconductivity spectrum. At all excitation power levels the line shape consists of a superposition of δ-function–like lines of radiative recombination between states in the dots[7,8] so that the uplift (to the point of transformation into a plateau) of a short-wavelength shoulder at high excitation levels characteristic of quantum wells is absent. The plateau corresponding to the two-dimensional density of states in the photoconductivity spectrum is also absent. As the excitation power is increased, the photoluminescence line corresponding to luminescence from the quantum dots (~ 1.25 eV) broadens somewhat and a new maximum appears at higher energies (~ 1.35 eV). The shape

of the lines remains nearly symmetrical. At higher excitation levels excited states in the quantum dots (in addition to their ground states) probably also begin to luminesce, and also smaller-size dots. The symmetry of shape also testifies to the zero-dimensional density of states of the luminescing objects. For filling of almost all the states in the quantum dots by photo-excited carriers, starting at a pump power of 10^5 W/cm^2 luminescence appears from the GaAs layers. The significant width of the photoluminescence peak may be due to dispersion of the size of the quantum dots or to inhomogeneity of composition of the solid solution. The above-described peculiarities in the photoluminescence spectra allow us to conclude that we have observed photoluminescence of quantum dots.

4. DISCUSSION

The transformation of an InAs quantum layer into quantum dots was studied by observing differences in the photoluminescence of samples with different growth time of the pure InAs (H149–H158). In this series of samples photoluminescence was observed if the deposition time exceeded 8 s. As the deposition time was increased, the line corresponding to photoluminescence of InAs shifted toward longer wavelengths (this was also observed in Ref. 9). To analyze the photoluminescence spectra, it is convenient to express the amount of deposited InAs in units of nominal monolayers $n_{\rm imag}$ as if layered growth had taken place. On the basis of the data on the growth of the wetting layer for relatively short deposition times ($t_{\rm dep}<16$ s) $n_{\rm imag}\approx t_{\rm dep}/8$ s. Figure 5a plots the dependence of the position of the photoluminescence peak for this series of samples and its half-width as functions of $n_{\rm imag}$ under the assumption of extending the relation between $n_{\rm imag}$ and $t_{\rm dep}$ to the entire range of growth times. It can be readily seen from this figure that there exist two regions of characteristic dependence: $n_{\rm imag}<4$, when growth of the wetting layer takes place, and $n_{\rm imag}>4$, when InAs objects with dimensionality lower than that of a quantum well (quantum dots) are formed. This conclusion is supported, in particular, by the conclusions of other studies on breakdown of layered growth of InAs for such high quantities of deposited material due to elastic deformation effects.[10] At larger values of $n_{\rm imag}$ these objects become larger, accompanied by an increase in the spread in their size, which leads to a broadening and further shift of the photoluminescence peak.

As one goes from the layered mechanism of growth to three-dimensional formation of islands, the estimate of $n_{\rm imag}$ can become inexact since the rate of InAs deposition from the gas phase will change. To explain this circumstance, we will compare the photoluminescence and $C-V$ profiling data. From the $C-V$ profiling results we can estimate the surface charge accumulated in the two-dimensional layer for $t_{\rm dep}\leqslant 16$ s, or $n_{\rm imag}\leqslant 2$ (Fig. 5b), and also the position of the Fermi level E_F in it. The estimates show the Fermi level to lie 40 meV below the bottom of the GaAs conduction band at the layer boundary and noticeably higher than the electron ground-state energy in the layer (with which, strictly speaking, is also connected charge redistribution in the structure). For $t_{\rm dep}=32$ s ($n_{\rm imag}=4$) quantum dots are formed on the

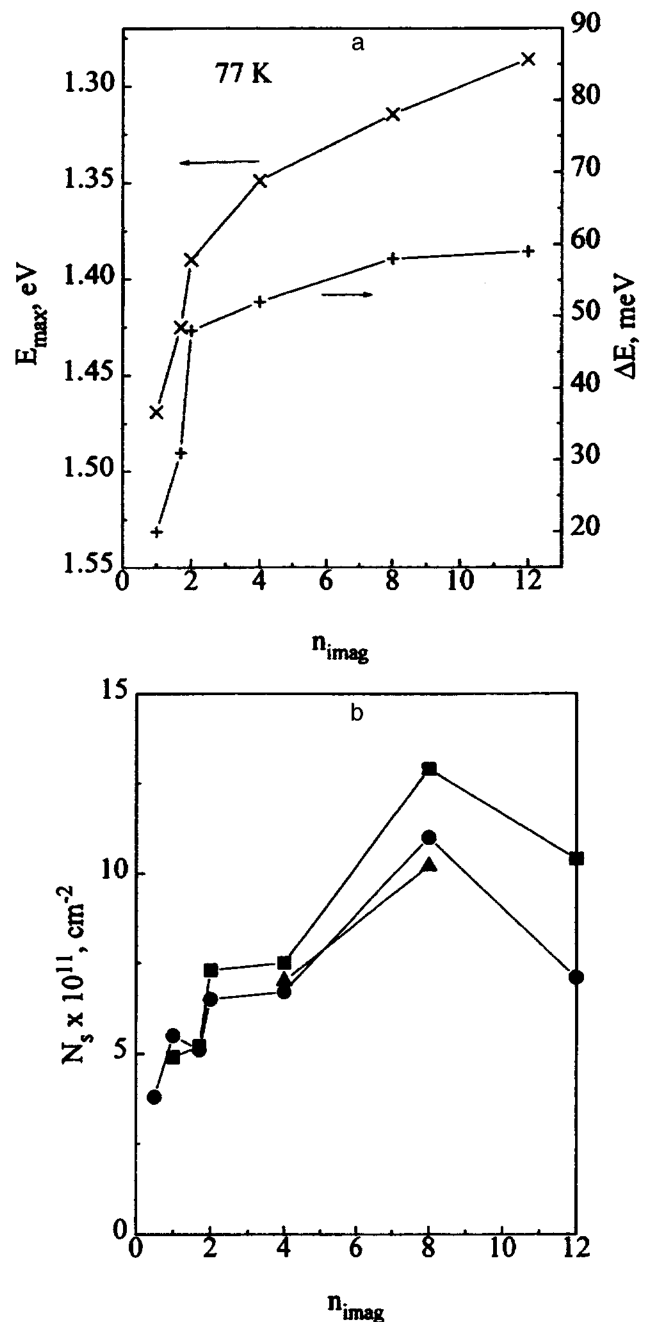

FIG. 5. Position of the maximum ($E_{\rm max}$) and the peak half-width (ΔE) of photoluminescence (a) and surface density of states N_s (b) as functions of the amount of deposited InAs (in nominal monolayers $n_{\rm imag}$). $T=300$ (■), 77 (●), 4.2 K (▲).

surface of the two-dimensional wetting layer. From the position of the photoluminescence line, based on the model of pyramidal shape of the dots,[11] we can estimate their size and the electron ground-state energy, which also turns out to lie below the Fermi level and is consequently filled. This allows us to set the filling factor of the quantum dots, β, equal to unity and find their surface concentration from the $C-V$ measurements. In turn, knowing the surface concentration and physical volume of a single dot, it is not hard to show that as $t_{\rm dep}$ is increased from 16 s to 32 s, the quantity of deposited InAs grows by 30%, not 100%. Such a change in

the rate of growth indicates a shift in the growth mechanism from layered to island-forming. The validity of this assertion is tied up, of course, with the applicability of the model of pyramidal shape of the quantum dots.

With further increase of t_{dep}, the quantum dots increase in size. A second quantum-well level appears, with the filling of which N_s should double, as is observed for the structure with $t_{dep}=64$ s. Continued deposition of InAs should lead to overlap of the quantum dots and formation of a quasicontinuous layer. The growth on it of a GaAs finishing (cap) layer should be accompanied by the formation of a layer with an increased content of dislocations and structural defects. Electrochemical $C-V$ profiling, sensitive to imperfections in the crystal structure of semiconductors,[12] shows that the GaAs cap layer for structures H156 and H158 (deposition times 64 s and 96 s, respectively) differs from the underlying matrix. This is seen first in the fact that a GaAs cap layer of thickness 0.1 μm undergoes electrochemical etching without illumination and for zero bias, which is not usually observed for n-GaAs. Second, electrochemical $C-V$ profiling gives p-type conductivity for the cap layer of sample H158, which is indicative of a high concentration of deep levels of acceptor type. Such a phenomenon was observed earlier in ion-damaged n-GaAs layers.[13]

5. CONCLUSIONS

Identification of zero-dimensional nano-objects based on $GaAs/In_xGa_{1-x}As$ heterostructures has proved to be possible because of the combined use of optical methods of $C-V$ profiling and electron microscopy. This in turn has made it possible to develop the MOCVD technology of quantum-dot formation during spontaneous transformation of the wetting layer of the solid solution. The technology of growing quantum dots in $GaAs/In_xGa_{1-x}As$ heterostructures with model composition x close to unity has shown itself to be more advanced, but the regularities of formation of islands in structures with $x\sim0.4$ are less pronounced and require further study.

The most reliable information about the presence of quantum dots in a heterostructure can be operationally obtained by the photoluminescence method with repeated measurements at different intensities of the exciting radiation. Such measurements are based on the δ-function–like nature of the density of states in a quantum dot. Here it is important to distinguish other objects with similar properties of the density of states—excitons, point defects. These studies are central to the present work and were carried out in conjunction with other optical and electrical methods in comparison with similar measurements of low-dimensional objects in $GaAs/In_xGa_{1-x}As$ quantum-dot heterostructures.

In conclusion, we may discuss the possibilities of another, apparently effective method of observing quantum dots (absorption spectroscopy). It is well known that spatial localization of electron motion increases their Coulomb interaction energy. In quantum dots, where the motion of the electrons is localized in three directions, Coulomb interaction leads to a number of phenomena which are absent in quantum wells and quantum wires. Because of the strong Coulomb interaction, the number of electron and hole states in a quantum dot, and also their energies, depend substantially on the number of electrons and holes present in it. Analogous phenomena are characteristic of simple and multicharged centers in semiconductors. The dependence of the energy spectrum of a quantum dot on its filling by charge carriers leads to peculiarities in the Burstein–Moss effect.

Let us consider two cases: 1) the Coulomb interaction energy of two electrons E_{ee} exceeds the ionization energy of the ground state of the electron E_{1e} in the quantum dot, and 2) the opposite case $E_{1e}>E_{ee}$. In the first case, only one electron can be found in the quantum dot in the absence of a photohole. Upon the absorption of a photon (here and in what follows we are dealing with interband transitions between quantum-well levels) a hole with energy E_{1h} and an electron with energy E_{1e} with interaction energy $E_{eh}(E_{eh}>0)$ are generated in the quantum dot. Interband absorption in the initially "empty" quantum dot is possible with a precisely fixed photon energy $E_0=E_g-E_{1e}-E_{1h}-E_{eh}$ (E_g is the width of the band gap of a wideband material). In this case the photo-induced electron and hole can be in either of two spin states. If in the initial state of the quantum dot an electron is already found in it, then the energy of the absorbed photon will vary by the interaction energy of this electron with the generated electron–hole pair $(E_0)'=E_0-E_{eh}+E_{ee}$. The generated photoelectron can occupy only one free spin state. Therefore, the probability of absorption of the photon by a charged dot should be half that for absorption by a neutral dot. If $E_{ee}>E_{1e}-E_{eh}$, then the initially charged quantum dot is not able to absorb a photon. Thus, interband absorption by a charged quantum dot and by a neutral quantum dot differs in intensity and frequency.

In the second case, more than one electron may be placed in the discrete levels of the quantum dot. If there is only one quantum-well level, which is occupied by two electrons in the quantum dot, then absorption at the frequency of the interband transition between their ground states is impossible. In the remaining variants it is possible to invoke the foregoing arguments.

This work was carried out with the support of Grants No. 95-02-05870, 95-02-05606, and 97-02-17337 from the Russian Fund for Fundamental Research and Grants No. 2-018/3 and 2-007 from the Ministry of Science and Technology Programs.

We are grateful to Yu. N. Drozdov and M. N. Drozdov for carrying out the x-ray diffraction analysis and elemental analysis of the structures.

[1)]These quantum objects are difficult to distinguish on the basis of the $C-V$ profiles.[4,5] Corresponding conclusions based on the optical measurements are made in the following section.

[2)]By appropriate selection of the GaAs growth regime the width of these terraces can be varied from 8.1 to 60 nm with the height of the steps varying correspondingly from 0.28 to 2.1 nm.

[1] Zh. I. Alferov, N. A. Berg, Yu. A. Egorov, A. E. Zhukov, P. S. Kop'ev, A. O. Kosogov, I. L. Krestnikov, N. N. Ledentsev, A. V. Lunev, M. V. Maksimov, A. V. Sakharov, V. M. Ustinov, A. F. Tsatsul'nikov, Yu. M. Shernyakov, and D. Bimberg, Fiz. Tekh. Poluprovodn. **30**, 351 (1996) [Semiconductors **30** 194, (1996)].

[2] Zh. I. Alferov, N. Yu. Gordeev, S. V. Zaĭtsev, P. S. Kop'ev, I. V. Kochnev, V. V. Komin, I. L. Krestnikov, N. N. Ledentsev, A. V. Lunev, M. V.

maksimov, S. S. Ruvimov, A. V. Sakharov, A. F. Tsatsul'nikov, Yu. M. Shernyakov, and D. Bimberg, Fiz. Tekh. Poluprovodn. **30**, 357 (1996) [Semiconductors **30**, 197 (1996)].
[3] V. Ya. Aleshkin, E. V. Demidov, B. N. Zvonkov, A. V. Murel', and Yu. A. Romanov, Fiz. Tekh. Poluprovodn. **25**, 1047 (1991) [Sov. Phys. Semicond. **25**, 631 (1991)].
[4] P. N. Brounkov, S. G. Konnikov, T. Benyatton, and G. Guillot, Phys. Low-Dimens. Semicond. Struct. **10/11**, 197 (1995).
[5] P. N. Brudnikov, S. G. Konnikov, V. M. Ustinov, A. E. Zhukov, A. Yu. Egorov, M. V. Maksimov, N. N. Ledentsev, and P. S. Kop'ev, Fiz. Tekh. Poluprovodn. **30**, 924 (1996) [Semiconductors **30**, 492 (1996)].
[6] V. A. Sleshkin, Z. F. Krasil'nik, and D. G. Revin, Fiz. Tekh. Poluprovodn. **27**, 1190 (1993) [Semiconductors **27**, 655 (1993)].
[7] M. Grundmann, J. Christen, N. N. Ledentsov, J. Böhrer, D. Bimberg, S. S. Ruvimov, P. Werner, U. Richter, U. Gösele, J. Heydenreich, V. M. Ustinov, A. Yu. Egorov, A. E. Zhukov, P. S. Kop'ev, and Zh. I. Alferov, Phys. Rev. Lett. **74**, 4043 (1995).
[8] J.-Y. Marzin, J.-M. Gérard, A. Izraël, D. Barrier, and G. Bastard, Phys. Rev. Lett. **73**, 716 (1994).
[9] B. N. Zvonkov, E. R. Lin'kova, I. G. Malkina, D. O. Filatov, and A. L. Chernov, JETP Lett. **63**, 439 (1996).
[10] W. J. Schaffer, M. D. Lind, S. P. Kowalchuk, and R. V. Grant, J. Vac. Sci. Technol. B **1**, 688 (1983).
[11] M. Grundmann, O. Stier, and D. Bimberg, Phys. Rev. B **52**, 11969 (1995).
[12] P. Blood, Semicond. Sci. Technol. **1**, 7 (1986).
[13] Yu. A. Danilov, A. V. Murel', and I. Yu. Drozdova, Vysokochistye Veshchestva **2**, 71 (1995).

Translated by Paul F. Schippnick